UNIVERSIDAD DE CONCEPCIÓN
DIRECCIÓN DE POSTGRADO

ON THE PREDICTION OF THERMODYNAMIC AND STRUCTURAL PROPERTIES IN SYSTEMS OF DEEP EUTECTIC SOLVENTS BY MOLECULAR MODELING TECHNIQUES

POR

Esteban Alejandro Cea Klapp

Tesis presentada a la Dirección de Postgrado de la Universidad de Concepción para optar al grado académico de Doctorado en Ciencias de la Ingeniería con Mención en Ingeniería Química

Profesor guía

Prof. José Matías GARRIDO
Universidad de Concepción

Profesor co-guía

Prof. Roberto CANALES
Pontificia Universidad Católica de Chile

Comité de Evaluación

Prof. Andrés MEJÍA
Universidad de Concepción

Prof. Lourdes F. VEGA
Khalifa University

Prof. Frederico TAVARES
Universidade Federal do Rio de Janeiro

junio 2025
Concepción (Chile)

Acknowledgements

First and foremost, I would like to express my deepest gratitude to my advisors, Professor José Matías Garrido and Professor Roberto Canales. Beyond their invaluable academic guidance throughout this thesis, we have built a strong and genuine friendship over the years—something I truly cherish. Their support, encouragement, and mentorship have been essential in shaping both this work and my growth as a researcher.

I would also like to sincerely thank the members of my thesis committee—Professors Andrés Mejía, Lourdes Vega, and Frederico Tavares—for dedicating their time to review this thesis and for their insightful feedback, which has undoubtedly enriched its quality.

Throughout the course of my Ph.D., I was fortunate to carry out several research stays. I am especially thankful to the professors who hosted me during these experiences: Professor Christoph Held at TU Dortmund, Professor Manuel Piñeiro at the University of Vigo, and Professor Edward Maginn at the University of Notre Dame. Their guidance, generosity, and scientific input significantly contributed to my development.

I am also grateful to my loyal collaborators—Nicolás Gajardo-Parra, Andrés Arroyo, Sebastián Ormazábal, Bastián González, Paulo Aravena, and Héctor Quinteros—whose contributions are reflected across multiple chapters of this thesis. It has been a pleasure to work alongside such talented colleagues.

To my family, for their unconditional love, unwavering support, and encouragement throughout every step of this journey—thank you.

Lastly, I want to thank all my friends in Chile and those I had the joy of meeting during my travels. Your companionship and kindness were essential in making this experience so memorable.

To all of you—thank you, sincerely.

Resumen

La creciente demanda por alternativas sostenibles a los disolventes orgánicos convencionales ha incrementado el interés en los *deep eutectic solvents* (DES) debido a su baja toxicidad, biodegradabilidad y propiedades ajustables. Sin embargo, la comprensión integral de su comportamiento termodinámico y estructural —especialmente en presencia de cosolventes, aún es limitada. Esta tesis aborda esto mediante la integración de ecuaciones de estado de base molecular y simulaciones moleculares para predecir y analizar las propiedades de equilibrio de fases y de interfase de DES derivados de precursores verdes como cloruro de colina, betaína, glicoles y terpenos.

Se evaluaron las capacidades predictivas de la ecuación de estado PC-SAFT para una amplia gama de mezclas de DES, evidenciando las limitaciones del enfoque tradicional de componente pseudopuro en sistemas donde ocurre una fuerte asociación cruzada con alcoholes. Se encontró que una estrategia de modelado basada en los componentes individuales permite una mejor representación de las propiedades termodinámicas en exceso y de los equilibrios de fases. Además, se implementó una nueva formulación de la teoría del gradiente de densidad (DGT) combinada con PC-SAFT para describir la tensión superficial utilizando únicamente un parámetro ajustado, lo que permitió analizar esta propiedad y el efecto del cosolvente.

Las simulaciones de dinámica molecular (MD) se emplearon para obtener información a nivel molecular sobre los efectos del agua y de alcoholes de cadena corta en la estructura y propiedades de DES hidrofílicos. Estas simulaciones revelaron la competencia entre interacciones por enlaces de hidrógeno, dando lugar a una reorganización estructural del DES provocando cambios en densidad, viscosidad y tensión superficial. Paralelamente, se generaron datos experimentales originales para una serie de DES hidrofílicos, lo que permitió validar las predicciones teóricas y cubrir vacíos en la literatura, especialmente respecto al efecto del contenido de agua.

Adicionalmente, el estudio se extendió a DES hidrofóbicos basados en mentol, timol y ácido octanoico para la extracción de alcohol furfurílico desde agua. Se midieron por primera vez datos de equilibrio líquido-líquido para estos sistemas. Tanto PC-SAFT como simulaciones de MD con modelos coarse-grained predijeron con éxito el comportamiento de fases, demostrando el potencial del marco propuesto para el diseño de procesos de separación basados en DES.

En conjunto, este trabajo contribuye al avance de modelos termodinámicos predictivos aplicados a DES, ofreciendo herramientas para el diseño racional de disolventes sostenibles con aplicaciones industriales y medioambientales, en apoyo a una química más verde.

Abstract

The growing demand for sustainable alternatives to conventional organic solvents has increased interest in deep eutectic solvents (DESs) due to their low toxicity, biodegradability, and tunable properties. However, a comprehensive understanding of their thermodynamic and structural behavior—especially in the presence of cosolvents—remains incomplete. This thesis addresses this gap by integrating molecular-based equations of state and molecular simulations to predict and analyze the bulk and interfacial properties of DESs derived from green precursors such as choline chloride, betaine, glycols, and terpenes.

The predictive capabilities of the PC-SAFT equation of state were evaluated for a wide range of DES mixtures, revealing the limitations of traditional pseudo-pure component approaches in systems where strong cross-association with alcohols occurs. An individual component modeling strategy was found to better capture excess thermodynamic properties and phase equilibria. A novel implementation of density gradient theory (DGT) combined with PC-SAFT was also developed to describe surface tension using only a single fitted parameter, enabling the analysis of DES surface tension and how it is affected by cosolvent addition.

Molecular dynamics (MD) simulations were employed to provide molecular-level insights into the effects of water and short-chain alcohols on the structure and properties of hydrophilic DESs. These simulations revealed competition among hydrogen-bonding interactions, leading to a reorganization of the DES structure and changes in density, viscosity, and surface tension. In parallel, original experimental data were generated for a series of hydrophilic DESs, providing critical validation for the theoretical predictions and filling gaps in the existing literature, particularly regarding the effect of water.

Additionally, the study was extended to hydrophobic DESs based on menthol, thymol, and octanoic acid for the extraction of furfuryl alcohol from water. Liquid–liquid equilibrium (LLE) data for these systems were measured for the first time. Both PC-SAFT and coarse-grained MD simulations (MARTINI 3) successfully predicted the phase behavior, demonstrating the potential of the proposed framework for the design of DES-based separation processes.

Integrating these molecular modeling techniques advances the predictive capabilities of thermodynamic models for DESs, offering valuable insights for the rational design and optimization of sustainable solvent systems. These advancements contribute to the development of DES formulations tailored for industrial and environmental applications, supporting the transition toward greener chemical processes.

Contents

List of Figures

List of Tables

List of Abbreviations

Abbreviation	Definition
AARD	Average Absolute Relative Deviation
Bet	Betaine
ChCl	Choline Chloride
CN	Coordination Number
DES	Deep Eutectic Solvent
DGT	Density Gradient Theory
EG	Ethylene Glycol
EoS	Equations of State
FA	Furfuryl Alcohol
FVT	Free Volume Theory
G	Glycerol
HBA	Hydrogen Bond Acceptor
HBD	Hydrogen Bond Donor
LA	Levulinic Acid
LINCS	Linear Constraint Solver
LLE	Liquid-Liquid Equilibrium
MD	Molecular Dynamics
MOH	Methanol
NADES	Natural Deep Eutectic Solvent
NEMD	Non-Equilibrium Molecular Dynamics
NMR	Nuclear Magnetic Resonance
OctA	Octanoic Acid
OPLS	Optimized Potential for Liquid Simulations
OS	Organic Solvent
PC-SAFT	Perturbed Chain - Statistical Associating Fluid Theory
Ph	Phenol

PME	Particle-Mesh Ewald
RDF	Radial Distribution Function
RMSD	Root-Mean-Square-Deviations
SAFT	Statistical Associating Fluid Theory
SLE	Solid-Liquid Equilibrium
TBABr	Tetrabutylammonium Bromide
TBACl	Tetrabutylammonium Chloride
Thy	Thymol
TPD	Tangent Plane Distance
TPT1	First-Order Thermodynamic Perturbation Theory
VLE	Vapor-Liquid Equilibrium
VOC	Volatile Organic Compound
12P	1,2-Propanediol
13P	1,3-Propanediol
14B	1,4-Butanediol

List of Symbols

Symbol	**Definition**
a_0	Helmholtz energy density at a local composition
$\tilde{a}^{\text{assoc}}$	Association Helmhotlz energy contribution
$\tilde{a}^{\text{chain}}$	Chain Helmhotlz energy contribution
$\tilde{a}^{\text{disp}}$	Dispersion Helmhotlz energy contribution
$\tilde{a}^{\text{hc}}$	Hard-chain Helmhotlz energy contribution
$\tilde{a}^{\text{hs}}$	Hard-sphere Helmhotlz energy contribution
$\tilde{a}^{\text{res}}$	Hard-residual Helmhotlz energy contribution
A	Helmholtz energy
$\Delta^{A_iB_j}$	Association strength
B	Free-volume overlap parameter
$c_{cosolvent}$	Cosolvent influence parameter
c_{DES}	DES influence parameter
c_{ij}	Influence parameters matrix
$\Delta_m C_{p,i}$	Heat capacity change upon melting condition
d_i	Temperature-dependent segment diameter of a component i
D	Distribution coefficient
E	Energy
$\hat{f}_i$	Fugacity
F_c	Correction factor
$\mathbf{F}$	Force vector
g_{ij}	Radial distribution function
$\mathcal{H}$	Hamiltonian
$\tilde{H}^{\text{res}}$	Residual molar enthalpy
$\Delta_m H_i$	Melting enthalpy
k_{ij}	Binary interaction parameter
L_v	Length FVT parameter

L_z	Box length in the z-direction
m_i	Number of spherical segments
m_i	Particle mass
$\bar{m}$	Mean segment number
M_w	Molecular weight
n_c	Number of components
N	Number of particles
p_ξ	Momentum
P_z	Normal pressure
P	Pressure
r_{cut}	Cut-off distance for interactions calculations
r_{list}	Cut-off distance for the short-range neighbor list
r	Radial distance between two segments
$\mathbf{r}_i$	Particle positions vector
S^{Ai}	Number of association sites of type A
S	Selectivity
T_{ad}	Dimensionless temperature
$T_{m,i}$	Melting temperature
T	Temperature
t	Time
Δt	Time interval
U_{angles}	Angles energy contribution
U_{bonds}	Bonds energy contribution
$U_{\text{non-bonded}}$	Non-bonded energy contribution
U_{torsion}	Torsion energy contribution
U	Potential energy
$u(r)$	Pair potential
v	Molar volume
$\mathbf{v}$	Particle velocity
V	Volume
x_i	Mole fraction of the component i
$\underline{\mathbf{x}}$	Mole fraction vector
X^{Ai}	Fraction of molecules of component i that remain unbonded at site A
Z	Compressibility factor
γ	Surface tension
γ_i	Activity coefficient of a component i in a mixture

$\Gamma_{FA}^{(W)}$	Relative adsorption of FA to water
$\varepsilon^{A_iB_j}$	Association energy
ε	Depth of the potential well
η_0^{mix}	Dilute-gas viscosity of a mixture
η	Packing fraction
η	Dynamic viscosity
$\Delta\eta$	Dense fluid viscosity
κ_T	Isothermal compressibility
$\kappa^{A_iB_j}$	Association volume
λ	Reduced well width
μ_i	Chemical potential of a component *i* in a mixture
π	Number of phases in equilibrium
ρ_m	Number density
ρ	Molar density
$\nabla\rho_i$	Local density gradients
σ	Temperature-independent segment diameter
σ	Collision diameter
τ_P	Time constant for barostat
τ_T	Time constant for thermostat
$\hat{\phi}_i$	Fugacity coefficient of a component
$\Omega^{(2,2)}$	Collision integral
Ω	Possible association sites in a set

1. Introduction

Precisely characterizing fluid systems, from pure substances to complex mixtures, is indispensable to optimize processes in laboratory experiments and large-scale industrial applications. This significance is magnified when considering fluids composed of complex molecules, which are becoming increasingly crucial in the ever-changing landscape of chemical manufacturing. Deep eutectic solvents (DESs) exemplify this relevance, featuring diverse components that exhibit unique phase behaviors and tunable properties for applications like green chemistry, energy storage, and materials synthesis. Understanding the behavior of DESs is difficult because of the complex interactions of their constituent molecules. Accurate DES characterization plays a central role in harnessing their potential across various industries, underscoring the critical role of fluid characterization in modern technology.

Many industrial processes involve fluids that experience physical and chemical transformations and have different properties depending on the desired task. Traditionally, industrial processes have widely used volatile organic compounds (VOCs), such as hydrocarbons, chlorinated solvents, and aromatics. However, their high toxicity, environmental persistence, and contribution to air pollution and human health risks have raised concerns about their sustainability [1, 2]. As a result, accurately predicting thermophysical and transport properties along the phase equilibrium diagram is crucial for industries seeking to enhance product yield, energy efficiency, and environmental sustainability. In this context, understanding the thermodynamic principles governing these transformations and their associated properties enables the design of new environment-friendly and tunable solvents. This has become a central focus of green chemistry, driving the development of the concept of a "green" solvent [3]. Two primary strategies for green solvent development have been proposed: (i) substituting petroleum-derived solvents with those from renewable resources and (ii) replacing hazardous solvents with alternatives that exhibit improved environmental, health, and safety properties [4].

Deep eutectic solvents (DESs) have emerged as a promising alternative in the search for new solvents due to their versatility, as they can be tailored to specific applications [5]. They are prepared by carefully selecting and mixing precursors, typically a hydrogen bond acceptor (HBA) and a hydrogen bond donor (HBD), which are not necessarily liquids in their pure state [6, 7]. When mixed, strong hydrogen-bonding interactions between HBA and HBD cause a significant depression in the melting point of the mixture compared to the ideal behavior, forming a stable liquid phase at the desired operating temperature [8, 9]. However, due to the expense and complexity of measuring entire solid-liquid phase diagrams to confirm the negative deviations from thermodynamic ideality that lead to this deep melting point depression [9, 10], many simple eutectic mixtures are often (incorrectly) classified as DESs in the literature [11].

DESs offer several advantages, including low vapor pressure, chemical and thermal stability, non-flammability, high tunability, and the ability to remain liquid at ambient temperature. In addition, the selected precursors typically possess low toxicity and environmentally friendly properties and are relatively inexpensive. For these reasons, DESs are often classified as "green solvents" [12–16]. DES applications have been reported in biomass processing [17–24], bioprocesses [25–27], gas capture [28–31], biocatalysis [32–36], metal processing [7, 37, 38], pharmaceutical formulations [39–41], and energy applications [42–44], among others. Despite growing interest in DESs, there remains a significant gap in understanding their molecular interactions and physical properties [13].

The wide range of DES applications stems from the extensive variety of DESs reported in the literature, resulting from numerous possible combinations of HBAs and HBDs. Initially, the term DES referred exclusively to mixtures formed from quaternary ammonium salts and HBD [6, 45]. However, it was eventually extended to encompass all eutectic mixtures exhibiting negative deviations from the thermodynamic ideality. Nowadays, DESs are classified into five types based on their precursors. Type I consists of quaternary ammonium salts and metal chlorides, while Type II combines metal hydrates with quaternary ammonium salts. Type III, the most extensively studied in the literature, is typically formed from quaternary ammonium salts and organic compounds such as amides, carboxylic acids, alcohols, or polyols. Type IV consists of metal halides and organic HBDs, whereas Type V, introduced by Coutinho et al. in 2019 [46], consists of non-ionic eutectic mixtures such as those based on phenolic compounds and monocarboxylic acids [47]. In recent years, the search for greener solvents has intensified interest in natural deep eutectic solvents (NADES), a subset of Type III or Type V DESs composed of natural metabolites, including amino acids, organic acids, sugars, and choline derivatives [48].

The wide variety of DES is further increased by introducing an additional solvent along with the original HBA and HBD constituents [11]. Motivations for this approach include intentionally modifying the properties of DES, such as lowering the viscosity [15] or reducing the melting point [49], thereby enhancing their practical applicability. However, the presence of external compounds in DES can sometimes be unintended, either due to DES hygroscopicity or other impurities [50, 51]. Regardless of intent, adding an extra solvent or cosolvent increases the system's complexity by introducing additional intermolecular interactions, which must be carefully considered in the design and application of DES.

Molecular modeling techniques provide a systematic approach to studying the effect of cosolvents on DESs and understanding their influence at the molecular level [11]. Among these techniques, molecular dynamics (MD) simulations [52, 53] stand out as a powerful tool, providing detailed insight into how the addition of cosolvents affects the structural and thermodynamic characteristics of DES. Specifically, MD simulations enable a comprehensive analysis of intermolecular interactions, hydrogen bonding networks, and physicochemical properties, shedding light on the molecular organization and dynamics within these systems [54]. Several studies have successfully used MD to explore DES properties, mainly without the addition of an external solvent. Perkins et al. [55] calculated the thermophysical and transport properties of choline chloride (ChCl)-based DESs, achieving good agreement with experimental thermophysical data, although predicting transport properties remains challenging. Salehi et al. [56] utilized MD simulations, primarily with the OPLS force field, to determine Hildebrand and Hansen solubility parameters. Shehata et al. [57] investigated ChCl–urea DES through MD simulations, elucidating the impact of water content on DES performance as reaction media. Similarly, Atilhan et al. [58] employed MD simulations to evaluate the interactions between DES and nanomaterials, emphasizing the fundamental role of hydrogen bonding in these mixtures. Naik et al. [59] also used MD to examine phase equilibrium in phosphonium- and ammonium-based DESs, analyzing their structural and interaction properties in detail.

Quantum chemistry methods have further complemented these MD-based insights by providing molecular-level clarity on hydrogen bonding and intermolecular interactions despite their much higher computational cost. For example, Wang et al. [54] combined experimental analyses with quantum chemistry techniques to study hydrogen bonding in mixtures of ChCl with polyols, revealing the significant role of chloride–hydroxyl interactions. Ashworth et al. [60] employed ab initio quantum chemistry methods to uncover the complex association patterns within ChCl–urea DES, highlighting the diverse hydrogen bonding interactions that differentiate these mixtures from traditional solvents. Similarly, Abranches et al. [39] studied the design of DESs for pharmaceutical applications using COSMO-RS.

Molecular-based equations of state (EoS), particularly those from the Statistical Associating Fluid Theory (SAFT) family, offer a faster alternative to computationally intensive methods such as MD or quantum chemistry calculations. The SAFT family explicitly incorporates molecular interactions, enabling robust and accurate predictions of phase equilibria and thermodynamic properties, thus effectively bridging molecular-level insights with macroscopic system behavior. SAFT equations are grounded in Wertheim's thermodynamic perturbation theory, effectively capturing the association contributions due to hydrogen bonding interactions, which play a fundamental role in the formation and behavior of DESs. In the literature, several studies have successfully applied different SAFT variants to model DES properties. For example, PC-SAFT has been extensively used to predict gas solubility in DES [61, 62], while soft-SAFT has also demonstrated its capability to accurately model gas solubility and other thermodynamic properties of DES systems [63, 64].

1.1. Hypothesis

The thermodynamic and structural properties of DES can be accurately predicted using molecular modeling techniques, providing critical insights into their behavior in both pure and mixed systems. In this sense, MD simulations combined with molecular-based equations of state (e.g., PC-SAFT) can show the presence of hydrogen bond networks, elucidating the structural ordering introduced by cosolvent addition.

1.2. Main Objective

Predict and analyze the structural and thermodynamic properties of DESs based on green precursors (e.g., choline chloride, betaine, glycols, terpenes), with an emphasis on the effect of cosolvent addition, utilizing MD simulations and molecular-based equations of state such as PC-SAFT.

Specific objectives

- Evaluate the accuracy and predictive capability of PC-SAFT, employing different parametrization strategies, to describe the phase equilibria and thermodynamic properties of the most experimentally studied DESs, namely choline chloride-based DESs.
- Develop and validate a methodology coupling PC-SAFT to predict physicochemical properties such as viscosity and surface tension, and to quantify the effects of cosolvent addition on these properties in various DESs based on green precursors with available experimental data.
- Characterize the structural and thermophysical properties of choline chloride-based DES mixed with short-chain alcohol (e.g., methanol) or water using MD simulations and evaluate the predictive performance of PC-SAFT.
- Apply molecular modeling techniques to investigate the behavior of hydrophobic DESs in the extraction of furfuryl alcohol from water, with a focus on predicting liquid-liquid equilibria.

2. Molecular-based equation of state

This chapter will describe the fundamental framework of the Perturbed Chain - Statistical Associating Fluid Theory (PC-SAFT) equation of state. As a crucial element in the comprehensive modeling of Deep Eutectic Solvents (DESs), PC-SAFT offers a versatile and accurate tool for understanding the complex thermodynamic behavior of these systems. This equation of state provides a robust foundation for describing the intermolecular interactions governing the phase behavior of DES systems. This chapter will explore the theoretical background, mathematical formulations, and practical applications of PC-SAFT, paving the way for a deeper exploration of DES modeling in subsequent sections of this thesis.

2.1. Introduction

Equations of state (EoS) are mathematical models that describe the relationships among key thermodynamic properties of a substance, such as pressure (P), volume (v), and temperature (T). They are crucial in thermodynamics for predicting the behavior of fluids and gases under various conditions and are widely used in chemical engineering, physics, and materials science to model fluid properties and phase equilibria. Introduced in 1873, the van der Waals equation [65] was one of the first EoS to account for the finite size of molecules and intermolecular attractions, improving upon the ideal gas law. Since then, many cubic equations of state—such as the Redlich-Kwong [66], Soave-Redlich-Kwong [67], and Peng-Robinson [68] equations—have been developed, primarily to predict phase equilibria in mixtures [69]. As understanding of molecular behavior has advanced, more elaborate equations have been formulated to better predict the behavior of real gases and fluids.

In this context, the Statistical Associating Fluid Theory (SAFT) [70–73], which employs statistical mechanical methods, particularly Wertheim's first-order thermodynamic perturbation theory (TPT1) [74–77], represents a significant advancement in the equation of state modeling. SAFT is designed to predict the thermodynamic properties of complex fluids with greater precision, particularly those involving molecular associations such as hydrogen bonding [78, 79]. Unlike simpler

EoS models, SAFT takes into account detailed molecular structures, specific interactions, and association effects, making it especially useful for modeling fluids with polar components, polymers, and other complex systems, such as DESs and ILs.

In a typical SAFT-based EoS, the fluid is initially modeled as a collection of equal-sized hard spheres to represent repulsive interactions. Attractive forces are then incorporated through an additional dispersive potential, commonly a square-well or Lennard-Jones potential. To capture molecules that can form chains, the spheres are connected via bonding sites. Specific interaction sites are subsequently introduced along the chains to represent directional interactions such as hydrogen bonding, typically modeled using square-well association potentials. Each of these contributions (reference repulsion, dispersion, chain formation, and association) adds a corresponding term to the residual Helmholtz free energy ($\tilde{a}^{\text{res}}$), as expressed in Eq. 2.1:

$$\tilde{a}^{\text{res}} = \tilde{a} - \tilde{a}^{\text{id}} = \tilde{a}^{\text{seg}} + \tilde{a}^{\text{chain}} + \tilde{a}^{\text{assoc}} \tag{2.1}$$

where $\tilde{a}^{\text{seg}}$ is the segment contribution to the Helmholtz free energy, including both the hard-sphere reference and dispersion terms; $\tilde{a}^{\text{chain}}$ is the contribution from chain formation; and $\tilde{a}^{\text{assoc}}$ is the contribution from association. Additionally, $\tilde{a}$ refers to the reduced Helmholtz energy of the system, while $\tilde{a}^{\text{id}}$ represents the contributions of the ideal gas.

Since Chapman developed the original SAFT model in the 1990s [70–73], several variations have emerged, with the main differences lying in the reference fluid and the potential used to describe it. One of the first modifications was introduced by Huang and Radosz (SAFT-HR) [80, 81], which replaced the Lennard-Jones potential with a square-well potential. Since then, numerous adaptations have been proposed, including SAFT-VR-SW [82, 83], SAFT-VR-Mie [84], soft-SAFT [85, 86], and PC-SAFT [87, 88], among others [89, 90]. Several reviews in the literature provide detailed descriptions of each of these versions, highlighting their achievements and limitations [78, 91–93].

In this thesis, PC-SAFT (Perturbed-Chain SAFT) is used as the primary model to describe the thermodynamic properties of DESs, due to its proven ability to accurately capture systems with significant hydrogen bonding and complex molecular interactions such as ionic liquids (ILs) [94], amino acids [95] and different osmolytes [96, 97]. Developed by Gross and Sadowski [87, 88], PC-SAFT extends the original SAFT model by incorporating chain length effects and more refined descriptions of molecular shape and size, making it particularly well suited for complex fluids, including those with significant non-idealities, such as DES. Its ability to model associating and polar fluids reliably provides a strong framework for capturing the unique interactions in DES systems, such as hydrogen bonding and other specific interactions between components. Furthermore, the flexibility of PC-SAFT in handling mixtures with a wide range of molecular sizes and interactions makes it an ideal choice for modeling DESs, where the molecular structures of both the HBD and HBA critically influence thermodynamic behavior.

2.2. PC-SAFT molecular model

In the PC-SAFT framework, unlike most SAFT versions, dispersive interactions are incorporated into the chain contribution rather than the hard-sphere reference term. The pair potential between segments in a chain is described using a modified square-well potential, as defined in Eq 2.2 [98].

$$u(r) = \begin{cases} \infty & r < (\sigma - 0.12\sigma) \\ 3\epsilon & (\sigma - 0.12\sigma) \leq r < \sigma \\ -\epsilon & \sigma \leq r < \lambda\sigma \\ 0 & r \geq \lambda\sigma \end{cases} \tag{2.2}$$

Here, $u(r)$ is the pair potential, r is the radial distance between two segments, σ is the temperature-independent segment diameter, ε indicates the depth of the potential well, and λ is the reduced well width.

Based on the modified square-well potential defined in Eq. 2.2 and employing perturbation theory, the PC-SAFT EoS is described as a sum of energetic contributions to the reduced residual Helmholtz energy, as shown in Eq. 2.3,

$$\tilde{a}^{\text{res}} = \tilde{a} - \tilde{a}^{\text{id}} = \tilde{a}^{\text{hc}} + \tilde{a}^{\text{disp}} + \tilde{a}^{\text{assoc}} \tag{2.3}$$

where $\tilde{a}^{\text{hc}}$ is the reduced Helmholtz energy contribution of the hard-chain reference fluid, $\tilde{a}^{\text{disp}}$ represents the contribution of the dispersive interactions, and $\tilde{a}^{\text{assoc}}$ accounts for the association between molecules.

All the contributions of the PC-SAFT EoS to the Helmholtz energy are illustrated in Figure 2.1. This figure shows how m spherical segments form covalent bonds, leading to the formation of the hard-chain reference contribution. The hard-chain reference further accounts for the attractive forces between segments through the dispersion contribution. Finally, if the molecule possesses association sites where highly directional interaction forces can occur, these interactions are captured by the association contribution.

The following sections describe each of these terms in detail.

2.2.1. Hard-Chain reference contribution

The hard-chain reference term in Eq. 2.3 consists of two contributions: the hard-sphere contribution ($\tilde{a}^{\text{hs}}$), which comes from the number of spherical segments in each molecule (m_i), and the chain contribution ($\tilde{a}^{\text{chain}}$), which results from the bonding of these segments within each molecule. This is shown in Eq. 2.4:

$$\tilde{a}^{\text{hc}} = \bar{m}\tilde{a}^{\text{hs}} + \tilde{a}^{\text{chain}} \tag{2.4}$$

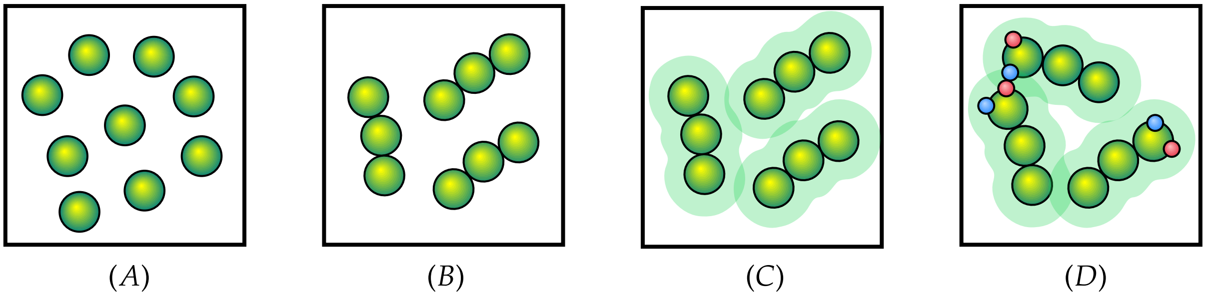
(A) (B) (C) (D)

FIGURE 2.1: Formation of a molecule in the PC-SAFT framework: (A) hard-sphere molecules, (B) hard-chain molecules, (C) molecules with attractive forces due to dispersion, and (D) molecules with association sites exhibiting highly directional interactions.

Here, $\bar{m}$ is the mean segment number in the mixture of n_c components, as given by Eq. 2.5,

$$\bar{m} = \sum_{i=1}^{n_c} x_i m_i \tag{2.5}$$

where x_i is the mole fraction of the molecules of the component i.

The hard-sphere term is given by the expression developed by Boublík [99] and Mansoori et al. [100], which reduces to the formulation proposed by Carnahan and Starling [101] for pure fluids. This is shown in Eq. 2.6,

$$\tilde{a}^{\text{hs}} = \frac{1}{\zeta_0(1-\zeta_3)}\left[3\zeta_1\zeta_2 + \frac{\zeta_2^3}{\zeta_3(1-\zeta_3)^2} + \left(\frac{\zeta_2^3}{\zeta_3^2} - \zeta_0\right)\ln(1-\zeta_3)\right] \tag{2.6}$$

where ζ_n is defined by the number density of molecules, ρ_m, in Eq. 2.7,

$$\zeta_n = \frac{\pi\rho_m}{6}\sum_{i=1}^{n_c} x_i m_i d_i^n \quad n \in \{0,1,2,3\} \tag{2.7}$$

where d_i represents the temperature-dependent segment diameter of a component i, given by Eq. 2.8,

$$d_i = \sigma_i\left[1 - 0.12\exp\left(-3\frac{\varepsilon_i}{k_B T}\right)\right] \tag{2.8}$$

where k_B is the Boltzmann constant.

The chain formation contribution is one of the fundamental terms in any SAFT-type EoS. This contribution is derived from Wertheim's first-order thermodynamic perturbation theory [74–77], which assumes that the segments are tangentially bonded at a distance $r = \sigma$. The resulting expression is given in Eq. 2.9.

$$\tilde{a}^{\text{chain}} = \sum_{i=1}^{n_c} x_i(1 - m_i) \ln g_{ii}(\sigma_{ii}) \tag{2.9}$$

Here, $g_{ii}(\sigma_{ii})$ is the radial distribution function (RDF), which describes how the particle density in a system varies with the distance from a reference particle. PC-SAFT incorporates only the zero-order RDF, as determined by the Boublík [99] and Mansoori et al. [100] expression for a hard-sphere segment, as shown in Eq. 2.10.

$$g_{ij}^{hs}(\sigma_{ij}) = \frac{1}{(1-\xi_3)} + \left(\frac{d_i d_j}{d_i + d_j}\right) \frac{3\xi_2}{(1-\xi_3)^2} + \left(\frac{d_i d_j}{d_i + d_j}\right)^2 \frac{2\xi_2^2}{(1-\xi_3)^3} \tag{2.10}$$

2.2.2. Dispersion contribution

After the hard-chain reference fluid has been defined, the perturbation theory developed by Barker and Henderson is applied to account for the attractive part of the chain interactions [102, 103]. This second-order perturbation theory expresses the Helmholtz free energy as the sum of first- and second-order contributions, as shown in Eq. 2.11

$$\tilde{a}^{\text{disp}} = \tilde{a}_1 + \tilde{a}_2 \tag{2.11}$$

Each contribution can be written in a simplified form, as shown in Eqs. 2.12 [87].

$$\tilde{a}_1 = -2\pi\rho \bar{I}_1(\eta, \bar{m}) \overline{m^2 \epsilon \sigma^3} \tag{2.12a}$$

$$\tilde{a}_2 = -\pi\rho \bar{m} C_1 \bar{I}_2(\eta, \bar{m}) \overline{m^2 \epsilon^2 \sigma^3} \tag{2.12b}$$

Here, $\bar{I}_1(\eta, \bar{m})$ and $\bar{I}_2(\eta, \bar{m})$ are integrals over the intermolecular potential defined in Eq.2.2 and the radial distribution function between segments. The analytical solution is approximated using power series expansions in the reduced segment density (commonly referred to as the packing fraction, η, which is equal to ξ_3 as defined in Eq.2.7), as given by Eqs. 2.13 [87],

$$\bar{I}_1\left(\eta, \bar{m}\right) = \sum_{i=0}^{6} a_i\left(\bar{m}\right) \eta^i \tag{2.13a}$$

$$\bar{I}_2\left(\eta, \bar{m}\right) = \sum_{i=0}^{6} b_i\left(\bar{m}\right) \eta^i \tag{2.13b}$$

where the coefficients a_i and b_i are given by Eqs. 2.14.

$$a_i\left(\bar{m}\right) = a_{0i} + \frac{\bar{m}-1}{\bar{m}} a_{1i} + \frac{\bar{m}-1}{\bar{m}} \frac{\bar{m}-2}{\bar{m}} a_{2i} \tag{2.14a}$$

$$b_i\left(\bar{m}\right) = b_{0i} + \frac{\bar{m}-1}{\bar{m}} b_{1i} + \frac{\bar{m}-1}{\bar{m}} \frac{\bar{m}-2}{\bar{m}} b_{2i} \tag{2.14b}$$

The model constants introduced in these series (a_{ij} and b_{ij}) were fitted to the properties of pure *n*-alkanes (vapor pressure and volumetric data) and can be found in the original publication [87].

In Eq. 2.12, C_1 is an analytical expression related to the compressibility factor and can be calculated using Eq. 2.15,

$$C_1 = \left(1 + \bar{m}\frac{8\eta - 2\eta^2}{\left(1-\eta\right)^4} + \left(1-\bar{m}\right)\frac{20\eta - 27\eta^2 + 12\eta^3 - 2\eta^4}{\left[\left(1-\eta\right)\left(2-\eta\right)\right]^2}\right)^{-1} \tag{2.15}$$

The terms $\overline{m^2\epsilon\sigma^3}$ and $\overline{m^2\epsilon^2\sigma^3}$ arise from applying the van der Waals one-fluid mixing rules to the perturbation terms, resulting in Eqs. 2.16.

$$\overline{m^2\epsilon\sigma^3} = \sum_{i=1}^{n_c}\sum_{j=1}^{n_c} x_i x_j m_i m_j \left(\frac{\varepsilon_{ij}}{k_B T}\right)\sigma_{ij}^3 \tag{2.16a}$$

$$\overline{m^2\epsilon^2\sigma^3} = \sum_{i=1}^{n_c}\sum_{j=1}^{n_c} x_i x_j m_i m_j \left(\frac{\varepsilon_{ij}}{k_B T}\right)^2\sigma_{ij}^3 \tag{2.16b}$$

The parameters for unlike segments are obtained using the conventional Berthelot-Lorentz combining rules [104], as shown in Eqs. 2.17,

$$\sigma_{ij} = \frac{1}{2}\left(\sigma_i + \sigma_j\right) \tag{2.17a}$$

$$\varepsilon_{ij} = \sqrt{\varepsilon_i\varepsilon_j}\left(1 - k_{ij}\right) \tag{2.17b}$$

where the binary interaction parameter k_{ij} is introduced to correct the segment-segment interactions between unlike chains.

2.2.3. Association contribution

The association term forms the foundation for SAFT-type EoS. This term, derived from Wertheim's first-order thermodynamic perturbation theory [74–77], accounts for highly directional interactions, such as hydrogen bonding. It enables the accurate representation of associating fluids by describing the specific interactions between molecules at the association sites. The contribution of the association term to the Helmholtz free energy, which reflects these interactions, is given by Eq. 2.18.

$$\tilde{a}^{\text{assoc}} = \sum_{i=1}^{n_c} x_i \sum_{A\in\Omega}^{|\Omega|} S^{Ai}\left[\ln X^{Ai} - \frac{X^{Ai}}{2} + \frac{1}{2}\right] \tag{2.18}$$

Here, the sum is over the n_c components in the mixture and their respective $|\Omega|$ possible association sites in a set Ω of different kinds of site. S^{Ai} denotes the number of association sites of type A on each molecule of component i, while X^{Ai} represents the fraction of molecules of component i that remain unbonded at the site A.

For every molecule in the mixture, S^{Ai} should be known according to the defined association scheme, while X^{Ai} changes according to the thermodynamic conditions of the system and can be obtained by solving the mass balance shown in Eq. 2.19 [105].

$$X^{Ai} = \left[1 + \rho_m \sum_{k=1}^{n_c} x_k \sum_{B\in\Omega, B\neq A}^{|\Omega|} S^{Bi} X^{Bj} \Delta^{A_iB_j}\right]^{-1} \tag{2.19}$$

Here, $\Delta^{A_iB_j}$ is the association strength between the site type A in component i and the site type B in component j, which can be obtained from Eq. 2.20,

$$\Delta^{A_iB_j} = \sigma_{ij}^3 g_{ij}^{hs}(\sigma_{ij}) \kappa^{A_iB_j}\left[\exp\left(\frac{\varepsilon^{A_iB_j}}{k_B T}\right) - 1\right] \tag{2.20}$$

where $\kappa^{A_iB_j}$, the association volume, is a measure of the volume available for bonding between a site of type A in component i and a site of type B in component j, and $\varepsilon^{A_iB_j}$, the association energy, is the well depth of the site-site interaction potential. If the association is between the same molecule, it is referred to as self-association; otherwise, it is a case of cross-association. Also, the association interaction is symmetrical, which means $\varepsilon^{A_iB_j} = \varepsilon^{B_jA_i}$. In the case where the association site type A cannot associate with site type B, $\varepsilon^{A_iB_j} = 0$, which means $\Delta^{A_iB_j} = 0$ by using Eq. 2.20. Otherwise, the parameters for cross-association can be obtained using the mixing rules of Wolbach and Sandler [106], as given by Eqs. 2.21.

$$\varepsilon^{A_iB_j} = \frac{1}{2}\left(\varepsilon^{A_iB_i} + \varepsilon^{A_jB_j}\right) \tag{2.21a}$$

$$\kappa^{A_iB_j} = \sqrt{\kappa^{A_iB_i}\kappa^{A_jB_j}}\left(\frac{\sqrt{\sigma_i\sigma_j}}{\sigma_{ij}}\right)^3 \tag{2.21b}$$

Association schemes are used to represent or visualize how association occurs between molecules. The association schemes used throughout the literature were originally proposed by Huang and

Radosz [80]. In general, these schemes are simplified by recognizing that there are three types of association sites: positive electron-accepting sites, negative electron-donating sites, and bipolar (or bivalent) sites. Positive sites interact with both negative and bipolar sites, negative sites interact with both positive and bipolar sites, and bipolar sites interact with all sites. Examples of association schemes following this notation are shown in Figure 2.2.

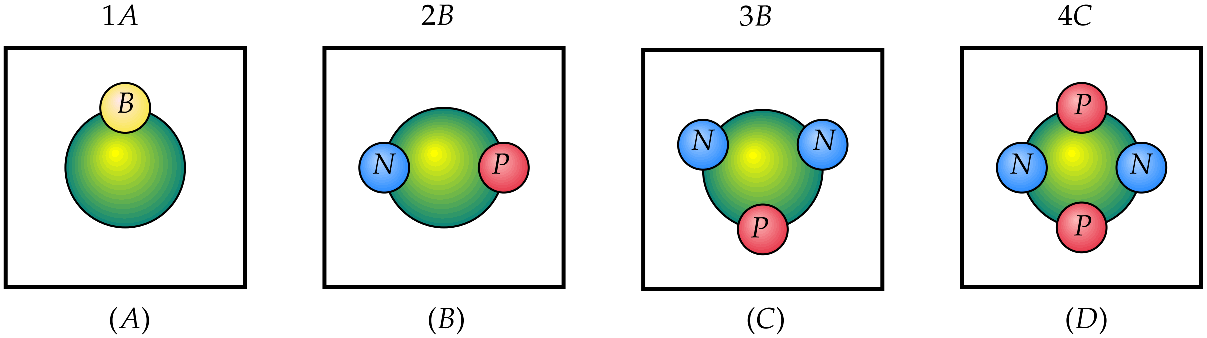

FIGURE 2.2: Examples of association schemes based on Huang and Radosz notation [80], considering three different types of sites: Bivalent (B), Positive (P), and Negative (N). The association schemes shown are: (A) 1A, (B) 2B, (C) 3B, and (D) 4C.

2.3. PC-SAFT parametrization

Following the detailed discussion of the individual contributions in PC-SAFT, attention is now directed toward the parametrization of the model, which requires the definition of its molecular parameters. At least three parameters are necessary for defining a pure component: the effective number of segments, m_i, the segment diameter, σ_i, and the dispersive energy between segments, ε_i. For molecules with association sites, two additional parameters are required: the association energy, ε^{AiBi}, and the association volume, κ^{AiBi}. These parameters are illustrated in Figure 2.3.

The typical parametrization used for cubic EoS is usually not applied in SAFT-type EoS as these models tend to overpredict the critical point. This limitation arises because SAFT models, like other mean-field theories, cannot accurately account for long-wavelength density fluctuations unless a crossover term is explicitly introduced [107–109]. Instead, it is common practice to perform a regression to fit experimental data on density and vapor pressure, without considering data around the critical point. However, for some molecules, this strategy is difficult to apply due to the lack of experimental data. This is particularly the case for molecules that are usually solid under atmospheric conditions or have very low vapor pressures, which makes it challenging to obtain reliable experimental data. One solution is to perform the regression using data from a reference mixture. For example, several osmolytes have been fitted using aqueous density and osmotic pressure data [97, 110].

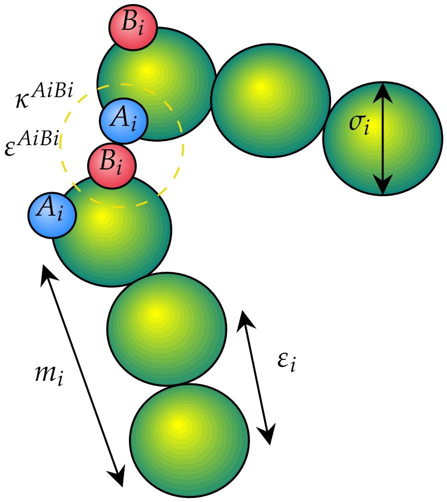

FIGURE 2.3: Illustration of PC-SAFT molecular parameters for pure components, including the effective number of segments (m_i), segment diameter (σ_i), dispersive energy (ε_i), and association parameters for molecules with association sites (ε^{AiBi} and κ^{AiBi}).

2.4. Calculation of thermodynamic properties

The Helmholtz energy is a key thermodynamic potential in SAFT-type EoS, and its derivatives provide access to various thermodynamic properties. For instance, the first derivative of the Helmholtz energy with respect to density is related to the pressure, while its derivative with respect to temperature is related to the entropy. Additionally, second derivatives are useful for calculating response functions such as isothermal compressibility and heat capacities. Thus, by taking appropriate derivatives of the Helmholtz energy, a wide range of thermodynamic properties can be obtained.

In the following, the expressions for the most commonly used properties are presented using the reduced Helmholtz energy as a function of temperature T, molar density ρ, and the mole fraction vector $\underline{\mathbf{x}}$.

2.4.1. Pressure and density

The pressure, P, can be obtained using Eq. 2.22,

$$P\left(T,\rho,\underline{\mathbf{x}}\right) = RT\rho^2 \left(\frac{\partial \tilde{a}}{\partial \rho}\right)_{T,x_i} \tag{2.22}$$

where R is the ideal gas constant.

Additionally, the molar density at a target condition, $\left(P_{\text{target}}, T, \underline{\mathbf{x}}\right)$, can be determined by solving the nonlinear equation $P\left(T,\rho,\underline{\mathbf{x}}\right) - P_{\text{target}} = 0$, where P is calculated using Eq. 2.22.

The compressibility factor, Z, can be obtained using a similar derivative, as shown in Eq. 2.23.

$$Z = 1 + \rho \left(\frac{\partial \tilde{a}^{res}}{\partial \rho} \right)_{T,x_i} \tag{2.23}$$

2.4.2. Chemical potential and fugacity coefficient

The chemical potential of a component i in a mixture, μ_i, can be obtained using Eq. 2.24.

$$\frac{\mu_i}{RT} = \tilde{a} + Z + \left(\frac{\partial \tilde{a}}{\partial x_i} \right)_{T,\rho,x_{j \neq i}} - \sum_{j=1}^{n_c} x_j \left(\frac{\partial \tilde{a}}{\partial x_j} \right)_{T,\rho,x_{k \neq i}} \tag{2.24}$$

The fugacity coefficient of a component i in a mixture, $\hat{\phi}_i$, can be obtained using Eq. 2.25.

$$\ln \hat{\phi}_i \left(P, T, \underline{\mathbf{x}} \right) = \tilde{a}^{\text{res}} + (Z - 1) + \left(\frac{\partial \tilde{a}^{\text{res}}}{\partial x_i} \right)_{T,\rho,x_{j \neq i}} - \sum_{j=1}^{n_c} x_j \left(\frac{\partial \tilde{a}^{\text{res}}}{\partial x_j} \right)_{T,\rho,x_{k \neq i}} \tag{2.25}$$

The activity coefficient of a component i in a mixture, γ_i, can be obtained using Eq. 2.26.

$$\gamma_i \left(P, T, \underline{\mathbf{x}} \right) = \frac{\hat{\phi}_i \left(P, T, \underline{\mathbf{x}} \right)}{\hat{\phi}_i \left(P, T, x_i = 1 \right)} \tag{2.26}$$

2.4.3. Enthalpy

The residual molar enthalpy, $\tilde{H}^{\text{res}}$, can be obtained using Eq. 2.27.

$$\frac{\tilde{H}^{\text{res}}}{RT} = -T \left(\frac{\partial \tilde{a}^{res}}{\partial T} \right)_{\rho,x_i} + (Z - 1) \tag{2.27}$$

2.5. Calculation of phase equilibrium

A mixture of chemical compounds can be distributed across multiple phases (solid, liquid, vapor), with the exchange of components continuing until phase equilibrium is established. At equilibrium, intensive properties, such as temperature, pressure, density, and composition, remain constant in all coexisting phases. Intensive properties are independent of the size, mass, or shape of each phase. Equilibrium thermodynamics provides a mathematical framework to quantitatively describe the relationships between these variables and the state of the system.

Phase equilibrium conditions are derived by applying a differential entropy balance within a closed system [111]. Thus, for π phases in equilibrium, thermal, mechanical, and chemical equilibrium conditions should satisfy the set of Eqs. 2.28.

$$T^{I} = T^{II} = ... = T^{\pi} \tag{2.28a}$$

$$P^{I} = P^{II} = ... = P^{\pi} \tag{2.28b}$$

$$\mu_i^{I} = \mu_i^{II} = ... = \mu_i^{\pi} \quad ; \quad i = 1, ..., n_c \tag{2.28c}$$

The chemical potential condition, Eq. 2.28c, ensures that there is no net mass transfer between phases. The chemical potential, μ_i, can be related to the fugacity, $\hat{f}_i$, a thermodynamic property that accounts for deviations from ideal behavior in real systems. The relationship between the chemical potential and the fugacity of the component i can be expressed by Eq. 2.29.

$$\mu_i = \mu_i^0 - RT \ln\left(\hat{f}_i^0\right) + RT \ln\left(\hat{f}_i\right) = \Gamma^0 + RT \ln\left(x_i \hat{\phi}_i P\right) \tag{2.29}$$

where μ_i^0 and $\hat{f}_i^0$ are the reference chemical potential and fugacity, respectively, R is the universal gas constant, and T is the temperature. At equilibrium, the fugacities of each component must be equal across all phases,which can be written using the fugacity coefficient by Eq 2.30.

$$x_i^{I} \hat{\phi}_i^{I} = x_i^{II} \hat{\phi}_i^{II} = \cdots = x_i^{\pi} \hat{\phi}_i^{\pi} \quad ; \quad i = 1, ..., n_c \tag{2.30}$$

This equality of fugacities across phases provides a practical way to calculate phase equilibrium in real systems, particularly for non-ideal mixtures. By using EoS or activity coefficient models, fugacities can be computed and used to evaluate equilibrium conditions.

2.5.1. Phase stability analysis

A stability analysis in phase equilibrium is a method used to determine whether a system at a given thermodynamic condition will remain in a single phase or split into multiple phases. The purpose of the test is to assess the stability of a homogeneous phase by checking if the Gibbs energy can be reduced by splitting the phase into two or more different phases. The tangent plane distance (TPD) method, developed by Michelsen [112], is frequently used for this analysis. In this method, the TPD function, F_{TPD}, is defined as the distance between the Gibbs energy surface of the mixture at a global composition $\underline{\mathbf{z}}$ and that of a hypothetical mixture with composition $\underline{\mathbf{w}}$, which, in terms of fugacity coefficients, is expressed in Eq. 2.31.

$$F_{\mathrm{TPD}}(\underline{\mathbf{w}}) = \sum_{i=1}^{n_c} w_i \left(\ln w_i + \ln \hat{\phi}_i(w) - \ln z_i - \ln \hat{\phi}_i(z)\right) \tag{2.31}$$

This function is minimized with respect to the phase composition $\underline{\mathbf{w}}$. If the value of F_{TPD} at the global minimum is negative, it implies that the phase is unstable at a global composition $\underline{\mathbf{z}}$ and should split into additional phases.

2.5.2. The particular case of a solid-liquid equilibrium

The case of solid-liquid equilibrium (SLE) cannot be directly solved by applying the iso-fugacity criterion (Eq. 2.30) with an EoS, as these are typically designed for fluid phases (liquids and gases) and do not adequately describe the solid phase. Under the assumption of a pure solid phase, the fugacity of a component in the solid phase is often related to its melting properties [111], resulting in Eq. 2.32.

$$\ln(x_i\gamma_i) = \frac{\Delta_m H_i}{R}\left(\frac{1}{T_{m,i}} - \frac{1}{T}\right) + \frac{\Delta_m C_{p,i}}{R}\left(\frac{T_{m,i}}{T} - \ln\frac{T_{m,i}}{T} - 1\right) \tag{2.32}$$

where $\Delta_m H_i$ is the melting enthalpy, $T_{m,i}$ is the melting temperature, and $\Delta_m C_{p,i}$ is the heat capacity change upon melting condition. Generally, the heat capacity term is negligible compared with the enthalpic term [111, 113], obtaining Eq. 2.33.

$$\ln(x_i\gamma_i) = \frac{\Delta_m H_i}{R}\left(\frac{1}{T_{m,i}} - \frac{1}{T}\right) \tag{2.33}$$

The melting properties of each compound can be found in the literature or can be obtained using group contribution methods [114].

2.6. Calculation of surface tension and viscosity

Surface tension and viscosity cannot be directly derived from an EoS because they primarily describe the thermodynamic equilibrium properties of a homogeneous system. However, the EoS can be integrated into additional theoretical frameworks to estimate these properties. For example, surface tension can be obtained using density gradient theory (DGT), which couples the EoS with a spatial variation in density at the interfaces. Similarly, viscosity can be estimated using free volume theory (FVT), where the EoS provides the necessary molecular parameters as well as the dependence of molar density on thermodynamic conditions.

2.6.1. Density Gradient Theory

The formulation of DGT can be traced back to the works of van der Waals [115], later translated by Rowlinson [116], and reformulated by Cahn and Hillard [117], in which arise its popularity in modeling interfacial properties. In this approach, the local Helmholtz energy (A) of an inhomogeneous fluid is expanded by the Taylor series under the assumption that the molecular gradients are negligible compared to the reciprocal of the intermolecular distances [118]. The Taylor series expansion is truncated after the second-order density gradient term, which results in the expression of the local Helmholtz free energy as a sum of the Helmholtz free energy at some homogeneous state and the inhomogeneity correction term; as shown in Eq. 2.34,

$$A\left(\rho\right)=\int\left(a_0\left(\rho\right)+\frac{1}{2}\sum_{i=1}^{n_c}\sum_{j=1}^{n_c}c_{ij}\nabla\rho_i\nabla\rho_j\right)\mathrm{d}^3r \tag{2.34}$$

where r is the position vector, $a_0\left(\rho\right)$ is the homogeneous Helmholtz free energy of the fluid at the local composition, $\nabla\rho_i$ and $\nabla\rho_j$ are the local density gradients, and c_{ij} is the matrix containing influence parameters, which are related to the molecular structure of the interface. These parameters govern how the local density gradients, $\nabla\rho_i$, respond to deviations in chemical potentials from the homogeneous phase.

To determine the density distribution, the following assumptions can be made [118–121]:

- The interface is flat.
- The influence parameters are independent of the density.

By applying the minimum energy principle to Eq.2.34, and considering these assumptions, the equilibrium densities of the components, $\rho_i(z)$, are obtained by solving the system of Euler-Lagrange differential equations, as shown in Eq.2.35.

$$\sum_j c_{ij}\frac{d^2\rho_j}{dz^2}=\mu_i\left(\underline{\rho}\right)-\mu_i^0 \tag{2.35}$$

Here, μ_i is the chemical potential, defined as $\mu_i=\left(\partial a_0/\partial\rho_i\right)_{T,V,\rho j\neq i}$, and μ_i^0 is the chemical potential of component i in the homogeneous phase. Solving this system of equations provides the density profile across the interface. The cross-influence parameters, c_{ij}, needed for mixtures, are typically calculated using the geometric mean combination rule [119], as shown in Eq. 2.36.

$$c_{ij}=\left(1-\beta_{ij}\right)\sqrt{c_ic_j} \tag{2.36}$$

The asymmetry parameter β_{ij} is fitted to experimental surface tension data for each binary mixture. When β_{ij} is zero, the system simplifies, and the differential equations reduce to a set of algebraic equations [118, 120, 122], as shown in Eq. 2.37.

$$\sqrt{c_{ss}}\left(\mu_k-\mu_k^0\right)=\sqrt{c_{kk}}\left(\mu_s-\mu_s^0\right),\quad k=1,2,\cdots,s-1,s+1,\cdots,n_c \tag{2.37}$$

In this expression, s represents the reference component, which typically has a monotonic density profile across the interface. The least volatile component is often selected as the reference, although this criterion may not always hold. If no component meets the monotonicity requirement, Eq.2.37 must be solved using a path function, as proposed by Liang et al.[123].

Once the density profiles are determined, the surface tension, γ, can be computed using Eq. 2.38.

$$\gamma = \sum_{i=1}^{n_c} \sum_{j=1}^{n_c} c_{ij} \int \frac{d\rho_i}{dz} \frac{d\rho_j}{dz} dz \tag{2.38}$$

From Eqs. 2.34-2.38, it is evident that the calculation of $\rho_i(z)$ and γ requires knowledge of the influence parameters c_{ij} and the Helmholtz energy density of the homogeneous fluid, $a_0(\rho)$.

The exact determination of the influence parameters is challenging, as it involves estimating the radial distribution function of pure substances in the homogeneous state [124, 125]. An alternative approach is to use molecular models of the pure components, as described by Garrido et al. [126]. Alternatively, the influence parameters can be obtained by fitting to experimental surface tension data for each pure fluid.

2.6.2. Free Volume Theory

FVT was first proposed by Allal et al. [127] to model the viscosity of Newtonian fluids. The main feature of FVT, compared to other viscosity models, lies in its incorporation of the free volume concept, in conjunction with molecular diffusion models—specifically, the microscopic friction factor [127]. This approach has gained significant attention in the scientific community due to its ability to accurately model the viscosity of both low-density fluids (e.g., gases) and high-density fluids (e.g., liquids) [128].

According to FVT, the dynamic viscosity η of a fluid can be expressed as the sum of two contributions, as shown in Eq. 2.39,

$$\eta = \eta_0 + \Delta\eta \tag{2.39}$$

where η_0 represents the viscosity of the dilute gas, and $\Delta\eta$ accounts for the contribution from the dense fluid.

For hard-sphere molecules of a pure component, the dilute-gas viscosity, η_0, is accurately described by kinetic theory, as formulated by Chapman and Enskog [129]. This theory considers the intermolecular forces influencing molecular behavior in low-density conditions. Chung [130] later extended this model to encompass molecules of varying shapes and anisotropic molecular forces, providing a more generalized expression for η_0, given by Eq. 2.40.

$$\eta_0 = \frac{5}{16} \frac{\sqrt{M_W k_B T/(N_A \pi)}}{\sigma^2 \Omega^{(2,2)}} F_c \tag{2.40}$$

In this equation, N_A is the Avogadro's number, M_w represents the molecular weight, σ is the collision diameter, $\Omega^{(2,2)}$ is the collision integral, and F_c is the correction factor accounting for the effects of chain bonding, hydrogen bonding, and polarity. $\Omega^{(2,2)}$ can be calculated by the empirical equation proposed by Neufeld et al. [131], given by Eq. 2.41.

$$\Omega^{(2,2)} = \left(\frac{A}{T_{\text{ad}}B}\right) + \frac{C}{\exp(DT_{\text{ad}})} + \frac{E}{\exp(FT_{\text{ad}})} + GT_{\text{ad}}^{B}\sin\left(ST_{\text{ad}}^{W} - H\right) \tag{2.41}$$

where $A = 1.16145$, $B = 0.14874$, $C = 0.52487$, $D = 0.77320$, $E = 2.16178$, $F = 2.43787$, $G = -6.435 \times 10^{-4}$, $H = 7.27371$, $S = 18.0323$, and $W = -0.76830$. The dimensionless temperature T_{ad} is related to the potential energy parameter, ε, by Eq. 2.42.

$$T_{\text{ad}} = \frac{k_B T}{\varepsilon} \tag{2.42}$$

The dilute-gas viscosity of a mixture, η_0^{mix}, is typically calculated using the dilute-gas viscosities of its n_c components. A widely used mixing rule, proposed by Wilke [132], is shown in Eq. 2.43.

$$\eta_0^{mix} = \sum_{i=1}^{n_c} \frac{\eta_0^i}{1 + \frac{1}{x_i}\sum_{j=1,j\neq i}^{n_c} x_j \phi_{ij}} \tag{2.43}$$

In this expression, η_0^i is the dilute-gas viscosity of component i, and ϕ_{ij}, is a function of the interaction between components i and j as a correction due to different molecular weight, given by Eq. 2.44,

$$\phi_{ij} = \frac{\left[1 + \left(\frac{\eta_0^i}{\eta_0^j}\right)^{\frac{1}{2}} \left(\frac{M_w^i}{M_w^j}\right)^{\frac{1}{4}}\right]^2}{\left(\frac{4}{\sqrt{2}}\right)\left(1 + \frac{M_w^i}{M_w^j}\right)^{\frac{1}{2}}} \tag{2.44}$$

In this work, the dilute-gas term is neglected, as its contribution is negligible for liquids [132].

The dense fluid viscosity of a Newtonian pure fluid can be calculated through Eq. 2.45,

$$\Delta\eta = L_v(P + \alpha\rho^2 M_w)\sqrt{\frac{M_w}{3RT}}\exp\left[B\left(\frac{P + \alpha\rho^2 M_w}{\rho RT}\right)^{\frac{3}{2}}\right] \tag{2.45}$$

where L_v is an adjustable length parameter, P is the absolute pressure, α is an adjustable parameter associated with the barrier energy that molecules must overcome to diffuse, ρ is the molar density, and B is characteristic of the free-volume overlap, which is also an adjustable parameter. These parameters can be fitted to the viscosity data of a pure component.

In this work, the dense fluid viscosity for a mixture of n_c components was calculated using the same model described earlier. The approach follows that of other authors [127, 128] for the mixing rule of FVT parameters, employing a simple mixing rule as shown in Eqs. 2.46.

$$\alpha^{mix} = \sum_{i=1}^{n_c} \alpha_i x_i \tag{2.46a}$$

$$B^{mix} = \sum_{i=1}^{n_c} B_i x_i \tag{2.46b}$$

$$L_v^{mix} = \sum_{i=1}^{n_c} L_{v,i} x_i \tag{2.46c}$$

It is important to note that only the parameters of the pure components are used to calculate the viscosity of mixtures, which indicates that the model is predictive for mixtures.

3. Fundamentals and computational methods of molecular dynamics

---

This chapter presents the essential theoretical background of molecular dynamics (MD). This powerful computational method is used to model the complex behavior of DESs in the context of this thesis. MD offers a crucial framework for understanding molecular interactions, structural properties, and thermodynamic behaviors in various systems. By delving into these fundamental concepts, the aim is to establish a robust foundation for subsequent analyses and insights into the unique properties of DESs.

3.1. Introduction

Molecular simulation has become a powerful computational tool for understanding and predicting the behavior of molecular systems [52, 53]. It provides insights into molecular-level phenomena that are often inaccessible to experimental techniques. Using statistical mechanics principles, molecular simulation bridges the gap between microscopic phenomena and macroscopic behavior, facilitating the study of thermodynamic, structural, and transport properties [53]. Since its inception several decades ago, molecular simulation has become an indispensable tool in molecular science [133]. During this period, advances in computational hardware and algorithms have significantly expanded the scope and efficiency of simulations, making it possible to study increasingly complex systems with remarkable accuracy and detail.

Among the most widely used molecular simulation techniques is molecular dynamics (MD), a computational method that relies on mechanical principles derived from Newton's laws of motion, where the future state of the system can be predicted based on its current state [134]. In MD, atoms are represented as mass points that interact through a specified force field. These force fields simplify the calculations by ignoring the movement of electrons and instead treating the energy of a system solely as a function of nuclear positions. By neglecting electron motion, MD simulations compute results in much shorter time scales than quantum mechanics methods while still achieving high accuracy when adequately calibrated.

This chapter introduces the core concepts and methodologies central to MD simulations, aiming to provide a clear understanding of the foundational principles and practical steps involved. Key elements such as potential energy functions, force fields, and thermodynamic ensembles are discussed to establish the theoretical framework. In addition, the methodology used in MD simulations is introduced, including system initialization, application of periodic boundary conditions, and execution of the production phase. Special attention is paid to methodologies for calculating key properties such as surface tension and viscosity.

3.2. Fundamental principles in molecular dynamics

3.2.1. Potential energy functions and force fields

MD simulation relies on statistical mechanical models to predict molecular geometry, energy, and other properties based on physical interactions. In these models, molecules are represented as systems of particles (e.g., atoms) connected by bonds and interacting through intramolecular and intermolecular forces. Force fields describe these interactions mathematically, capturing bonded interactions, such as variations in bond lengths and angles, as well as non-bonded interactions like van der Waals forces and electrostatics. These interactions govern the dynamics of the system, including rotation, vibration, and translation, resulting in energetically favorable conformations.

The typical potential energy in MD, $U(\mathbf{r}_1, \mathbf{r}_2, \ldots, \mathbf{r}_N)$, can be expressed as a sum of energy contributions, as shown in Eq. 3.1,

$$U(\mathbf{r}_1, \mathbf{r}_2, \ldots, \mathbf{r}_N) = \sum U_{\text{bonds}} + \sum U_{\text{angles}} + \sum U_{\text{torsion}} + \sum U_{\text{non-bonded}} \tag{3.1}$$

which depends on the positions $\mathbf{r}_i$ for the N particles in the system. The first term in Eq. 3.1 models the interaction between bonded atom pairs and how they stretch or compress relative to a reference equilibrium state. The second term represents the energy caused by the angle motion formed between three adjacent atoms. The third term is a torsional potential, which models how the energy changes as the bond rotates. The fourth term represents the contribution of the non-bonded or intermolecular interactions, calculated between all pairs of atoms across all molecules. This last term typically uses the Coulomb potential for electrostatic interactions and the Lennard-Jones potential for van der Waals interactions.

Force fields such as OPLS [135], CHARMM [136], and AMBER [137] parameterize these interactions using empirical or quantum mechanical data to ensure accurate representations of molecular systems. The choice of force field depends on the specific system under study, with each force field optimized for particular types of molecules, such as proteins, small organic compounds, or polymers.

MD simulations can adopt different levels of resolution to represent molecules with a particular force field, ranging from all-atom models to coarse-grained approaches:

- **All-atom models**: These models explicitly represent every atom in the system, including hydrogen atoms, providing the highest level of detail. They are widely used for systems where precise interactions, such as hydrogen bonding and detailed electrostatics, are critical. However, the high level of detail makes all-atom models computationally expensive, especially for large systems or long simulation times.

- **United-atom models**: In these models, groups of atoms, such as CH_3, CH_2, or CH, are treated as single interaction sites [138]. This simplification reduces computational cost compared to all-atom models while still capturing essential molecular features. United-atom models are commonly used to simulate hydrocarbons, lipids, and other systems in which hydrogens have a minimal impact on overall properties.
- **Coarse-grained models**: Coarse-graining further simplifies the system by grouping multiple atoms into a single particle or "bead". These models are particularly useful for studying large-scale phenomena, such as protein folding, membrane dynamics, or polymer aggregation, where fine atomic details are less critical. The MARTINI force field is a popular example of a coarse-grained model [139, 140], optimized for biomolecular and material simulations. Coarse-grained approaches enable simulations of much larger systems over longer time scales but sacrifice some accuracy in representing molecular interactions.

The choice of model resolution (all-atom, united-atom, or coarse-grained) depends on the research question and the balance between computational efficiency and the level of detail required. Combining these approaches in multiscale simulations can provide insights across different spatial and temporal scales.

3.2.2. Finite difference methods and integration algorithms

Under the influence of continuous potentials such as Lennard-Jones, Coulomb, or Mie, the motion of particles in MD simulations is inherently coupled, resulting in a highly complex system of equations. Analytical solutions for these equations are rarely possible, necessitating numerical approaches. The finite-difference method is widely used for integrating the equations of motion in MD simulations. The central idea of this approach is to discretize time into small intervals of fixed length, Δt, typically on the order of femtoseconds (10^{-15} s). At each time step, the total force acting on a particle is computed as the sum of the interactions with all other particles in the system. From this force, the acceleration is determined using Newton's second law of motion. The positions and velocities of the particles at the next time step, $t + \Delta t$, are then calculated from their values at time t, assuming that the force remains constant within the time step.

Various integration algorithms have been developed to solve the equations of motion in MD simulations. These algorithms are based on the Taylor series expansion of positions, velocities, or accelerations over time, which aim to balance computational efficiency, accuracy, and physical fidelity. To ensure successful simulations, a desirable integration algorithm should [53]:

- Be computationally efficient, requiring minimal memory.
- Permit the use of sufficiently long time steps, Δt, without sacrificing accuracy.
- Accurately reproduce the classical trajectory of the particles.
- Conserve key physical quantities, such as energy and momentum, ensuring time-reversibility.

- Be simple to implement and robust in application.

The Verlet algorithm [141] is perhaps the most widely known integration method in MD due to its simplicity and numerical stability. It works by discretizing time into fixed steps, Δt, and calculates new positions ($\mathbf{r}$) and velocities ($\mathbf{v}$) iteratively using the acceleration ($\mathbf{a}$), according to the formulation of equations for the integration of the equations of motion over a single timestep from t to $t+\Delta t$, as shown in Eqs. 3.2a–3.2c.

$$\mathbf{v}\left(t+\frac{1}{2}\Delta t\right) = \mathbf{v}(t) + \frac{1}{2}\Delta t\mathbf{a}(t) \tag{3.2a}$$

$$\mathbf{r}(t+\Delta t) = \mathbf{r}(t) + \Delta t\mathbf{v}\left(t+\frac{1}{2}\Delta t\right) \tag{3.2b}$$

$$\mathbf{v}(t+\Delta t) = \mathbf{v}\left(t+\frac{1}{2}\Delta t\right) + \frac{1}{2}\Delta t\mathbf{a}(t+\Delta t). \tag{3.2c}$$

In the first step (3.2a), the velocities are "half-advanced" to an intermediate time $t+\frac{1}{2}\Delta t$ using the accelerations at time t. These intermediate velocities are then used in step (3.2b) to propagate the particle coordinates from t to $t+\Delta t$. Finally, the accelerations at the new positions are computed, allowing the velocities to be fully updated in step (3.2c).

Other variations and improvements have been developed from this algorithm. A commonly used algorithm is Leapfrog [142], which estimates velocities at half-time steps $\left(t+\frac{1}{2}\Delta t\right)$ using the relations shown in Eqs. 3.3a-3.3b.

$$\mathbf{r}(t+\Delta t) = \mathbf{r}(t) + \Delta t\mathbf{v}(t+\frac{1}{2}\Delta t) \tag{3.3a}$$

$$\mathbf{v}(t+\frac{1}{2}\Delta t) = \mathbf{v}(t-\frac{1}{2}\Delta t) + \Delta t\mathbf{a}(t) \tag{3.3b}$$

The only difference between the Leapfrog algorithm and the Verlet algorithm is that the velocities are not calculated at the same time as positions.

3.2.3. Constraint algorithms

In MD simulations, modeling some molecules requires maintaining fixed specific bond lengths and angles, especially those involving hydrogen atoms, which have high frequencies and thus require a small integration time step for correct sampling. Using constraint algorithms allows for larger integration time steps, thereby improving computational efficiency.

The SHAKE algorithm, introduced by Ryckaert et al. [143], is a widely used method. Operating within the Verlet integration algorithm, SHAKE iteratively adjusts atomic positions to satisfy bond length constraints. Initially, the algorithm computes unconstrained positions; it then applies corrections based on constraint forces to ensure that the bond lengths stick to the specified values. This iterative process continues until all constraints satisfy a predefined tolerance. However, SHAKE's convergence can slow with increasing molecular complexity as the number of iterations required increases with the number of constraints.

For systems involving water molecules, the SETTLE algorithm offers a more efficient alternative [144]. Explicitly designed for rigid water models, SETTLE provides an analytical solution to the constraints, allowing for quick and accurate enforcement of bond lengths and angles within water molecules. This efficiency makes SETTLE particularly advantageous in simulations in which water constitutes a significant portion of the system.

Another notable method is the LINCS (Linear Constraint Solver) algorithm [145], which resets bond lengths after an unconstrained update. LINCS is non-iterative and generally more stable and faster than SHAKE, but it can only be used with bond and isolated angle constraints. Because of its stability, LINCS is especially useful for large molecules.

3.2.4. Periodic boundary conditions

Periodic boundary conditions allow simulations to be performed using a relatively small number of particles, letting them experience forces as if in the bulk of the fluid. Replicating a cubic box that contains particles in all directions creates a periodic arrangement. Figure 3.1 illustrates a two-dimensional example, where each box is surrounded by eight identical boxes (a three-dimensional box would have 26). The figure shows how molecules enter or leave the box through any of its faces.

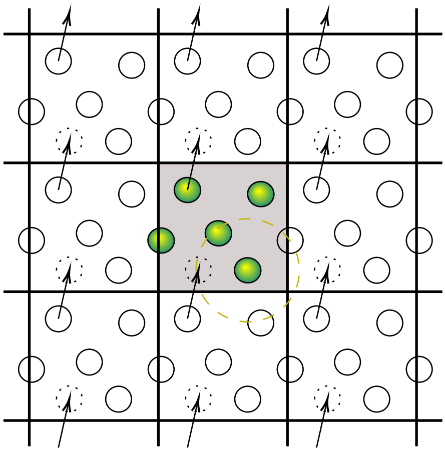

FIGURE 3.1: Two-dimensional representation of periodic boundary conditions.

As long as the potential is short-ranged, the minimum image convention can be adopted, where each atom interacts with the nearest image in the periodic arrangement. Therefore, if a particle leaves the box during a simulation, it is replaced by its image entering from the opposite face of the box, as illustrated in Figure 3.1. This keeps the number of particles in the central box constant.

Care must be taken with long-range potentials, such as those for charged or dipolar systems, to prevent molecules from interacting with themselves.

3.2.5. Neighbor searching

Calculating non-bonded interactions for interatomic forces in MD simulations involves many calculations: each atom i interacts with every atom j, meaning that the separation r_{ij} must be computed. If short-range interactions are considered with a cutoff radius r_{cut}, particles with $r_{ij} > r_{\text{cut}}$ can be omitted from the calculation, reducing the computational cost. However, examining all pair separations for a system with N particles is proportional to the number of distinct pairs, $\frac{1}{2}N(N-1)$, and for each pair, at least r_{ij}^2 must be computed, which is still computationally expensive.

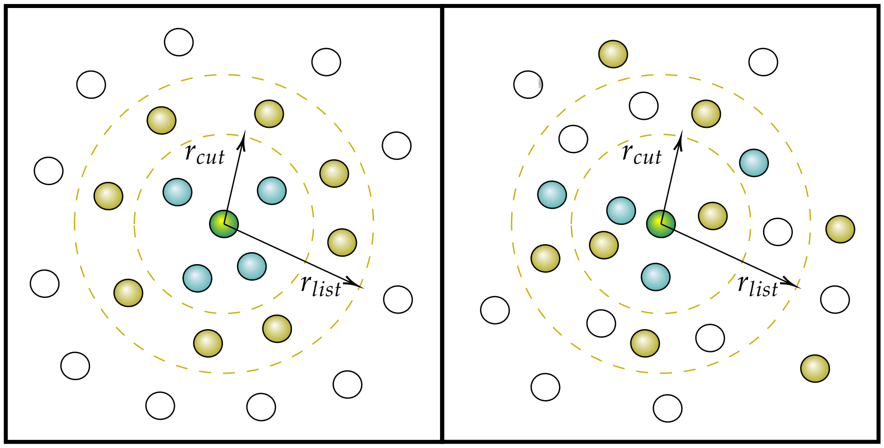

FIGURE 3.2: Two-dimensional representation of the Verlet neighbor list in two different snapshots: at the moment the list was created and several steps later.

A more efficient computational strategy is to use a list of the nearest atom pairs. Verlet proposed this technique in 1967 to improve program speed, known as the Verlet neighbor list [146]. In this technique, a cutoff sphere of radius r_{cut} around a particle is surrounded by a shell of radius r_{list}, as shown in Figure 3.2. At the first simulation step, a list is constructed and stored for each atom, indicating all neighbors within a separation of r_{list}. In subsequent iterations, force calculations are only performed for atom pairs in the list, and the list is reconstructed periodically. The choice of r_{list} affects performance: longer lists need less frequent reconstruction but do not reduce computational time as effectively as shorter lists.

3.2.6. Thermodynamic ensembles

Thermodynamic ensembles originate from the statistical mechanics theory, which serves as the molecular foundation of thermodynamics. An ensemble is the set of all possible states and microstates consistent with the constraints that characterize the macroscopic system. There are three typical ensembles:

- **Microcanonical**: This ensemble consists of all states with fixed total energy E, fixed size (number of particles N), and fixed volume V. It describes an isolated system with no interaction with the surroundings.
- **Canonical**: This ensemble consists of all microstates with a fixed number of particles N and fixed volume V. The energy can fluctuate; however, the system remains in equilibrium while being in contact with a heat bath at a fixed temperature T.
- **Grand Canonical**: This ensemble describes a system with a variable composition (allowing the exchange of particles with the surroundings) that is in chemical and thermal equilibrium with a thermodynamic reservoir. This reservoir has a fixed temperature T and a fixed chemical potential μ for various particle types at constant volume V.

3.2.7. Simulation controls: thermostats and barostats

MD simulations are traditionally performed in the microcanonical ensemble (NVE). However, many applications require simulations in the canonical ensemble (NVT), which maintains a constant temperature, or the isothermal-isobaric ensemble (NPT), which maintains constant temperature and pressure. Depending on the purpose of the simulation, it may or may not be necessary to generate the exact ensemble and to understand its characteristics rigorously. The following sections describe methods for controlling temperature and/or pressure during simulations using a thermostat and/or a barostat, respectively.

Berendsen thermostat

The Berendsen thermostat [147] assumes that the system is immersed in a heat bath that maintains the temperature at a constant value, with energy exchange occurring gradually between the system and the bath. The instantaneous temperature T_i is gradually brought to the desired temperature T, with the rate of change of the instantaneous temperature proportional to the temperature difference, given by Eq. 3.4.

$$\frac{dT_i}{dt} = \frac{T - T_i}{\tau_T} \tag{3.4}$$

In this temperature relaxation process, the velocity $\mathbf{v}$ of each particle is scaled at every step by a factor λ, which is defined by Eq. 3.5,

$$\lambda = \left[1 + \frac{\Delta t}{\tau_T}\left(\frac{T}{T_i} - 1\right)\right]^{1/2} \tag{3.5}$$

where Δt is the integration time step, and τ_T is a time constant that determines the time scale to reach the desired temperature T. The coupling strength between the heat bath and the system is controlled by τ_T. A smaller τ_T value indicates stronger coupling and faster convergence to the desired temperature, while a larger τ_T value results in weaker coupling.

Velocity rescaling thermostat

From the Berendsen thermostat (Eq. 3.5), two important cases for τ_T can be noted. In the first case, if $\tau_T = \Delta t$, the Berendsen thermostat is reduced to Eq. 3.6.

$$\lambda = \sqrt{\frac{T}{T_i}} \tag{3.6}$$

This equation corresponds to the velocity rescaling method [148], the most straightforward and most commonly used approach to maintain constant temperature. In the second case, if τ_T is very large, then $\lambda = 1$ decouples the system from the heat bath and reproduces the microcanonical (NVE) ensemble.

Nosé-Hoover Thermostat

The Nosé-Hoover thermostat was proposed by Nosé [149] and later modified by Hoover [150]. This method modifies the system's Hamiltonian ($\mathcal{H}$) by introducing a heat reservoir and a friction term into the equations of motion. The frictional force is proportional to the product of the velocity of the particle and a friction parameter ξ. This parameter, a dynamic variable of the heat bath, has its own momentum p_ξ and equation of motion.

The particle equations of motion are modified as shown in Eq. 3.7,

$$\frac{d^2\mathbf{r}_i(t)}{dt^2} = \frac{\mathbf{F}_i}{m_i} - \frac{p_\xi}{Q}\frac{d\mathbf{r}_i}{dt} \tag{3.7}$$

where m_i and $\mathbf{F}_i$ are the mass and force applied to the particle, and the heat bath motion ξ is governed by a first-order differential equation, given by Eq. 3.8.

$$\frac{dp_\xi}{dt} = (T - T_0) \tag{3.8}$$

Here, T_0 is the reference temperature, and T is the instantaneous temperature of the system. The coupling strength is determined by the parameter Q, often referred to as the mass parameter of the reservoir, in combination with the reference temperature.

The extended Hamiltonian produced by the Nosé-Hoover thermostat is expressed by Eq. 3.9,

$$\mathcal{H} = \sum_{i=1}^{N} \frac{\mathbf{p}_i^2}{2m_i} + U(r_1, r_2, \ldots, r_N) + \frac{p_\xi^2}{2Q} + N_f k_B T \xi \tag{3.9}$$

where N_f is the number of degrees of freedom.

Berendsen Barostat

Similarly to the Berendsen thermostat, the Berendsen barostat [147] rescales the box vectors at each step to maintain a constant pressure P_0. A first-order coupling constant τ_P controls the simulation pressure P, as shown in Eq. 3.10.

$$\frac{dP}{dt} = \frac{P_0 - P}{\tau_P} \tag{3.10}$$

For isotropic scaling, the factor μ by which the coordinates and box dimensions are scaled by Eq. 3.11,

$$\mu = 1 - \frac{\kappa_T \Delta t}{3\tau_P}(P_0 - P) \tag{3.11}$$

where κ_T is the isothermal compressibility of the system, and Δt is the integration time step.

This scaling ensures that the system's volume changes in response to the pressure difference, facilitating the exponential pressure relaxation towards the reference value. These equations enable the Berendsen barostat to effectively control system pressure by modulating volume. However, it's important to note that this method does not generate a correct statistical mechanical ensemble and may not accurately reproduce pressure fluctuations.

Parrinello-Rahman Barostat

Unlike the Berendsen barostat, the Parrinello-Rahman barostat [151, 152] accounts for system fluctuations to provide a better sampling of the isothermal-isobaric ensemble. It uses a scheme similar to the Nosé-Hoover thermostat, where the box vector lengths are governed by the Eq. 3.12,

$$\frac{d^2 b}{dt^2} = \frac{V}{Wb'}(P_0 - P) \tag{3.12}$$

where V is the box volume, b is the box vectors, and W is the matrix that determines the coupling strength of the barostat.

3.3. Simulation methodology

MD simulations begin with the creation of an initial configuration, where particles are arranged within a simulation box. The first step is to define the number of molecules and the dimensions of the simulation box. A cubic box is typically used for homogeneous systems, with dimensions at least twice the cut-off distance for molecular interactions to prevent self-interaction. An estimation of the density of the system can be used either to calculate the number of molecules based on the volume of the simulation box or to determine the box volume based on the number of molecules to be inserted. Molecules are then placed randomly within the box, but care must be taken to avoid overlaps that can result in unrealistic, high-energy configurations, which is particularly challenging for complex systems. Packmol software is often used to generate the initial configuration by packing molecules into defined spatial regions while ensuring minimal overlap to avoid short-range repulsive interaction. Once the molecular positions are determined, initial velocities are assigned according to a Maxwell-Boltzmann distribution at the desired temperature.

Once the initial configuration is prepared, the system needs to be energy minimized. This step reduces the potential energy of the system by adjusting the atomic positions to resolve any physically unrealistic configurations, such as overlapping atoms or excessive bond distortions. Energy minimization ensures mechanical stability and prevents numerical instabilities in subsequent simulation steps. For this purpose, algorithms like the steepest descent method or the more efficient conjugate gradient method are commonly used. The result is a configuration with minimized potential energy that provides a stable starting point for dynamic simulations.

Following energy minimization, the system enters the equilibration phase, which prepares it to represent the desired thermodynamic state, such as a specific temperature or pressure. This phase consists of thermal equilibration and, if necessary, pressure equilibration. The Berendsen thermostat and barostat are excellent tools for quickly equilibrating systems to a desired temperature or pressure. However, they do not accurately generate the correct thermodynamic ensembles, and the data from this process should not be used for further analysis. Throughout this process, properties such as temperature, pressure, and energy are monitored until they stabilize, indicating that the system is equilibrated.

The final phase of an MD simulation is the production run, during which the equilibrated system is simulated over time to generate data for analysis. In this phase, the system evolves according to Newton's equations of motion, with minimal external interference, allowing the natural dynamics of the system to unfold. Temperature and pressure can be controlled using the Nosé-Hoover thermostat and the Parrinello-Rahman barostat, respectively. Both methods are more accurate for ensemble generation, while the desired temperature and pressure are kept constant. Long simulation times are often required during production to ensure that the results are representative of the system's equilibrium state and that the calculated properties converge statistically.

There are slight differences in the simulation methodology when dealing with inhomogeneous systems to calculate surface tension and when performing non-equilibrium molecular dynamics (NEMD) simulations to calculate viscosity. The details of these differences are discussed in the following sections.

3.3.1. Viscosity calculation

For the viscosity calculation, the same methodology described previously can be applied. The only distinction arises when using the NEMD approach, where an external force is periodically applied during the production phase, typically in the x-direction [153]. Although the liquid phase is homogeneous and isotropic, the Cartesian coordinate system is used to define the direction of the applied force and to resolve the resulting velocity field. This force induces a flow in the fluid, from which the viscosity can be determined. To ensure consistency with periodic boundary conditions and to minimize local shear rates, both the acceleration and velocity profiles must be smooth and periodic [153]. VLETherefore, Eq. 3.13 is typically chosen to provide the external force $a_x(z)$:

$$a_x(z) = \mathcal{A}\cos\left(\frac{2\pi}{L_z}z\right) \tag{3.13}$$

In this case, according to the Navier–Stokes equation, the generated velocity profile at equilibrium is given by Eq. 3.14:

$$v_x(z) = \mathcal{A}\frac{\rho}{\eta}\left(\frac{L_z}{2\pi}\right)^2\cos\left(\frac{2\pi}{L_z}z\right) \tag{3.14}$$

In Eqs. 3.13 and 3.14, $\mathcal{A}$ is the acceleration amplitude, which indicates the magnitude of the applied force, ρ is the density of the liquid, η is the viscosity, and L_z is the box length in the z-direction.

As shown in Eq. 3.14, the velocity amplitude is proportional to the acceleration amplitude, and both are related to the viscosity of the system. Furthermore, this procedure should be repeated at different $\mathcal{A}$ values, ranging from 0.08 to 0.20 nm/ps^2, to extrapolate the viscosity to zero acceleration amplitude and obtain a more accurate estimate under equilibrium conditions.

3.3.2. Surface tension calculation

In the surface tension calculation, it is important to simulate the interface between the liquid and vapor phases. Due to the low vapor pressure of DES, the vapor phase can be assumed to be a vacuum. As illustrated in Figure 3.3, the initial configuration must be an inhomogeneous system where the simulation box for the liquid phase is extended along the z-axis (normal to the interface), producing two liquid-vapor interfaces. The molecules are inserted only in the middle of the simulation box. This configuration should be run in the NVT ensemble (without a pressure controller) to avoid collapsing into a homogeneous phase.

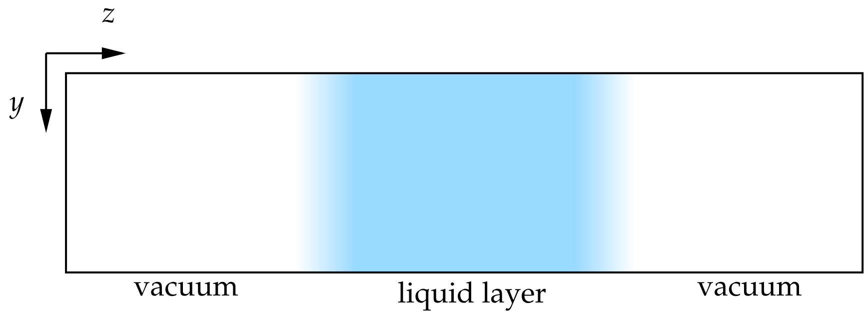

FIGURE 3.3: Schematic representation of the initial configuration of an inhomogeneous system for surface tension calculation using molecular dynamics.

After the simulation runs for enough time, the surface tension can be computed using the inhomogeneity of the pressure tensor [116, 154], as shown in Eq. 3.15.

$$\gamma = \frac{L_z}{2}\left(P_{zz} - \frac{P_{xx} + P_{yy}}{2}\right) \tag{3.15}$$

In Eq. 3.15, and P_{xx}, P_{yy}, and P_{zz} are the directional components of the pressure tensor.

4. Estimation of thermodynamic properties and phase equilibria of DESs using PC-SAFT

This chapter will explore two modeling strategies to study the capabilities and shortcomings of the PC-SAFT equation of state applied to predict properties and phase equilibria in DES systems. The first strategy employs a pseudo-pure approach, treating the DES mixture as a single, complex fluid with effective interactions. The second strategy adopts an individual component approach, treating each component of the DES mixture separately and accounting for their unique interactions. By comparing and contrasting these two approaches, this chapter aims to provide valuable insight into DES modeling, contributing to a deeper understanding of their complex thermodynamic behavior. [*]

4.1. Introduction

DESs offer a nearly limitless range of combinations due to the flexibility to choose their components: HBA and HBD [155]. This versatility expands further when DESs are mixed with additional solvents, such as organic solvents (OS) or water, which are commonly used to reduce DES viscosity while maintaining their desired properties [156, 157]. By adjusting the ratio of components, these mixtures can be fine-tuned for specific applications, making them highly attractive for industrial and environmental uses. However, to fully exploit their potential, it is crucial to develop a single, unified model with a consistent parameter set capable of accurately predicting the behavior of DES mixtures across a broad range of thermodynamic conditions. A model like this could facilitate its implementation across different industries and enhance its integration into diverse technological processes.

---

[*] This chapter is adapted with permission from:
E. Cea-Klapp, I. Polishuk, R. I. Canales, H. Quinteros-Lama, and J. M. Garrido, "Estimation of Thermodynamic Properties and Phase Equilibria in Systems of Deep Eutectic Solvents by PC-SAFT EoS", Industrial & Engineering Chemistry Research **59**, 22292–22300 (2020). Copyright 2020 American Chemical Society.

Despite the versatility of DES, relatively few studies have explored their behavior when mixed with other solvents, such as OS or water. Most studies have concentrated on experimental volumetric properties, particularly density and excess volume [157–170]. However, investigations into other thermodynamic properties, such as excess enthalpy [156, 171, 172], are still limited. In terms of phase equilibria, experimental data on vapor-liquid equilibrium (VLE) have mainly concentrated on gas solubility, such as CO_2[29, 31, 173–176]. In addition, some studies have explored the use of DESs in extraction processes, where liquid-liquid equilibrium (LLE) measurements are available [177, 178]. To address the current gaps in comprehensive data across a broader range of thermodynamic and phase equilibrium properties, the development of a general predictive model would be highly advantageous. Such a model could bridge the gap between experimental studies and provide a more complete understanding of DES behavior in a wide range of applications.

In this context, SAFT EoS [70] are particularly promising for modeling DES and additional solvent systems. The main advantage of SAFT-type EoS is their ability to account for various intermolecular interactions, such as hydrogen bonding and multipolar forces. Although SAFT has been applied to LLE in some studies [179, 180], to our knowledge, these models have not been systematically applied to the excess properties of DES + OS mixtures. SAFT models typically regress the parameters of pure compounds to experimental vapor pressures and saturated liquid densities. However, multiple sets of parameters can produce equivalent results for pure compounds, while yielding different predictions for mixture phase equilibria [181–184]. Moreover, conventional parameterization methods may not be well suited for DESs, as the available experimental data are often limited to homogeneous liquid phases or vapor pressures [185].

Zubeir et al. [61] proposed two strategies to apply the PC-SAFT EoS [87, 88] to DES systems. In the first approach, DESs are treated as pseudo-pure components, with model parameters fitted to available density data. This approach, while simple, requires a unique set of parameters for each HBD-HBA ratio and cannot describe solid-liquid equilibria (SLE), where eutectic compositions may vary. The second and more realistic strategy treats DESs as a mixture of individual components, allowing composition-independent molecular parameters to describe SLE, although it requires temperature-dependent binary adjustable parameters [61, 63, 64, 88, 128, 186] and specific association schemas for HBD and HBA. Although molecular simulations [60, 187, 188] suggest that DESs may require more than two association sites, increasing the complexity of the model does not always improve accuracy [128]. Furthermore, it is challenging to assess whether performance gains are due to better molecular modeling or merely the introduction of additional substance-specific parameters. As a result, the simpler 2B association scheme [80] is commonly used [61].

In this chapter, the predictive capabilities of the pseudo-pure and individual compound approaches are evaluated by analyzing excess properties, solubility, and LLE of mixtures containing DESs composed of choline chloride combined with levulinic acid, ethylene glycol, or phenol in a 1:2 molar ratio, and mixed with water, n-alkanols, n-alkanes, CO_2, and NH_3. To the best of our knowledge, this is the first thermodynamic assessment using PC-SAFT that simultaneously addresses a broad range of properties—including excess enthalpies—for these systems. The selected DESs were chosen based on the wide availability of experimental data in the literature, allowing for a consistent evaluation of their modeling across multiple thermodynamic properties and phase equilibria for a consistent DES type.

4.2. Modeling strategies

The PC-SAFT EoS is a widely used tool for modeling complex fluids, particularly those involving associative interactions such as hydrogen bonding, and is especially suited to predict the phase behavior of mixtures containing polar and associating molecules [87, 88]. DESs, considered a complex fluid, were modeled using two strategies with PC-SAFT EoS, as illustrated in Figure 4.1. Details about the PC-SAFT framework and its theoretical background can be found in Section 2.

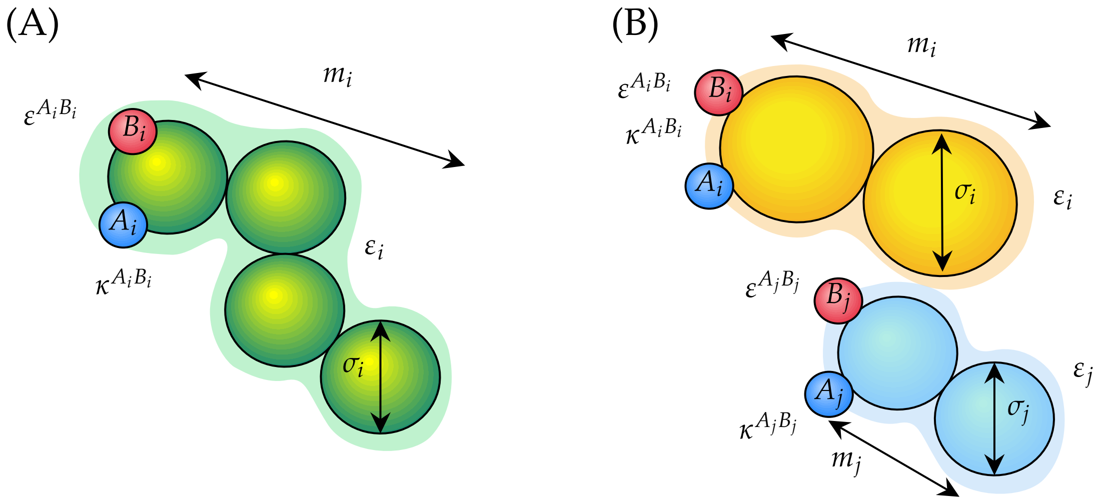

FIGURE 4.1: Schematic representation of the modeling strategies: (A) DES modeled as a pseudo-pure component and (B) DES modeled as mixture of its individual components.

The first strategy, known as the pseudo-pure component approach, follows the method proposed by Zubeir et al. [61]. In this approach, DESs are modeled as single pseudo-pure components, with their average molar masses calculated based on the compositions of their constituent HBA and HBD. The two-site association contribution (2B scheme of Huang and Radosz [80]) is applied to model the self-association between HBA and HBD in all the DES systems considered. The relevant molecular parameters of PC-SAFT are shown in Table 4.1A. The ε^{AiBi}/k_B values for the DESs are approximately two to three times higher than those of pure alkanols modeled with the same 2B scheme [88]. Furthermore, the κ^{AiBi} values for the DESs in the pseudo-pure approach are more than ten times smaller than those for ethanol and propanol, and about 80 times smaller than those for water.

The second strategy treats DESs as mixtures of independent components, requiring molecular parameters for both the HBA and the HBD. For choline chloride (ChCl), a common HBA, two association sites (one positive and one negative) is used to model the cation–anion interactions [61]. Levulinic acid (LA) [189], ethylene glycol (EG) [190], and phenol (Ph) [191] are modeled using the 2B association scheme, which allows the treatment of hydroxyl groups in a manner similar to that of 1-alkanols [88]. The molecular parameters for the DES precursors and other compounds are presented in Tables 4.1B and 4.1C.

TABLE 4.1: PC-SAFT molecular parameters used in this chapter. The [B, P, N] notation indicates the number of bivalent, positive, and negative association sites, respectively, as defined in Figure 2.2.

Compounds	M_w **[g/mol]**	m_i	σ_i **[Å]**	ε_i/k_B **[K]**	S^{Ai} **[B, P, N]**	ε^{AiBi}/k_B **[K]**	κ^{AiBi}	**Sources**
(A) DES modeled as a pseudo-pure component								
ChCl:LA (1:2)	123.95	3.4672	3.6847	477.7234	[0, 1, 1]	4601.31	0.003000	[192]
ChCl:EG (1:2)	87.92	3.5408	3.2782	465.0741	[0, 1, 1]	4971.99	0.002110	[192]
ChCl:Ph (1:2)	109.28	2.6552	3.8998	490.6306	[0, 1, 1]	5209.00	0.001360	[192]
(B) DES modeled as an individual component								
choline chloride	139.620	13.020	2.3680	228.0700	[0, 1, 1]	8000.00	0.200000	[61]
levulinic acid	116.120	2.0311	4.1241	266.4953	[0, 1, 1]	4578.37	0.017100	[189]
ethylene glycol	62.070	2.4366	3.2328	344.0600	[0, 1, 1]	2702.60	0.022160	[190]
phenol	94.110	2.6844	3.5660	250.3700	[0, 1, 1]	2827.60	0.086578	[191]
(C) Cosolvents and gases								
ethanol	46.069	2.3827	3.1771	198.2400	[0, 1, 1]	2653.40	0.032384	[88]
1-propanol	60.096	2.9997	3.2522	233.4000	[0, 1, 1]	2276.80	0.015268	[88]
1-butanol	74.123	2.7515	3.6139	259.5909	[0, 1, 1]	2544.56	0.006700	[88]
2-butanol	74.123	3.4400	3.3130	224.2000	[0, 1, 1]	2067.63	0.010400	[193]
1-pentanol	88.150	3.6260	3.4508	247.2800	[0, 1, 1]	2252.10	0.010319	[88]
ammonia	17.031	1.4302	2.7927	145.0059	[0, 1, 1]	1600.00	0.221193	[194]
water	18.015	1.2046	$\sigma(T)^a$	353.9449	[0, 1, 1]	2425.67	0.045090	[195]
carbon dioxide	44.010	2.0727	2.7852	169.2100	[0, 1, 1]	0.00000	0.100000	[87]
n-hexane	86.177	3.0576	3.7983	236.7700	[0, 0, 0]	-	-	[87]
n-heptane	100.203	3.4831	3.8049	238.4000	[0, 0, 0]	-	-	[87]

[a] Temperature-dependent function is given by σ [Å] $= 2.7927 + 10.11\exp(-0.01775\text{T[K]}) + 1.417\exp(-0.01146\text{T[K]})$.

4.3. Results

4.3.1. Density

Figure 4.2 shows the density modeling results using PC-SAFT for three ChCl-based DESs. The pseudo-pure component approach accurately describes the atmospheric pressure densities of these DESs, largely because the model was fitted to this thermophysical property. In contrast, the individual component approach does not reproduce this property as accurately. However, when the individual component approach incorporates the same experimental data for fitting, specifically by adjusting the binary interaction parameters between the HBA and HBD, its accuracy in describing the temperature dependence of the density improves considerably. In this case, the PC-SAFT EoS provides a linearly temperature-dependent binary interaction parameter, k_{ij}, to correct the dispersive energy in the mixture according to Eq. 2.17b. These k_{ij} values listed in Table 4.2 are all positive at 298.15 K, indicating a reduction in the effective dispersion interaction between the components compared to the geometric mean approximation.

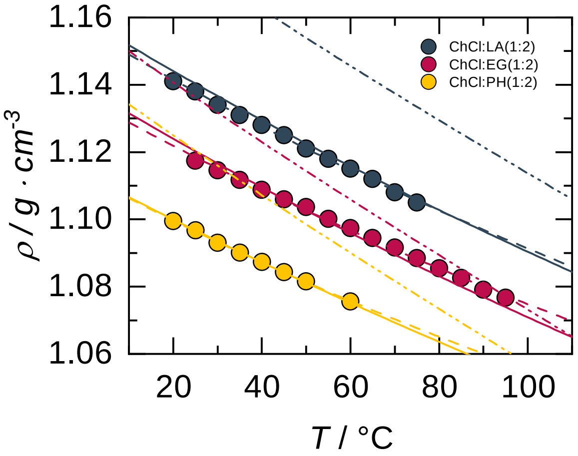

FIGURE 4.2: Densities at atmospheric pressure for ChCl-based DESs. Symbols are experimental data [196–201]. Solid lines: pseudo-pure component approach. Dot-dashed lines: individual component approach without fitted parameters. Dashed lines: individual component approach with fitted k_{12} values (Table 4.2).

TABLE 4.2: PC-SAFT binary interaction parameters, $k_{ij} = k_{ij,a} + k_{ij,T}\,(T\,[\mathrm{K}] - 298.15)$, according to Eq. 2.17b used in this chapter.

Pair	k_{ij}	
	$k_{ij,a}$	$k_{ij,T}$
ChCl-LA	0.17491	-0.001090
ChCl-EG	0.09598	-0.001390
ChCl-PH	0.11675	-0.000144

4.3.2. Excess properties

The excess thermodynamic properties of mixtures containing DESs with organic solvents and water are analyzed in this section. igure 4.3 displays the excess molar volumes for systems composed of ChCl-based DESs and various alcohols across the full composition range. Figure 4.3A presents the mixtures of three ChCl-based DESs with 1-butanol at 313.15 K [156], while Figure 4.3B shows the excess volumes of the DES ChCl:LA(1:2) mixed with the n-alkanol series at 298.15 K [157]. In all cases, the excess molar volumes exhibit negative deviations from ideality, which are attributed to strong specific interactions such as hydrogen bonding between the DES components and alcohol molecules. These interactions lead to structural rearrangement and volume contraction upon mixing. The PC-SAFT equation of state, applied using both the pseudo-pure component and individual component approaches, qualitatively reproduces the negative excess volume behavior. However, it tends to overestimate the magnitude of the deviations. Among the two modeling approaches, the individual component yields slightly better agreement with the experimental data.

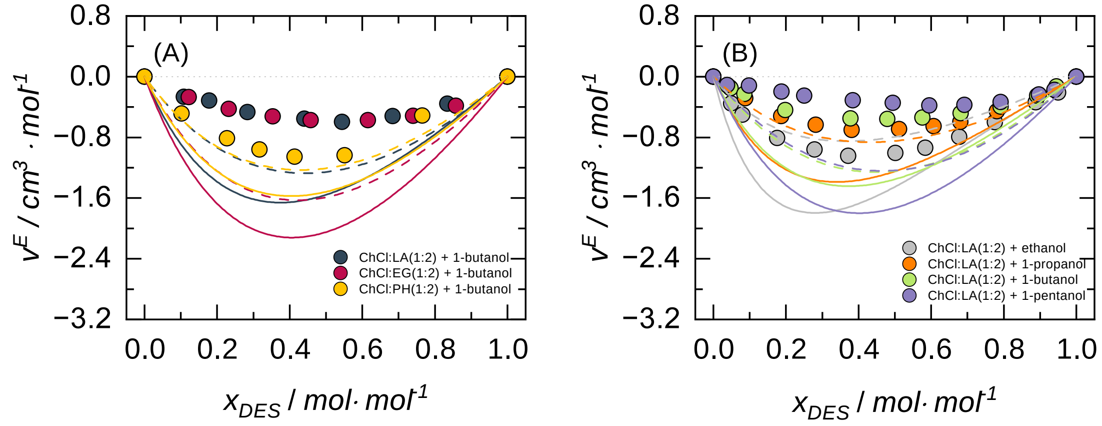

FIGURE 4.3: Excess volumes for mixtures of (A) ChCl-based DESs with 1-butanol at 313.15 K , and for mixtures of (B) ChCl:LA(1:2) with n-alcohols at 298.15 K. Symbols: experimental data [156, 171]. Solid lines: pseudo-pure component approach. Dashed lines: individual component approach with fitted k_{12} values (Table 4.2).

Figure 4.4 shows the excess enthalpies predicted for mixtures of ChCl-based DESs with 1-butanol and water. The individual-compound approach provides a better prediction of the negative excess enthalpies in all cases compared to the pseudo-pure component approach [156, 171], consistent with the exothermic nature of the mixing process. Although the pseudo-pure component approach includes association sites, it treats the DES as a single, indivisible entity. As a result, the model cannot capture the breaking or rearrangement of the original HBA–HBD hydrogen-bond network to allow for cross-association with the cosolvent. This limitation prevents the model from accurately representing the strong specific interactions (e.g., hydrogen bonding) that drive the exothermic mixing behavior and the negative excess volume. In contrast, the individual component approach explicitly considers the HBA and HBD as separate species, enabling the formation of cross-association interactions with cosolvent molecules. However, in the case of 1-butanol, this approach tends to overpredict the magnitude of the negative excess enthalpy, likely due to an overestimation of the cross-association strength between 1-butanol and the DES components.

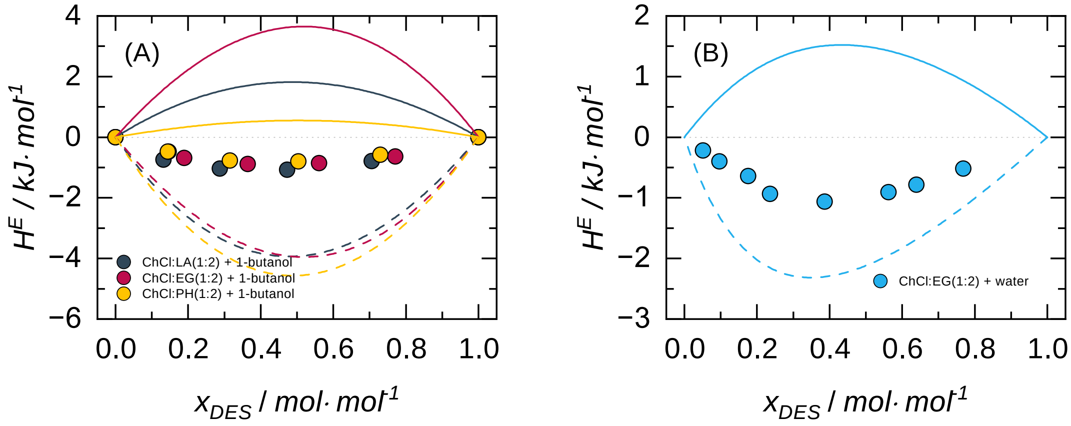

FIGURE 4.4: Excess enthalpies for mixtures of (A) ChCl-based DESs with 1-butanol at 313.15 K, and for mixtures of (B) ChCl:EG(1:2) with water at 308.15 K. Symbols: experimental data [156, 172]. Solid lines: pseudo-pure component approach. Dashed lines: individual component approach with fitted k_{12} values (Table 4.2).

The individual-compound approach allows for the exploration of DES behavior at different molar ratios of HBA and HBD using the same set of molecular parameters, which the pseudo-pure component approach cannot do. Figure 4.5 illustrates the excess volumes and excess enthalpies of the ChCl:EG and 1-butanol system in different molar ratios of HBA and HBD at 313.15 K. As the amount of HBD in the DES increases, the excess volume and excess enthalpy become less negative. This is because the HBD, in this case ethylene glycol, is an alcohol similar to 1-butanol, causing the mixture to become more homogenous in its components.

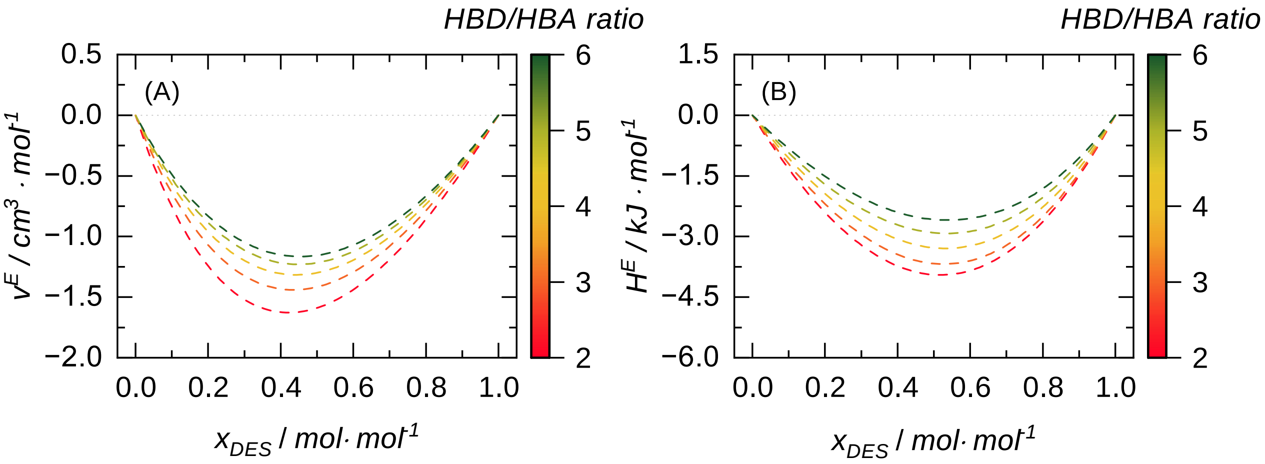

FIGURE 4.5: For mixtures of ChCl:EG with 1-butanol at 313.15 K at different HBA and HBD molar ratios: (A) excess volumes and (B) excess enthalpies. Dashed lines: individual component approach with fitted k_{12} values (Table 4.2).

4.3.3. Phase equilibria

In the following discussion, the capabilities of the models in predicting phase equilibria for systems containing the studied DESs are examined. Figure 4.6 shows the solubilities of CO_2 and NH_3 in ChCl-based DES systems. Unfortunately, the available experimental data [29, 202–205] are limited to a relatively narrow T-P range, which restricts a comprehensive comparison of the approaches. The VLE data were modeled by accounting for cross-association interactions between DES and CO_2 through the lone pairs on one of the oxygen atoms. Thus, CO_2 was modeled with two association sites (see Table 4.1C) [61], considering this induced association while neglecting the self-association between CO_2 molecules. As shown, the pseudo-pure approach provides reasonable predictions for CO_2 solubility in ChCl:LA(1:2) and ChCl:EG(1:2) (Figure 4.6A,B). In contrast, the individual-compound approach tends to overestimate the experimental solubility. For the solubility of CO_2 in ChCl:PH(1:2), both approaches perform poorly, with significant overpredictions. In the case of NH_3, both models underestimate the solubility, although the individual component approach provides closer estimates to the experimental data.

Figure 4.6 shows the predictions for the available LLE in multicompound systems comprising ChCl-based DESs, without the use of additional binary parameters. According to the pseudo-pure component approach, these systems are treated as ternary, whereas the individual component approach treats them as quaternary. For simplification, the individual component approach assumes that the 1:2 molar ratio remains constant in each phase. To achieve this, a chemical potential for DES is defined as a function of the chemical potentials of the individual components, as shown in Eq. 4.1

$$\mu_{DES} = \frac{\mu_{HBA} + s\mu_{HBD}}{1+s} \tag{4.1}$$

where s is the ratio between HBD and HBA, which remains constant, and μ_{HBA} and μ_{HBD} are the chemical potentials of HBA and HBD, respectively, obtained directly from PC-SAFT. This definition ensures that the Gibbs energy calculated using the DES chemical potential is the same as that obtained using the chemical potentials of its individual components. This transformation makes it possible to solve the LLE as a ternary system for both approaches: treating the DES as a pseudo-pure component or as individual components.

As seen in Figure 4.7, the pseudo-pure compound approach fails to accurately predict the data, resulting in a significant overestimation of phase splits in all the cases and concentration ranges considered. In contrast, the predictions from the individual-compound approach are much more realistic; however, they show a considerable amount of DES in the *n*-alkane-rich phase, which is not observed experimentally.

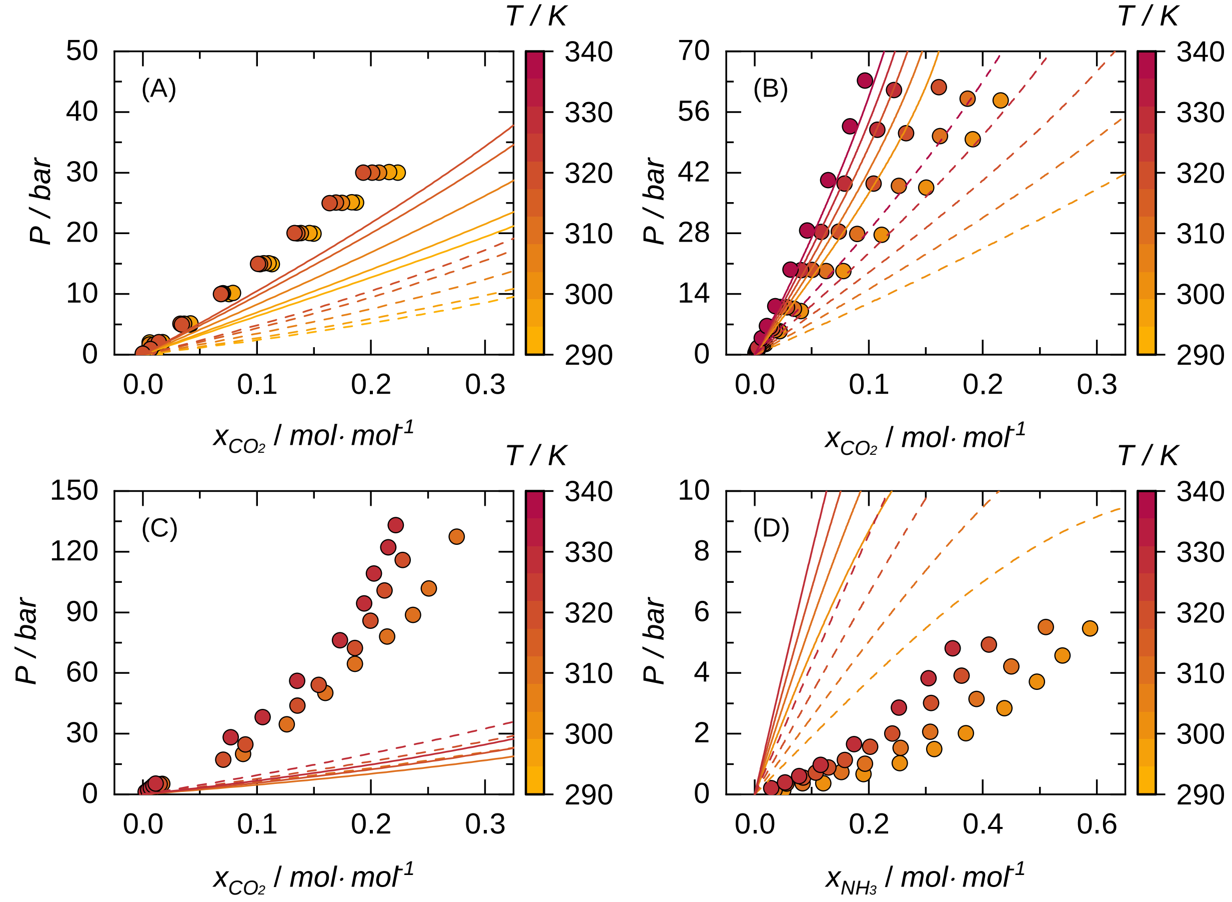

FIGURE 4.6: Gas solubility at different temperatures: (A) CO_2 in ChCl:LA(1:2), (B) CO_2 in ChCl:EG(1:2), (C) CO_2 in ChCl:PH(1:2), and (D) NH_3 in ChCl:EG(1:2). Symbols: experimental data [29, 202–205]. Solid lines: pseudo-pure component approach. Dashed lines: individual component approach with fitted k_{12} values (Table 4.2).

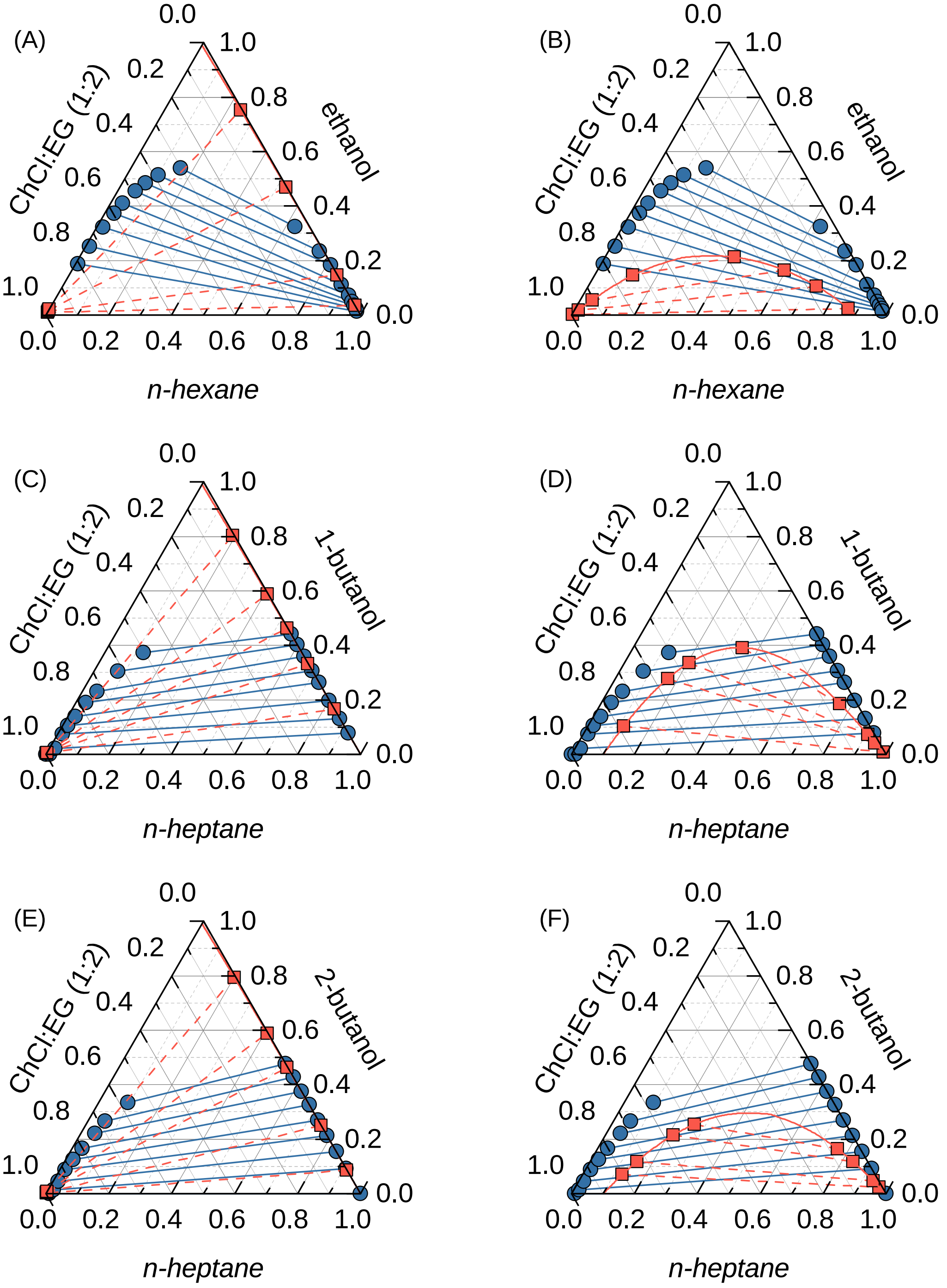

FIGURE 4.7: Liquid-liquid equilibrium phase diagrams for *n*-alkane + 1-alkanol + ChCl:EG(1:2) at 1.013 bar and 298.15 K (compositions in mass fraction). Circles: experimental data [206, 207]. Squares and solid lines: PC-SAFT calculations. (A), (C) and (D): the pseudo-pure compound approach. (B), (D) and (F) the individual-compound approach with fitted k_{12} values (Table 4.2).

4.4. Conclusions

This study provides one of the first comprehensive assessments of the PC-SAFT equation of state for ChCl-based DES, with a particular focus on its predictive performance across a diverse set of thermodynamic properties. A key novelty of this work lies in the consistent use of the same set of molecular parameters to model multiple properties—including excess volume, excess enthalpy, gas solubility, and LLE. Notably, this includes the modeling of excess enthalpy, a property that is experimentally available for only a few DES-containing systems and has rarely been addressed in previous DES modeling studies.

Experimental data for DES with 1-alkanols/water clearly show a pronounced negative deviation in both excess volume and excess enthalpy, suggesting a strong affinity between the DES precursors and the added co-solvent. One the one hand, the pseudo-pure component approach qualitatively described excess volume but poorly predicted excess enthalpies for mixtures of DES with 1-butanol and water. This limitation is likely due to the inability of the 2B association scheme used for the DES to capture the strong associative interactions with the co-solvents (1-alkanols or water). Since the pseudo-pure approach treats the DES as a fixed molecular entity, it inherently assumes that the HBA–HBD structure remains intact upon mixing. This prevents the model from accounting for the breaking or weakening of HBA–HBD interactions in favor of new, stronger associations with this types of co-solvents which can form new hydrogen bonds. On the other hand, the individual-component approach, when employed with temperature-dependent binary interactions between HBAs and HBDs, successfully captured the negative deviations in excess enthalpy. This reflects its superior ability to model cross-association and competitive interactions between DES components and co-solvents, providing a more realistic representation of the molecular reorganization occurring in these mixtures.

Although the individual-component approach did not show a significant advantage in predicting gas solubilities, it outperformed the pseudo-pure approach in estimating LLE in multi-component systems containing alkanols and *n*-alkanes. These performance differences likely arise not only from the different parameterization strategies, phase equilibrium data for the individual component approach versus density data for the pseudo-pure approach; but also from the ability of the individual component approach to represent molecular-level interactions more flexibly. In particular, it allows the weakening of original HBA–HBD associations and the formation of new hydrogen bonds between the DES precursors and the co-solvents.

5. Interfacial properties of DESs by density gradient theory

In this chapter, the implementation of the density gradient theory (DGT) coupled with the PC-SAFT equation of state is presented for the estimation of surface tension in DESs and their mixtures. The combination of DGT with PC-SAFT provides a robust framework for capturing the influence of molecular interactions and compositional inhomogeneities near interfaces. This approach allows for a more accurate prediction of surface tension, which is a critical property in the design and application of DES-based systems. The underlying theoretical principles, as well as the computational methodology employed, are discussed in this chapter. [*]

5.1. Introduction

Surface tension reflects the cohesive forces within a fluid and is defined as the energy required to alter the surface area of a liquid [208]. This property is pivotal in various processes, including wetting [209], permeability [210], and lubrication [211]. In addition, surface tension significantly influences the design and operation of mass transfer processes, such as distillation, absorption, separation, and extraction [212]. In DESs, surface tension depends on the molar ratio of the HBA and HBD, as well as the thermodynamic conditions. The literature reports various data for choline-based DESs mixed with compounds such as D-fructose, D-glucose, malonic acid, glycerol, and ethylene glycol, as well as for ternary systems including urea/glycerol and acetylcholine/urea mixtures.

Modeling the surface tension of DESs has been approached in numerous ways, although many are empirical. For example, Shahbaz et al. [213] correlated the surface tension of DES using the Othmer equation, producing satisfactory results for specific systems. Ghaedi et al. [214] applied polynomial expansions, though these exhibit limited transferability. A more advanced approach

---

[*] This chapter is adapted with permission from:
E. Cea-Klapp, N. Gajardo-Parra, P. Aravena, H. Quinteros-Lama, C. Held, R. I. Canales, and J. M. Garrido, "Interfacial properties of deep eutectic solvents by density gradient theory", Industrial& Engineering Chemistry Research **61**, 2580–2591 (2022). Copyright 2022 American Chemical Society.

by Haghbakhsh et al. [215, 216] utilized a corresponding states model, further refined through a group contribution method for 112 DES. These models, though accurate and practical, remain empirical and provide limited molecular-level insights, highlighting the need for theory-based estimation methods.

In this regard, DGT offers a framework for the prediction of interfacial properties when coupled with a robust equation of state (EoS) for the liquid phase [115]. SAFT equations, in particular, have been successfully integrated with DGT to predict surface tension for various pure fluids [217, 218] and mixtures [219–228]. In DES applications, Lloret et al. [63] used the soft-SAFT model with DGT for DESs of tetrabutylammonium bromide, producing accurate predictions but requiring unique molecular parameters for each HBA/HBD ratio.

This work applies DGT coupled with the PC-SAFT model, introduced by Gross and Sadowski [87], to predict the surface tension of DESs, based on its demonstrated success in representing the bulk properties of DES [61]. Specifically, the aim is to predict interfacial properties, including surface tension, in DES-water and DES-organic solvent mixtures, focusing on ChCl-glycerol and ChCl-lactic acid systems with solvents such as water, phenol, isopropanol, ethanol, ethyl acetate, and acetone. The approach follows the individual property calculation approach of Zubeir et al. [61], which enhances flexibility and broad applicability for various DES mixtures.

5.2. PC-SAFT Modeling

PC-SAFT EoS is applied as described in Section 2.2 to model the thermodynamic properties of the systems under investigation. Specifically, PC-SAFT is used with an individual approach, where each precursors in the DES and cosolvent systems is treated independently. This approach ensures an accurate representation of molecular interactions, phase equilibria, and other bulk properties of the systems. As noted in Chapter **??**, modeling DES as a mixture of their individual constituents has been shown to accurately predict excess properties (such as volume and enthalpy), solubility data, and liquid-liquid equilibria in ternary systems.

For surface tension modeling, an additional theoretical framework is required. As described in Section 2.6.1, the DGT is employed, which requires an EoS such as PC-SAFT to evaluate the Helmholtz free energy density in each homogeneous phase. In this work, the PC-SAFT parameters used the individual component approach with parameters for the HBA and HBD precursors. However, a key simplification is introduced to enable the application of DGT to DES: the molar ratio between HBA and HBD is held constant across the interface. This constraint allows the DES to be treated as a pseudo-pure compound within the interfacial region, while the bulk phases remain described by the individual components.

Under this assumption, the DGT framework can be applied using a single influence parameter per DES, which can be fitted directly to the available surface tension data. To make this formulation consistent, a chemical potential for the DES is defined as a function of the chemical potentials of its HBA and HBD components, which are directly provided by the individual component approach using PC-SAFT EoS. This hybrid approach maintains the physical realism of the individual component description in the bulk phase while enabling a practical and robust implementation of DGT for surface tension predictions.

The chemical potential of the DES, μ_{DES}, is defined as the weighted average of the chemical potentials of μ_{HBA} and μ_{HBD}, according to Eq. 5.1

$$\mu_{\text{DES}} = \frac{\mu_{\text{HBA}} + s\mu_{\text{HBD}}}{1 + s} \tag{5.1}$$

where $s = x_{\text{HBD}}/x_{\text{HBA}}$ is the molar ratio between the HBD and HBA constituents, which remains constant. This definition is consistent with the work of Tan et al. [229] and Shen et al. [225], where the ionic species were modeled using PC-SAFT.

In order to apply the modeling approaches outlined above, accurate PC-SAFT pure-component parameters are essential for capturing the thermodynamic behavior of the systems. For the compounds studied in this chapter, the molecular parameters were either regressed from experimental vapor pressure and liquid density data or sourced from the literature. The complete set of PC-SAFT parameters used in this study is presented in Table 5.1.

TABLE 5.1: PC-SAFT molecular parameters used in this chapter. The [B, P, N] notation indicates the number of bivalent, positive, and negative association sites, respectively, as defined in Figure 2.2.

Compounds	M_w **[g/mol]**	m_i	σ_i **[Å]**	ε_i/k_B **[K]**	S^{Ai} **[B, P, N]**	ε^{AiBi}/k_B **[K]**	κ^{AiBi}	**Sources**
choline chloride (ChCl)	139.62	13.0200	2.3680	228.07	[0, 1, 1]	8000.0	0.2000	[61]
tetrabutylammonium chloride (TBACl)	277.92	17.0800	2.8040	159.51	[0, 1, 1]	5000.0	0.1000	[61]
tetrabutylammonium bromide (TBABr)	322.37	9.5840	3.4433	150.27	[0, 1, 1]	5000.0	0.1000	[230]
thymol (Thy)	150.22	4.0120	3.8160	290.22	[0, 1, 1]	1660.0	0.0616	[47]
1,2-ethanediol	62.07	2.4366	3.2328	344.06	[0, 1, 1]	2702.6	0.0222	[190]
glycerol	92.05	5.1560	2.7380	247.65	[0, 2, 2]	1765.5	0.3018	[231]
1,4-butanediol	90.12	3.9030	3.1666	252.50	[0, 1, 1]	3755.0	0.0187	[21]
lactic acid	90.08	4.0800	2.8510	275.53	[0, 1, 1]	100.3	0.0010	[61]
diglycolic acid	134.09	2.9632	3.8071	390.43	[0, 1, 1]	950.0	0.0020	This work
methoxy-1,2-propanediol	106.12	6.6286	2.6757	231.36	[0, 1, 1]	1732.5	0.1330	This work
monoethanolamine	61.08	4.5354	2.6019	204.04	[0, 2, 1]	2383.5	0.1185	[232]
fructose	180.16	7.3870	2.8490	237.19	[0, 5, 5]	5000.0	0.1000	[233]
glucose	180.16	6.6260	2.9860	244.53	[0, 5, 5]	5000.0	0.1000	[233]
triethylene glycol	150.17	3.1809	4.0186	333.17	[0, 2, 2]	2080.0	0.0235	[234]
octanoic acid	144.21	7.0480	3.1360	234.36	[0, 1, 1]	1889.2	0.0200	[47]
decanoic acid	172.26	7.1472	3.3394	242.46	[0, 1, 1]	2263.0	0.0200	[235]
water	18.015	1.2046	$\sigma(T)^a$	353.95	[0, 1, 1]	2425.8	0.0451	[195]
ethanol	46.07	2.3827	3.1771	198.24	[0, 1, 1]	2653.4	0.0324	[88]
2-propanol	60.10	3.0929	3.2085	208.42	[0, 1, 1]	2253.9	0.0247	[88]
phenol	94.11	3.5533	3.2747	303.76	[0, 1, 1]	2497.5	0.0008	[236]
acetone	58.08	3.0925	3.0848	168.32	[0, 1, 1]	1321.2	0.9639	[237]
ethyl ethanoate ^{b}	88.11	3.5375	3.3079	230.80	[0, 1, 1]	0.0	0.0100	[87]

[a] Temperature-dependent function is given by σ [Å] $= 2.7927 + 10.11 \exp(-0.01775\mathrm{T[K]}) + 1.417 \exp(-0.01146\mathrm{T[K]})$.

[b] An induced association in mixtures with associating components is considered.

5.3. Results

5.3.1. Density of DESs

An essential component of DGT is the thermodynamic model that accurately represents the bulk density. This is why it is essential to calculate the binary interaction parameter, k_{ij}, between HBA and HBD to achieve precise modeling of thermophysical properties, as outlined by Zubeir et al. [61]. The interaction parameters were fitted to DES density data and are summarized in Table 5.2, along with the Absolute Average Relative Deviation (AARD), calculated by Eq. 7.3,

$$\text{AARD} = \frac{100}{N} \sum_{i=1}^{N} \left| \frac{\delta_i^{\text{exp}} - \delta_i^{\text{calc}}}{\delta_i^{\text{exp}}} \right| \tag{5.2}$$

where N is the data number, δ_i is the fitted property, and the superscripts *exp* and *calc* are the experimental and calculated values, respectively.

TABLE 5.2: Binary interaction parameters, $k_{ij} = k_{ij,a} + k_{ij,T}\,(T\,[\text{K}] - 298.15)$, for each DES, along with the AARD for density with and without the binary interaction.

Pair	k_{ij}		N	AARD	AARD	Sources
	$k_{ij,a}$	$k_{ij,T}$		$\rho_{k_{ij}=0}$	$\rho_{k_{ij}\text{ fit}}$	
ChCl + 1,2-ethanediol	0.1029	-0.0016	48	1.15%	0.05%	[15, 156, 159, 238–240]
ChCl + glycerol	0.0670	-0.0016	23	0.67%	0.05%	[159, 238, 241]
ChCl + 1,4-butanediol	0.0969	-0.0014	9	1.37%	0.02%	[15]
ChCl + lactic acid	0.2234	-0.0018	14	3.74%	0.03%	[242]
ChCl + diglycolic acid	-0.3637	-0.0012	9	5.15%	0.01%	[243]
ChCl + methoxy-1,2-propanediol	0.1351	-0.0017	7	1.97%	0.02%	[244]
ChCl + monoethanolamine	-0.0899	-0.0008	28	1.93%	0.11%	[245]
ChCl + fructose	0.0842	-0.0015	28	0.79%	0.63%	[246]
ChCl + glucose	0.1910	-0.0017	28	2.20%	0.95%	[247]
TBACl + 1,2-ethanediol	-0.6449	-0.0003	21	9.41%	0.23%	[248]
TBACl + glycerol	0.5045	-0.0014	21	11.04%	0.99%	[248]
TBACl + triethylene glycol	-0.1216	-0.0025	28	2.70%	1.04%	[248]
TBABr + monoethanolamine	-0.0423	-0.0010	28	1.68%	0.56%	[245]
Thy + octanoic acid	0.0571	-0.0007	62	0.82%	0.18%	[249]
Thy + decanoic acid	0.0598	-0.0006	51	0.82%	0.21%	[249]
ChCl + water [a]	-0.0584	0.0001	-	-	-	
LA + water [a]	-0.0387	-	-	-	-	

[a] Binary interactions used that were retrieved from the original source [61].

As shown in Table 5.2, PC-SAFT achieves high accuracy across all mixtures based on choline chloride (ChCl), tetrabutylammonium chloride (TBACl), tetrabutylammonium bromide (TBABr), and thymol (Thy). Additional visual comparisons with literature data are provided in Figures 5.1 -

5.3, where the PC-SAFT calculations incorporate the fitted binary interaction parameters. In most cases, the same binary interaction parameter for the HBD and HBA successfully reproduces the temperature dependence between different ratios between the HBD and HBA.

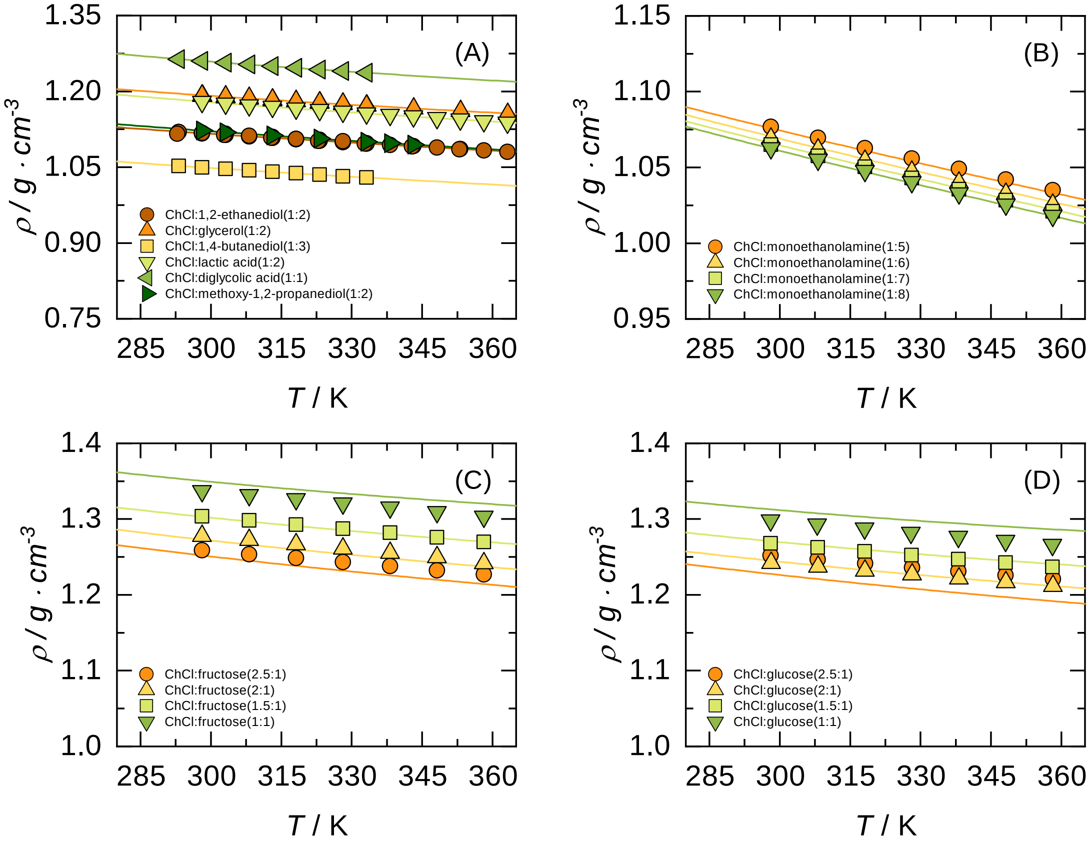

FIGURE 5.1: Temperature dependence of density for ChCl-based DES. Symbols are experimental data. Solid lines represent the PC-SAFT calculations.

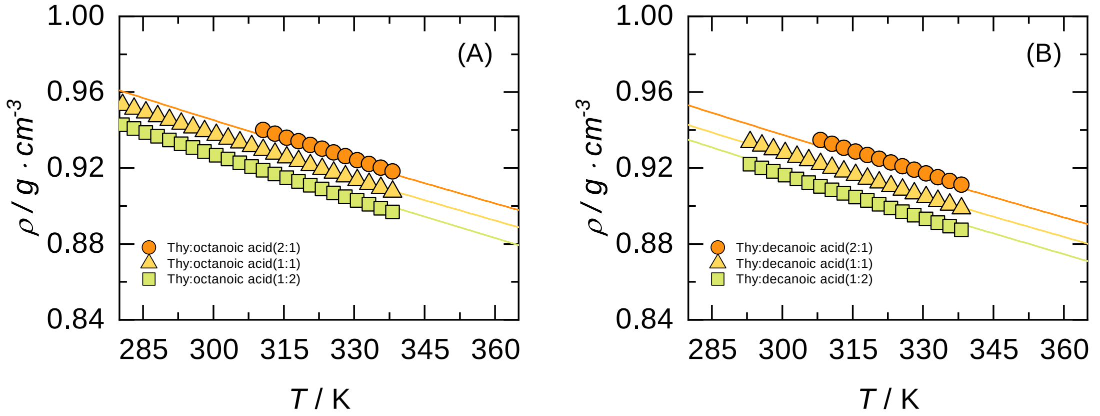

FIGURE 5.2: Temperature dependence of density for Thy-based DES. Symbols are experimental data. Solid lines represent the PC-SAFT calculations.

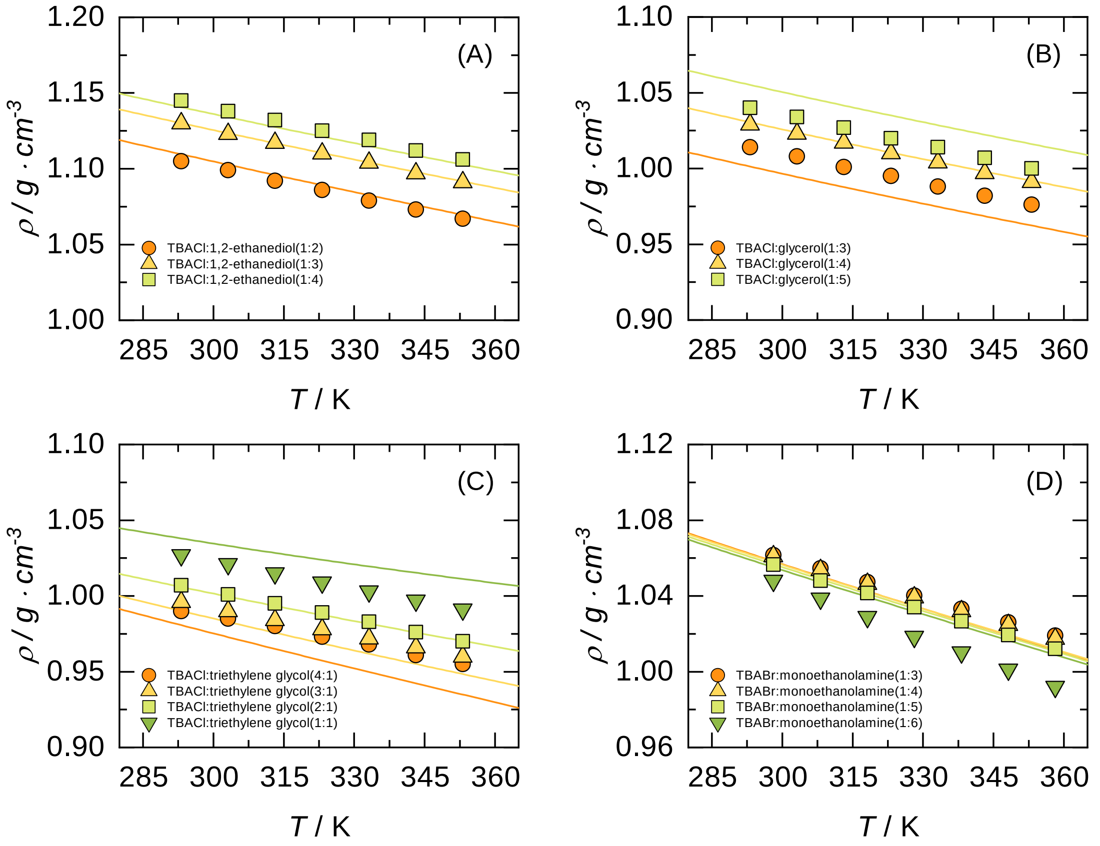

FIGURE 5.3: Temperature dependence of density for TBA-based DES. Symbols are experimental data. Solid lines represent the PC-SAFT calculations.

5.3.2. Surface tension of DESs

With the accuracy of PC-SAFT results for bulk density established, the surface tension can be calculated. First, the influence parameters must be estimated. Using surface tension data from the available literature on DES, the influence parameter for each DES was determined by fitting experimental surface tensions across the temperature ranges of the data, approximately spanning from 293 to 343 K. All the influence parameters obtained are summarized in Table 5.3, along with the AARD for the surface tension. As previously mentioned, the DGT framework is applied using a pseudopure approach, even though the PC-SAFT parameters correspond to the individual components of each DES. Consequently, each specific HBD-HBA ratio in a DES requires a particular influence parameter.

The influence parameters presented in Table 5.3 show an approximate linear relationship with the mole fraction of the HBA in each DES family, as illustrated in Figure 5.4. A similar trend can be observed when considering the DES molecular weight, which is linearly correlated with the mole fraction. Notably, Lloret et al. [63] previously discussed this linear relationship in TBACl-based mixtures using the pseudopure compound approach in conjunction with the DGT and soft-SAFT EoS.

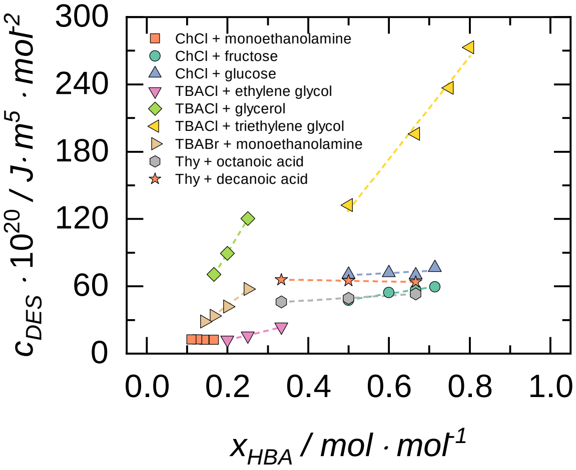

FIGURE 5.4: Observed relationship between influence parameters and the mole fraction of HBA.

The accuracy of the DGT framework, coupled with PC-SAFT, in capturing the temperature dependence of the surface tension for the available DESs is analyzed in Figures 5.5 - 5.7. In each case, an excellent agreement with experimental data is observed, displaying a consistent linear dependence on temperature. Overall, these results indicate that the PC-SAFT+DGT model can be applied to calculate the surface tension of different molar ratios of HBDs and HBAs without sacrificing accuracy. This analysis highlights the current form of PC-SAFT+DGT, using the chemical potential of individual components as expressed in Eq. 5.1, substantially improves the description of experimental data compared to the pseudo-component approach previously applied to TBACl-family DESs [63], as shown in Figure 5.7A-C. Additionally, the individual-component approach accurately captures the thermal properties of hydrophobic DESs (Figure 5.6), where interfacial properties are critical for water-immiscible extractants. To the best of our knowledge, this represents the first application of a thermodynamic model, either empirical or molecular-based, to this class of eutectic solvents.

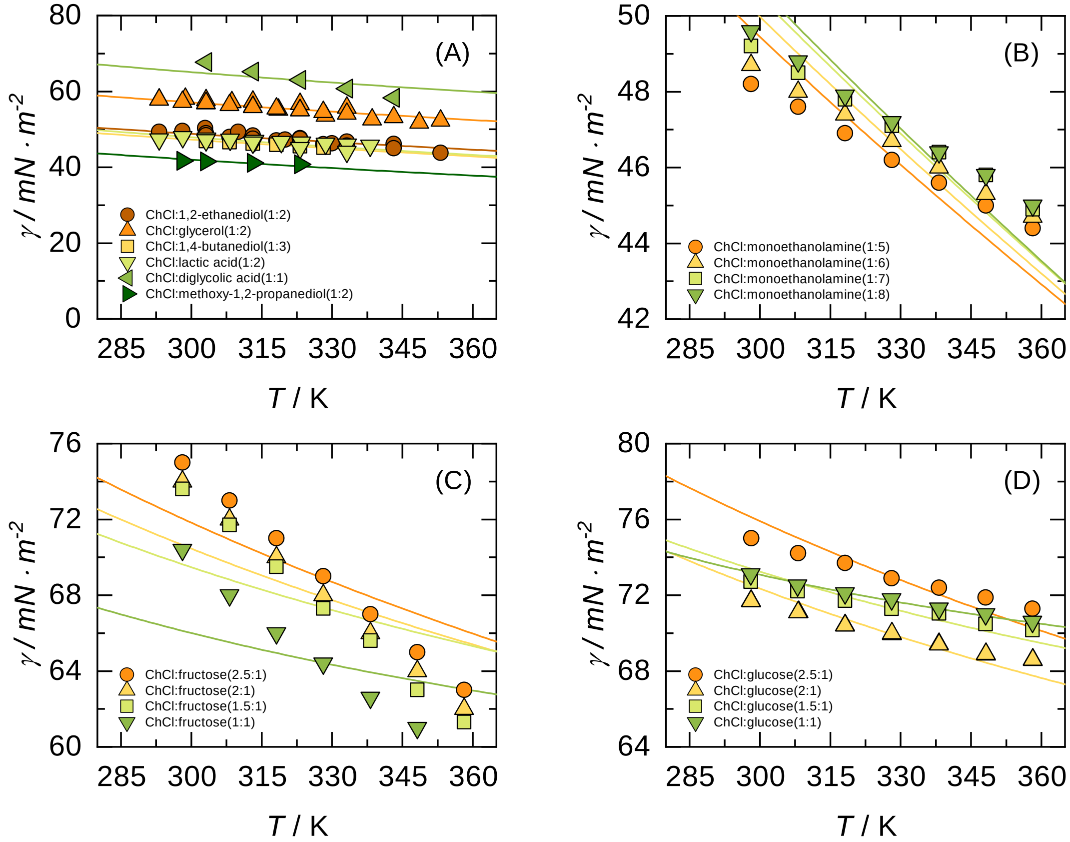

FIGURE 5.5: Temperature dependence of surface tension for ChCl-based DES. Symbols are experimental data. Solid lines represent the PC-SAFT+DGT calculations.

To evaluate the overall performance of the proposed model and to complement the AARD values for surface tension in Table 5.3, a parity plot comparing all experimental data and theoretical predictions is included for a visual evaluation. Figure 5.8 shows that the PC-SAFT+DGT model remains within the region defined by 8% error lines, representing the maximum observed deviation. Notably, the model achieves an overall average deviation of just 1.26%, indicating a significantly improved performance over models in the literature, as seen in the parity plots for models proposed by Haghbakhsh et al. [215, 216]. Although these models exhibit deviations above the 8% error threshold, they still demonstrate the utility of atomistic and group contribution methods for obtaining preliminary surface tension estimates.

It is seen that the proposed model for DESs is not only more accurate than other available correlations and models [63, 215], but is also broader in terms of applicability range and mixture conditions. Indeed, although the correlation of Haghbakhsh et al. [215, 216] may provide surface

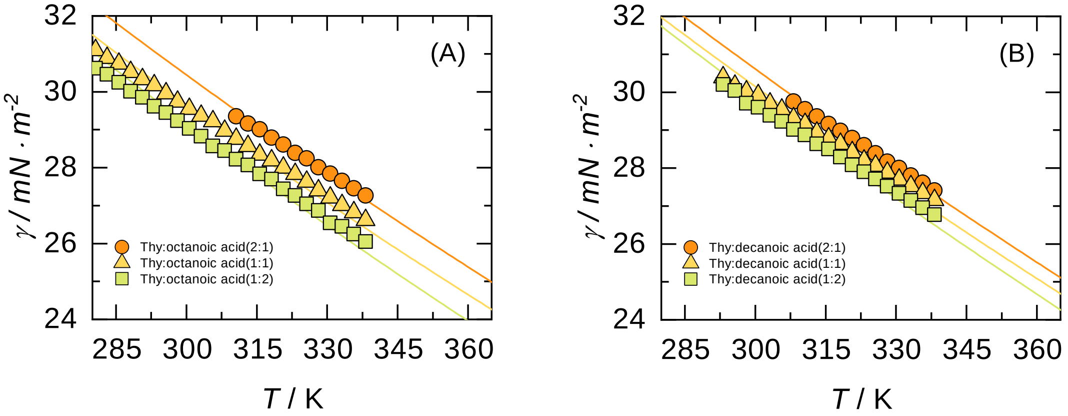

FIGURE 5.6: Temperature dependence of surface tension for Thy-based DES. Symbols are experimental data. Solid lines represent the PC-SAFT+DGT calculations.

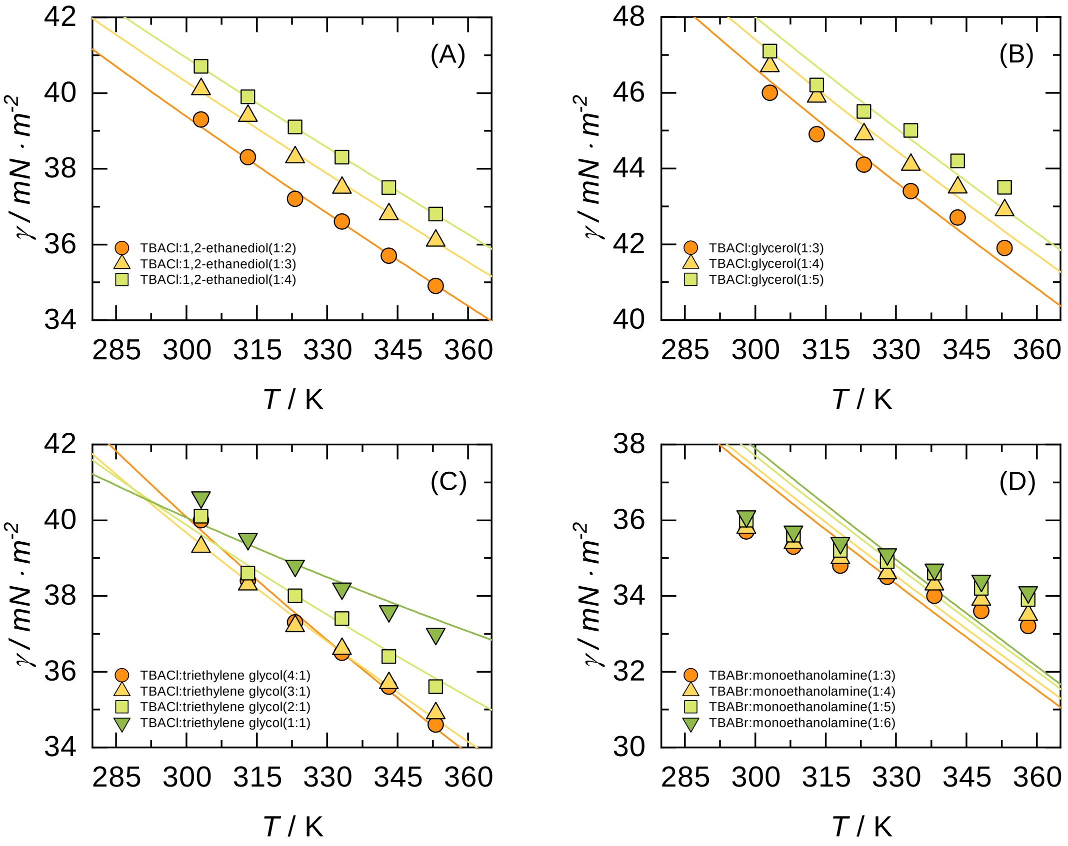

FIGURE 5.7: Temperature dependence of surface tension for TBA-based DES. Symbols are experimental data. Solid lines represent the PC-SAFT+DGT calculations.

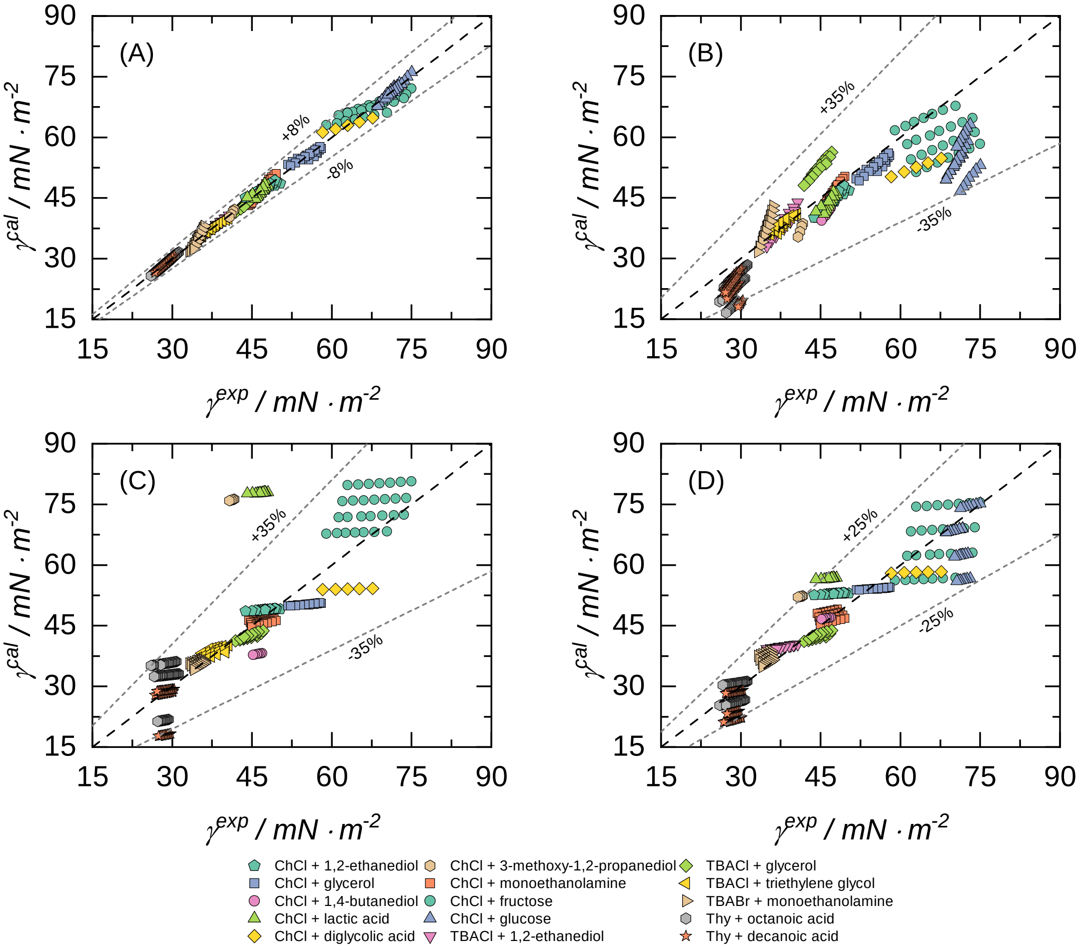

FIGURE 5.8: Parity plots of surface tension calculation versus the experimental values: (A) PC-SAFT+DGT model, (B) Haghbakhsh et al. [215] empirical model, (C) Haghbakhsh et al. [216] group-contribution model, and (D) Haghbakhsh et al. [216] atomistic model.

tensions in different DESs, it does not provide detailed information along the interfacial region. Furthermore, these kinds of correlations cannot evaluate the effect of cosolvents on interfacial behavior. These handicaps make a theoretical estimation of PC-SAFT+DGT even more significant. The critical evaluation of this proposed model and the development of new DESs are undoubtedly highly desirable goals. Therefore, obtaining an accurate description of the interfacial behavior (i.e., density profiles, surface tension, Gibbs adsorption, among other properties) is a key step toward a better understanding of the physics of the macroscopic behavior of DES and cosolvents.

5.3.3. Surface tension of DESs + cosolvent mixtures

In the following, a preliminary assessment of the adequacy of the PC-SAFT+DGT model in describing the vapor-liquid surface tension in mixtures of water and organic solvents with DESs is presented. In order to extend further its theoretical capabilities in the calculation of interfacial properties, the geometric mixing rule of Eq. 2.36 was used between the DES and cosolvents. In addition, β_{ij} has been set to zero, thus making the calculation of interfacial properties fully predictive.

ChCl:lactic acid(1:2) and ChCl:glycerol(1:2) with various cosolvents—water, ethanol, 2-propanol, phenol, ethyl acetate, and acetone—are examined here. The influence parameter for each cosolvent must be fitted to apply the mixing rules. These values are summarized in Table 5.4, and their effectiveness in modeling the temperature dependence of surface tension is shown in Figure 5.9.

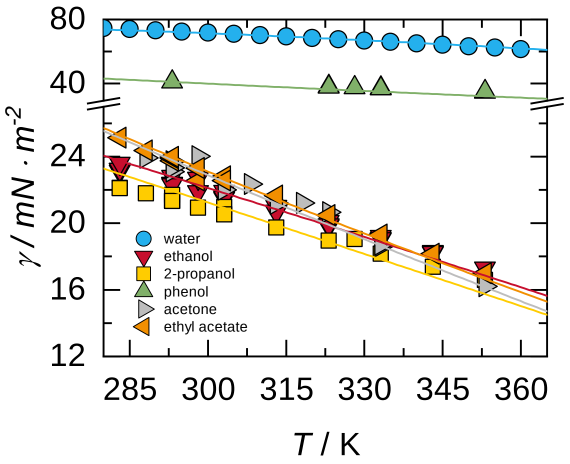

FIGURE 5.9: Temperature dependence of surface tension for cosolvents. Symbols are experimental data. Solid lines represent the PC-SAFT+DGT calculations.

The resulting descriptions for DES + cosolvent mixtures are compared with existing experimental data [252–255] for ChCl:glycerol(1:2) and ChCl:lactic acid(1:2), as shown in Figure 5.10A and B, respectively. As illustrated, these data align well with the predictions from the PC-SAFT+DGT model. Specifically, DES surface tension increases with the addition of water and decreases with adding organic solvents.

From another perspective, Figures 5.10A and B show that the effect of adding DESs on the surface tension is stronger in water than in other solvents. In both mixtures, since water has a much higher surface tension than these DESs, the initial decrease in surface tension can be explained by the migration of water into the bulk phase, which promotes a rearrangement of the DES components, leading to a reduction in surface tension. This is particularly evident in the subsequent increase in surface tension observed for the ChCl:lactic acid (1:2) system, which results in a minimum known as an aneotrope [256]. This behavior can be attributed to the existence of a critical concentration of water that can be incorporated into the bulk; beyond this point, additional water tends to segregate at the interface. As noted, the PC-SAFT+DGT framework is not capable of predicting this type of behavior in this DES.

For ChCl:glycerol (1:2), Ferreira et al. [257] showed that water interacts simultaneously with ChCl and glycerol through hydrogen bonds up to a mass concentration of 11% ($x_{water} = 0.42$), where water acts as a "glue" between the HBA and HBD. Beyond 11 wt%, water molecules begin to solvate the ChCl and glycerol individually, weakening the hydrogen bond network that forms the DES [258, 259]. This continues until around 35 wt% ($x_{water} = 0.76$), where the DES structure is disrupted, and the system transitions into a DES-in-water solution. Also, the study by Ferreira et al. [257] showed that water addition up to this limit (35 wt%) leads to a pronounced decrease in shear viscosity, without strongly compromising the DES properties arising from its nanostructural organization—in this case, the surface tension.

In contrast, for mixtures of DESs with organic solvents, a more straightforward behavior is observed. Despite the fact that the pure organic solvents have lower surface tension than both DESs, the addition of these solvents results in a monotonic decrease in surface tension. This trend suggests the absence of a complex interfacial restructuring as seen with water. The observed behavior can be attributed to weaker or less directional hydrogen bonding interactions between the organic solvents and the DES components, which do not lead to pronounced nanostructural rearrangements at the interface.

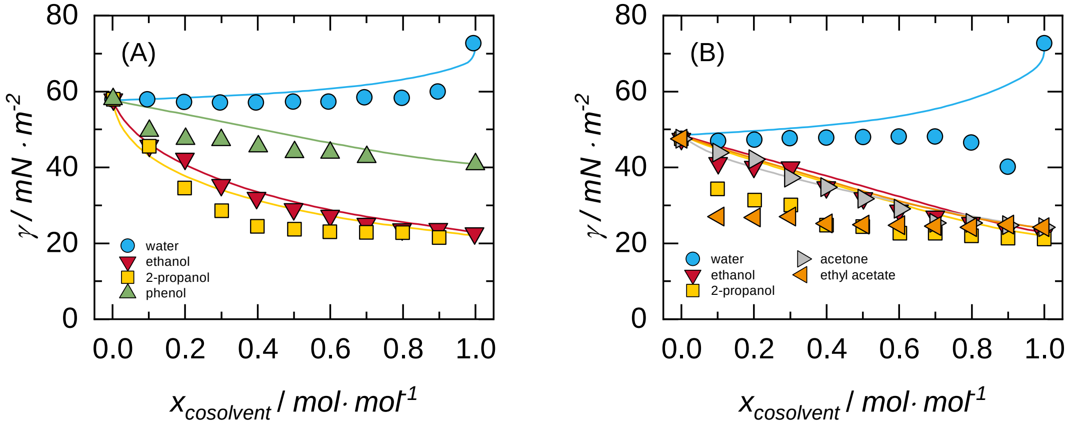

FIGURE 5.10: Effect of water and organic solvents on the surface tension of (A) ChCl:glycerol(1:2) and (B) ChCl:lactic acid(1:2) at 293.15 K. Symbols are experimental data [252–255]. Solid lines represent the PC-SAFT+DGT predictions.

A deeper analysis of interfacial properties can be obtained through density profiles across the interface. Figure 5.11 and 5.12 show the density profiles for ChCl:glycerol(1:2) and ChCl:lactic acid(1:2) at different mole fractions of various cosolvents. As shown in Figure 5.11B and 5.12B, water density profiles follow the traditional hyperbolic tangent shape behavior [115, 117]. Additionally, density profiles of ethanol, 2-propanol, phenol and acetone exhibit positive surface activity (i.e., $d\rho_i/dz = 0$; $d^2\rho_i/dz^2 < 0$). This positive surface activity reflects adsorption (or accumulation) of the organic solvent in the interfacial region of ChCl:glycerol(1:2) or ChCl:lactic acid(1:2). On the one hand, density profiles of ethanol and 2-propanol display strong positive surface activity in the interfacial region, which decrease as the mole fraction of cosolvent increases. On the other hand, although phenol presents a positive surface activity for ChCl:glycerol(1:2) mixtures, it is much lower than ethanol and 2-propanol. It is possible to conclude that components with lower surface tension (i.e., ethanol and 2-propanol) accumulate at the interfacial zone. Overall, the behavior of density profiles suggests that the surface is enriched with DES components for the DES + water mixtures. In contrast, it is enriched with diluent for the other ternary systems (ethanol, 2-propanol, and phenol). It is important to remark that all the characteristics described by density profiles considered the DES to be pseudopure. In order to make this framework fully universal and capable of predicting the entire set of thermophysical properties in different DES, the correlation must be coupled by a full description of HBDs and HBAs from a molecular viewpoint.

TABLE 5.3: Influence parameters, c_{DES}, for each DES used in this chapter and AARD of surface tensions γ.

DES	x_{HBD}	$c_{DES} \times 10^{20}$ **[J m^5/mol^2]**	**N**	**AARD** γ	**Sources**
ChCl:1,2-ethanediol(1:2)	0.67	13.76	24	1.08%	[238, 240, 250, 251]
ChCl:glycerol(1:2)	0.67	23.76	25	0.99%	[14, 241, 250, 252]
ChCl:1,4-butanediol(1:3)	0.75	28.48	6	0.14%	[200]
ChCl:lactic acid(1:2)	0.67	25.77	14	1.20%	[242, 252]
ChCl:diglycolic acid(1:1)	0.50	32.12	5	2.74%	[243]
ChCl:methoxy-1,2-propanediol(1:2)	0.67	22.83	4	0.85%	[244]
ChCl:monoethanolamine(1:5)	0.83	12.17	7	1.69%	[245]
ChCl:monoethanolamine(1:6)	0.86	12.30	7	1.68%	[245]
ChCl:monoethanolamine(1:7)	0.88	12.48	7	1.72%	[245]
ChCl:monoethanolamine(1:8)	0.89	12.55	7	1.63%	[245]
ChCl:fructose(2.5:1)	0.29	59.62	7	2.57%	[246]
ChCl:fructose(2:1)	0.33	56.84	7	2.94%	[246]
ChCl:fructose(1.5:1)	0.40	54.38	7	3.53%	[246]
ChCl:fructose(1:1)	0.50	47.53	7	3.49%	[246]
ChCl:glucose(2.5:1)	0.29	76.62	7	0.85%	[247]
ChCl:glucose(2:1)	0.33	70.05	21	0.66%	[238, 247, 250]
ChCl:glucose(1.5:1)	0.40	71.90	7	0.54%	[247]
ChCl:glucose(1:1)	0.50	70.46	7	0.10%	[247]
TBACl:1,2-ethanediol(1:2)	0.67	23.78	6	0.24%	[248]
TBACl:1,2-ethanediol(1:3)	0.75	15.81	6	0.24%	[248]
TBACl:1,2-ethanediol(1:4)	0.80	12.34	6	0.06%	[248]
TBACl:glycerol(1:3)	0.75	120.48	6	0.66%	[248]
TBACl:glycerol(1:4)	0.80	89.26	6	0.64%	[248]
TBACl:glycerol(1:5)	0.83	70.51	6	0.91%	[248]
TBACl:triethylene glycol(4:1)	0.20	272.91	6	0.43%	[248]
TBACl:triethylene glycol(3:1)	0.25	236.93	6	0.32%	[248]
TBACl:triethylene glycol(2:1)	0.33	195.72	6	0.52%	[248]
TBACl:triethylene glycol(1:1)	0.50	132.22	6	0.71%	[248]
TBABr:monoethanolamine(1:3)	0.75	57.46	7	2.67%	[245]
TBABr:monoethanolamine(1:4)	0.80	41.89	7	2.85%	[245]
TBABr:monoethanolamine(1:5)	0.83	33.59	7	3.02%	[245]
TBABr:monoethanolamine(1:6)	0.86	28.34	7	3.08%	[245]
Thy:octanoic acid(2:1)	0.33	53.10	12	0.24%	[249]
Thy:octanoic acid(1:1)	0.50	49.36	25	0.53%	[249]
Thy:octanoic acid(1:2)	0.67	46.09	25	0.64%	[249]
Thy:decanoic acid(2:1)	0.33	63.65	13	0.23%	[249]
Thy:decanoic acid(1:1)	0.50	64.93	19	0.60%	[249]
Thy:decanoic acid(1:2)	0.67	65.87	19	0.56%	[249]

TABLE 5.4: Influence parameters, $c_{cosolvent}$, for each cosolvent used in this chapter and AARD of surface tensions γ.

Cosolvent	$c_{cosolvent} \times 10^{20}$ **[J m^5/mol^2]**	**N**	AARD γ
water	1.06	17	0.51%
ethanol	8.41	7	1.34%
2-propanol	5.48	7	2.43%
phenol	18.24	7	0.56%
acetone	22.54	7	1.63%
ethyl acetate	13.84	7	1.06%

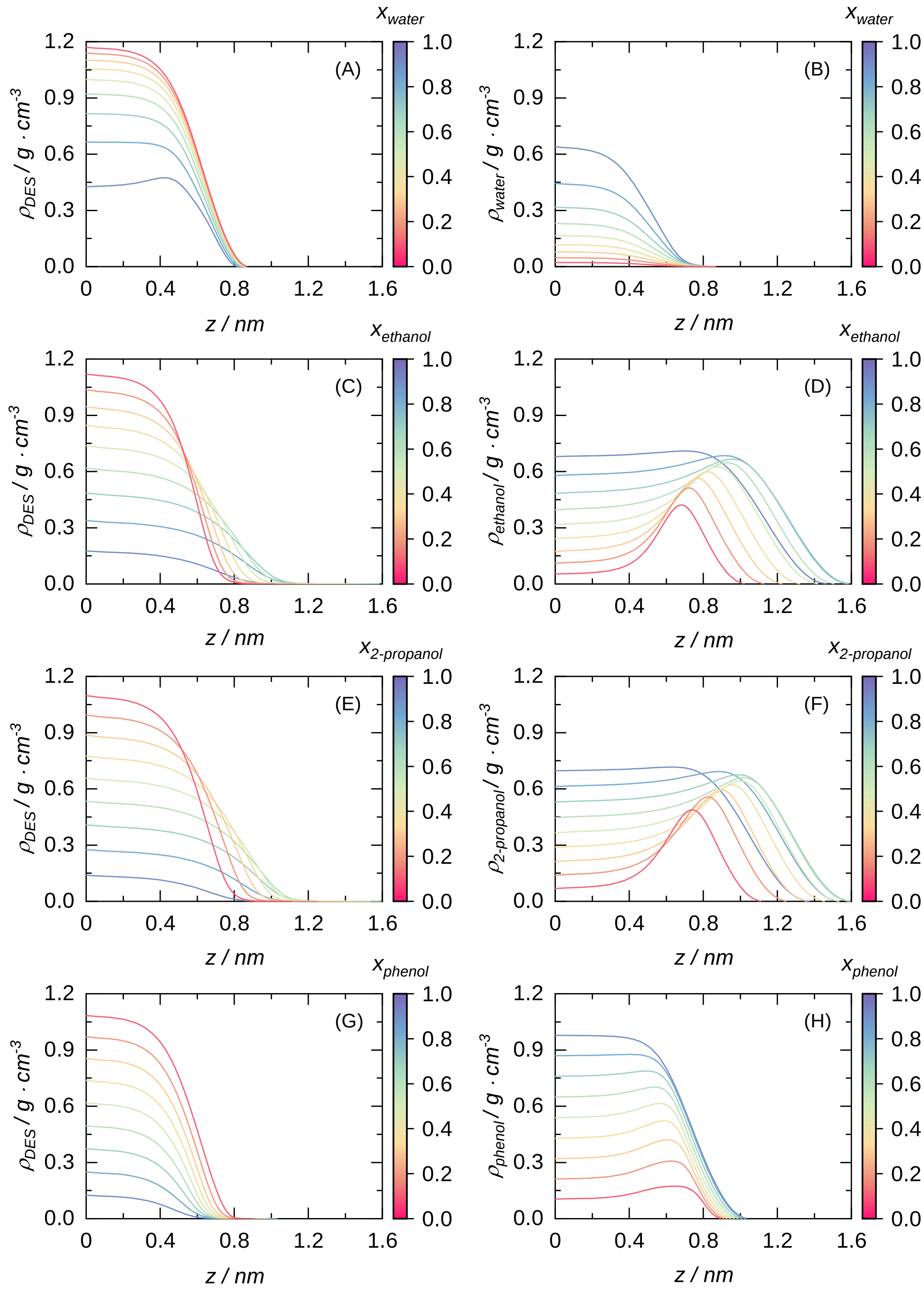

FIGURE 5.11: Density profiles of species, ρ_i, along the interfacial region, z, for ChCl:glycerol(1:2) systems at different mole fractions of cosolvent. Cosolvents: (A, B) water, (C, D) ethanol, (E, F) 2-propanol, and (G, H) phenol.

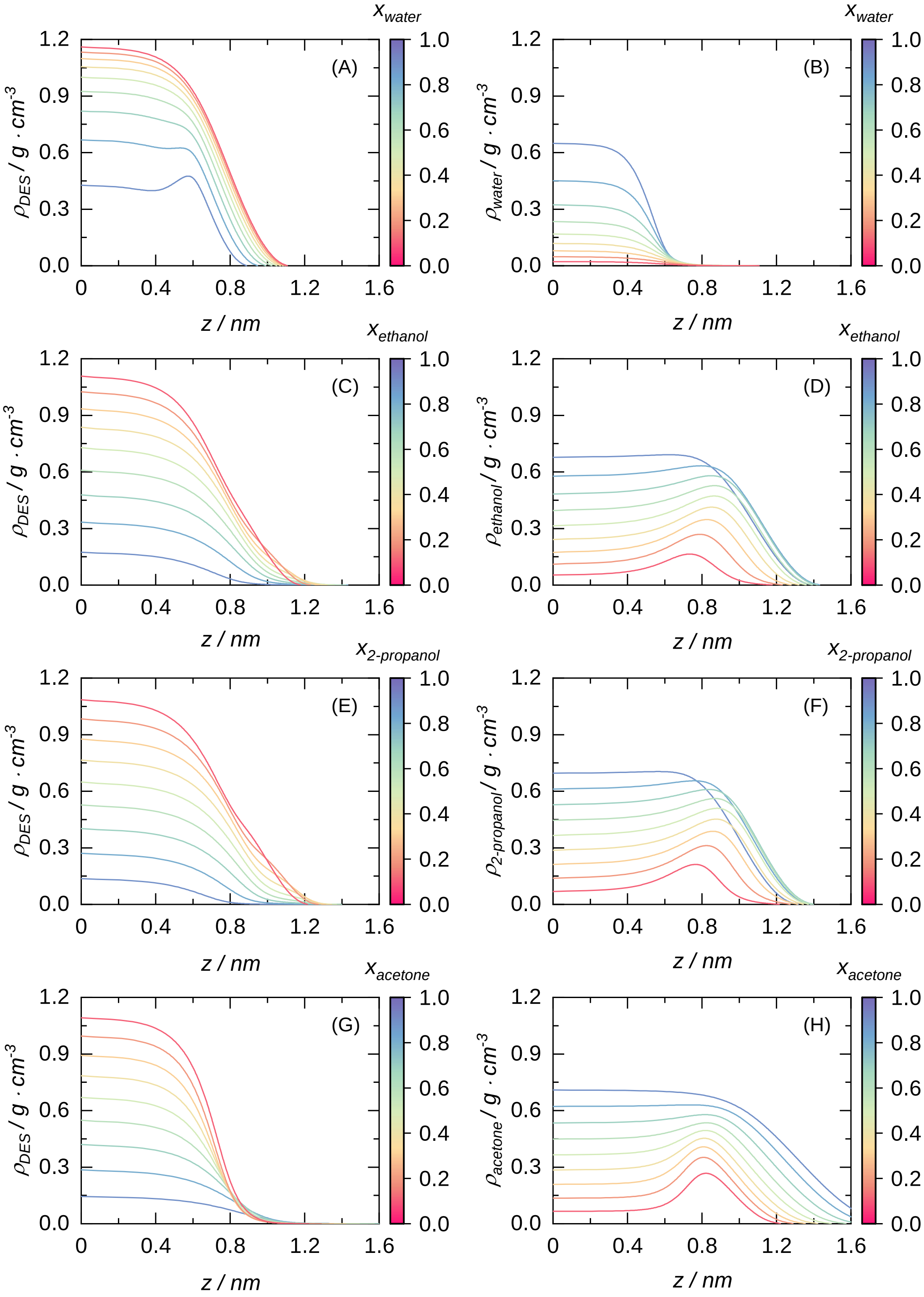

FIGURE 5.12: Density profiles of species, ρ_i, along the interfacial region, z, for ChCl:lactic acid (1:2) systems at different mole fractions of cosolvent. Cosolvents: (A, B) water, (C, D) ethanol, (E, F) 2-propanol, and (G, H) acetone.

5.4. Conclusions

In this chapter, the interfacial behavior of DES systems has been studied using DGT in combination with the PC-SAFT EoS, where each HBA and HBD is described using its own molecular parameters to represent the bulk phase. Under the assumption that the DES molar ratio remains constant at the interface, the PC-SAFT+DGT framework reliably describes the surface tension of DESs as a function of the HBA/HBD composition and temperature, and it enables at least qualitatively accurate predictions of surface tension in DES + cosolvent mixtures. It was found that the influence parameter used in the DGT framework can be correlated with the mole fraction of HBA for each DES, allowing interpolation of this parameter for molar ratios without requiring experimental surface tension data.

The methodology yields an average absolute relative deviation of 1.29% and a maximum deviation of 8.0% compared with experimental data. DGT, when coupled with the individual approach of PC-SAFT, allows for the modeling of solvent–DES mixtures and provides detailed insights into the interfacial region, making the evaluation of cosolvent effects on interfacial behavior a promising research direction.

The small addition of ChCl:glycerol (1:2) or ChCl:lactic acid (1:2) to water significantly decreases the surface tension of water. The density profiles obtained from the PC-SAFT+DGT approach show that this decrease is caused by the accumulation of DES at the interface, which disappears with further DES addition. For organic solvents such as ethanol, 2-propanol, phenol, and acetone, the opposite effect is observed. This means that the addition of these organic solvents to each DES decreases the surface tension of the DES. In the cases analyzed, all of these organic solvents exhibit noticeable surface activity at different concentrations, although the effect slightly diminishes with further addition.

6. Hydrogen bond influence on viscosity and density in choline chloride-based DESs with methanol

---

This section investigates the influence of hydrogen bonding on the viscosity and density of choline chloride-based DES, using glycerol and 1,2-ethanediol as HBD and methanol as cosolvent. Both PC-SAFT modeling and MD simulations were employed to analyze how the hydrogen bonding between choline chloride, acting as the HBA, and the selected HBDs affect the key thermophysical properties of the mixtures. By focusing on viscosity and density, the study provides a detailed understanding of the impact of molecular interactions within the system, offering insights into the behavior of these DES-methanol mixtures.[*]

6.1. Introduction

Molecular modeling techniques can contribute to both macroscopic and microscopic insights into the behavior of fluids, particularly new solvents. In DESs, hydrogen bonds and their interactions have a strong impact on phase behavior and transport properties [54]. Besides, EoS have been essential thermodynamic tools for more than a century, since the model proposed by van der Waals acquired a usable form [115–117]. Despite this, in DESs, more sophisticated models are required due to their short range-strong interactions. SAFT family EoS [70, 72, 84, 87, 88], which come from the Barker and Henderson perturbation theory [102, 103] and Wertheim's theory of association [74–77], solve the above problem, including a direct contribution of these interactions. Additionally, integrating computational techniques with theoretical modeling tools addresses another critical challenge in DES modeling: the limited reliability of experimental data, especially for mixtures involving water and organic solvents.

Alkhatib et al. [260] provided guidelines for DES modeling, outlined the current challenges, and suggested pathways for future developments. Perkins et al. [187] employed simulation techniques

---

[*] This chapter is adapted with permission from:
E. Cea-Klapp, J. M. Garrido, and H. Quinteros-Lama, "Insights into the orientation and hydrogen bond influence on thermophysical and transport properties in choline-based deep eutectic solvents and methanol", Journal of Molecular Liquids **345**, 117019 (2022). Copyright 2022 Elsevier B.V.

to compute thermophysical and transport properties of choline chloride (ChCl)-based DESs (1,2-ethanediol, glycerol, and malic acid), obtaining good agreement with experimental data for thermophysical properties, though predictions of transport properties proved more challenging. Salehi et al. [56] computed the Hildebrand and Hansen solubility parameters using the OPLS force field by molecular dynamics (MD). Wang et al. [54] experimentally analyzed and applied quantum chemistry techniques to the hydrogen-bonding behavior of ChCl with polyols, showing that the stronger interaction in these mixtures is the association between the chlorine (Ch) cation and the hydroxy group. González de Castilla et al. [155] explore the possibilities of DES modeling using excess models, EoS, and MD, emphasizing equilibrium predictions. Shehata et al. [57] analyze the hydration effect in ChCl plus urea DES by MD and its influence on the DES performance as reaction media.

In the same line, Abranches et al. [39] applied COSMO-RS to design DESs for pharmaceutical applications. Atilhan et al. [261] used MD simulations to analyze interactions at the interfaces between DESs and nanomaterials, demonstrating the critical influence of hydrogen bonds on mixture behavior. Naik et al. [59] explored phase equilibria of phosphonium- and ammonium-based DESs, providing analyses of coordination numbers (CN) and radial distribution functions (RDFs). Ashworth et al. [60] employed ab initio quantum chemistry methods to characterize complex association behaviors in ChCl and urea systems, identifying diverse hydrogen-bond interactions distinct from the homogeneous short-range interactions typical of traditional solvents. Baz et al. [262] examined aqueous mixtures of ChCl:glycerol (1:2) using MD simulations and modeling, confirming structured hydrogen-bond networks characterized by substantial ordering interactions. They observed that water, when introduced into DESs, integrates into this network, significantly reducing viscosity while preserving solvent characteristics. Furthermore, the formation and stability of DESs were linked to both the quantity and spatial arrangement of hydrogen-bond donor and acceptor groups. Triolo et al. [263] recently conducted MD studies on natural DESs composed of ChCl and water, revealing the structural importance of choline cations in organizing the aqueous environment and highlighting the significant role of hydrogen bonding among water molecules and between water and anions.

This chapter aims to link the thermophysical properties from experimental data, molecular simulations, and theoretical modeling using SAFT EoS, emphasizing the hydrogen-bonding interactions of ChCl:1,2-ethanediol(1:2) and ChCl:glycerol(1:2) plus methanol. The above work is performed by all-atoms MD simulations of thermodynamic and structural properties and contrasting the results with predictive modeling using the PC-SAFT EoS [87, 88] together with the free volume theory (FVT) for viscosity. The subsequent sections include detailed simulation and modeling methodologies, results and discussions, and concluding remarks.

6.2. Molecular modeling

6.2.1. PC-SAFT modeling

The PC-SAFT EoS is applied using the individual component approach outlined in Chapter **??**. In this chapter, ChCl and methanol (MOH) are modeled with the 2B association scheme [61, 88]. In contrast, to examine the association capabilities of hydrogen bond donors, 1,2-ethanediol (EG) and glycerol (G) are represented by both 2B and 4C association schemes [61, 231, 264]. A summary of the pure-component parameters used is provided in Table 6.1.

TABLE 6.1: PC-SAFT molecular parameters used in this chapter. The [B, P, N] notation indicates the number of bivalent, positive, and negative association sites, respectively, as defined in Figure 2.2.

Compounds	M_w **[g/mol]**	m_i	σ_i **[Å]**	ε_i/k_B **[K]**	S^{Ai} **[B, P, N]**	ε^{AiBi}/k_B **[K]**	κ^{AiBi}	**Sources**
choline chloride (ChCl)	139.62	13.0200	2.3680	228.07	[0, 1, 1]	8000.0	0.2000	[61]
1,2-ethanediol (EG-2B)	62.07	2.4366	3.2328	344.06	[0, 1, 1]	2702.6	0.0222	[190]
1,2-ethanediol (EG-4C)		1.9090	3.5910	325.23	[0, 2, 2]	2080.0	0.0235	[264]
glycerol (G-2B)	92.05	2.0070	3.8150	430.82	[0, 1, 1]	4633.5	0.0019	[97]
glycerol (G-4C)		5.1560	2.7380	247.65	[0, 2, 2]	1765.5	0.3018	[231]
methanol (MOH)	32.04	1.5255	3.2300	188.90	[0, 1, 1]	2899.5	0.0352	[88]

An additional framework is required for viscosity modeling. As outlined in Section 2.6.2, the FVT is applied for this purpose. The FVT utilizes molecular parameters and density models, which are provided by a molecular EoS such as PC-SAFT. The FVT parameters are shown in Table 6.2.

TABLE 6.2: FVT parameters used in this Chapter.

Compounds	α **[J m^3/(mol kg)]**	$B \times 10^3$	L_v **[Å]**	**Sources**
ChCl	190.54	6.520	0.0878	[186]
EG-2B	379.34	2.434	0.0330	[186]
EG-4C	379.34	2.934	0.0017	This work
G-2B	267.90	7.701	0.0025	[186]
G-4C	267.90	7.595	0.0030	This work
MOH	312.00	1.574	0.0886	This work

6.2.2. Molecular dynamics details

MD simulations were performed using the GROMACS 5.1.4 program package [265] to simulate the homogeneous systems. Force field parameters for choline chloride, 1,2-ethanediol, and glycerol were described using the all-atom optimized potential for liquid simulations (OPLS-AA) developed by Doherty and Acevedo [266], while OPLS-AA potential from Jorgensen et al. [135] was used for methanol. Cubic boxes were constructed using the Packmol package [267], containing choline chloride pairs with the ratio of 1,2-ethanediol, glycerol and the proper mole fraction of methanol (x_{MOH}). Table 6.3 lists the number of HBD, HBA, and methanol molecules included in each simulation box for the 1,2-ethanediol- and glycerol-based DES systems.

TABLE 6.3: Number of molecules for each DES + methanol system at different methanol mole fraction (x_{MOH}). Choline and chloride are abbreviated as Ch and Cl, respectively.

x_{MOH}	N_{Ch}	N_{Cl}	N_{HBD}	N_{MOH}
0	500	500	1000	0
0.1	450	450	900	150
0.2	400	400	800	300
0.3	350	350	700	450
0.4	300	300	600	600
0.5	250	250	500	750
0.6	200	200	400	900
0.7	150	150	300	1050
0.8	100	100	200	1200
0.9	50	50	100	1350
1	0	0	0	1500

Periodic boundary conditions were employed with the short-range electrostatic cutoff set to 1.6 nm. Long-range electrostatics were treated with Particle-Mesh Ewald (PME) summations [268, 269] with a PME-order of four. Minimization of each box was performed using a steepest-descent algorithm for at least 5000 steps. Temperature ranges were held constant using a velocity rescaling with a stochastic term [148], and the pressure was maintained at 1.0 bar using the Berendsen coupling method [270] during an isothermal-isobaric ensemble for 10 ns of equilibration. Equations of motion were integrated with the leapfrog algorithm [142] using a time step of 1 fs. The LINCS method [145, 271] constrained all covalently bound hydrogen atoms with an order of four. The number of iterations to correct for rotational lengthening in LINCS was set to two. Production runs were carried out for an additional 50 ns by using the Parrinello-Rahman barostat [151, 152] by isotropic coupling with a coupling constant of $\tau_P = 2$ ps. The trajectory of the last 25 ns was used for the calculation of thermodynamic and structural properties using the GROMACS analysis tools.

Additional independent simulations were performed for another 10 ns to compute the viscosity at selected concentrations of methanol. The approach, based on the perturbation method proposed by Hess [153] and described in Section 3.3.1, was applied in this chapter.

6.3. Results

6.3.1. Thermophysical and transport properties

Density, excess volume, and viscosity were determined by computational methods and theoretical prediction at 308.15 K and atmospheric pressure, and the results are summarized in Table 6.4. Following the idea of Zubeir et al. [61], to obtain a more accurate result, a linear temperature-dependent binary interaction parameter, k_{ij}, between ChCl and HBDs was fitted using density data. It is important to mention that they were not adjusted to experimental data obtained for the DES + methanol mixtures. Thus, PC-SAFT does not require any calibration for methanol mixtures and was applied in a fully predictive manner. The interaction parameters optimized to the density data [186] for each associative scheme are listed in Table 6.5.

TABLE 6.4: Density, excess volume, and viscosity of the DESs + methanol mixtures at 308.15 K and atmospheric pressure from MD calculations.

	ChCl:EG(1:2) + methanol			**ChCl:G(1:2) + methanol**		
$\mathbf{x}_{MOH}$	ρ **[g/cm^3]**	η **[mPa s]**	v^E **[cm^3/mol]**	ρ **[g/cm^3]**	η **[mPa s]**	v^E **[cm^3/mol]**
0	1.1238 ± 1e-3	35.3 ± 5.4	0	1.1919 ± 2e-3	235.8 ± 10.1	0
0.1	1.1085 ± 1e-3	26.5 ± 3.2	-0.29 ± 0.02	1.1803 ± 1e-3	134.4 ± 10.4	-0.62 ± 0.19
0.2	1.0917 ± 1e-3	20.2 ± 3.9	-0.59 ± 0.08	1.1626 ± 2e-3	85.3 ± 10.8	-0.93 ± 0.13
0.3	1.0725 ± 1e-3	17.0 ± 3.1	-0.86 ± 0.01	1.1419 ± 2e-3	59.1 ± 10.3	-1.22 ± 0.11
0.4	1.0498 ± 2e-3	12.6 ± 4.6	-1.08 ± 0.21	1.1174 ± 2e-3	48.5 ± 6.9	-1.45 ± 0.01
0.5	1.0231 ± 2e-3	12.0 ± 2.9	-1.23 ± 0.12	1.0882 ± 2e-3	24.7 ± 5.5	-1.64 ± 0.07
0.6	0.9916 ± 2e-3	5.0 ± 2.1	-1.32 ± 0.37	1.0523 ± 2e-3	14.6 ± 3.7	-1.74 ± 0.19
0.7	0.9533 ± 1e-3	3.8 ± 1.3	-1.29 ± 0.02	1.0076 ± 2e-3	9.3 ± 3.9	-1.72 ± 0.04
0.8	0.9068 ± 2e-3	1.9 ± 0.7	-1.13 ± 0.23	0.9509 ± 2e-3	4.2 ± 1.2	-1.54 ± 0.06
0.9	0.8489 ± 2e-3	0.6 ± 0.2	-0.75 ± 0.39	0.8771 ± 2e-3	1.2 ± 0.4	-1.09 ± 0.10
1	0.7748 ± 1e-3	0.5 ± 0.2	0	0.7748 ± 1e-3	0.5 ± 0.2	0

TABLE 6.5: Binary interaction parameters, $k_{ij} = k_{ij,a} + k_{ij,T}\,(T\,[\mathrm{K}] - 298.15)$, for each DES, along with the AARD for DES density at a molar ratio of 1:2, with and without binary interaction.

Pair	k_{ij}		**N**	**AARD**	**AARD**	**Sources**
	$k_{ij,a}$	$k_{ij,T}$		$\rho_{k_{ij}=0}$	$\rho_{k_{ij}\ \mathrm{fit}}$	
ChCl + EG-2B	0.1029	-0.0016	48	1.15%	0.05%	[15, 156, 159, 238–240]
ChCl + EG-4C	-0.0109	-0.0013		0.64%	0.05%	
ChCl + G-2B	0.2064	-0.0015	23	2.97%	0.05%	[159, 238, 241]
ChCl + G-4C	0.0670	-0.0016		0.67%	0.05%	

Figure 6.1 shows the density and excess volume of both mixtures at 308.15 K and atmospheric pressure, comparing experimental data from the literature [272] with results from MD simulations and PC-SAFT calculations. For density, the average absolute relative deviations (AARD) with MD are 0.641% and 0.532% for the ChCl:EG(1:2) plus methanol and the ChCl:G(1:2) plus methanol mixtures, respectively. In contrast, the predictive PC-SAFT model, with both associative models for the HBDs, yields more minor deviation. It is interesting to note that 2B and 4C models for the HBDs are in close agreement.

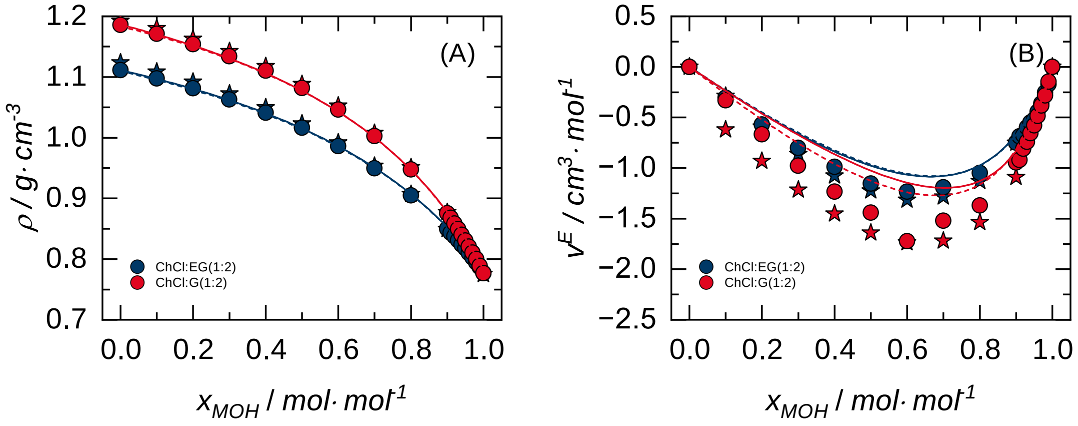

FIGURE 6.1: For DES plus methanol at 308.15 K and atmospheric pressure: (A) density and (B) excess volume. Circles represent experimental data [272], while stars indicate MD calculations. Solid lines show PC-SAFT predictions with the 2B association scheme for the HBD component, and dashed lines represent PC-SAFT predictions using the 4C association scheme for the HBD component.

Figure 6.1B shows that the HBDs form non-ideal mixtures with methanol, exhibiting negative excess volumes across the entire concentration range. MD simulations and PC-SAFT calculations are in fair agreement with the experimental data reported by Wang et al. [272]. The observed negative excess volume indicates stronger interactions between DESs and methanol, primarily due to the formation of new hydrogen bonds in the mixture. From a microscopic perspective, the self-association between individual species (DES or methanol) is weaker than the hetero-association between DES and methanol molecules, which explains the contraction in volume. This behavior is consistent with previous volumetric studies on ChCl:EG [15, 165] and ChCl:G [169], where negative excess volumes were also reported. Experimental evidence suggests that this trend is similar across various alcohols [15, 164]; however, the magnitude of volumetric contraction decreases as the alkyl chain length of the alcohol increases. This can be attributed to the growing steric hindrance and reduced polarity with increasing chain length, which limit the ability of longer-chain alcohols to engage in strong, directional hydrogen bonding with the DES components—thus diminishing the extent of volume contraction upon mixing.

The viscosity values at 308.15 K for the ChCl:EG(1:2) plus methanol and the ChCl:G(1:2) plus methanol mixtures are shown in Figure 6.2. Despite the MD values having more discrepancy with the experimental data, their uncertainty is higher, and the approach also implies more dispersion. The accuracy of the method is compromised in the middle range of concentrations, despite the procedure having a good performance in the pure compound limit [266]. However, it is well-known that macroscopic viscosity is strongly linked with the behavior of hydrogen bonds in the mixture due to the viscosity being an indicator of the resistance of the fluid to flow [273, 274]. Therefore, the viscosity directly correlates with the strength of the hydrogen bonds [54]. The viscosities of DESs plus alcohols are reported in the literature at different molar ratios [274, 275]. The aforementioned effect can be explained by changing the association strength between DESs and methanol in the mixture. MD calculations yield AARD of 34.52% and 30.72% for ChCl:EG(1:2) and ChCl:G(1:2), respectively.

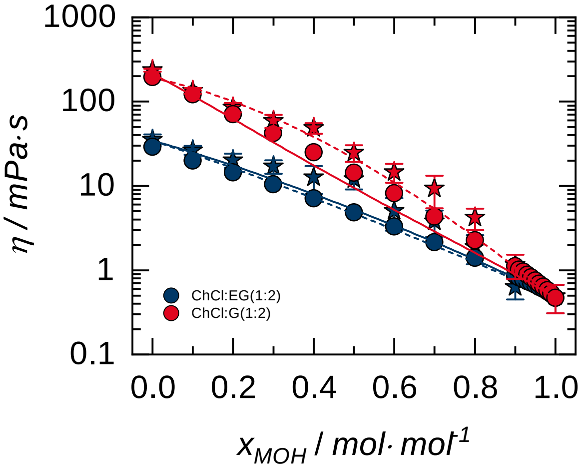

FIGURE 6.2: Viscosity of DES plus methanol at 308.15 K and atmospheric pressure. Circles represent experimental data [272], while stars indicate MD calculations. Solid lines show PC-SAFT predictions with the 2B association scheme for the HBD component, and dashed lines represent PC-SAFT predictions using the 4C association scheme for the HBD component.

Further, both association schemes give similar AARD for both DESs, with values of 9.31% and 16.99% for ChCl:EG(1:2) and ChCl:G(1:2) plus methanol, respectively. Consequently, in the middle range of the mixture, the self-association of methanol gets weaker, and the cross-association between DESs and methanol is promoted. The effect described above is challenging to predict accurately and quantitatively. In the present case, the behavior is found qualitatively and overestimated. The accurate prediction of viscosity and other properties is a solid reason to accurately model and understand in detail the influence of molecular behavior and the hydrogen-bonding networks. The FVT, together with PC-SAFT EoS, which has proven to be a solid framework to predict viscosity [192], is applied to predict the viscosity of the mixture. In both combinations of association schemes, the results can be considered satisfactory. However, the quality of the prediction of the FVT varies in the middle range of concentrations, given the convoluted behavior of the molecules in the mixture. Alternatives to FVT coupled with different EoS are the friction theory [276] and the entropy scaling [277, 278]. For the sake of ensuring the predictability of the viscosity using the FVT, there are no additional parameters fitted. Parameters for ChCl were sourced from Crespo et al. [186], while those for methanol and the HBDs were fitted using DIPPR data. Although FVT can account for water content, the comparison with experimental data in this work was conducted under the assumption of negligible water content in the system. This assumption simplifies the analysis but overlooks the critical role of water, which significantly impacts the transport properties of DESs due to their hygroscopic nature [15, 279].

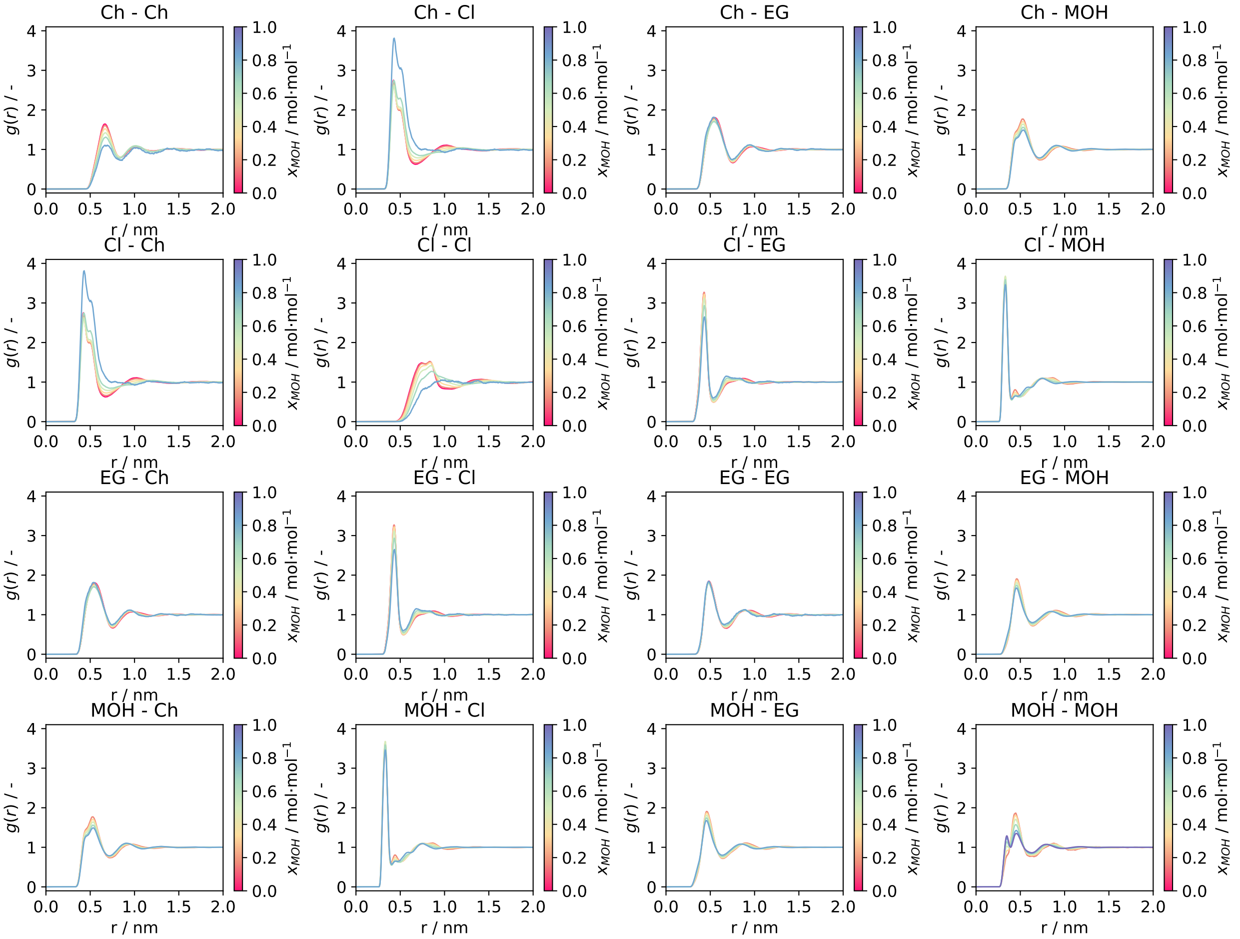

FIGURE 6.3: Center-of-mass RDFs for ChCl:EG(1:2) plus methanol at different methanol mole fraction.

6.3.2. Structural behavior

Radial distribution functions

Figure 6.3 shows the center-of-mass RDFs for ChCl:EG(1:2) plus methanol at different methanol mole fractions. The largest peaks are associated with interactions involving the chloride anion, excluding its self-interaction. This prominence can be attributed to the Cl anion's negative charge and high electronegativity, enabling it to act as an HBA for hydroxyl groups in the mixture. Additionally, the Cl anions are smaller than the other components, facilitating its accumulation in the first solvation shell of hydroxyl groups, resulting in higher peak intensities for Cl-related interactions than other hydrogen-bonding interactions.

Beyond Cl-related interactions, Figure 6.3 also displays a clear first peak for interactions involving hydroxyl-containing compounds, albeit with smaller heights (approximately 2). The positions of these peaks are influenced by steric effects. For instance, the MOH-MOH interaction, involving smaller and less sterically hindered molecules, exhibits a peak closer to the center of mass (around 0.5 nm). Conversely, the Ch-Ch interaction is significantly impacted by steric hindrance due to the larger, bulkier structure of Ch, leading to a peak shift to greater distances (beyond 0.6 nm), reflecting spatial constraints in accommodating these molecules.

Interestingly, the addition of methanol does not significantly affect the RDFs involving 1,2-ethanediol, as the peak positions and heights remain nearly unchanged. Rather than displacing 1,2-ethanediol in its interactions with Ch, methanol primarily interacts with Ch, weakening Ch-Ch interactions. This is evidenced by a decrease in the intensity of the first peak in the Ch-Ch RDF with increasing methanol concentration. Meanwhile, the consistent shape and intensity of the Ch-EG and Ch-methanol RDFs indicate that methanol integrates seamlessly into the hydrogen-bonding network, mimicking 1,2-ethanediol's behavior. This suggests that methanol serves as a competitive HBD within the DES + methanol mixture.

A similar conclusion can be drawn for ChCl:G(1:2) plus methanol mixtures, as can be seen in Figure A.1 in the Appendix A. In these mixtures, the addition of methanol also affects the interactions between DES components. However, a notable difference is observed in the self-interaction of glycerol molecules. As methanol concentration increases, the self-interaction of glycerol (G-G) becomes more pronounced, as indicated by a rise in the intensity of the first RDF peak. This increase is likely due to the redistribution of Cl ions, driven by the formation of MOH-Cl interactions. Methanol interacts strongly with Cl anions, reducing their availability to participate in glycerol-related hydrogen bonding. Consequently, glycerol molecules tend to self-associate more strongly in the presence of methanol, compensating for the weakened interactions with Cl.

Thus, methanol acts both as an additional HBD and as a modulator of the hydrogen-bonding dynamics within the DES mixture. It selectively weakens specific interactions, such as Ch-Ch and Cl-G, while maintaining or emulating others, such as Ch-HBD. In the case of ChCl:G(1:2), methanol also indirectly enhances the glycerol self-interaction by reducing the Cl-mediated cross-interaction. This dual role highlights methanol's competitive and complementary effects in reshaping the DES structure, with subtle differences depending on the specific HBD used in the system. Also, it shows why the modeling and prediction of this type of system continue to be a challenge due to the complexity of the association behavior of these mixtures.

Hydrogen bonds behavior

The number of hydrogen bonds is calculated under the simulated conditions using a geometrical criterion to complete the structural description of the systems [280, 281]. This approach considers the maximum distance and angle between donor-acceptor and hydrogen-donor-acceptor groups. Figures 6.4 and A.2 present the combined distribution functions correlating these radial and angular distributions for ChCl:EG(1:2) plus methanol and ChCl:G(1:2) plus methanol, respectively. These plots elucidate the average orientation at different methanol concentrations for hydrogen bond formation. Across all cases, a high occurrence of interactions is observed at distances below 0.35 nm and angles below 40°, indicating the presence of a well-structured hydrogen-bonding network. This network involves HBA-HBD interactions (e.g., Ch or Cl as HBA), HBA-HBA interactions (between Ch and Cl), and HBD-HBD interactions.

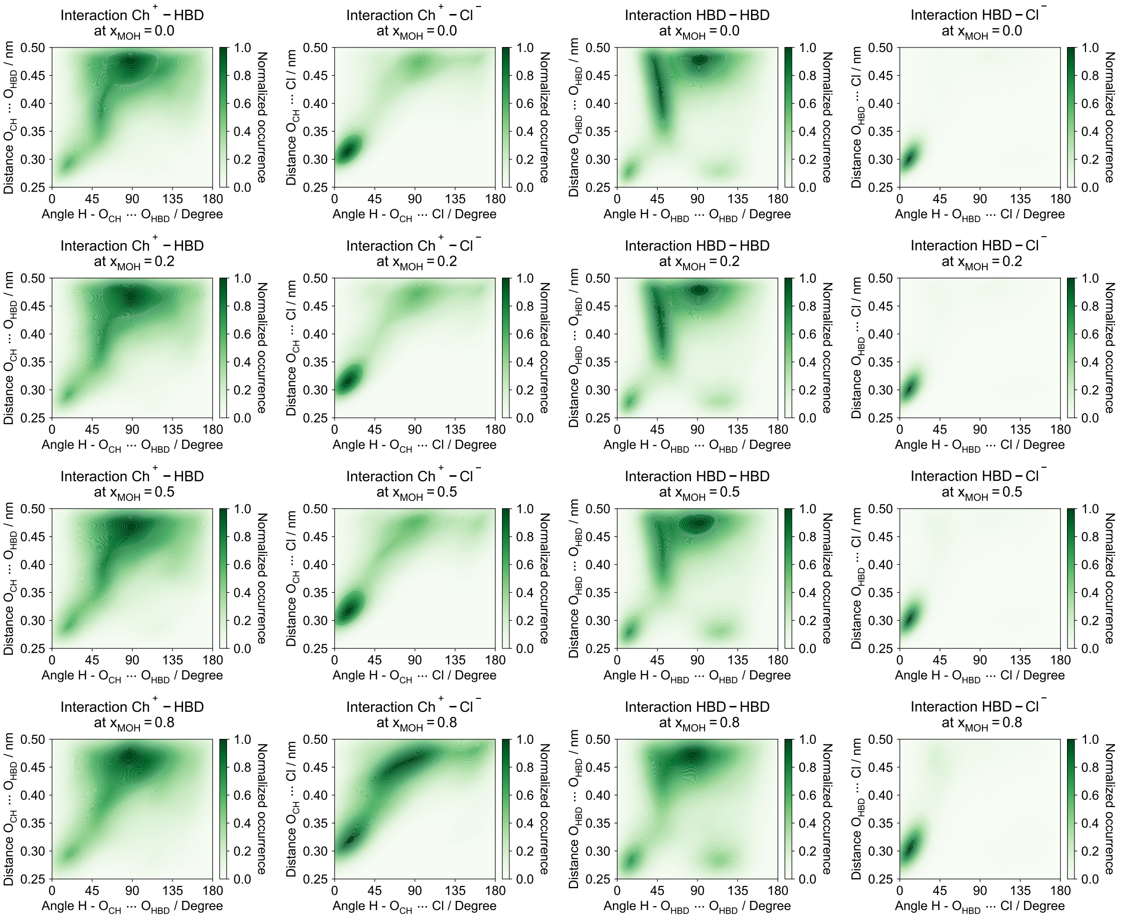

FIGURE 6.4: Combined distribution functions for ChCl:EG(1:2) plus methanol at different methanol mole fraction. The plot illustrates the relationship between the angle and distance for interactions involving the choline oxygen atom (O_{OH}), the chloride anion (Cl), and the HBD oxygen atom (O_{HBD}).

It is particularly interesting that interactions involving chloride ions are highly oriented around the hydroxyl groups. This confirms that the small size of the chloride ion enables it to achieve a higher degree of ordering within the hydroxyl groups. The addition of methanol to the system only slightly affects Ch–Cl interactions, as the distribution becomes more diffuse with respect to distance while maintaining a high intensity. This behavior reflects the affinity of methanol for Ch, leading to a subtle reorganization of chloride ions around choline and a compact structural arrangement.

For interactions involving the HBD, the addition of methanol does not appear to disrupt the hydrogen-bonding network significantly. The combined distribution functions for these interactions remain largely unchanged, suggesting that methanol integrates into the network without breaking significantly the hydrogen bonds between the hydroxyl groups of 1,2-ethanediol or glycerol. These interactions are more diffuse compared to others, a result of the multiple hydroxyl groups present in both HBDs. For instance, in the case of 1,2-ethanediol, when one hydroxyl group forms a hydrogen bond, the second hydroxyl group remains in close proximity due to intramolecular interactions, though its orientation appears more diffuse.

From the selection of the geometrical criterium, some specific structural properties can be calculated. One of them is the fraction of molecules involved in self-association, defined as the ratio between the number of molecules involved in a hydrogen bond (at least once) with itself and the total number of the same molecules. It is worth noticing that this structural property can be compared independently from the calculation from Wertheim's thermodynamic perturbation theory [282] into PC-SAFT EoS. The latter turns out to be a useful additional feature of the new theory in developing more realistic models of the hydrogen-bonding interaction in DES.

As can be seen in Figure 6.5, ChCl decreases monotonically, while methanol interaction increases. In both cases, the 2B associative model qualitatively reproduces the behavior. An interesting case occurs for both HBDs. While the 2B associative model shows that almost linearly 1,2-ethanediol and glycerol decrease their interaction, MD results show that the addition of methanol in the system is not affected by nearly 30% of methanol concentration. When the methanol content is higher than 30%, the methanol begins to create a network of hydrogen bonds with the components of the mixture. Therefore, the networks among Ch, Cl, 1,2-ethanediol, and glycerol are disrupted. It is important to remark that this effect is most evident in 1,2-ethanediol, and also, the 4C associative model represents this behavior qualitatively.

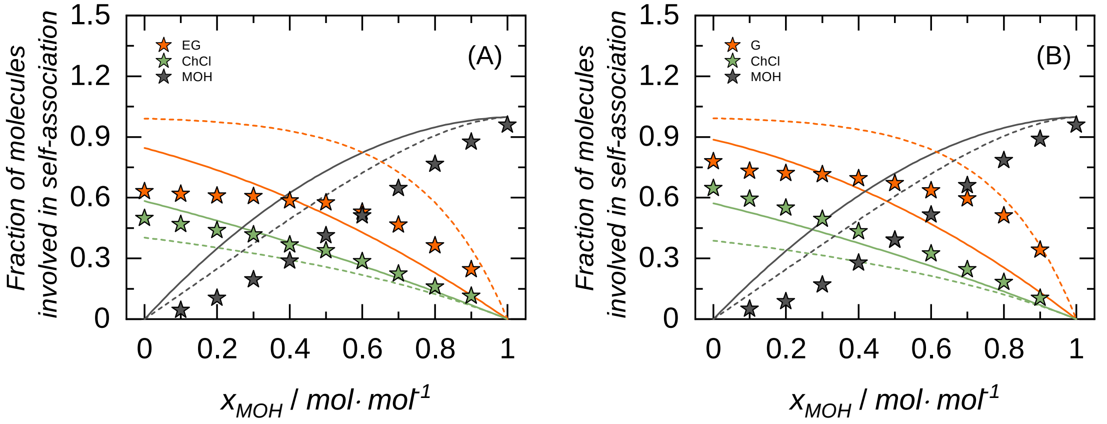

FIGURE 6.5: Fraction of molecules involved in self-association at 308.15 K and atmospheric pressure for: (A) ChCl:EG(1:2) plus methanol and (B) ChCl:G(1:2) plus methanol. Stars represent MD results, while solid lines indicate PC-SAFT predictions using the 2B association scheme and dashed lines show PC-SAFT predictions with the 4C association scheme for HBDs.

Additional insights can be gained by comparing the number of hydrogen bonds obtained through MD simulations and the PC-SAFT model. As shown in Figure 6.6, the contribution of hydrogen bonds reaches a maximum at approximately 60% mole fraction of methanol. Beyond this point, methanol-methanol hydrogen bonds begin to dominate over HBD-HBD and HBD-methanol bonds. Among the cross interactions, the methanol-HBA interactions are the most significant, confirming the trends observed in the previous sections. These methanol-HBA interactions are likely the primary cause of the negative excess volume behavior observed. Overall, these findings align qualitatively with results obtained in aqueous solutions using vibrational spectroscopy [283], which provide insights into similar types of interactions.

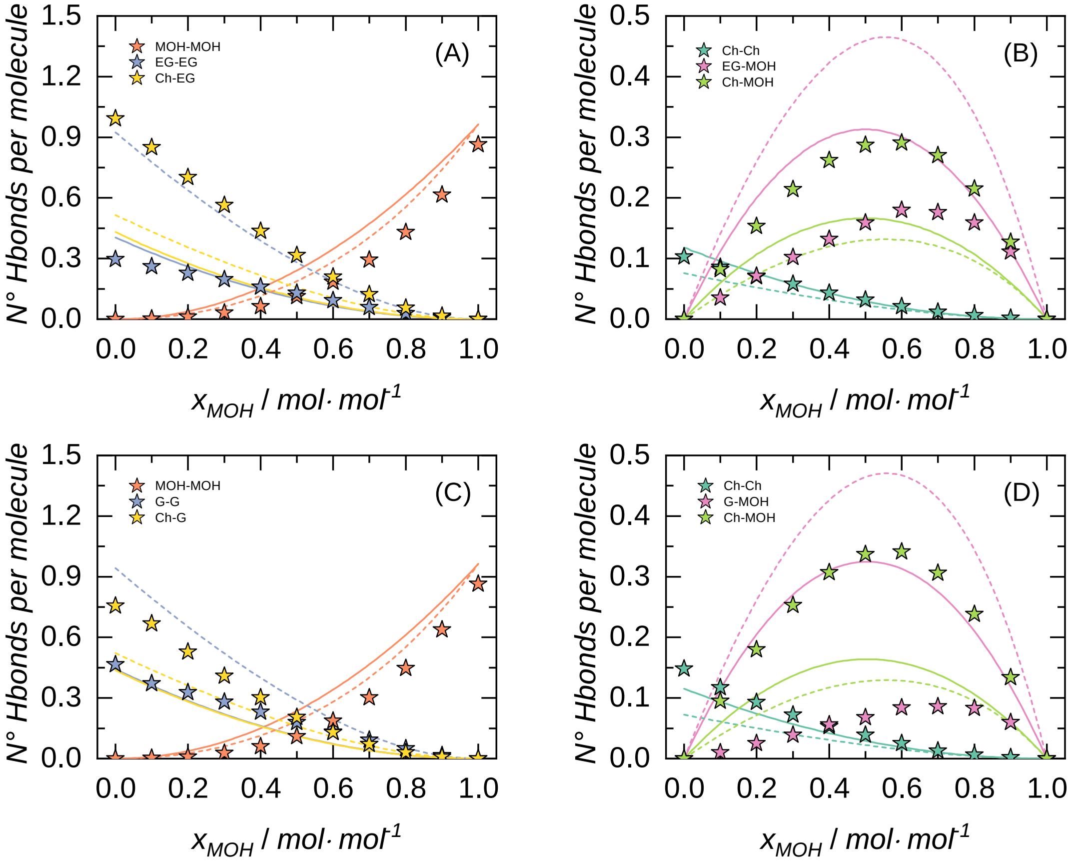

FIGURE 6.6: Normalized number of hydrogen bonds at 308.15 K and atmospheric pressure for: (A, B) ChCl:EG(1:2) + methanol and (C, D) ChCl:G(1:2) + methanol. Stars represent MD results, while solid lines indicate PC-SAFT predictions using the 2B association scheme and dashed lines show PC-SAFT predictions with the 4C association scheme for HBDs.

6.4. Conclusions

This chapter has been devoted to the study of the thermophysical, transport, and microstructural properties of the ChCl:EG(1:2) plus methanol and ChCl:G(1:2) plus methanol mixtures. For both systems, properties, such as density, excess volume, and viscosity, were determined using MD simulations and predicted using the PC-SAFT EoS with two different association schemes. On the one hand, good agreement is observed between MD, PC-SAFT predictions, and experimental data for those properties, demonstrating the robustness of the PC-SAFT EoS in capturing key trends. On the other hand, some discrepancies between MD calculations and experimental data remain, attributed to the complexity of the associative behavior in these mixtures and the strong interactions between methanol and the DES components.

Regarding structural behavior, the RDFs and hydrogen bond features were analyzed in detail. The results highlight consistent characteristics of short-range intermolecular forces across the studied systems. Both ChCl:EG(1:2) and ChCl:G(1:2) form solvation shells with methanol that differ from those observed in the pure DES. The incorporation of methanol into the mixtures does not substantially alter the orientation of the original DES precursors but has a pronounced impact on the prominence of HBA interactions. Methanol acts as an additional HBD within the system, leading to changes in the hydrogen-bonding network and modulating the interactions within the mixture.

7. Investigating the physicochemical properties of DESs made by choline chloride or betaine, and low molecular weight glycols

This chapter presents a comprehensive study of the thermophysical properties of selected DESs and their mixtures with water. Density, viscosity, and surface tension were experimentally measured for DESs comprising choline chloride or betaine as the HBA and various HBDs, including 1,2-ethanediol, 1,2-propanediol, 1,3-propanediol, and 1,4-butanediol, across different HBA:HBD molar ratios, temperatures, and water contents. Experimental data were complemented by including the PC-SAFT EoS, coupled with the Free-Volume Theory and Density Gradient Theory, as well as MD simulations. By integrating experimental measurements with thermodynamic modeling and MD simulations, this chapter reveals the impact of HBA type, HBD chain length, temperature, and water content on the properties of glycol-based DESs, offering valuable insights to facilitate their design and application. [*]

7.1. Introduction

DESs exhibit remarkable versatility in their physical properties, which can be tailored by adjusting the combinations of HBAs and HBDs, varying molar ratios, controlling water content, and optimizing operating temperatures [8, 14, 284]. Despite this adaptability, there is a notable lack of reliable physicochemical properties data, particularly for DES mixtures with water or other solvents. Such data are critical for determining the parameters required for designing efficient chemical and biological processes [258]. For instance, the high viscosity of some DESs can hinder their practical use but may be mitigated by small water additions or by increasing process temperatures

---

[*] This chapter is adapted with permission from:
P. Aravena, E. Cea-Klapp, N. F. Gajardo-Parra, C. Held, J. M. Garrido, and R. I. Canales, "Effect of water and hydrogen bond acceptor on the density and viscosity of glycol-based eutectic solvents", Journal of Molecular Liquids **389**, 122856 (2023). Copyright 2023 Elsevier B.V.
P. Aravena, E. Cea-Klapp, N. F. Gajardo-Parra, A. F. Olea, H. Carrasco, J. M. Garrido, and R. I. Canales, "Influence of hydrogen bond acceptors and water content on surface tension in glycol-based eutectic mixtures", Industrial & Engineering Chemistry Research **63**, 11184–11195 (2024). Copyright 2024 American Chemical Society.

[14, 15, 285]. This highlights the urgent need for comprehensive studies of their physicochemical properties.

Although experimental measurements are essential for studying DESs, they must be complemented with modeling techniques to optimize solvents for specific applications. This is particularly important given the practically infinite combinations of HBAs and HBDs. For example, machine learning, coupled with group contribution methods [286], has shown superior performance in predicting density compared to conventional atomic and group contribution approaches [216]. However, its limitations include challenges in providing physical insights into cosolvents under varying thermodynamic conditions.

Among the commonly used thermodynamic modeling tools, the PC-SAFT EoS is particularly well-suited for describing the thermodynamic properties of DESs. It captures both macroscopic and molecular-level features and has been applied to study phase behavior, predict phase diagrams, and investigate properties such as density and heat capacity [235, 258]. Nevertheless, the ability of PC-SAFT to model molecular-level and structural features is restricted. To address this, computational chemistry techniques such as MD simulations provide deeper insights into the structural and dynamic properties of DESs. MD simulations offer a detailed view of atomic and molecular-scale behavior, including solvation and dynamic properties, which are challenging to obtain experimentally [287–292]. These methods have been widely applied to DESs containing diverse HBAs (e.g., choline chloride, betaine) and HBDs (e.g., urea, glycerol, ethylene glycol) to determine properties such as phase equilibrium, density, viscosity, and diffusion coefficients [289, 292]. Integrating these computational approaches with experimental data enables a comprehensive understanding of DESs, facilitating their optimization for various applications.

This chapter presents a comprehensive study of the density, viscosity, and surface tension of ChCl-based and betaine-based DESs. The selection of these HBAs, which share similar molecular structures (see Figure 7.1), enables the evaluation of the effect of distinct functional groups in the HBA structure. These HBAs were combined with various glycols with low molecular weight, for the investigation of the impact of alkyl chain length in the HBD. In addition, the DESs were studied at different HBA:HBD molar ratios, temperatures, and water contents. The PC-SAFT equation of state was employed to model density, while the FVT and DGT were coupled with PC-SAFT to describe viscosity and surface tension, respectively. To gain deeper molecular-level insight, MD simulations were conducted to predict these properties and analyze structural organization. This work seeks to bridge experimental data, thermodynamic modeling, and molecular simulations to enhance the understanding of these complex solvents and support their rational design.

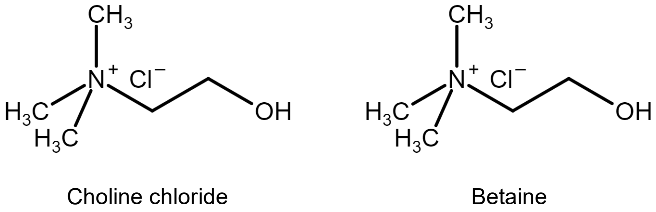

FIGURE 7.1: Molecular structure of choline chloride and betaine.

7.2. Experimental section

7.2.1. Materials

The specifications of chemicals used in this work are shown in Table 7.1, which contains their CAS number, source, and purity.

TABLE 7.1: Specifications of chemicals used in this work.

Compounds	CAS	Supplier	Purity
choline chloride (ChCl)	67-48-1	Acros Organics	>0.990
betaine (Bet)	107-43-7	Acros Organics	>0.980
1,2-ethanediol (EG)	107-21-1	Acros Organics	>0.998
1,2-propanediol (12P)	54-55-6	Sigma Aldrich	>0.980
1,3-propanediol (13P)	504-63-2	Sigma Aldrich	>0.980
1,4-butanediol (14B)	110-63-4	Sigma Aldrich	>0.990
water	7732-18-5	Merck	LC-MS Grade

7.2.2. DESs and DES + water mixtures preparation

ChCl and Bet were used as HBAs, while 1,2-ethanediol (EG), 1,2-propanediol (12P), 1,3-propanediol (13P), and 1,4-butanediol (14B) were used as HBDs. DESs with ChCl as the HBA and different glycols as HBDs were prepared with molar ratios of 1:3, 1:4, 1:5, and 1:6. However, for Bet-based DESs, only a subset of these ratios was prepared, as lower amounts of HBD resulted in non-homogeneous mixtures. For instance, the DES composed of Bet and 14B formed a homogeneous liquid only at a molar ratio of 1:6 at 20 °C.

Before the preparation of the DESs, HBAs were dried under a high vacuum in a Schlenck line for three days at 10^{-4} mbar and 50 °C to reduce their water content. For the same purpose, non-anhydrous HBDs were placed under molecular sieves for three days. Then, DESs were prepared by weighing the respective components in a vial using an analytical balance (Practum 224-1s Sartorius, Germany, uncertainty ± 0.1 mg). The vials were promptly sealed to prevent the rising in the water concentration of the DESs. The HBA and HBD precursors were mixed in two steps; first, the samples were placed under magnetic stirring at 50 °C for one hour; then, they were mixed in a sonicator (iSonic P4862-IT, Australia) at 40 °C for 15 minutes to ensure proper mixing and prevent bubble formation. After this procedure, DESs showed the aspect of a homogeneous clear liquid. The water content of each DES was measured in triplicate using a Karl Fisher (831KF Metrohm, Switzerland) Coulometer. Table B.1 shows the prepared DESs with the respective abbreviation, HBA:HBD molar ratio, molar mass, and their average water content after preparation.

DESs used for DES + water mixtures were prepared with an HBA:HBD mole ratio of 1:3 for ChCl-based DESs and 1:6 for Bet-based. To evaluate the effect of water, DESs were mixed with water at molar percentages of 5%, 10%, 30%, 50%, 70%, 90%, and 95%. To prepare DES + water mixtures, both components were mixed in a vial using a vortex, and then the mixture was sonicated (iSonic P4862-IT, Australia) at 40 °C for 10 minutes. The water content of the mixture was measured twice in a volumetric Karl Fischer Titrino Plus (870 Metrohm, Switzerland). Table B.2 shows DES + water mixtures prepared, including the HBA:HBD molar ratio, molar mass, and average molar water content.

7.2.3. Density and viscosity measurements

Density (ρ) and dynamic viscosity (η) were measured for each Bet-based DES. For comparison, ChCl-based DESs with HBA:HBD molar ratio 1:3 were measured, while information for other molar ratios was retrieved from Gajardo-Parra et al. [15]. Also, the same properties were measured for all the prepared DES + water mixtures. An Anton Paar DMA4500 Densimeter (Graz, Austria) and an Anton Paar Lovis 2000ME micro viscometer (Graz, Austria) were used in an integrated system to measure density and viscosity simultaneously at a pressure of 101.3 kPa and temperatures between 20 - 60 °C. The densimeter uses a vibrating U-tube technology with a repeatability of 0.00001 $g \cdot cm^{-3}$. The temperature inside the tube was measured using a Pt-100 thermometer with an uncertainty of 0.01 K. The viscometer used was a rolling-ball type; steel balls and calibrated glass capillaries with internal diameters of 1.59 mm and 1.80 mm were used for the analyses. Considering manufacturer information and according to the author's previous measurements, the repeatability and accuracy of the instrument are approximately 0.2% and 3%, respectively, depending on the capillary type employed. Also, to avoid contamination, the densimeter and viscometer were thoroughly cleaned with distilled water twice and methanol once, and subsequently, they were dried using air for a few minutes.

7.2.4. Surface tension measurements

Surface tension (γ) was measured using a Kruss K9 tensiometer through the Du Noüy ring method. The tensiometer was equipped with a heating jacket (water as service fluid), and the temperature of the sample was measured using a Pt-100 thermometer with an accuracy of 0.01°C. Values measured by the tensiometer were corrected using the expression proposed by Zuidema et al. [293] according to Eq. 7.1, which includes an equipment correction factor (F_{eq}), experimentally obtained employing water, EG, 12P, 13P, and 14B measurements at the temperature range of 25-60°C.

$$\gamma = F_{eq} \cdot \sigma^* \cdot \left(0.725 + \sqrt{\frac{0.00363\,\sigma^*}{(\pi R_{ring})^2 \Delta\rho} + 0.04534 - \frac{1.679r}{R}}\right) \tag{7.1}$$

In Eq. 7.1, σ^* is the uncorrected measured interfacial tension value (in $\mathrm{mN \cdot m^{-1}}$), R_{ring} is the mean ring radius (0.9545 cm), r is the radius of the wire cross-section (0.0185 cm), $\Delta\rho$ is the density difference between phases (in $\mathrm{g \cdot cm^{-3}}$) and F_{eq} is the experimentally determined equipment correction factor (fixed value of 1.031). Considering Eq. 7.1, it is worth to mention that in a Du Noüy ring tensiometer the surface tensions are not measured directly. Consequently, the uncertainties of γ are influenced by the temperature, pressure, density difference, the experimental reproducibility of γ itself, and its standard uncertainties. To quantify these effects in the expanded or combined relative uncertainty of γ, the following relationship has been used:

$$u_r^2(\gamma) = \left[\frac{1}{\gamma}\left(\frac{\partial \gamma}{\partial P}\right)_T \delta P\right]^2 + \left[\frac{1}{\gamma}\left(\frac{\partial \gamma}{\partial T}\right)_P \delta T\right]^2 + \left[\frac{\delta \Delta \rho}{\Delta \rho}\right]^2 + \left[\frac{\vartheta(\gamma)}{\gamma}\right]^2 \tag{7.2}$$

where δP, δT and $\delta\Delta\rho$ correspond to the standard uncertainties in pressure, temperature and density, respectively. $\vartheta(\gamma)$ is the standard deviation of γ, which has been directly estimated from experimental measurements along with the maximal values of partial derivatives of γ by T. The instrument standard uncertainty for the interfacial tension is $\pm$ 0.1 $\text{mN} \cdot \text{m}^{-1}$ and the average combined expanded uncertainty (0.95 level of confidence, $k = 2$) for $u_r(\gamma)$ is 0.2 $\text{mN} \cdot \text{m}^{-1}$.

Before each measurement, the platinum-iridium ring and glassware were thoroughly cleaned with distilled water and ethanol to avoid contamination. Later, the ring was flamed to remove any trace of solvent. Surface tension measurements were performed three times for each sample, and liquid temperature was measured before and after surface tension measurement, reporting the mean values.

7.3. Molecular Modeling

7.3.1. PC-SAFT Modeling

PC-SAFT EoS, detailed in Section 2.2, is utilized to describe the thermodynamic behavior of the investigated DESs. Each component within the DES and water are modeled individually, enabling a precise representation of molecular interactions. Table 7.2 shows all the PC-SAFT parameters used in this Chapter.

TABLE 7.2: PC-SAFT molecular parameters used in this chapter. The [B, P, N] notation indicates the number of bivalent, positive, and negative association sites, respectively, as defined in Figure 2.2.

Compounds	M_w **[g/mol]**	m_i	σ_i **[Å]**	ε_i/k_B **[K]**	S^{Ai} **[B, P, N]**	ε^{AiBi}/k_B **[K]**	κ^{AiBi}	**Sources**
choline chloride (ChCl)	139.62	13.0200	2.3680	228.07	[0, 1, 1]	8000.0	0.2000	[61]
betaine (Bet)	117.15	8.4660	2.5470	266.59	[0, 1, 1]	2541.6	0.0384	[97]
1,2-ethanediol (EG)	62.07	2.4366	3.2328	344.06	[0, 1, 1]	2702.6	0.0222	[190]
1,2-propanediol (12P)	76.09	4.2084	2.9015	247.46	[0, 1, 1]	2174.4	0.1199	[21]
1,3-propanediol (13P)	76.09	3.0120	3.2481	280.29	[0, 1, 1]	3575.6	0.0190	This work
1,4-butanediol (14B)	90.12	3.9030	3.1666	252.50	[0, 1, 1]	3755.0	0.0187	[21]
water	18.02	1.2046	$\sigma(T)^a$	353.95	[0, 1, 1]	2425.8	0.0451	[195]

[a] Temperature-dependent function is given by σ [Å] $= 2.7927 + 10.11 \exp(-0.01775T[\text{K}]) + 1.417 \exp(-0.01146T[\text{K}])$.

PC-SAFT was applied using a binary interaction parameter, k_{ij}, fitted to the experimental density measured in this work for each HBA-HBD pair. Accurately reproducing density is fundamental for reliable modeling of viscosity and surface tension, especially when coupling with other theories. Table 7.3 lists the binary interaction parameters for each pair of DES components, including those involving water. On the one hand, the k_{ij} parameters for HBA-water systems were retrieved from the literature [61, 97]. On the other hand, the k_{ij} parameters for HBD-water interactions of EG and 13P were set to zero, while the parameters for 12P and 14B were fitted to vapor-liquid equilibrium data from the literature [294–297]. This adjustment was necessary to prevent the prediction of unrealistic liquid-liquid equilibrium in mixtures of HBD and water involving these glycols.

TABLE 7.3: PC-SAFT binary interaction parameters, $k_{ij} = k_{ij,a} + k_{ij,T}\,(T\,[\mathrm{K}] - 298.15)$, used in this work.

Pair	k_{ij}	
	$k_{ij,a}$	$k_{ij,T}$
ChCl + EG	0.0969	-0.00151
ChCl + 12P	0.0368	-0.00144
ChCl + 13P	0.0757	-0.00154
ChCl + 14B	0.0997	-0.00166
Bet + EG	0.1179	-0.00129
Bet + 12P	0.0762	-0.00151
Bet + 13P	0.0911	-0.00144
Bet + 14B	0.1340	-0.00193
ChCl + water[a]	-0.0584	-0.00010
Bet + water[a]	-0.0922	0
12P + water[b]	-0.0484	0
14B + water[b]	-0.0266	0

[a] Binary interactions used that were retrieved from the original source [61, 97].

[b] Fitted to isobaric [294, 296] and isothermal [295, 297] vapor-liquid equilibrium.

The viscosity of the DES systems is calculated using the FVT in combination with the PC-SAFT EoS, as detailed in Section 2.6.2. This method integrates molecular-level descriptors and thermodynamic properties, such as density, derived from PC-SAFT, to predict the viscosity. The parameters of the FVT model, shown in Table 7.4, were fitted independently to the literature viscosity for each HBD [15, 298–306] and water [307]. In contrast, each HBA was fitted implicitly using the DESs viscosities measured in this work.

The surface tension of the DES systems is determined using DGT in combination with the PC-SAFT EoS, as detailed in Section 2.6.1. DGT calculates surface tension based on density profiles across interfaces, obtained through energy minimization of the Helmholtz energy provided by the PC-SAFT model for each bulk phase. For DESs, as shown in Chapter 5, DGT is applied using a pseudo-pure component approach, where the influence parameters are fitted independently for each DES at a particular molar ratio. Interestingly, these influence parameters tend to exhibit a linear relationship with the mole fraction of the HBA, where the intercept corresponds to the case of the pure HBD, which can also be fitted independently. Table 7.5 presents the influence parameters for each HBD, along with the linear relationship used to determine each DES at any molar ratio. It was observed that the slope of these relationships also follows a linear trend with the molecular

TABLE 7.4: Molecular parameters for PC-SAFT + FVT used in this work.

Compounds	α **[J m^3/(mol kg)]**	$B \times 10^3$	L_v **[Å]**
ChCl	381.3441	3.2081	0.044242
Bet	380.4809	4.0818	0.055774
EG	401.9910	2.4252	0.021870
12P	379.1580	3.6194	0.018220
13P	379.3350	3.1372	0.038050
14B	379.3390	3.7175	0.032950
water	406.8630	1.5787	0.009530

TABLE 7.5: Influence parameters of HBDs and DESs fitted in this work.

Compounds or DES	c_{ii} **x 10^{20} [J m^5/mol^2]**
EG	7.4580
12P	9.8875
13P	17.8077
14B	26.9288
ChCl:HBD[a]	$c_{HBD} + (66.5658 - 6.2620 \cdot M_{w,HBD}) \cdot x_{HBA}$
Bet:HBD[a]	$c_{HBD} + (59.7050 - 6.6960 \cdot M_{w,HBD}) \cdot x_{HBA}$
ChCl:12P	$c_{12P} + 13.4077 \cdot x_{HBA}$
Bet:12P	$c_{12P} + 6.8799 \cdot x_{HBA}$
water	1.0624

[a] Only for the 1,2-alkanediol family as HBD.

weight of the 1,2-alkanediol HBD family ($M_{w,HBD}$), which could be valuable for extrapolating to other HBDs in this family.

The Absolute Average Relative Deviation (AARD) was used to quantify the deviation between calculated and experimental values. The AARD equation is shown in Eq. 7.3.

$$\%AARD = \frac{100}{n} \sum_{i=1}^{n} \left| \frac{\delta_i^{exp} - \delta_i^{calc}}{\delta_i^{exp}} \right| \tag{7.3}$$

where n is the total number of experimental points, δ_i is the property (density, viscosity or surface tension), and the superscripts exp and $calc$ are the experimental and calculated values, respectively.

7.3.2. Molecular dynamics details

MD simulations were carried out to gain a more comprehensive understanding of the molecular level for DES and DES + water mixtures. For 12P, 13P, and 14B, the mixed OPLS-AA force field was used [308], and for ChCl and EG, the OPLS-DES force field was used [266]. The Bet was modeled with the OPLS-AA considering the modification developed by Monteiro et al. [287]. The TIP4P/2005 force field was used for water molecules [309]. These non-polarizable force fields describe electrostatic and van der Waals interactions with Coulomb potential and Lennard Jones potential, respectively. The nonbonded interactions were calculated with the cut-off distance set to 1.9 nm. The long-range electrostatic interactions were handled using the Particle-Mesh Ewald technique with a fourth-order interpolation [268]. All the equations of motion were integrated with the leapfrog algorithm [142] using a time step of 1 fs.

PACKMOL was used to generate a random initial configuration for each simulation box [267], according to the number of molecules shown in Table 7.6 for a desirable mole fraction of water. The simulations of ChCl-based DESs were only conducted at a molar ratio of 1:3, while Bet-based DESs were only simulated at a molar ratio of 1:6 to reduce the number of systems to run. The prepared systems were energy minimized using the steepest descent algorithm for 5000 steps. After that, the system was equilibrated using the NPT ensemble for 10 ns, which allowed the temperature and pressure of the system to reach a stable state. The temperature was kept constant using velocity rescaling with a stochastic term [148], and the pressure was kept constant using the Berendsen barostat [147]. The equilibrated system was simulated in the NPT ensemble for 50 ns. During the production simulation, the temperature was controlled using the Nose-Hoover thermostat [149, 150] with a coupling constant of 1 ps, and the pressure was controlled using the Parrinello-Rahman barostat [151, 152] with a coupling constant of 5 ps. The trajectory of the last 25 ns was employed to calculate thermodynamic and structural properties, where the error estimation was done using the average over 10 blocks. GROMACS 2022.1 [310] was used as a molecular dynamics package to run all the simulation steps, and its analytical tools were used to process the information.

TABLE 7.6: The number of molecules in the simulation boxes for the systems ChCl:HBD (1:3) + water and Bet:HBD (1:6) + water.

	ChCl:HBD(1:3) + water			**Bet:HBD(1:6) + water**		
x_{water}	N_{water}	$N_{Ch} = N_{Cl}$	N_{HBD}	N_{water}	N_{Bet}	N_{HBD}
0	0	250	750	0	190	1140
0.1	100	225	675	140	180	1080
0.3	360	210	630	504	168	1008
0.5	800	200	600	1120	160	960
0.7	1400	150	450	1960	120	720
0.9	2880	80	240	3780	60	360
1	4000	0	0	4000	0	0

The viscosity was calculated using NEMD method, where an external force was applied periodically to the liquid phase in the x-direction [153, 266, 311], as described in Section 3.3.1. Basically, the external force will generate a velocity profile in the fluid that can be related to the viscosity. In this work, the acceleration amplitude ($\mathcal{A}$) was set at a different value from 0.08 to 0.20 nm/ps^2 to enable extrapolation of the viscosity to zero acceleration amplitude, thereby improving the accuracy of the estimate. Each perturbation was simulated by extending the production run of the homogeneous phase by 10 ns.

Independent simulations were conducted for each system to obtain the surface tension values. The simulation box dimensions were set to 4.8 nm × 4.8 nm × L_z, where L_z represents the box length in the z-direction (normal to the interface), ranging from 7 to 10 nm depending on the density of each system. Molecules were randomly placed forming homogeneous phases, with the number of molecules consistent with those listed in Table 7.6. The prepared systems were energy minimized using the steepest descent algorithm for 5000 steps. Next, the homogeneous system was equilibrated using the NP$_{zz}$AT ensemble for 20 ns, during which the temperature, the normal pressure, and the interfacial area reached a stable state while L_z was changing. To keep constant the temperature and pressure, the velocity rescaling with a stochastic term [148] and the Berendsen barostat [147] were used, respectively. Each equilibrated system was extended in the z-axis by a factor of five to produce two liquid-vapor interfaces. These inhomogeneous simulations were run for 200 ns in the NVT ensemble, where the temperature was controlled using the Nose-Hoover thermostat [149, 150] with a coupling constant of 1 ps. The procedure was repeated in three independent simulations to obtain an error estimation for the surface tension. The surface tension was computed using the inhomogeneity of the pressure tensor [154, 312], where the last 100 ns were considered.

7.4. Results

7.4.1. Thermophysical properties of glycol-based DES

The experimental density, viscosity, and surface tension were studied at atmospheric pressure and temperatures ranging from 20 °C to 60 °C for all prepared DESs. For Bet-based DESs, the measured properties are provided in the Appendix B (Table B.3). For ChCl-based DESs, density and viscosity data were obtained from Gajardo-Parra et al. [15], while the surface tension measured in this work is presented in Table B.4. All these data are compared with the PC-SAFT modeling results in Figure B.4 for densities, Figure B.5 for viscosities, and Figure B.6 for surface tension. The excellent agreement with experimental data, quantified by the AARD values in Table 7.7, is expected, as part of the experimental data was used to fit the parameters reported previously.

The following sections provide a detailed analysis of each property, taking into account the different behaviors of each HBA and HBD.

Density

For Bet-based DESs measured in this work, a comparison with literature data is shown in Figure B.1 [313–325]. The available data for Bet-based DESs are limited, and only a few systems allow for a fair comparison, as several studies report DESs with a higher mole fraction of HBA than those in this work. Specifically, the literature often describes DESs with an HBA:HBD molar ratio of

TABLE 7.7: AARD of density, viscosity and surface tension obtained through PC-SAFT for each DES family

	AARD ρ	**AARD** η	**AARD** γ	**AARD** ρ	**AARD** η	**AARD** γ
HBD	**ChCl-based DESs**			**Bet-based DESs**		
EG	0.05%	6.36%	0.55%	0.10%	3.49%	0.32%
12P	0.05%	5.38%	0.57%	0.06%	7.92%	0.44%
13P	0.08%	5.53%	0.57%	0.08%	2.72%	0.48%
14B	0.16%	3.86%	0.44%	0.31%	1.90%	0.52%

1:3, compared to the 1:4 ratio predominantly used in this study. Consequently, DESs reported in the literature generally exhibit higher densities. However, excluding data for different HBA:HBD molar ratios, as well as the densities published by Mulia et al. [313, 322] and Zahrina et al. [321], the average deviation does not exceed ±0.5%.

The density at atmospheric pressure and various temperatures was also simulated using MD for the glycols and DESs at different mole ratios, as shown in Figure 7.2 (ChCl-based) and Figure B.7 (Bet-based). While the simulated densities underestimate the experimental values, they provide qualitatively accurate trends in all cases, demonstrating the reliability of the selected force field. As expected, nearly linear trends are observed for density as a function of temperature for each DES. At all studied temperatures, the DESs exhibit higher densities than the pure HBDs used to produce them. This behavior can be attributed to the reduction in free volume caused by the formation of a strong hydrogen-bond network between the HBA and HBD [326, 327].

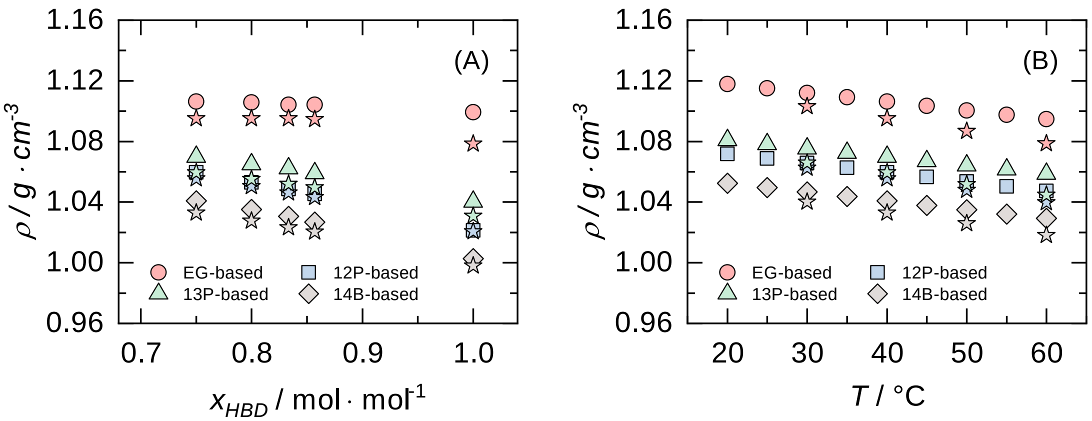

FIGURE 7.2: Densities at atmospheric pressure for ChCl-based DESs formed with different glycols: (A) as a function of the HBD mole fraction at 40°C, and (B) as a function of temperature for an HBA:HBD molar ratio of 1:6. Symbols except for stars: experimental data. Stars symbols: MD simulations.

In all these systems, it is observed that density decreases with increasing HBD chain length, which is consistent with the density decrease observed for pure HBDs. This trend aligns with the density reduction caused by longer alkyl chains in organic acids [294], likely explained by the increased free volume associated with the less efficient packing of longer chains or steric effects. Specifically, for 12P- and 13P-based DESs, at the same HBA:HBD molar ratios and temperatures, the higher density of 13P-based DESs compared to 12P-based DESs is attributed to differences in their molecular packing behavior. These differences arise from the more extended and linear structure of 13P, which facilitates stronger intermolecular hydrogen bonding and more efficient packing compared to the compact structure of 12P. This behavior is analyzed in the following sections from a molecular perspective.

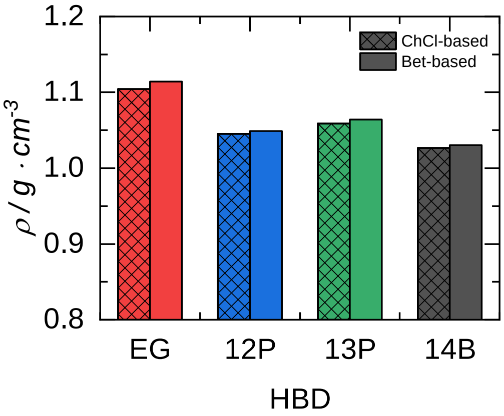

FIGURE 7.3: Experimental densities at atmospheric pressure and 40°C for DESs at a molar ratio of 1:6, comparing HBAs and HBDs.

To examine the effect of the HBA on density, Figure 7.3 presents experimental data for ChCl-based and Bet-based DESs, both with an HBA:HBD molar ratio of 1:6 and at a temperature of 40 °C. Despite their similar chemical structures, Bet-based DESs exhibit higher densities under the same temperature and HBA:HBD ratio compared to ChCl-based DESs. This trend is consistently observed across other HBA:HBD molar ratios and temperature as well. A plausible explanation is the stronger HBA-HBD interactions in Bet-based DESs, likely resulting from the carboxylate groups in Bet, which enhance hydrogen bonding, compared to the hydroxyl groups in ChCl.

Viscosity

A comparison between viscosity values measured in this work for Bet-based DESs and values reported in the literature [313–315, 317–319, 321, 324, 325] are shown in Figure B.2. Although deviations seem very high, only some of the literature data are comparable with values measured in this work because several authors do not report the water content of their DESs. Water content is relevant because a small amount strongly reduces the viscosity in DESs [156, 258, 279]. Additionally, DESs reported in the literature exhibit higher mole fractions of HBA than DESs reported in this work. In this matter, a higher mole fraction of HBA strongly increases the viscosity, as it has been reported by Gajardo-Parra et al. [15] for ChCl-based DESs. However, the measured data agree with the literature, except for the data published by Kucan et al. [318], which shows significant deviations in temperature trends.

As expected, viscosity decreases exponentially with increasing temperature due to enhanced molecular mobility and the weakening of attractive interactions in the DES, as shown in Figure B.5. DES viscosities are higher than those of pure HBDs at all temperatures, which can be attributed to the strong hydrogen bonding between the HBA and HBD. This also explains why an increase in HBA concentration leads to higher viscosity, as previously reported in the literature [15].

At the same temperature and HBA:HBD molar ratios, the viscosity of the DESs in this study increases with the HBD chain length, as shown in Figure 7.4, following a similar trend observed for pure HBDs. Interestingly, this HBD trend is opposite to that of density, even for the specific case of 12P-based and 13P-based DESs. Although 12P exhibits less efficient packing compared to 13P (which explains its lower density for the same molecular chain length), the intermolecular interactions are stronger in 12P (resulting in higher viscosity). This can be attributed to the closer proximity of the two hydroxyl groups in 12P, which create steric hindrance that disrupts packing efficiency but simultaneously enable cooperative interactions through hydrogen bonding, strengthening the intermolecular network.

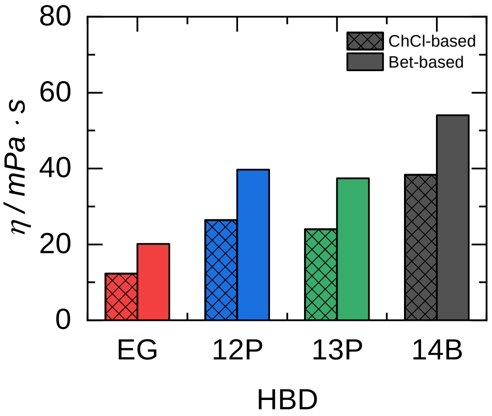

FIGURE 7.4: Experimental viscosities at atmospheric pressure and 40°C for DESs at a molar ratio of 1:6, comparing HBAs and HBDs.

Figure 7.4 also compares experimental data for both HBAs with each HBD under identical conditions to analyze the effect of the HBA on viscosity. Although ChCl and Bet share similar chemical structures, Bet-based DESs consistently exhibit higher viscosities under the same conditions. This behavior can be attributed to the stronger hydrogen bond network formed by the carboxylate groups in Bet, compared to the hydroxyl groups in ChCl. This stronger network not only increases viscosity but also reduces free space, leading to higher densities.

Surface Tension

Surface tensions of glycols and DESs measured in this work are compared with values reported in the literature [7, 156, 200, 207, 240, 248, 252, 319, 328–343] in Figure B.3. ChCl:EG(1:2) was measured and included in the comparison as a benchmark system because its surface tension is the most frequently reported. It is worth noticing that some of the literature data correspond to different HBA:HBD molar ratios or temperatures, requiring careful analysis. The comparison reveals that the values obtained in this study are consistent with previously reported results, except for those by Kityk et al. [338], which show significant deviations in their temperature-dependent trends.

As shown in Figure B.6, the results demonstrate a nearly linear decrease in surface tension with increasing temperature, a common behavior observed in liquids. This trend arises from the weakening of intermolecular forces as temperature increases. For DESs, the surface tensions are higher than those of pure HBDs at the same temperature. This can be attributed to the robust hydrogen-bonding network formed between the HBA and HBD components in DESs, which creates a denser interfacial region with stronger cohesive forces. These enhanced interactions increase the energy required to disrupt the liquid phase, resulting in higher surface tension.

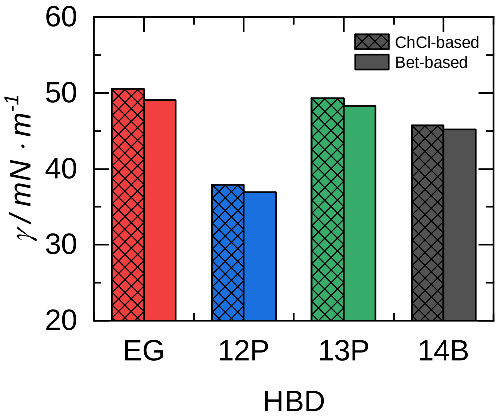

FIGURE 7.5: Experimental surface tension at atmospheric pressure and 40°C for DESs at a molar ratio of 1:6, comparing HBAs and HBDs.

To better understand the impact of HBAs and HBDs on surface tension, Figure 7.5 presents experimental data for ChCl-based and Bet-based DESs with an HBA:HBD molar ratio of 1:6 at 40 °C for each HBD. On the one hand, the surface tensions of DESs decrease as the chain length of the HBD glycols with alcohol endpoints increases. This behavior aligns with the surface tensions observed for the pure HBDs. Among the DESs studied, those based on 12P exhibit lower surface tensions than DESs containing other glycols. This is likely due to the unique location of the hydroxyl groups in 12P, which creates two well-defined polar and apolar regions, making the molecule behave similarly to a typical surfactant. On the other hand, despite the similar chemical structures of the HBAs, Bet-based DESs consistently display lower surface tensions than ChCl-based DESs under the same temperature and HBA:HBD molar ratio conditions.

TABLE 7.8: AARD of density, viscosity and surface tension obtained through PC-SAFT for DES + water mixtures for each family

	AARD ρ	AARD η	AARD γ	AARD ρ	AARD η	AARD γ
HBD	**ChCl-based DESs**			**Bet-based DESs**		
EG	0.58%	27.96%	1.07%	0.77%	20.38%	1.32%
12P	0.57%	36.37%	3.20%	0.65%	34.55%	4.39%
13P	0.55%	32.12%	1.40%	0.66%	30.19%	1.80%
14B	0.43%	41.46%	2.50%	0.35%	40.68%	2.55%

7.4.2. Effect of water in glycol-based DESs

In addition to the previously discussed experimental data, density and viscosity were measured at temperatures between 20 and 60 °C across the full range of water content. These data are reported in Table B.5 (for density) and Table B.6 (for viscosity) for each DES studied. Furthermore, surface tension was measured across the full range of water content but only at 40 °C, with the results reported in Table B.7. All these data are modeled using PC-SAFT in a predictive manner, as none were included in the fitting procedure. For instance, the density modeling as a function of temperature and water content is compared with experimental data in Figure B.8. A similar plot for viscosity is shown in Figure B.9. The predictive capability can be evaluated using the AARD for each DES family, as reported in Table 7.8.

Density

To the best of our knowledge, densities of Bet-based DES + water mixtures have not been extensively reported in the literature. Barzegar-Jalali et al. [323] studied DES + water mixtures with Bet-EG (1:3) and Bet-12P (1:5) in all ranges of water content at temperatures between 15 °C and 45 °C and they correlated their results with several models suggesting that the DES acts as a structure-maker in the presence of water. Fuad et al. [325] also studied different Bet-based systems (i.e. with glycerol 1:2, 12P 1:4, and lactic acid 1:2) at ambient temperature and water content range of 0-50 wt%. Meanwhile, ChCl-based DES + water mixtures have been extensively reported in the literature (i.e with glycerol 1:2 [272, 335], urea 1:2 [335, 344], EG 1:2 [272, 290, 335], malonic acid [345], glutaric acid [345]). As expected, a non-linear decay in the density upon water addition is observed due to hydrogen bond network disruption after water solvates the DESs structure (i.e. both HBA and HBA). Particularly, Li et al. [346] and Nowosielski et al. [347] reported other DES + water mixtures that show an increase in density with an increasing water content at low water content.

Figure 7.6 shows the density behavior as a function of water content for both ChCl-based and Bet-based DESs. The figure also includes the PC-SAFT predictions alongside the MD results. On the one hand, compared to the experimental data for DESs, the PC-SAFT predictions for DES + water mixture densities are slightly underestimated, which could be improved by incorporating additional binary interaction parameters. On the other hand, while MD results also underestimate the experimental values, they provide qualitatively accurate trends, achieving a total average AARD of 0.64% and a maximum average AARD of 1.28% (for the Bet:13P family). The AARD values from MD obtained for each DES family are summarized in Table B.8.

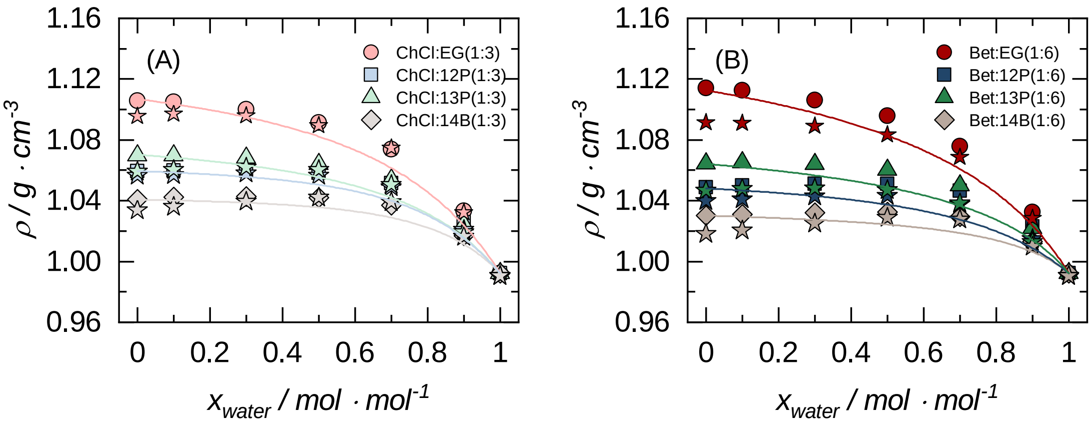

FIGURE 7.6: Density at 40°C as a function of the mole fraction of water in mixtures with (A) ChCl-based DESs and (B) Bet-based DESs. Symbols except for stars: experimental data. Stars symbols MD simulation results. Solid lines represent the PC-SAFT using parameters reported in Tables 7.2 and 7.3.

The density exhibits non-ideal behavior in DES + water mixtures, with experimental densities exceeding those expected for an ideal mixture. The degree of non-ideality increases with the HBD chain length, resulting in deviations from ideality that are particularly pronounced for 14B-based DESs with both HBAs. This trend is shown in Figure 7.6, where the addition of water to each DES does not significantly change the density at low water content. This effect becomes more evident as the HBD chain length increases.

Viscosity

To the best of our knowledge, only Fuad et al. [325] have done an exhaustive study of the viscosity of different Bet-based (i.e. with glycerol 1:2, 12P 1:4 and lactic acid 1:2) DES + water mixtures at ambient temperature and water content range of 0-50% (m/m). Also, the viscosity as a function of the water content of ChCl-based [272, 290, 348] and other HBA-based [335, 346, 347, 349, 350] DES + water mixtures also have been reported. As expected, the viscosity of DES + water mixtures decrease with increasing water content similar to the results obtained in this work.

The PC-SAFT + FVT framework for viscosity prediction of DES + water mixtures underestimates the observed values, likely due to the propagation of errors from the density input, which is a critical parameter in the FVT framework. Viscosity at 40 °C was also simulated using MD for all DESs with an HBA:HBD molar ratio of 1:3 (for ChCl-based) or 1:6 (for Bet-based). The MD results, along with experimental data and PC-SAFT predictions, are shown in Figure 7.7. The AARD values obtained from MD for each DES family are summarized in Table B.8, with a total average AARD of 111.78% and a maximum average AARD of 228.28% (for the ChCl:12P family).

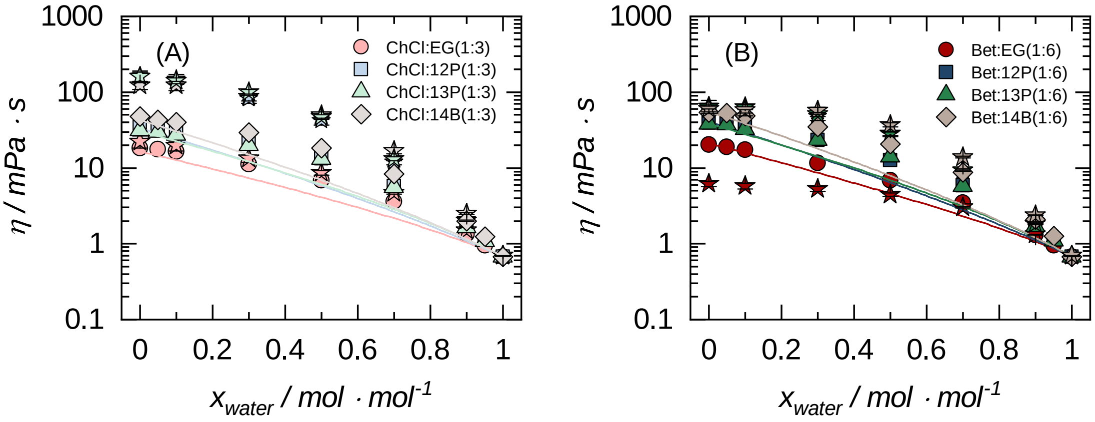

FIGURE 7.7: Viscosity at 40°C as a function of the mole fraction of water in mixtures with (A) ChCl-based DESs and (B) Bet-based DESs. Symbols except for stars: experimental data. Stars symbols MD simulation results. Solid lines represent the PC-SAFT + FVT using parameters reported in Tables 7.2, 7.3 and 7.4.

The viscosity of all the DES + water mixtures decreases exponentially with temperature, as previously reported for glycols and DESs. Also, the viscosity decrease is nearly linear with increasing the water content until approximately x_{water} = 0.5. Over x_{water} = 0.5, the viscosity decreases exponentially, approaching water viscosity. Unlike the density of DES + water mixtures, the viscosity is barely influenced by the HBD, as water plays the dominant role in reducing viscosity, making the HBD's effect negligible.

Surface Tension

The surface tension of DES + water mixtures has not been extensively studied in the literature. Chen et al. [252] studied the surface tension of DES + water mixtures of ChCl:lactic acid (1:2 and 1:4), ChCl:glycerol (1:2) and BET:lactic acid (1:2) at 20°C and all ranges of water content; Fuad and Nadzir [325] studied different BET-based (i.e. with glycerol 1:2, 12P 1:4 and lactic acid 1:2) DES + water mixtures at ambient temperature and molar water content range of 0-50%; and Al-Murshedi et al. [335] studied different ChCl-based (with glycerol 1:2, urea 1:2 and EG 1:2) DES + water mixtures at ambient temperature and molar water content range of 0-20%. Their results show a constant surface tension for low water content that increases exponentially at high water contents until the surface tension of water. An interesting result was presented by Chen et al. [252] for ChCl:lactic acid DESs prior to the exponential increase at high water content, its surface tension slightly decreased around x_{water} = 0.9.

Figure 7.8 shows the surface tension as a function of water content for both ChCl-based and Bet-based DESs, comparing experimental measurements with predictions from PC+DGT and results from MD simulations at 40°C. For each DES + water mixture, accurate predictions are obtained by PC-SAFT + DGT with a total average AARD and maximum average AARD of 2.28% and 2.39%, respectively. The surface tensions from MD have a total average AARD and maximum

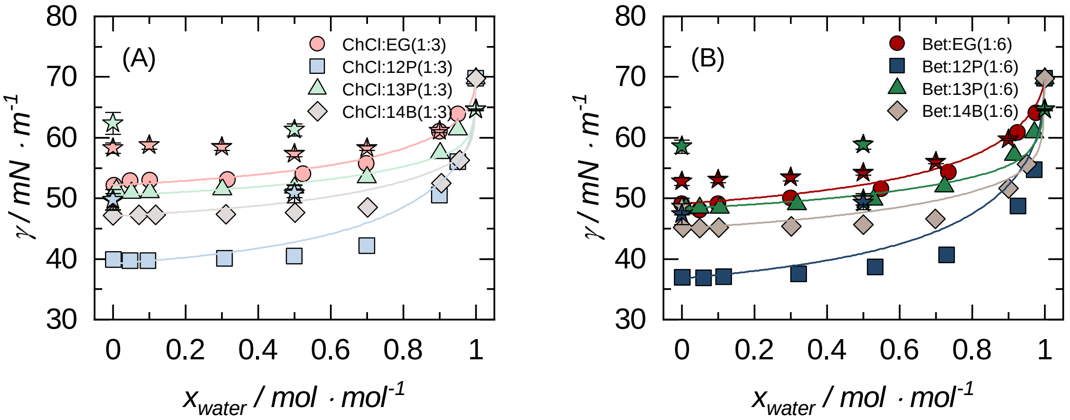

FIGURE 7.8: Surface tension at 40°C as a function of the mole fraction of water in mixtures with (A) ChCl-based DESs and (B) Bet-based DESs. Symbols except for stars: experimental data. Stars symbols MD simulation results. Solid lines represent the PC-SAFT + DGT using parameters reported in Tables 7.2, 7.3 and 7.5.

average AARD of 12.09% and 24.61%, respectively. Clearly, the EG-based DESs (ChCl:EG(1:3) and BET:EG(1:6)) and 14B-based DESs (ChCl:14B(1:3) and BET:14B(1:6)) show qualitatively accurate results with respect to experimental data in comparison with the other DESs.

The surface tension of each mixture remains relatively constant at low water content. However, as the water content increases and approaches pure water, the surface tension rises significantly, ultimately reaching the value characteristic of pure water. This increase becomes more pronounced with a longer HBD chain in the DES, leading to a steeper slope in the surface tension curve. From the perspective of water, this steeper slope reflects a greater reduction in its surface tension caused by the addition of a small amount of DES. These trends are not only observed experimentally but are also well captured by both PC-SAFT calculations and MD simulations.

7.4.3. Molecular insights in glycol-based DESs

Hydrogen Bonds

An essential characteristic of DES is the hydrogen bond network between HBA and HBD. From MD simulations, the number of hydrogen bonds between molecule *i* and *j* is quantified for the different molecule pairs, which can establish this kind of interaction. Figure 7.9 (for ChCl-based at the molar ratio of 1:3) and Figure B.10 (for Bet-based at the molar ratio of 1:6) show the hydrogen bonds between molecule *i* and *j* per molecule *i* as a function of water content.

The number of hydrogen bonds per molecule in the HBA-HBD pair of ChCl-based DESs (Figure 7.9B or 7.9D) decreases with increasing water content across all DESs. This behavior is expected, as water promotes hydrogen bond formation with both HBA and HBD, as shown by the trends in Figures 7.9C and 7.9F. A similar trend is observed for Bet-based DESs, where water reduces the number of hydrogen bonds in the HBA-HBD pair (Figure B.10B or B.10D). When comparing

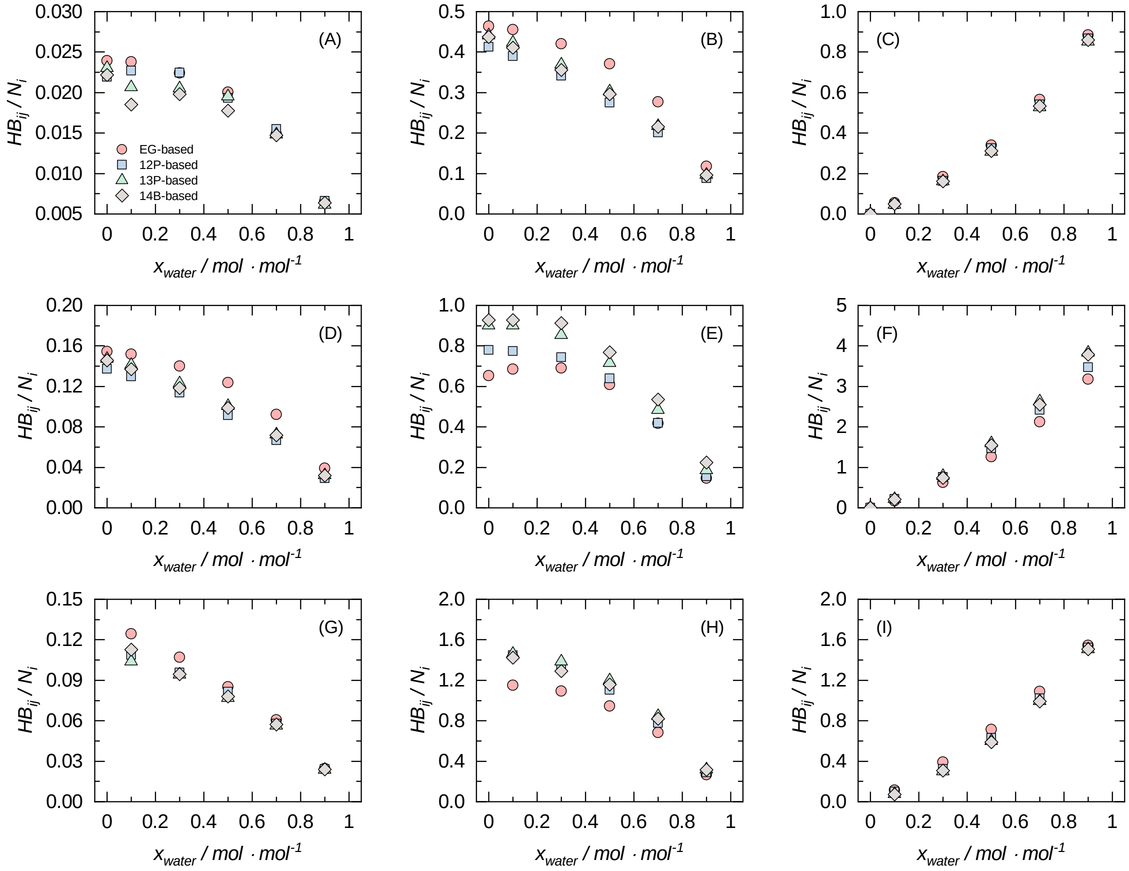

FIGURE 7.9: Number of hydrogen bonds between molecule i and j per molecule i (HB_{ij}/N_i) as a function of the water mole fraction at 40°C for ChCl-based DESs obtained through MD. Molecule pairs i-j: (A) HBA-HBA, (B) HBA-HBD, (C) HBA-water, (D) HBD-HBA, (E) HBD-HBD, (F) HBD-water, (G) water-HBA, (H) water-HBD and (I) water-water.

different HBDs, EG interacts more easily with the HBA due to its smaller size, which facilitates closer packing with the HBA. Conversely, increasing the HBD size decreases the number of hydrogen bonds in the HBA-HBD pair. Interestingly, 12P-based DESs exhibit a distinct trend depending on the HBA. In ChCl-based DESs, the HBA-HBD hydrogen bonds per molecule are fewer than in 14B-based DESs, while for Bet-based DESs, the hydrogen bond numbers are nearly identical.

Although the smaller size of EG allows for a more compact structure, Figures 7.9F and B.10F show that at high water content, EG-based DESs have fewer hydrogen bonds per HBD molecule between HBD and water compared to other linear glycols. This behavior can be attributed to the proximity of EG's two hydroxyl groups, which enables a single water molecule to interact with both hydroxyl groups simultaneously. A similar trend explains why the HBD-water interactions per HBD molecule are lower for 12P-based DESs than for 13P-based DESs; however, the values for 12P-based DESs are not as low as those for EG-based DESs, due to the larger size of 12P molecules compared to EG. Interestingly, despite differences in the number of HBD molecules between ChCl-based and Bet-based DESs, both exhibit nearly identical HBD-water interactions per HBD molecule.

The behavior of HBD-HBD hydrogen bonds per molecule as a function of water content is slightly different between ChCl-based DESs (Figure 7.9E) and Bet-based DES (Figure B.10E). The ChCl-based DESs only notoriously decrease their interactions per molecule once x_{water} = 0.3 and even show a maximum for the case of DES-A4 at this water content. Meanwhile, the Bet-based DESs show a more evident decrease in their HBD-HBD hydrogen bonds per molecule in all water contents. Regarding the HBD effect, results for ChCl-based DESs reveal a decreasing number of hydrogen bonds per molecule for HBD-HBD interactions as the HBD chain length decrease, meanwhile, a similiar behavior is observed for Bet-based DESs. On the other hand, 12P-based DESs show HBD-HBD interactions closer to EG-based DESs than 13P-based DESs for both HBA. The fact that EG-based DESs and 12P-based DESs show a lower number of hydrogen bonds per molecule is explained by the proximity of the two OH groups in EG and 12P that allow the possibility of the interaction of both OH groups with another OH group at the same time.

Even though the number of HBA molecules, which limits the possible HBD-HBA hydrogen bonds, is higher for ChCl-based DES; the Bet-based DESs show more interaction per molecule between HBA and HBD. This result can be attributed to the fact that ChCl can self-associate (cf. Figure 7.9) because the Ch structure has a hydroxyl group (hydrogen bond donor) and it is a salt, so its constituents (Cl and Ch ions) are separated in solution. This self-association reduces the possibility of interactions between HBD and HBA. On the other hand, Bet molecules can not establish self-association due to their hydrophobic carboxylate molecule, as is shown in Figure B.10. This can explain that, at the same state and composition, the density and viscosity of Bet-based DESs are higher than ChCl-based DESs, although the molecules have a similar structure.

Molecular arrangement

The RDFs and coordination numbers (CNs) for each molecular pair were calculated from MD simulations to investigate the structure of DESs. The Appendix B provides RDFs between the centers of mass of each molecule for all possible pair combinations as a function of water content, covering ChCl:EG (1:3) (Figure B.11), ChCl:12P (1:3) (Figure B.12), ChCl:13P (1:3) (Figure B.13), ChCl:14B (1:3) (Figure B.14), Bet:EG (1:6) (Figure B.15), Bet:12P (1:6) (Figure B.16), Bet:13P (1:6) (Figure B.17), and Bet:14B (1:6) (Figure B.18). A key observation is the reduction in peak intensity in most RDFs with increasing water content, indicating that water interacts with all molecules in the mixtures and diminishes specific pair interactions. The subsequent discussion will explore into specific features of particular molecular pairs in the RDFs.

The RDFs for Cl-Cl reveal the appearance of a second peak at approximately 0.5 nm, emerging immediately with the addition of small amounts of water. This second peak indicates that the Cl ions adopt shorter interionic distances, forming structures distinct from those in ChCl-based DESs without water. Notably, the appearance of the second peak in Cl-Cl RDFs is related to the Cl-water RDF peak located at approximately 0.3 nm across all water contents. This distance is shorter than the Cl-Cl second peak and the first coordination shells of Cl-HBD and Cl-Ch pairs.

For instance, Figure 7.10 illustrates this behavior for ChCl:EG(1:3), which is also observed in other ChCl-based DESs studied here (see Figures B.12–B.14). This phenomenon arises because two Cl ions can simultaneously interact with a single water molecule, with each Cl ion associating with one proton, thereby reducing the distance between the Cl ions.

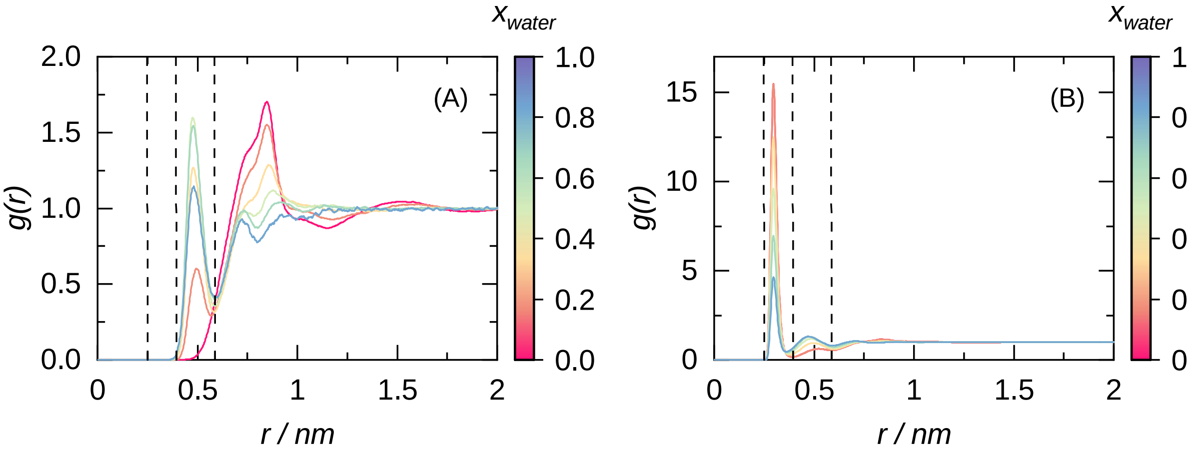

FIGURE 7.10: Center-of-mass RDFs as a function of water content for ChCl:EG(1:3) + water mixtures, showing the pairs: (A) Cl–Cl and (B) Cl–water.

Another behavior is observed in the RDFs for HBD-HBD interactions. These RDFs show a nearly constant peak intensity at low water content until approximately $x_{water} = 0.3$, after which the intensity decreases. This behavior is related to changes in the HBD-HBD hydrogen bonds as the water content increases, as discussed in the previous section. To understand this behavior more deeply and to examine how the molecular liquid structure evolves with varying water content, it is necessary to analyze the CNs using water as a reference. Figure 7.11 presents these CNs for the EG-based DESs as an example; similar behavior is observed in the other DESs, as shown in Figure B.19. The CNs reveal that water molecules are primarily surrounded by HBA and HBD in the first solvation shell, maintaining a nearly constant conformation until a water content of approximately $x_{water} = 0.75$ (most notably with HBD in most DESs). Similar behavior has been reported for different DESs in the literature [272, 287]. Beyond this water content, water molecules preferentially surround themselves, causing the conformation with HBA and HBD to change abruptly, forming an aqueous solution of HBA and HBD.

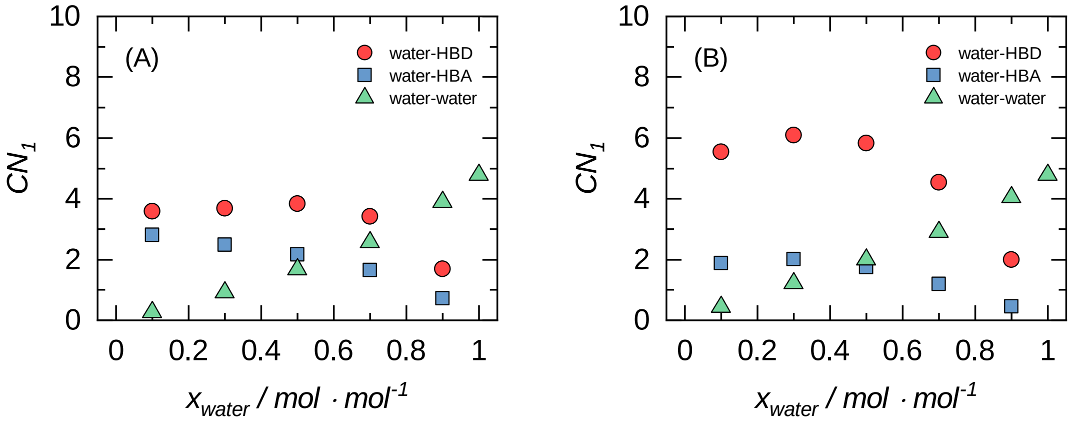

FIGURE 7.11: First coordination numbers (CN_1) obtained for different molecular pairs in water mixtures of (A) ChCl:EG(1:3) and (B) Bet:EG(1:6) as a function of the water content.

An interesting relationship between the Ch-Cl RDFs and Ch-water RDFs emerges with increasing water content for all the ChCl-based DESs. The peaks for both molecular pairs are double and overlap at similar distances. As the water content increases, the intensity of both peaks diminishes; however, the first peak decreases more rapidly with water addition compared to the second. This behavior is illustrated in Figure 7.12 for ChCl:EG(1:3) and is consistent across the other ChCl-based DESs (see Figures B.12–B.14). This phenomenon suggests that at higher water content, the coordination pattern preferentially stabilizes the arrangement corresponding to the second peak [288].

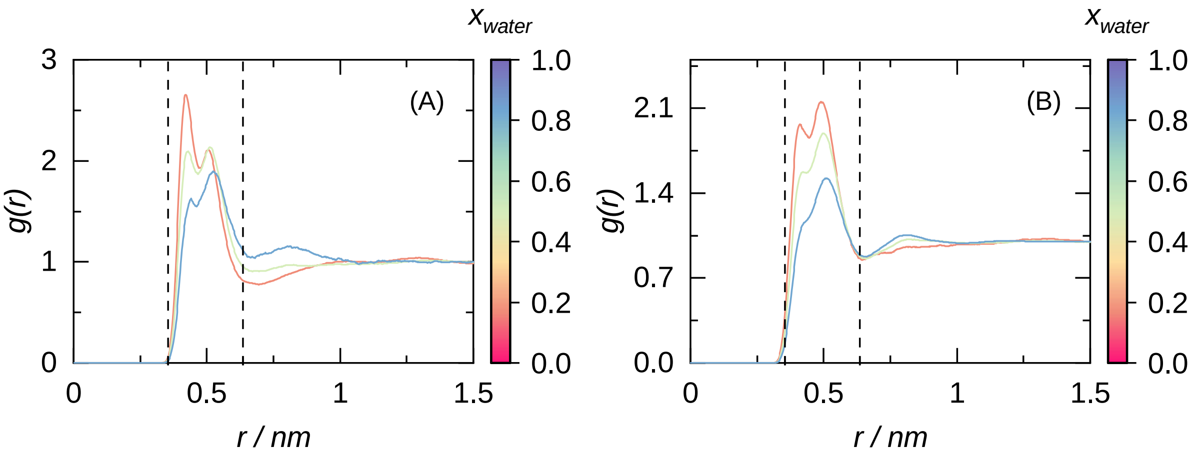

FIGURE 7.12: Center-of-mass RDFs as a function of water content for ChCl:EG (1:3) + water mixtures, showing the pairs: (A) Ch–Cl and (B) Ch–water.

Related to the HBD effect, the Cl-HBD RDFs exhibit distinct coordination patterns for each HBD, as shown in Figure 7.13 without water content. It is evident that EG and 12P display a single clear peak, while 13P and 14B exhibit two peaks. This difference is attributed to the proximity of the OH groups, as a single Cl ion can simultaneously interact with both OH groups in the case of EG and 12P, as discussed earlier in Section 7.4.3.

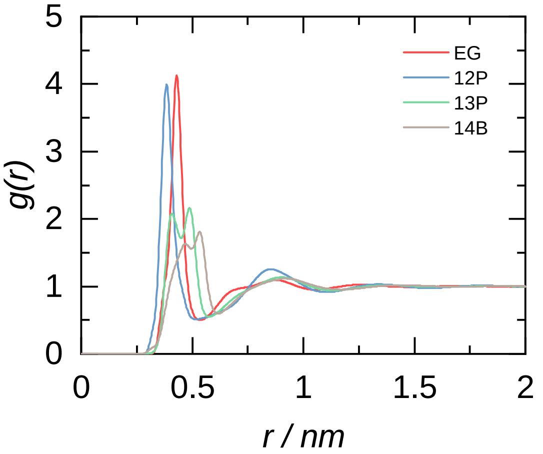

FIGURE 7.13: Center-of-mass RDFs for the pairs Cl-HBD in the ChCl-based DESs without water content.

To determine how water molecules solvate the HBA of each DES, the spatial distribution functions (SDFs) for the EG-based DES at different water contents were calculated from the trajectories using the TRAVIS package [351]. The distribution of molecules around the HBA is not significantly influenced by the HBD involved, making the findings applicable to the other DESs. As shown qualitatively in Figure 7.14, in both HBAs, HBD molecules approach the nitrogen atom as closely as possible due to its positive charge, creating three voids aligned with the N-methyl group axis [263]. However, the addition of water causes a rearrangement of the molecules around both HBAs, particularly around the nitrogen atom, to the point where the HBD molecules that form the DES structure are completely displaced. When the HBD molecules are mostly replaced by water molecules, it clearly indicates that the DES structure is no longer preserved and that the system behaves as a simple solution of HBA and HBD.

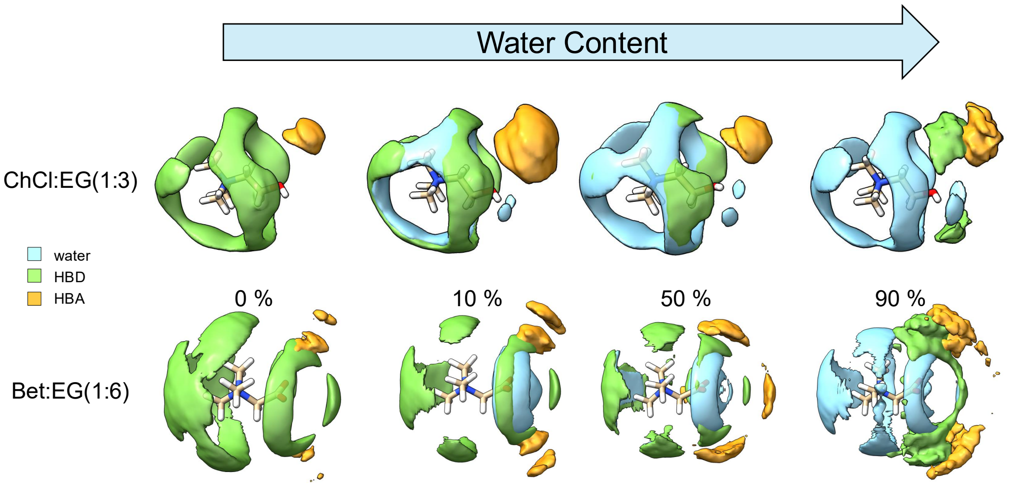

FIGURE 7.14: Spatial distribution functions of each HBA at different water contents, using ChCl:EG (1:3) and Bet:EG (1:6) as representative systems. For clarity, chloride ions have been omitted.

For a more quantitative comparison of the water effects on each HBA, Figure 7.15 shows the SDF projection on the XY plane for the water molecules around each HBA at 50% water content. The differences in the SDFs are attributed to the varying functional groups of Ch and Bet, with Bet being more extensively solvated due to its delocalized negative charge. The carboxylate group of Bet exhibits greater affinity than the hydroxyl group of Ch. This is consistent with the higher number of HBA–water hydrogen bonds observed for Bet-based DESs in Section 7.4.3.

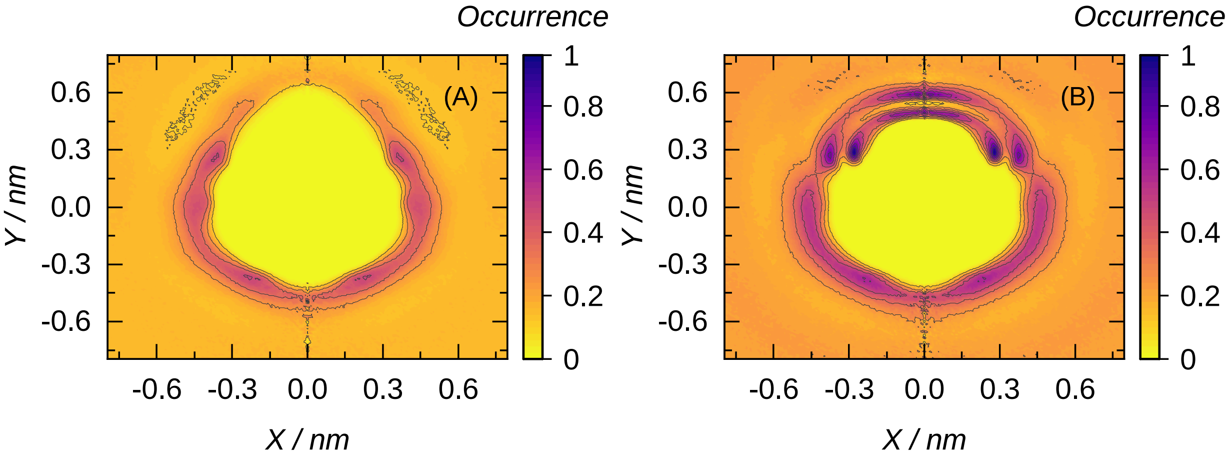

FIGURE 7.15: SDFs projection in the plane XY of (A) Ch and (B) Bet surrounded by water in EG-based DESs at 50% water content. The origin is placed in the nitrogen atoms of each HBA, and the positive Y-axis is placed in the functional group direction.

Density profiles along the interface

Density profiles for each compound in the DES + water mixture were calculated using PC-SAFT + DGT and MD simulations to provide insights into the interfacial region. Figure 7.16 shows the density profiles of DES and water as a function of water content for EG-based DES + water mixtures. The corresponding density profiles for other DES + water mixtures are very similar and are provided in the Appendix B (Figures B.21 and B.22). For this comparison, it is necessary to define the DES density profile in the MD simulation as the sum of the HBA and HBD density profiles, since PC-SAFT + DGT can only provide the density profile of the DES as a pseudo-pure approach. The PC-SAFT + DGT results show good agreement with the MD results, showing interface adsorption (or accumulation) of the DES at high water content. This accumulation becomes increasingly pronounced with increasing water content and aligns well with the reduction in water surface tension observed with a small addition of DES, as previously shown in Figure 7.8.

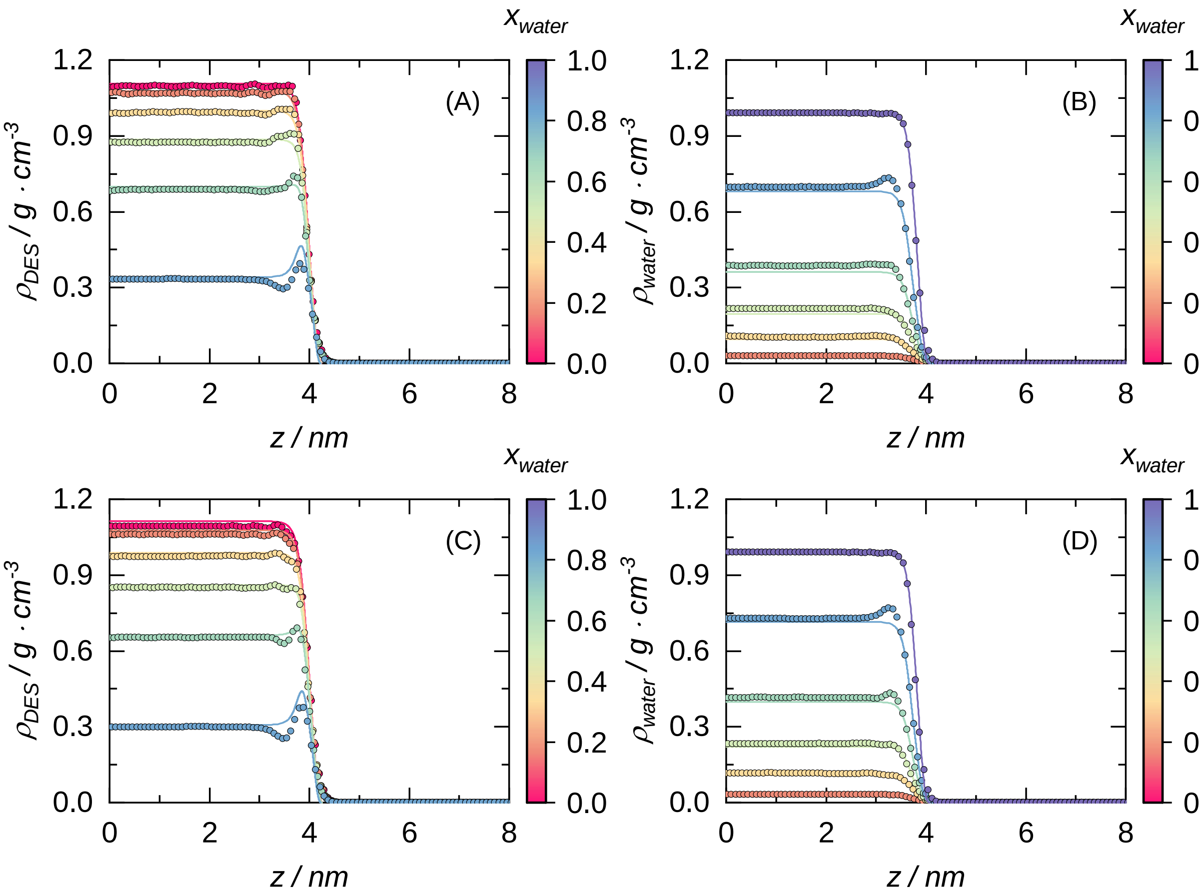

FIGURE 7.16: Density profiles at 40°C along the interfacial region (z) of (A) ChCl:EG(1:3) in its mixtures with water, (B) water in its mixtures with ChCl:EG(1:3), (C) Bet:EG(1:6) in its mixtures with water, and (D) water in its mixtures with Bet:EG(1:6). Symbols represent MD simulation results, while solid lines correspond to the PC-SAFT + DGT calculations using parameters reported in Tables 7.2, 7.3, 7.5.

Figure 7.17 illustrates the density profiles of DESs at high water content ($x_{\text{water}} = 0.9$), highlighting the effect of HBD structure on ChCl-based and Bet-based DESs. The PC-SAFT + DGT results reveal a clear trend: the maximum adsorption of DES at the interface increases with HBD chain length. This increased adsorption corresponds to a greater reduction in water's surface tension, consistent with previously observed trends at high water content. For isomeric HBDs (12P and 13P), the PC-SAFT + DGT results show that 12P-based DESs exhibit higher adsorption compared to 13P-based DESs. This difference is attributed to the molecular structure of 12P, where the hydroxyl groups are positioned to create a molecule with distinct polar and apolar regions. Such a configuration enhances its surfactant-like behavior, with polar regions favoring the liquid phase and apolar regions favoring the vapor phase. Consequently, the higher adsorption of 12P aligns with its greater ability to reduce water's surface tension. MD simulation results also support these findings, showing adsorption trends consistent with PC-SAFT + DGT. However, the difference in adsorption between 12P- and 13P-based DESs is less pronounced in MD simulations, making the distinction in surface tension behavior between the two isomers less perceptible.

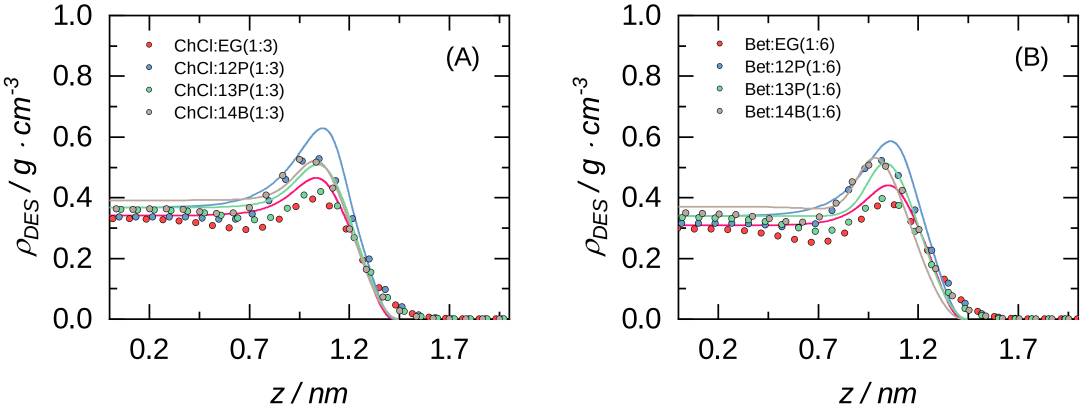

FIGURE 7.17: Density profiles of DESs with $x_{\text{water}} = 0.9$ at 40°C along the interfacial region, z, for: (A) ChCl-based and (B) Bet-based DESs. Symbols represent MD simulation results, while solid lines correspond to the PC-SAFT + DGT calculations using parameters reported in Tables 7.2, 7.3, and 7.5.

While PC-SAFT + DGT effectively represents surface tensions and density profiles of DES + water mixtures with lower computational cost and time compared to MD simulations, it treats DESs as pseudo-pure components in the interfacial region. As a result, MD simulations provide valuable complementary insights by accounting for the contributions of individual precursors. Figure 7.18 shows MD density profiles for ChCl:EG(1:3) and Bet:EG(1:6) DESs at high water content ($x_{\text{water}} = 0.9$). Similar trends are observed for other DES + water mixtures, as illustrated in the Appendix B (Figures B.23 and B.24). The previously observed DES adsorption behavior (Figure 7.17) is predominantly attributed to the HBD component. Notably, the density profiles of HBDs exhibit stronger positive surface activity, with accumulation closer to the air interface. In contrast, the HBA density profiles show a monotonic decrease from the liquid to the air interface. These results highlight that the DES molar ratio changes along the interface due to the distinct interfacial behaviors of their precursors, with HBDs playing a dominant role in surface activity.

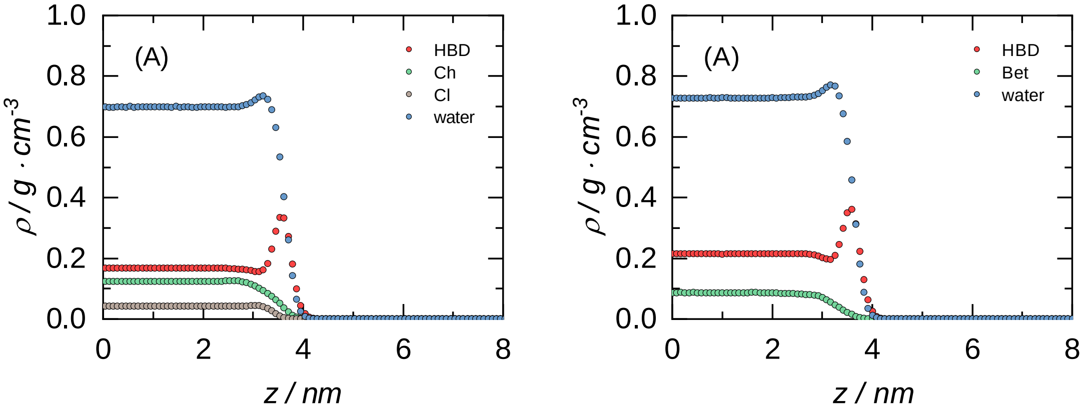

FIGURE 7.18: Density profiles of each compounds with $x_{\text{water}} = 0.9$ at 40°C along the interfacial region, z, for: (A) ChCl:EG(1:3) + water and (B) Bet:EG(1:6) + water. Symbols represent MD simulation results.

7.5. Conclusion

Density, viscosity, and surface tension of Bet-based and ChCl-based DESs with glycols (EG, 12P, 13P, and 14B) as HBDs were studied at various molar ratios, temperatures, and water contents to gain molecular-level insight into these properties. These investigations aim to support the rational design of DESs through a deeper understanding of how structural and compositional factors influence their behavior. The PC-SAFT equation of state, along with FVT and DGT, was used to model the density, viscosity, and surface tension of glycols and DESs, and to predict the same properties for DES + water mixtures. This theoretical framework achieved average absolute relative deviations (AARDs) of 0.11%, 4.65%, and 0.49% for the density, viscosity, and surface tension of glycols and DESs, respectively, and 0.57%, 32.97%, and 15.03% for DES + water mixtures.

Increasing temperature, HBD content, and water content were found to decrease the density and viscosity of DESs. Meanwhile, surface tension decreases with temperature but increases with water content. Additionally, increasing the HBD chain length generally leads to lower density and surface tension but higher viscosity. However, DESs based on 12P deviate from this trend in terms of surface tension. This deviation is attributed to the molecular structure of 12P, where the two hydroxyl groups are closely positioned on a short apolar backbone. This configuration enhances interfacial activity, promoting accumulation at the interface and resulting in a stronger effect on surface tension, resembling the behavior of a surfactant. Furthermore, Bet-based DESs exhibit higher density and viscosity and lower surface tension than ChCl-based DESs.

MD simulations were performed to calculate the same properties for selected DESs and for all DES + water mixtures. These simulations supported the experimental observations through the analysis of hydrogen bonding, RDFs, SDFs, and CNs between DES components. The intricate mixing behavior observed in DES + water systems arises from a complex interplay of competitive hydrogen bonding and differing electrostatic affinities between the components. Water molecules compete with HBDs for interactions with the HBA, often disrupting the original HBA–HBD hydrogen-bonding network that stabilizes the DES structure. As water content increases, it can progressively displace HBD molecules around the HBA, leading to a partial or complete breakdown of the eutectic structure. Additionally, electrostatic interactions play a critical role: water exhibits strong affinity for highly polar or charged moieties such as chloride ions or the carboxylate group of betaine, further altering the microscopic arrangement of the system. This competition and preferential solvation result in non-ideal mixing behavior, structural reorganization, and the emergence of interfacial layering phenomena, as evidenced by the density profiles. Therefore, understanding both the macroscopic properties and the molecular-level interactions is essential for accurately describing DES–water systems and for enabling their effective design and application in industrial processes.

8. Separation of furfuryl alcohol from water using hydrophobic DESs

---

This chapter explores the separation of furfuryl alcohol from water using hydrophobic DESs, highlighting their potential as an environmentally friendly alternative to conventional volatile organic solvents. By examining three DES formulations — thymol + octanoic acid (1:2), menthol + octanoic acid (1:2), and thymol + menthol (1:1) — this work evaluates their efficacy in liquid-liquid extraction processes. Through experimental liquid-liquid equilibrium measurements, PC-SAFT modeling, and MD simulations, the study provides a comprehensive assessment of the separation performance, emphasizing the role of DES in sustainable chemical processes. This chapter highlights the synergy between experimental and predictive modeling approaches for optimizing solvent systems in the context of FA extraction.[*]

8.1. Introduction

Lignocellulosic biomass, especially from inedible agricultural sources, is a promising feedstock for obtaining chemical compounds using environmentally friendly processes. Furfuryl alcohol (FA) is an important organic product from biomass, mainly used to produce furan resins with varied properties, such as plasticizers, solvents, and sustainable aviation fuels (SAF) [352–355]. Furthermore, FA aqueous solutions are present in a wide range of industrial applications such as dyes, synthetic fibers, rubber, and pesticides [356, 357]. However, FA is considered environmentally unfriendly, may cause adverse human health effects, and forms oligomers in the aqueous phase, compromising the FA capability to be converted into valuable products [358]. Purifications, separations, and solvent recoveries determine the economic feasibility of the FA production processes. The isolation of this component is the main challenge in the production of new raw materials. Until now, steam stripping and liquid-liquid extraction with Volatile Organic Solvents (VOCs) have been the most commonly applied isolation methods [359–361]. Steam stripping is highly energy-intensive

---

[*] This chapter is adapted with permission from:
E. Cea-Klapp, A. F. Arroyo-Avirama, S. Ormazábal-Latorre, N. F. Gajardo-Parra, C. Pazo-Carballo, H. Quinteros-Lama, T. Marzialetti, C. Held, R. I. Canales, and J. M. Garrido, "Separation of furfuryl alcohol from water using hydrophobic deep eutectic solvents", Journal of Molecular Liquids **384**, 122232 (2023). Copyright 2023 Elsevier B.V.

and problematic due to the presence of an azeotrope [362]. The effectiveness of liquid-liquid extraction depends on the solvent selection. For a rational solvent selection, the following properties should be considered: distribution ratio, selectivity, density, recoverability, environmental impact, viscosity, toxicity, flammability, and thermal and chemical stability.

A few research studies have been published on separating FA from aqueous systems, and a scarce amount of hydrophobic extracting solvents have been reported. Some of the main solvents investigated for removing FA from aqueous solutions are: ethyl acetate, methyl isobutyl ketone, 2-furaldehyde, and 1-butanol [359]; methyl tert-butyl ether, isopropyl ether, methylene chloride, and 4-methyl-2-pentanol [360]; 1-pentanol and n-propyl acetate [361]. However, a systematic solvent selection and better insights into the thermodynamics of the separation are necessary for the optimal solvent choice. Moreover, recent research on new extracting agents is focused on pursuing safer and more environmentally friendly solvents that not only improve the selectivity of the target solute but are recyclable and support the sustainability of the process [363–365].

Hydrophobic DESs have recently received attention due to their ability to extract polar compounds from aqueous mixtures [366]. The application of hydrophobic DES as an extraction medium has been reported to extract flavonoids, phenolic acids, polyphenols, and other bioactive compounds from biomass [367]. The first hydrophobic DES was developed by the group led by Marrucho using menthol as HBA, and natural organic acids as HBD [368]. The extraction potential of these DESs was validated by recovering several model biomolecules from aqueous phases [369, 370]. Despite the number of possible DESs combinations being very large due to their tailor-made nature, the study of the thermodynamic properties of target DESs can help to use these mixtures in specific applications and understand their extraction mechanisms for generating greater affinity with the substances. Thus, studying the thermodynamic behavior of FA when mixed with water and a hydrophobic DES is essential for designing separation processes of biomass-derived molecules that have some affinity with water [369].

Predictive theoretical models are essential for reducing the experimental effort, especially when compounds studied present scarce physicochemical and thermodynamic information in the literature [371]. Methods such as MD simulations, classical thermodynamic models, and quantum chemical calculations are strong tools for performing such predictive calculations [365, 372]. Specifically, PC-SAFT can predict the physicochemical properties and phase equilibria of many compounds and mixtures by directly including molecular interactions. Also, Coarse-grained (CG) models have become increasingly popular as an alternative to all-atom models by enhancing the time scale of the simulation [373]. A significant increase in computational speed can be achieved by converting atomic clusters, also known as CG beads, into functional interaction sites. The Martini force field is considered one of the most well-known examples of a CG model [140]. This force field has been successfully utilized in research on several biologically significant systems[373], and more recently, in extraction using DESs [374] and ionic liquids [375]. The high applicability of Martini force fields can be attributed partly to the top-down process used to parameterize it; that is, matching thermodynamic parameters for providing a level of transferability [376]. Therefore, the common use of thermodynamic modeling with molecular dynamics generates the necessary information to study the properties of novel solvents such as DESs [28].

Unlike the ChCl- and betaine-based DESs discussed in previous chapters, terpene- and carboxylic acid-based DESs exhibit a hydrophobic character, making them particularly well-suited for use as extractants in aqueous systems. The primary objective of this chapter is to enhance the understanding of FA extraction from water using hydrophobic DESs. In this study, DESs based on menthol, thymol, and octanoic acid were selected as extractants. Thus, the LLE for the pseudo-ternary systems composed of water + FA + hydrophobic DES at 313.15 K and 101.13 kPa are presented as the model mixtures for the extraction process. The DESs considered in this work are thymol + octanoic acid (1:2), menthol + octanoic acid (1:2), and thymol + menthol (1:1). The extraction performance of DESs is compared in terms of partition coefficients, selectivities, and density profiles. PC-SAFT and MD coarse-grained simulations were used to model and simulate the LLE, respectively, to obtain an accurate description of the experimental results. This approach generates a platform for reducing experimental measurements using predicted thermophysical properties, which is helpful for further selecting solvents that could be candidates for the FA extraction process.

8.2. Experimental

8.2.1. Materials

The compounds for preparing hydrophobic DESs, such as thymol, l-menthol, and octanoic acid, were supplied by Acros Organics B.V.B.A., whereas FA was acquired from Sigma-Aldrich. All of them were used without an additional purification stage. Table 8.1 shows the specifications of each compound used in this study, such as molar mass, CAS number, source, and purity.

TABLE 8.1: Specifications of chemicals used in this work.

Compounds	**CAS**	**Supplier**	**Purity**
water	7732-18-5	Sigma Aldrich	LC-MS Grade
thymol	89-83-8	Acros Organics	≥99.0
l-menthol	2216-51-5	Acros Organics	≥99.5
octanoic acid	124-07-2	Acros Organics	≥99.0
furfuryl alcohol	98-00-0	Sigma Aldrich	≥98.0

8.2.2. Preparation of DESs

Each DES was prepared by mass using an analytical balance (Practum 224-1s Sartorius, Germany, uncertainty 0.1 mg). The components were added to a vial and quickly closed with a septum cap. The mixture was placed in a sonicator (iSonic P4862-IT, Australia) at 323.15 K until a homogeneous liquid was formed. The water content was measured using a Karl Fischer Coulometer (831KF Metrohm, Switzerland). The LLE measurements were set up immediately after the DESs preparation. Table 8.2 shows the components (HBA and HBD), the molar ratio (HBA:HBD), and the water content for each DES prepared in this work.

TABLE 8.2: Abbreviation, components, mole ratio, and water content (wt.%) of DES used in this work.

Abbreviation	**HBA**	**HBD**	**Mole ratio HBA:HBD**	**water content (wt.%)**
Thy:OctA(1:2)	thymol	octanoic acid	1:1.9969	0.190
Men:OctA(1:2)	l-menthol	octanoic acid	1:1.9992	0.441
Men:Thy(1:1)	l-menthol	thymol	1:0.9872	0.043

8.2.3. Liquid-liquid equilibrium measurements

LLE measurements were performed inside a homemade jacketed glass cell with known feed compositions. All the mixtures were prepared using an analytical balance (Sartorius Practum 224-1s, Germany) with an accuracy of 0.1 mg. A thermoregulated water circulator kept the temperature constant during the experiment, and an RTD platinum thermometer (VWR® Traceable®, ± 0.1 K) in the top of the cell, measured the temperature in the liquid mixture. The mixture was stirred inside the equilibrium cell with a magnetic bar and a stirring plate for 4 h, then settled for at least 12 h to reach two clear liquid phases. For each phase, approximately 0.5 mL samples were collected with a syringe, weighted, and dissolved with a known mass of ethanol before being analyzed.

The samples were analyzed with a volumetric Karl Fischer (Metrohm 870 KF Titrino plus) for determining the water content and a gas chromatograph (Shimadzu Nexis GC-2030) equipped with a flame ionization detector, split-splitless injector, and an Elite 1 capillary column 100% dimethyl polysiloxane (30 m × 0.53 mm × 3.0 μm) with a flow rate of 15 $\mathrm{cm^3 \cdot min^{-1}}$ of nitrogen used as carrier gas. The temperature program included an isothermal analysis at 370 K, which lasted 3 min. Then, the first ramp of 60 $\mathrm{K \cdot min^{-1}}$ was used to increase the temperature to 445.80 K, the second ramp of 0.1 $\mathrm{K \cdot min^{-1}}$ increased the temperature to 446.00 K, and the final ramp of 80.00 $\mathrm{K \cdot min^{-1}}$ brought the temperature up to 523.00 K. The standard external method was used to quantify the amount of each compound in the mixture. The analysis was performed at least three times for three samples taken from each liquid phase. A Nuclear Magnetic Resonance (NMR) study was done to study the possibility that DESs were present in the water-rich phase. A Bruker Advance 400 Mhz Spectrometer was used to perform the ^{1}H-NMR analyses (Massachusetts, USA). Before ^{1}H-NMR analysis, samples were dissolved in deuterated water.

8.3. Molecular modeling

8.3.1. PC-SAFT modeling

PC-SAFT has already been described in the previous Section 2.2. The parameters used in this chapter are shown in Table 8.3 and were mainly retrieved from the literature. The FA parameters were fitted in this work using experimental density and vapor pressure data from the literature [377, 378]. It was not necessary to use binary interaction parameters for the modeling approach, so the model is fully predictive.

TABLE 8.3: PC-SAFT molecular parameters used in this chapter. The [B, P, N] notation indicates the number of bivalent, positive, and negative association sites, respectively, as defined in Figure 2.2.

Compounds	M_w **[g/mol]**	m_i	σ_i **[Å]**	ε_i/k_B **[K]**	S^{Ai} **[B, P, N]**	ε^{AiBi}/k_B **[K]**	κ^{AiBi}	**Sources**
thymol	150.220	4.0120	3.8160	290.22	[0, 1, 1]	0.0616	1660.00	[47]
l-menthol	156.270	4.1520	3.9030	262.40	[0, 1, 1]	0.0996	1785.60	[47]
octanoic acid	144.210	7.0480	3.1360	234.36	[0, 1, 1]	0.0200	1889.20	[47]
furfuryl alcohol	98.100	4.3611	3.0048	218.34	[0, 1, 2]	0.1462	1834.33	This work
water	18.02	1.2046	$\sigma(T)^a$	353.95	[0, 1, 1]	2425.8	0.0451	[195]

^{a} Temperature-dependent function is given by σ [Å] $= 2.7927 + 10.11\exp(-0.01775\text{T[K]}) + 1.417\exp(-0.01146\text{T[K]})$.

8.3.2. Molecular dynamics details

Coarse-grained simulations of the liquid-liquid phase equilibrium were carried out at the same experimental conditions (313.15 K and 101.13 kPa). The simulations were carried out using the direct coexistence technique in the $NP_z\mathcal{A}T$ ensemble [379]. In this ensemble, the volume in the simulation box is varied by changing its z-dimension (L_z), with the z-axis chosen perpendicular to the planar liquid-liquid interface. At the same time, while the number of molecules (N), the normal pressure (P_z), interfacial area ($\mathcal{A} = L_x \times L_y$), and temperature ($T$) remain constant.

The initial configuration for each phase was generated independently using PACKMOL [267], placing molecules aleatory in a box with dimensions of $L_x = L_y = 8$ nm and $L_z \approx 10$ nm. The boxes are prepared using as initial values for composition the predictions obtained from the PC-SAFT calculation at the same thermodynamic conditions for each phase. Then an energy minimization using the steepest descent algorithm with 10000 steps was performed. After that, an equilibration routine in the $NP_z\mathcal{A}T$ ensemble using four different time steps, 1 fs, 2 fs, 10 fs, and 20 fs, was realized for 80 ns in total. This equilibration procedure has been utilized in the past for hydrophobic DES systems employing the Martini 3 force field [374]. When both phases were equilibrated, the inhomogeneous system was ensembled along the z direction, joining an aqueous phase at each interface with the DES-rich phase, as is shown in Figure 8.1. Subsequently, the same energy minimization and equilibration procedures were realized. Finally, the production was run for 1 μs in the $NP_z\mathcal{A}T$ ensemble with a time step of 20 fs, where the last 500 ns were used for statistical analysis.

All MD simulations were carried out using GROMACS version 2021.2 [310, 380], and the equations of motion were integrated using the leap-frog algorithm [142]. The cut-off radius for electrostatic and van der Waals interactions was set to 1.1 nm, and periodic boundary conditions were used in all directions. Electrostatic interactions were computed using the reaction-field approach [381]. A velocity rescaling thermostat [148] with a time constant of $\tau_T = 1$ ps was used to keep the system temperature constant. In the equilibration stage, the pressure was kept constant using the Berendsen barostat [147] with a time constant $\tau_P = 2$ ps. During the production, the Parrinello-Rahman barostat [151, 152] was used with a time constant $\tau_P = 12$ ps. The system was divided

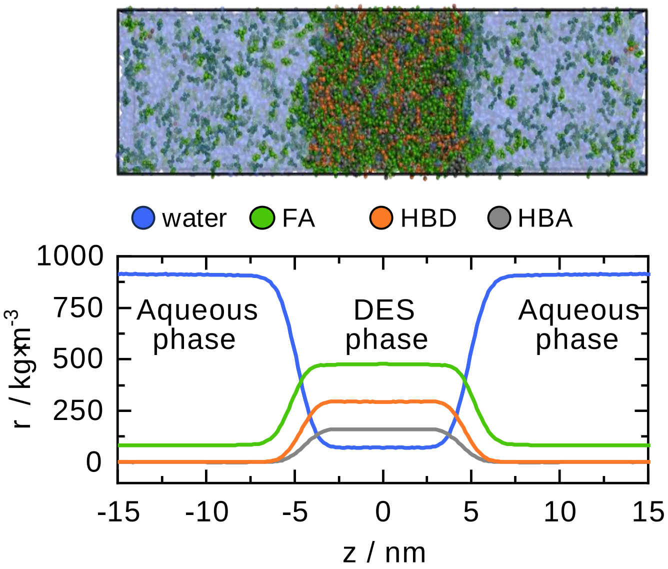

FIGURE 8.1: Density profile example for the system water + furfuryl alcohol + DES

TABLE 8.4: The logarithm of the water–octanol partition coefficients obtained with Martini 3 (log P_{MD}) and experimental data (log P_{Exp}) at 298.15 K and 101.13 kPa.

Compounds	log P_{MD}	log P_{Exp}	**Source**
menthol	3.02 ± 0.02	3.85 ± 0.11	[382]
octanoic acid	3.43 ± 0.03	3.03	[383]
thymol	2.76 ± 0.01	3.15 ± 0.09	[382]
furfuryl alcohol	0.64 ± 0.02	0.72 ± 0.02	This work [a]

[a] Standard uncertainties u are $u(T)$ = 0.05 K, $u(P)$ = 1 kPa. Relative standard uncertainty in our measure is $u_r(w_i)$= 0.06.

into 250 slabs along the z-axis to make the density profiles. The mass fraction in each phase was found by taking the average density profiles for each phase, as shown in Figure 8.1.

Martini 3 was used as the force field [140], and the parameters for each molecule are shown in the Appendix C (see Tables C.1 - C.8). The l-menthol parameters were retrieved from the work of Vainikka et al. [374], and the others were obtained following the strategy for small molecules proposed by Alessandri et al. [376]. Water-octanol partition coefficients (log P values) at 298.15 K were computed and compared to experimentally determined values to validate the new parameters, as shown in Table 8.4. The log P value for each simulated molecule was obtained using the thermodynamic integration described elsewhere [374].

8.4. Results

LLE data of water + FA + DES, measured at 313.15 K and 101.13 kPa, are shown in Table 8.5 and Figure 8.2 in mass fraction. As seen in Table 8.5, the DES-rich phase, for each water + DES system, contains a small amount of water (below 2 wt.%). Therefore, there is a wide miscibility gap between water and all the considered DESs, as shown in Figure 8.2, allowing the FA to separate at almost any initial condition of the FA + water mixture. In order to study the stability of the obtained solvents and to check that there is not a complete solubilization of HBD and HBA in the aqueous phase, a small amount for each system was analyzed by ^{1}H-NMR. The results in the Appendix C (see Figures C.2 - C.7) verify the stability and immiscibility of all solvents in water, detecting a negligible quantity of DESs in the water rich-phase for all the studied systems. It should be noted that the accuracy of the integrals for specific peaks, either of DESs or of starting compounds, is not high enough to determine the solubility quantitatively. As shown in Table 8.5, gradually adding FA grows its mass fraction in both phases. Also, the FA mass fraction in the DES-rich phase is significantly larger than in the aqueous phase. Therefore, a considerable immiscibility gap is reached as expected for extraction purposes. Thus, selected DESs can be an alternative to the organic solvents used in the literature. [359–361].

All the LLE systems were modeled with PC-SAFT with molecular parameters reported in Table 8.3. Cross-interaction parameters were not fit and PC-SAFT was used as a predictive tool. Results are presented in Figure 8.2, in which a qualitative description was obtained using PC-SAFT, where the model could reproduce the miscibility gap for all the systems under consideration. All the tie lines obtained from PC-SAFT are mainly parallel to the experimental one. Nevertheless, PC-SAFT predicts a phase separation between water and FA that has not been observed experimentally.

In addition, the results were complemented with MD simulations using the Martini 3 Coarse-Grained force field. Table 8.7 collects the MD results for the LLE for the water + FA + DES mixtures at the same experimental conditions. Those results are in good agreement with the experimental tie lines. However, an increasing excess of FA is observed in the DES-rich phase when the concentration of this solute is higher.

In order to assess the PC-SAFT and MD performances, the corresponding root-mean-square deviations (RMSD) values are calculated with Eq. (8.1).

$$\mathrm{RMSD} = \sqrt{\frac{\sum_{i=1}^{N}\left(w_i^{exp} - w_i^{cal}\right)^2}{N}} \tag{8.1}$$

where w_i^{exp} is the experimental mass fraction of each species, w_i^{cal} is the mass fraction calculated either with PC-SAFT or MD, and N is the compared number of points. All RMSD values were less than 0.05 (see Table 8.6). The lowest values were obtained with PC-SAFT, as also can be seen in Figure 8.2. However, the MD results are directly related to the initial configuration used, which could be improved iteratively to match the experimental tie line. These results support that the PC-SAFT EoS and Martini 3 force field adequately describe these systems.

TABLE 8.5: Experimental LLE data for the water + furfuryl alcohol + DES systems at 313.15 K and 101.13 kPa. The distribution coefficient, D, and selectivity, S, are calculated using Eqs. 8.2 and 8.3, respectively.

Tie	**DES-rich phase**			**Aqueous phase**				
line	w^{I}_{water}	w^{I}_{FA}	w^{I}_{DES}	w^{II}_{water}	w^{II}_{FA}	w^{II}_{DES}	D	S
DES: thymol + cctanoic acid (1:2)								
TLB	0.018	-	0.982	1.000	-	0.000	-	-
TL1	0.050	0.066	0.884	0.983	0.017	0.000	3.91	77.1
TL2	0.076	0.213	0.711	0.949	0.051	0.000	4.16	51.7
TL3	0.122	0.310	0.568	0.929	0.071	0.000	4.36	33.2
TL4	0.165	0.427	0.408	0.897	0.103	0.000	4.13	22.4
TL5	0.150	0.512	0.339	0.885	0.115	0.000	4.44	26.2
TL6	0.284	0.619	0.097	0.829	0.171	0.000	3.61	10.5
DES: menthol + octanoic acid (1:2)								
TLB	0.018	-	0.982	1.000	-	0.000	-	-
TL1	0.030	0.001	0.970	0.999	0.001	0.000	7.41	245.3
TL2	0.050	0.175	0.775	0.975	0.025	0.000	7.04	136.4
TL3	0.085	0.358	0.557	0.963	0.037	0.000	9.73	110.3
TL4	0.143	0.521	0.337	0.945	0.055	0.000	9.45	62.6
TL5	0.238	0.633	0.129	0.937	0.063	0.000	10.09	39.7
TL6	0.201	0.618	0.182	0.919	0.081	0.000	7.66	35.1
DES: menthol + thymol (1:1)								
TLB	0.021	-	0.979	1.000	-	0.000	-	-
TL1	0.030	0.050	0.920	0.987	0.014	0.000	3.70	121.5
TL2	0.042	0.138	0.821	0.978	0.022	0.000	6.17	144.4
TL3	0.060	0.242	0.698	0.970	0.030	0.000	8.07	131.6
TL4	0.098	0.332	0.570	0.962	0.038	0.000	8.70	85.7
TL5	0.140	0.463	0.397	0.961	0.039	0.000	11.87	81.5
TL6	0.234	0.543	0.223	0.926	0.074	0.000	7.34	29.1

[a] Standard uncertainties u are $u(T)$ = 0.05 K, $u(P)$ = 1 kPa. Relative standard uncertainties $u_r(w_i)$= 0.01.

[b] The w refers to the mass fraction and the superscripts I and II indicate the DES-rich phase and the aqueous phase.

TABLE 8.6: Root-mean-square deviations (RMSD) for the PC-SAFT EOS and MD calculations of the LLE of water + furfuryl alcohol + DES compared with experimental data.

DES	**RMSD$_{\text{PC-SAFT}}$**	**RMSD$_{\text{MD}}$**
Thy:OctA(1:2)	0.0227	0.0482
Men:OctA(1:2)	0.0208	0.0417
Men:Thy(1:1)	0.0187	0.0462

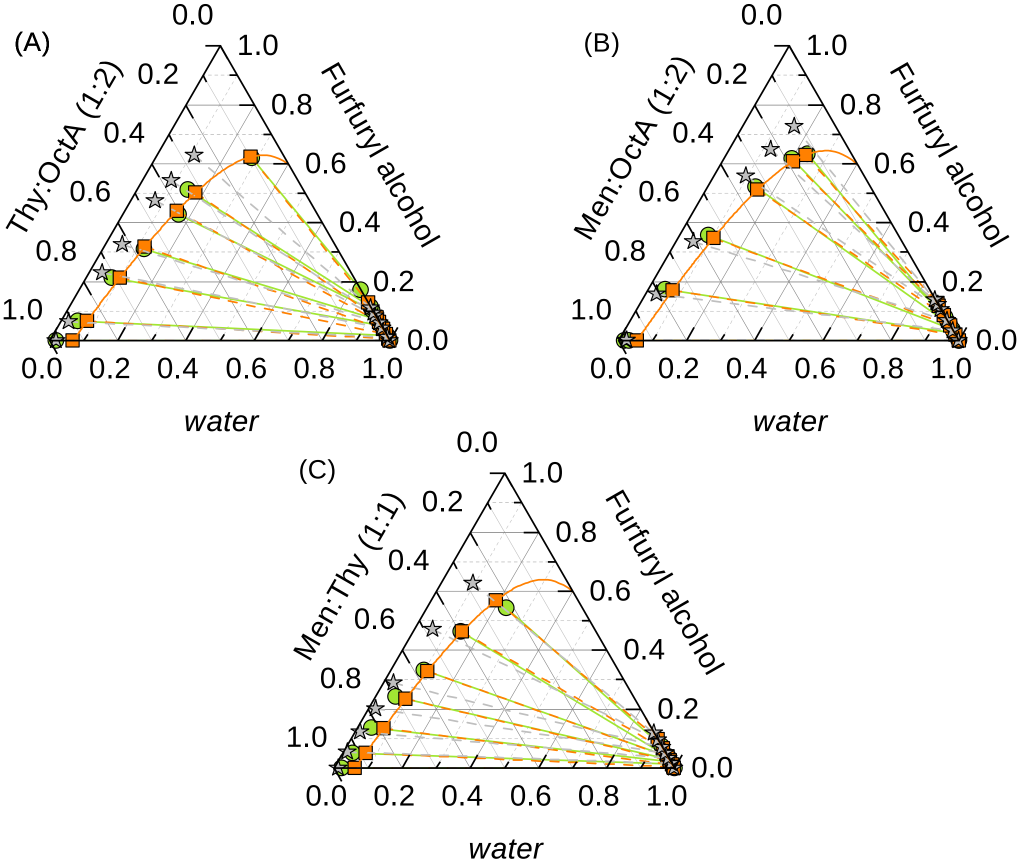

FIGURE 8.2: Phase diagram for the water + furfuryl alcohol + DES systems at 313.15 K and 101.13 kPa. DES: (A) Thy:OctA(1:2), (B) Men:OctA(1:2), and (C) Men:Thy(1:1). Circles: experimental data. Stars: MD simulation. Squares and solid lines: PC-SAFT calculations.

8.4.1. Distribution coefficient and selectivity

The distribution coefficient, D, and selectivity, S, are calculated using the mass fraction in the equilibrium with Eqs. 8.2 and 8.3, respectively.

$$D = w^{I}_{FA}/w^{II}_{FA} \tag{8.2}$$

$$S = \left(w^{I}_{FA}/w^{II}_{FA}\right) / \left(w^{I}_{\text{water}}/w^{II}_{\text{water}}\right) \tag{8.3}$$

Here, the superscripts I and II denote the DES-rich phase and the aqueous phase, while the subscripts stand either for FA or water.

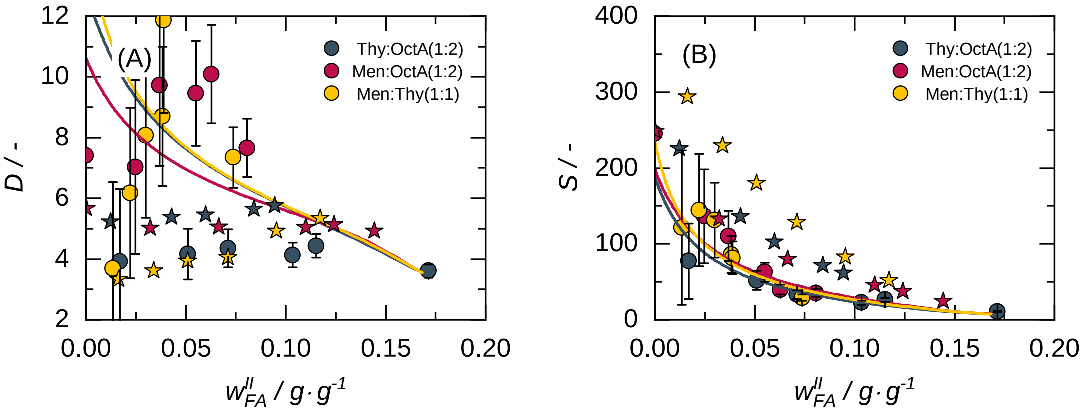

FIGURE 8.3: (A) Distribution coefficient and (B) Selectivity of furfuryl alcohol plotted against the mass fraction of furfuryl alcohol in the aqueous phase at 313.15 K and 101.13 kPa. Circles: experimental data. Stars: MD simulation. Solid lines: PC-SAFT calculations. Error bars are shown only for the experimental data, calculated using error propagation with a relative standard uncertainty of $u_r(w_i) = 0.01$.

Figure 8.3 shows the D and S values obtained from the experiments (also in Table 8.5), PC-SAFT, and MD simulations. PC-SAFT exhibits excellent agreement with experimental data, whereas the MD simulations slightly overestimate the selectivity. For all the systems, the values of D and S are greater than unity, reflecting the potential of the three hydrophobic DESs to extract FA from aqueous media. From the experimental data, it becomes clear that selectivity strongly decreases with increasing FA concentration. In contrast, distribution coefficients of FA are relatively constant upon increasing FA concentration. The maximum distribution coefficient is obtained by Men:Thy(1:1) at 3.9 wt% of FA in water. Thus, a cleaner raffinate of FA is achieved. At the same concentration, the trend is followed by Men:OctA(1:2) and Thy:OctA(1:2). From a thermodynamic point of view, PC-SAFT and MD results reveal that DESs are very appropriate for extracting FA from water at low FA concentrations. Overall, the predictions are consistent with the experimental values when considering the relatively high uncertainty in the data due to error propagation. Although the experimental values of the D are not matched precisely, the qualitative trend of the S is accurately captured.

TABLE 8.7: LLE data for water + furfuryl alcohol + DES systems at 313.15 K and 101.13 kPa from MD.

Tie	**DES-rich phase**			**Aqueous phase**				
line	w^{I}_{water}	w^{I}_{FA}	w^{I}_{DES}	w^{II}_{water}	w^{II}_{FA}	w^{II}_{DES}	D	S
				DES: Thymol + Octanoic acid (1:2)				
TLB	0.0187(1)	-	0.9813(1)	0.9983(1)	-	0.0017(1)	-	-
TL1	0.0229(1)	0.0654(1)	0.9117(1)	0.9855(2)	0.0125(1)	0.0020(1)	5.23(1)	225.2(7)
TL2	0.0378(1)	0.2307(1)	0.7315(1)	0.9553(2)	0.0429(1)	0.0018(1)	5.37(1)	135.9(2)
TL3	0.0498(1)	0.3264(1)	0.6238(1)	0.9380(2)	0.0598(3)	0.0022(1)	5.45(1)	102.8(2)
TL4	0.0718(1)	0.4744(2)	0.4538(2)	0.9138(4)	0.0842(2)	0.0020(1)	5.63(1)	71.7(2)
TL5	0.0848(1)	0.5440(1)	0.3712(1)	0.9037(5)	0.0945(3)	0.0018(1)	5.76(2)	61.3(2)
TL6	0.1091(1)	0.6299(1)	0.2610(1)	0.8856(4)	0.1122(3)	0.0022(1)	5.61(2)	45.6(1)
				DES: Menthol + Octanoic acid (1:2)				
TLB	0.0225(1)	-	0.9775(1)	0.9983(1)	-	0.0017(1)	-	-
TL1	0.0228(1)	0.0017(1)	0.9755(1)	0.9981(2)	0.0003(1)	0.0016(1)	5.67(6)	248.3(9)
TL2	0.0333(1)	0.1582(3)	0.8085(2)	0.9646(2)	0.0336(1)	0.0018(1)	4.71(1)	136.4(4)
TL3	0.0525(1)	0.3364(1)	0.6111(1)	0.9301(2)	0.0678(1)	0.0021(1)	4.96(1)	87.9(2)
TL4	0.0955(2)	0.5581(2)	0.3464(2)	0.8931(4)	0.1052(2)	0.0017(1)	5.31(1)	49.6(1)
TL5	0.1230(2)	0.6483(1)	0.2287(2)	0.8760(7)	0.1224(5)	0.0016(1)	5.30(2)	37.7(2)
TL6	0.1532(7)	0.7267(4)	0.1201(4)	0.8600(5)	0.1384(4)	0.0016(1)	5.25(1)	29.5(2)
				DES: Menthol + Thymol (1:1)				
TLB	0.0121(1)	-	0.9879(1)	0.9989(2)	-	0.0011(1)	-	-
TL1	0.0111(1)	0.0541(1)	0.9348(1)	0.9824(2)	0.0163(1)	0.0013(1)	3.32(1)	293.7(8)
TL2	0.0152(1)	0.1225(1)	0.8623(1)	0.9645(2)	0.0339(1)	0.0016(1)	3.61(1)	229.3(5)
TL3	0.0208(1)	0.2011(1)	0.7781(1)	0.9472(2)	0.0510(1)	0.0018(1)	3.94(1)	179.6(3)
TL4	0.0291(1)	0.2890(1)	0.6819(1)	0.9273(2)	0.0710(1)	0.0017(1)	4.07(1)	129.7(3)
TL5	0.0540(1)	0.4700(2)	0.4760(2)	0.9022(3)	0.0962(1)	0.0016(1)	4.89(1)	81.6(2)
TL6	0.0944(1)	0.6271(1)	0.2785(1)	0.8797(4)	0.1185(2)	0.0018(1)	5.29(1)	49.3(1)

The number in parentheses gives the uncertainty in the last digit; that is, 0.0187(1) means 0.0187 ± 0.0001.

The distribution coefficient and selectivity for FA with hydrophobic DESs and organic solvents used in the literature are compared in Figure 8.4. These parameters depend on the amount of FA, so the figure shows the range of values available. As shown in Figure 8.4A, hydrophobic DESs used in this work obtain the highest distribution coefficients, except for Thy:OctA(1:2), which behaves like the other organic solvents. Figure 8.4B shows that the highest selectivities are found for diisopropyl ether (DIPE) and methyl tertbutyl ether (MTBE). Nevertheless, the selectivity using DESs is comparable to that found in *n*-propyl acetate or ethyl acetate and superior to other traditional organic solvents, such as 1-pentanol and *n*-butanol. Even though selectivity and distribution coefficient are not the only variables affecting the process's efficiency, the results with hydrophobic DESs are promising. Indeed, these solvents could replace classical organic solvents due to their low costs and toxicity, making them suitable alternatives for separating FA.

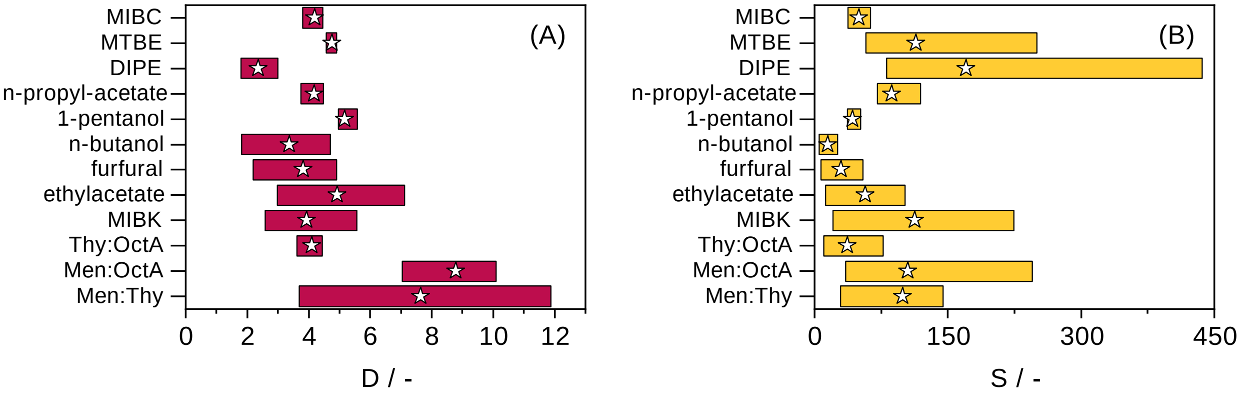

FIGURE 8.4: (a) Distribution coefficient and (b) selectivity of furfuryl alcohol compared to different solvents from the literature. The bars reflect the highest and minimum values reported, while the stars are the averages. Sources: methyl isobutyl ketone (MIBK), ethyl acetate, furfural, and 1-butanol from Wongsawa et al. at 298.2 K [359]; 1-pentanol and n-propyl acetate at 303.2 K, 313.2 K and 323.2 K from Han et al. [361]; diisopropyl ether (DIPE), methyl tert-butyl ether (MTBE), and methyl isobutylcarbinol (MIBC) at 298.2 K from Dong et al. [360].

8.4.2. Interfacial phenomena provided by the molecular dynamics

In addition to the mass fractions in the bulk phase, MD simulations provide a route to explore interfacial properties using the density profiles in the normal direction to the interface (ρ-z projections). Figure 8.5 shows the simulation results for FA density profiles for different amounts of FA according to Table 8.7. The results evidence surface activity or absolute adsorption of FA in the interfacial region. This surface activity is not exhibited for water and DES components. Figure 8.5 demonstrates that as the amount of FA increases, the maximum density decrease. When the surface activity of FA in different DES is compared, it is clear that Thy:Men(1:1) has the highest adsorption, while Thy:OctA(1:2) and Men:OctA(1:2) seem similar. The same trend is also found in the selectivity of FA using these solvents.

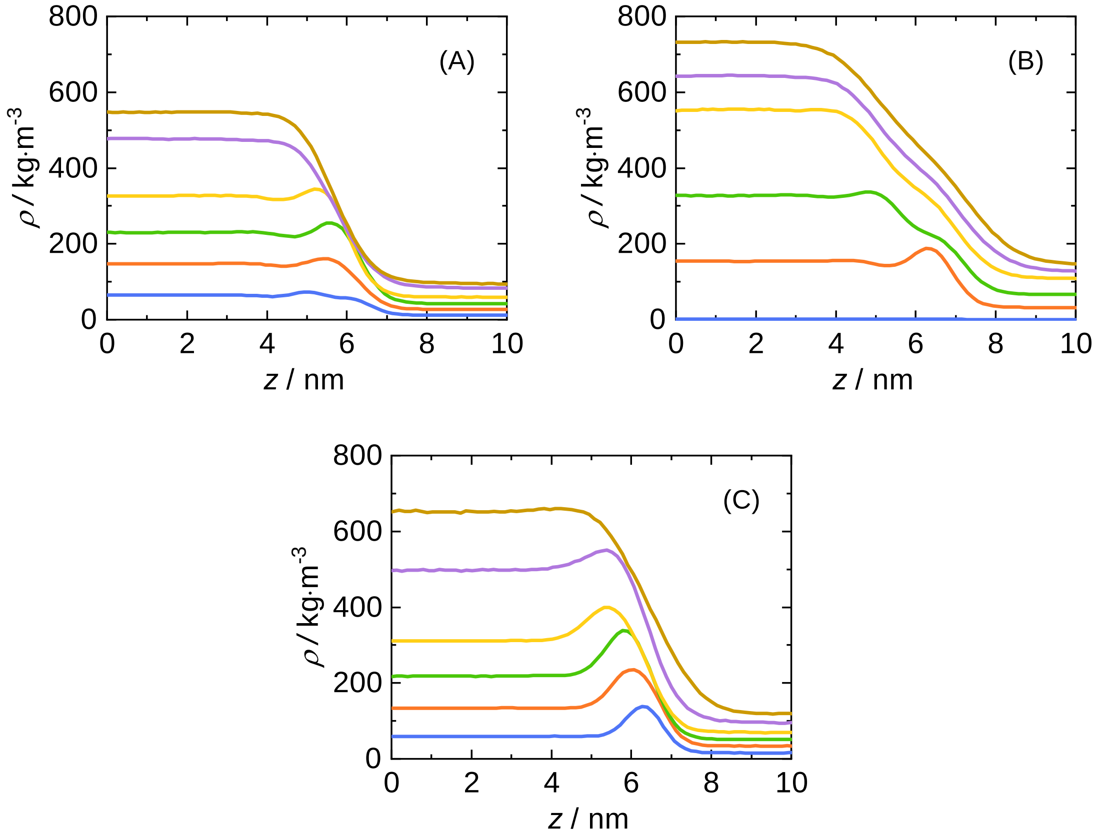

FIGURE 8.5: Furfuryl alcohol density profiles from Martini 3 simulations. Thy:OctA (A) , Men:OctA (B) and Men:Thy (C). Each simulated tie line is represented as follows: TL1 (—), TL2 (—), TL3 (—), TL4 (—), TL5 (—), TL6 (—).

In order to quantify the interfacial phenomena, the relative adsorption of FA to water can be expressed in terms of an integral equation, as shown in Eq. (8.4).

$$\Gamma_{FA}^{(W)} = -\left(\rho_{FA}^{I} - \rho_{FA}^{II}\right) \int_{-\infty}^{\infty} \left(\frac{\rho_W(z) - \rho_W^{I}}{\rho_W^{I} - \rho_W^{II}} - \frac{\rho_{FA}(z) - \rho_{FA}^{I}}{\rho_{FA}^{I} - \rho_{FA}^{II}} \right) dz \tag{8.4}$$

where $\rho_k(z)$, ρ_k^I, ρ_k^{II} represent the density profile, the density in the bulk (phase I and II) for a component k, where k can be water or FA.

Figure 8.6 demonstrates that mixtures with Men:Thy(1:1) have more FA in the interface than those with Thy:OctA(1:2) or Men:OctA(1:2). Also, it is possible to observe that with increases in the concentration of FA in water, the relative adsorption reaches a maximum value. The same behavior is displayed for all the systems. The maximum in the relative adsorption reflects two opposite effects related to interfacial width and the maximum density. When the concentration of FA in water increases, the interfacial width increases, allowing more FA in the interface. However, the maximum density in the interface decreases when the amount of FA in the aqueous phase increase.

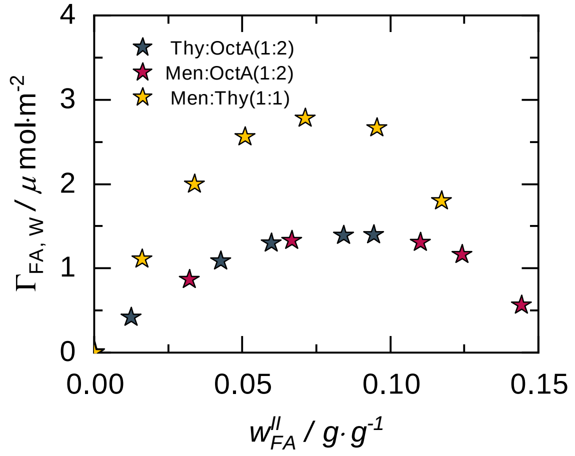

FIGURE 8.6: Relative adsorption of furfuryl alcohol with respect to water from Martini 3 simulations. Thy:OctA (★), Men:OctA (★), Men:Thy (☆).

8.5. Conclusion

In this work, the hydrophobic DESs Thy:OctA(1:2), Men:OctA(1:2), and Men:Thy(1:1) were investigated to extract FA from water at 313.15 K and 101.13 kPa. Three approaches were used: experimental LLE measurements, theoretical modeling with PC-SAFT, and MD with Martini 3. These three approaches have been applied to provide a complete and unified description of the liquid-liquid extraction process.

On the one hand, the experimental determination of the LLE displays that the selectivity of all the DESs presented in this work (e.g., Thy:OctA(1:2), Men:OctA(1:2), and Men:Thy(1:1)) has values comparable to those found in *n*-propyl acetate or ethyl acetate and superior to other traditional organic green solvents, such as 1-pentanol and *n*-butanol. On the other hand, high distribution coefficients were obtained for Men:OctA(1:2) and Men:Thy(1:1), whereas Thy:OctA(1:2) behaves like the other organic solvents in the literature. The combination of a molecular-based EoS (i.e., PC-SAFT) provides an adequate route to model the experimental data of ternary mixtures without interaction parameters. As a complement, MD simulations report moderate deviation for the LLE but complementarily to molecular-based calculations based on PC-SAFT. They allow us to describe the structure along the interfacial liquid-liquid region, providing some insights into the effectiveness of DES in process extraction. Indeed, MD simulations evidence a surface activity or absolute adsorption of FA in the interfacial region. When the surface activity of FA in different DES is compared, it is clear that Men:Thy(1:1) has the highest adsorption, correlated with the higher distribution coefficients and selectivities.

9. Conclusions and Outlook

9.1. Dissertation conclusions

Molecular modeling techniques have provided a powerful framework for understanding the thermodynamic and structural properties of DESs. In this thesis, the PC-SAFT EoS and MD simulations were successfully applied to predict and analyze DES behavior in both pure and mixed systems, offering valuable insights into their complex interactions. The work addressed both hydrophilic and hydrophobic DESs, primarily derived from green and bio-based components, providing novel insights into how cosolvent addition modulates their behavior in both bulk and interfacial regimes. The thesis not only expanded the application scope of PC-SAFT and MD but also generated new experimental data for validation, ultimately offering a multiscale framework that bridges molecular-level mechanisms with macroscopic thermodynamic predictions.

Initially, the study in Chapter 4 focused on evaluating the predictive capabilities of PC-SAFT using two common strategies: modeling DESs as pseudo-pure components or as mixtures of their precursors (the individual component approach). Through comparative analysis across multiple binary and ternary systems involving ChCl-based DESs, it was demonstrated that the pseudo-pure approach lacks the flexibility to account for the formation of new hydrogen-bonding interactions between cosolvents and DES constituents. In contrast, the individual component approach captured these effects more accurately, particularly in systems exhibiting strong cross-association, such as those with alcohols. This modeling insight was supported by analyses of excess volumes, excess enthalpies, and phase equilibria, where the individual component approach yielded superior agreement with experimental data.

Building on this foundation, a novel implementation of DGT was proposed to describe surface tension in DES systems using the PC-SAFT EoS in Chapter 5. This study introduced a hybrid treatment, previously used in the literature for ionic liquids, where PC-SAFT molecular parameters were applied to each DES precursor using the individual component approach for modeling the bulk phase, while the interface was treated using a pseudo-pure DES chemical potential derived from the molar contributions of the HBA and HBD. This method, which maintains thermodynamic consistency, enabled surface tension predictions with a single adjustable influence parameter, under the assumption that the molar ratio between HBA and HBD remains constant along the interface. This simplification allows the temperature dependence of surface tension to be described with a single adjustable parameter for most DESs with available experimental data, and also provides accurate predictions of the effects of solvent addition on surface tension.

The application of molecular dynamics simulations played a key role in elucidating the structural rearrangements induced by cosolvent addition. In particular, ChCl-based and betaine-based DESs mixed with methanol (in Chapter 6) or water (in Chapter 7) were investigated to understand the effects of hydrogen-bonding competition on macroscopic properties such as density, viscosity, and surface tension. MD simulations confirmed that cosolvents disrupt the internal hydrogen-bond network of DESs, leading to significant molecular reordering. This molecular reordering is especially pronounced in water-containing mixtures, where it becomes evident that the DES can be completely disrupted into its HBA and HBD components—essentially resulting in an aqueous solution of the individual constituents.

The thesis also included two chapters containing new experimental work. In Chapter 7, the density, viscosity, and surface tension of a wide range of hydrophilic DESs were measured across varying compositions, temperatures, and water contents. These data filled a gap in the literature, where previous measurements largely excluded water as a component, and also helped to validate the models used throughout the thesis. In Chapter 8, the first experimental LLE data for furfuryl alcohol extraction using hydrophobic DESs were reported. These DESs, based on menthol, thymol, and octanoic acid, were selected for their sustainability and potential relevance in green separation processes. Notably, both PC-SAFT and coarse-grained MD simulations (using the MARTINI 3 force field) showed excellent agreement with the LLE data, demonstrating the applicability of the modeling framework to complex, water-immiscible systems.

Across all chapters, PC-SAFT consistently provided a robust description of bulk-phase behavior and interfacial properties, while MD simulations offered molecular-level insights unattainable through the EoS alone. The integration of these methods enabled both accurate property prediction and a deeper mechanistic understanding of DES systems. This multiscale approach marks a significant step forward in the predictive modeling of DESs and their mixtures with cosolvents. Overall, this thesis advances the state of the art in DES thermodynamics by integrating novel experimental data, rigorous thermodynamic modeling, and molecular simulations. It establishes a validated, flexible, and scalable framework for investigating DES systems relevant to sustainable chemical processes, particularly under conditions where experimental measurements are limited or challenging.

9.2. Outlook

While the approaches applied in this thesis have significantly advanced the understanding and predictive modeling of DESs, several promising directions remain for future research. One such avenue is the integration of machine learning (ML) techniques into the parameterization and refinement of molecular-based models such as PC-SAFT. Data-driven strategies can uncover structure–property relationships across a wider spectrum of DESs, particularly in systems with limited experimental data. In this regard, the high-quality experimental data generated in this work offers a reliable foundation for training ML models, which critically depend on consistent and accurate datasets. Furthermore, ML-assisted parameter estimation could streamline model calibration, enabling faster and more robust screening of novel DES formulations.

Another opportunity lies in bridging molecular-level modeling with process-scale applications. The thermodynamic and structural insights gained from PC-SAFT and MD simulations provide a sound basis for designing DES-based separation processes. However, this translation requires the evaluation of additional properties relevant to process design—such as phase equilibria, transport properties (e.g., diffusivity and thermal conductivity), and separation metrics like selectivity and regeneration energy. These properties can be obtained through advanced molecular simulations or estimated via validated empirical correlations.

Coupling thermodynamic models with process simulation tools (e.g., Aspen Plus or gPROMS) would further enable the evaluation of DESs under realistic process conditions, allowing for comprehensive techno-economic and environmental assessments. This integration would bridge the gap between molecular insights and industrial implementation, facilitating the rational design and optimization of DESs for targeted applications.

Continued refinement of thermodynamic models, molecular simulations, and experimental validation strategies will be essential to fully realize the potential of DESs as sustainable, tunable, and high-performance solvents for green chemical processes.

Bibliography

[1] E. David and V.-C. Niculescu, “Volatile Organic Compounds (VOCs) as Environmental Pollutants: Occurrence and Mitigation Using Nanomaterials”, International Journal of Environmental Research and Public Health **18**, 13147 (2021).

[2] Y. Xiong, K. Du, and Y. Huang, “One-third of global population at cancer risk due to elevated volatile organic compounds levels”, npj Climate and Atmospheric Science **7**, 54 (2024).

[3] N. Winterton, “The green solvent: a critical perspective”, Clean Technologies and Environmental Policy **23**, 2499–2522 (2021).

[4] M. C. Bubalo, S. Vidović, I. R. Redovniković, and S. Jokić, “Green solvents for green technologies”, Journal of Chemical Technology & Biotechnology **90**, 1631–1639 (2015).

[5] L. I. Tomé, V. Baião, W. d. Silva, and C. M. Brett, “Deep eutectic solvents for the production and application of new materials”, English, Applied Materials Today **10**, 30–50 (2018).

[6] A. P. Abbott, G. Capper, D. L. Davies, R. K. Rasheed, and V. Tambyrajah, “Novel solvent properties of choline chloride/urea mixtures”, Chemical Communications **0**, 1st DES paper, 70–71 (2002).

[7] A. P. Abbott, G. Capper, K. J. McKenzie, and K. S. Ryder, “Electrodeposition of zinc–tin alloys from deep eutectic solvents based on choline chloride”, Journal of Electroanalytical Chemistry **599**, 288–294 (2007).

[8] B. B. Hansen, S. Spittle, B. Chen, D. Poe, Y. Zhang, J. M. Klein, A. Horton, L. Adhikari, T. Zelovich, B. W. Doherty, B. Gurkan, E. J. Maginn, A. Ragauskas, M. Dadmun, T. A. Zawodzinski, G. A. Baker, M. E. Tuckerman, R. F. Savinell, and J. R. Sangoro, “Deep Eutectic Solvents: A Review of Fundamentals and Applications”, Chemical Reviews **121**, 1232–1285 (2021).

[9] D. O. Abranches and J. A. Coutinho, “Everything You Wanted to Know about Deep Eutectic Solvents but Were Afraid to Be Told”, Annual Review of Chemical and Biomolecular Engineering **14**, 141–163 (2023).

[10] A. T. N. Fajar, T. Hanada, A. D. Hartono, and M. Goto, “Estimating the phase diagrams of deep eutectic solvents within an extensive chemical space”, Communications Chemistry **7**, 27 (2024).

[11] L. d. V. Engelbrecht, N. Cibotariu, X. Ji, A. Laaksonen, and F. Mocci, “Deep Eutectic Solvents Meet Non-Aqueous Cosolvents: A Modeling and Simulation Perspective-A Tutorial Review”, Journal of Chemical & Engineering Data **70**, 19–43 (2025).

[12] M. Zdanowicz, K. Wilpiszewska, and T. Spychaj, “Deep eutectic solvents for polysaccharides processing. A review”, Carbohydrate Polymers **200**, 361–380 (2018).

[13] T. E. Achkar, H. Greige-Gerges, and S. Fourmentin, "Basics and properties of deep eutectic solvents: a review", Environmental Chemistry Letters **19**, 3397–3408 (2021).

[14] A. Kovács, E. C. Neyts, I. Cornet, M. Wijnants, and P. Billen, "Modeling the Physicochemical Properties of Natural Deep Eutectic Solvents", ChemSusChem **13**, 3789–3804 (2020).

[15] N. F. Gajardo-Parra, V. P. Cotroneo-Figueroa, P. Aravena, V. Vesovic, and R. I. Canales, "Viscosity of Choline Chloride-Based Deep Eutectic Solvents: Experiments and Modeling", Journal of Chemical & Engineering Data **65**, 5581–5592 (2020).

[16] A. A. Quintana, A. M. Sztapka, V. d. C. S. Ebinuma, and C. Agatemor, "Enabling Sustainable Chemistry with Ionic Liquids and Deep Eutectic Solvents: A Fad or the Future?", Angewandte Chemie International Edition **61**, e202205609 (2022).

[17] J. A. Sirviö, M. Visanko, and H. Liimatainen, "Deep eutectic solvent system based on choline chloride-urea as a pre-treatment for nanofibrillation of wood cellulose", Green Chemistry **17**, 3401–3406 (2015).

[18] S. Xia, G. A. Baker, H. Li, S. Ravula, and H. Zhao, "Aqueous ionic liquids and deep eutectic solvents for cellulosic biomass pretreatment and saccharification", RSC Advances **4**, 10586–10596 (2013).

[19] J. G. Lynam, N. Kumar, and M. J. Wong, "Deep eutectic solvents' ability to solubilize lignin, cellulose, and hemicellulose; thermal stability; and density", Bioresource Technology **238**, 684–689 (2017).

[20] K. H. Kim, T. Dutta, J. Sun, B. Simmons, and S. Singh, "Biomass pretreatment using deep eutectic solvents from lignin derived phenols", Green Chemistry **20**, 809–815 (2018).

[21] A. F. Arroyo-Avirama, S. Ormazábal-Latorre, R. Jogi, N. F. Gajardo-Parra, C. Pazo-Carballo, M. Ascani, P. Virtanen, J. M. Garrido, C. Held, P. Mäki-Arvela, and R. I. Canales, "Improving the separation of guaiacol from n-hexane by adding choline chloride to glycol extracting agents", Journal of Molecular Liquids **355**, 118936 (2022).

[22] D. Smink, S. R. Kersten, and B. Schuur, "Process development for biomass delignification using deep eutectic solvents. Conceptual design supported by experiments", Chemical Engineering Research and Design **164**, 86–101 (2020).

[23] B. Wu, R. Lin, R. O'Shea, C. Deng, K. Rajendran, and J. D. Murphy, "Production of advanced fuels through integration of biological, thermo-chemical and power to gas technologies in a circular cascading bio-based system", Renewable and Sustainable Energy Reviews **135**, 110371 (2021).

[24] P. Kalhor and K. Ghandi, "Deep Eutectic Solvents for Pretreatment, Extraction, and Catalysis of Biomass and Food Waste", Molecules **24**, 4012 (2019).

[25] N. F. Gajardo-Parra, L. Meneses, A. R. C. Duarte, A. Paiva, and C. Held, "Assessing the Influence of Betaine-Based Natural Deep Eutectic Systems on Horseradish Peroxidase", ACS Sustainable Chemistry & Engineering **10**, 12873–12881 (2022).

[26] Y. He, Q. Huang, and P. Wang, "Design and evaluation of novel bio-based deep eutectic solvents for highly efficient bioproduction of chiral aryl alcohol", Journal of Chemical Technology & Biotechnology **95**, 1980–1988 (2020).

[27] J. O. Airouyuwa, H. Mostafa, A. Riaz, C. Stathopoulos, and S. Maqsood, "Natural Deep Eutectic Solvents and Microwave-Assisted Green Extraction for Efficient Recovery of Bioactive

Compounds from By-Products of Date Fruit (Phoenix dactylifera L.) Processing: Modeling, Optimization, and Phenolic Characterization", Food and Bioprocess Technology **16**, 824–843 (2023).

[28]G. Yu, N. F. Gajardo-Parra, M. Chen, B. Chen, G. Sadowski, and C. Held, "Aromatic volatile organic compounds absorption with phenyl-based deep eutectic solvents: A molecular thermodynamics and dynamics study", AIChE Journal **69**, `10.1002/aic.18053` (2023).

[29]R. B. Leron and M.-H. Li, "Solubility of carbon dioxide in a choline chloride–ethylene glycol based deep eutectic solvent", Thermochimica Acta **551**, 14–19 (2013).

[30]L. F. Zubeir, D. J. G. P. v. Osch, M. A. A. Rocha, F. Banat, and M. C. Kroon, "Carbon Dioxide Solubilities in Decanoic Acid-Based Hydrophobic Deep Eutectic Solvents", Journal of Chemical & Engineering Data **63**, 913–919 (2018).

[31]L. L. Sze, S. Pandey, S. Ravula, S. Pandey, H. Zhao, G. A. Baker, and S. N. Baker, "Ternary Deep Eutectic Solvents Tasked for Carbon Dioxide Capture", ACS Sustainable Chemistry & Engineering **2**, Carbon Dioxide Capture, 2117–2123 (2014).

[32]J. Hoppe, E. Byzia, M. Szymańska, R. Drozd, and M. Smiglak, "Acceleration of lactose hydrolysis using beta-galactosidase and deep eutectic solvents", Food Chemistry **384**, 132498 (2022).

[33]S. Li, Y. Deng, J. Peng, G. Liu, Z. Zhao, Z. Wei, Y. Zhang, X. Tang, P. Li, L. Hou, P. Zhou, and M. Zhang, "Design of functional glycerol-based deep eutectic solvents as reaction media for enzymatic deacidification of high-acid rice bran oil", Biochemical Engineering Journal **177**, 108257 (2022).

[34]M. G. Morán-Aguilar, M. Calderón-Santoyo, R. P. d. S. Oliveira, M. G. Aguilar-Uscanga, and J. M. Domínguez, "Deconstructing sugarcane bagasse lignocellulose by acid-based deep eutectic solvents to enhance enzymatic digestibility", Carbohydrate Polymers **298**, 120097 (2022).

[35]L. Meneses, N. F. Gajardo-Parra, E. Cea-Klapp, J. M. Garrido, C. Held, A. R. Duarte, and A. Paiva, "Improving the activity of horseradish peroxidase in betaine-based natural deep eutectic systems", RSC Sustainability **1**, Cited by: 9; All Open Access, Gold Open Access, 886–897 (2023).

[36]N. F. Gajardo-Parra, G. Rodríguez, A. F. Arroyo-Avirama, A. Veliju, T. Happe, R. I. Canales, G. Sadowski, and C. Held, "Impact of Deep Eutectic Solvents on Kinetics and Folding Stability of Formate Dehydrogenase", Processes **11**, 2815 (2023).

[37]G. R. Jenkin, A. Z. Al-Bassam, R. C. Harris, A. P. Abbott, D. J. Smith, D. A. Holwell, R. J. Chapman, and C. J. Stanley, "The application of deep eutectic solvent ionic liquids for environmentally-friendly dissolution and recovery of precious metals", Minerals Engineering **87**, 18–24 (2016).

[38]P. Cen, K. Spahiu, M. S. Tyumentsev, and M. R. S. J. Foreman, "Metal extraction from a deep eutectic solvent, an insight into activities", Physical Chemistry Chemical Physics **22**, 11012–11024 (2020).

[39]D. O. Abranches, M. Larriba, L. P. Silva, M. Melle-Franco, J. F. Palomar, S. P. Pinho, and J. A. Coutinho, "Using COSMO-RS to design choline chloride pharmaceutical eutectic solvents", Fluid Phase Equilibria **497**, 71–78 (2019).

[40]S. Emami and A. Shayanfar, "Deep eutectic solvents for pharmaceutical formulation and drug delivery applications", Pharmaceutical Development and Technology **25**, 779–796 (2020).

[41]M. H. Zainal-Abidin, M. Hayyan, G. C. Ngoh, W. F. Wong, and C. Y. Looi, "Emerging frontiers of deep eutectic solvents in drug discovery and drug delivery systems", Journal of Controlled Release **316**, 168–195 (2019).

[42] R. Abedin, S. Heidarian, J. C. Flake, and F. R. Hung, "Computational Evaluation of Mixtures of Hydrofluorocarbons and Deep Eutectic Solvents for Absorption Refrigeration Systems", Langmuir **33**, 11611–11625 (2017).

[43] R. Haghbakhsh, H. Peyrovedin, S. Raeissi, A. R. C. Duarte, and A. Shariati, "Energy Conservation in Absorption Refrigeration Cycles Using DES as a New Generation of Green Absorbents", Entropy **22**, 409 (2020).

[44] D. Deng, X. Duan, B. Gao, C. Zhang, X. Deng, and L. Gong, "Efficient and reversible absorption of NH 3 by functional azole–glycerol deep eutectic solvents", New Journal of Chemistry **43**, 11636–11642 (2019).

[45] A. P. Abbott, D. Boothby, G. Capper, D. L. Davies, and R. K. Rasheed, "Deep Eutectic Solvents Formed between Choline Chloride and Carboxylic Acids: Versatile Alternatives to Ionic Liquids", Journal of the American Chemical Society **126**, 9142–9147 (2004).

[46] D. O. Abranches, M. A. R. Martins, L. P. Silva, N. Schaeffer, S. P. Pinho, and J. A. P. Coutinho, "Phenolic hydrogen bond donors in the formation of non-ionic deep eutectic solvents: the quest for type V DES", Chemical Communications **55**, 10253–10256 (2019).

[47] M. A. R. Martins, E. A. Crespo, P. V. A. Pontes, L. P. Silva, M. Bülow, G. J. Maximo, E. A. C. Batista, C. Held, S. P. Pinho, and J. A. P. Coutinho, "Tunable Hydrophobic Eutectic Solvents Based on Terpenes and Monocarboxylic Acids", ACS Sustainable Chemistry & Engineering **6**, 8836–8846 (2018).

[48] A. Paiva, R. Craveiro, I. Aroso, M. Martins, R. L. Reis, and A. R. C. Duarte, "Natural Deep Eutectic Solvents – Solvents for the 21st Century", ACS Sustainable Chemistry & Engineering **2**, 1063–1071 (2014).

[49] X. Meng, K. Ballerat-Busserolles, P. Husson, and J.-M. Andanson, "Impact of water on the melting temperature of urea + choline chloride deep eutectic solvent", New Journal of Chemistry **40**, 4492–4499 (2016).

[50] C. Ma, A. Laaksonen, C. Liu, X. Lu, and X. Ji, "The peculiar effect of water on ionic liquids and deep eutectic solvents", Chemical Society Reviews **47**, 8685–8720 (2018).

[51] Y. Chen, D. Yu, W. Chen, L. Fu, and T. Mu, "Water absorption by deep eutectic solvents", Physical Chemistry Chemical Physics **21**, 2601–2610 (2019).

[52] D. Frenkel, *Understanding Molecular Simulation* (2002).

[53] M. P. Allen and D. J. Tildesley, *Computer Simulation of Liquids* (Oxford University Press, 2017).

[54] H. Wang, S. Liu, Y. Zhao, J. Wang, and Z. Yu, "Insights into the Hydrogen Bond Interactions in Deep Eutectic Solvents Composed of Choline Chloride and Polyols", ACS Sustainable Chemistry & Engineering **7**, 7760–7767 (2019).

[55] S. L. Perkins, P. Painter, and C. M. Colina, "Molecular Dynamic Simulations and Vibrational Analysis of an Ionic Liquid Analogue", The Journal of Physical Chemistry B **117**, 10250–10260 (2013).

[56] H. S. Salehi, M. Ramdin, O. A. Moultos, and T. J. Vlugt, "Computing solubility parameters of deep eutectic solvents from Molecular Dynamics simulations", Fluid Phase Equilibria **497**, 10–18 (2019).

[57] M. Shehata, A. Unlu, U. Sezerman, and E. Timucin, "Lipase and Water in a Deep Eutectic Solvent: Molecular Dynamics and Experimental Studies of the Effects of Water-In-Deep Eutectic Solvents on Lipase Stability", The Journal of Physical Chemistry B **124**, 8801–8810 (2020).

[58]M. Atilhan and S. Aparicio, “Molecular dynamics study on the use of Deep Eutectic Solvents for Enhanced Oil Recovery”, Journal of Petroleum Science and Engineering **209**, 109953 (2022).

[59]P. K. Naik, S. Paul, and T. Banerjee, “Physiochemical Properties and Molecular Dynamics Simulations of Phosphonium and Ammonium Based Deep Eutectic Solvents”, Journal of Solution Chemistry **48**, 1046–1065 (2019).

[60]C. R. Ashworth, R. P. Matthews, T. Welton, and P. A. Hunt, “Doubly ionic hydrogen bond interactions within the choline chloride–urea deep eutectic solvent”, Physical Chemistry Chemical Physics **18**, 18145–18160 (2016).

[61]L. F. Zubeir, C. Held, G. Sadowski, and M. C. Kroon, “PC-SAFT Modeling of CO2 Solubilities in Deep Eutectic Solvents”, The Journal of Physical Chemistry B **120**, 2300–2310 (2016).

[62]C. H. Dietz, D. J. v. Osch, M. C. Kroon, G. Sadowski, M. v. S. Annaland, F. Gallucci, L. F. Zubeir, and C. Held, “PC-SAFT modeling of CO2 solubilities in hydrophobic deep eutectic solvents”, Fluid Phase Equilibria **448**, 94–98 (2017).

[63]J. Lloret, L. Vega, and F. Llovell, “Accurate description of thermophysical properties of Tetraalkylammonium Chloride Deep Eutectic Solvents with the soft-SAFT equation of state”, Fluid Phase Equilibria **448**, 81–93 (2017).

[64]R. M. Ojeda and F. Llovell, “Soft-SAFT Transferable Molecular Models for the Description of Gas Solubility in Eutectic Ammonium Salt-Based Solvents”, Journal of Chemical & Engineering Data **63**, 2599–2612 (2018).

[65]J. D. v. d. Waals, *On the continuity of the gaseous and liquid states*, English, edited by J. S. Rowlinson, van der Waals’ Thesis (1873) (Dover Publications, Mineola, New York, 2004).

[66]O. Redlich and J. N. S. Kwong, “On the Thermodynamics of Solutions. V. An Equation of State. Fugacities of Gaseous Solutions.”, Chemical Reviews **44**, 233–244 (1949).

[67]G. Soave, “Equilibrium constants from a modified Redlich-Kwong equation of state”, Chemical Engineering Science **27**, 1197–1203 (1972).

[68]D.-Y. Peng and D. B. Robinson, “A New Two-Constant Equation of State”, Industrial & Engineering Chemistry Fundamentals **15**, 59–64 (1976).

[69]J. O. Valderrama, “The State of the Cubic Equations of State”, Industrial & Engineering Chemistry Research **42**, 1603–1618 (2003).

[70]W. G. Chapman, K. E. Gubbins, G. Jackson, and M. Radosz, “New reference equation of state for associating liquids”, Industrial & Engineering Chemistry Research **29**, 1709–1721 (1990).

[71]W. G. Chapman, G. Jackson, and K. E. Gubbins, “Phase equilibria of associating fluids”, Molecular Physics **65**, 1057–1079 (1988).

[72]W. Chapman, K. Gubbins, G. Jackson, and M. Radosz, “SAFT: Equation-of-state solution model for associating fluids”, Fluid Phase Equilibria **52**, 31–38 (1989).

[73]G. Jackson, W. G. Chapman, and K. E. Gubbins, “Phase equilibria of associating fluids”, Molecular Physics **65**, 1–31 (1988).

[74]M. S. Wertheim, “Fluids with highly directional attractive forces. I. Statistical thermodynamics”, Journal of Statistical Physics **35**, 19–34 (1984).

[75]M. S. Wertheim, “Fluids with highly directional attractive forces. II. Thermodynamic perturbation theory and integral equations”, Journal of Statistical Physics **35**, 35–47 (1984).

[76]M. S. Wertheim, “Fluids with highly directional attractive forces. III. Multiple attraction sites”, Journal of Statistical Physics **42**, 459–476 (1986).

[77] M. S. Wertheim, “Fluids with highly directional attractive forces. IV. Equilibrium polymerization”, Journal of Statistical Physics **42**, 477–492 (1986).

[78] G. I. Economou, “Statistical Associating Fluid Theory: A Successful Model for the Calculation of Thermodynamic and Phase Equilibrium Properties of Complex Fluid Mixtures”, Industrial & Engineering Chemistry Research **41**, 953–962 (2002).

[79] G. M. Kontogeorgis and I. G. Economou, “Equations of state: From the ideas of van der Waals to association theories”, The Journal of Supercritical Fluids **55**, 421–437 (2010).

[80] S. H. Huang and M. Radosz, “Equation of state for small, large, polydisperse, and associating molecules”, Industrial & Engineering Chemistry Research **29**, 2284–2294 (1990).

[81] S. H. Huang and M. Radosz, “Equation of state for small, large, polydisperse, and associating molecules: extension to fluid mixtures”, Industrial & Engineering Chemistry Research **30**, 1994–2005 (1991).

[82] A. Galindo, L. A. Davies, A. Gil-Villegas, and G. Jackson, “The thermodynamics of mixtures and the corresponding mixing rules in the SAFT-VR approach for potentials of variable range”, Molecular Physics **93**, 241–252 (1998).

[83] A. Gil-Villegas, A. Galindo, P. J. Whitehead, S. J. Mills, G. Jackson, and A. N. Burgess, “Statistical associating fluid theory for chain molecules with attractive potentials of variable range”, The Journal of Chemical Physics **106**, 4168–4186 (1997).

[84] T. Lafitte, A. Apostolakou, C. Avendaño, A. Galindo, C. S. Adjiman, E. A. Müller, and G. Jackson, “Accurate statistical associating fluid theory for chain molecules formed from Mie segments”, The Journal of Chemical Physics **139**, 154504 (2013).

[85] F. J. Blas and L. F. Vega, “Thermodynamic behaviour of homonuclear and heteronuclear Lennard-Jones chains with association sites from simulation and theory”, Molecular Physics **92**, 135–150 (1997).

[86] F. J. Blas and L. F. Vega, “Prediction of Binary and Ternary Diagrams Using the Statistical Associating Fluid Theory (SAFT) Equation of State”, Industrial & Engineering Chemistry Research **37**, 660–674 (1998).

[87] J. Gross and G. Sadowski, “Perturbed-Chain SAFT: An Equation of State Based on a Perturbation Theory for Chain Molecules”, English, Industrial & Engineering Chemistry Research **40**, 1244–1260 (2001).

[88] J. Gross and G. Sadowski, “Application of the Perturbed-Chain SAFT Equation of State to Associating Systems”, Industrial & Engineering Chemistry Research **41**, 5510–5515 (2002).

[89] N. v. Solms, M. L. Michelsen, and G. M. Kontogeorgis, “Computational and Physical Performance of a Modified PC-SAFT Equation of State for Highly Asymmetric and Associating Mixtures”, Industrial & Engineering Chemistry Research **42**, 1098–1105 (2003).

[90] I. Polishuk, “Standardized Critical Point-Based Numerical Solution of Statistical Association Fluid Theory Parameters: The Perturbed Chain-Statistical Association Fluid Theory Equation of State Revisited”, Industrial & Engineering Chemistry Research **53**, 14127–14141 (2014).

[91] S. P. Tan, H. Adidharma, and M. Radosz, “Recent Advances and Applications of Statistical Associating Fluid Theory”, Industrial & Engineering Chemistry Research **47**, 8063–8082 (2008).

[92] E. A. Müller and K. E. Gubbins, “Molecular-Based Equations of State for Associating Fluids: A Review of SAFT and Related Approaches”, Industrial & Engineering Chemistry Research **40**, 2193–2211 (2001).

[93] C. McCabe and A. Galindo, "Applied Thermodynamics of Fluids", *Applied thermodynamics of fluids* (The Royal Society of Chemistry, 2010), 215–279.

[94] X. Ji, C. Held, and G. Sadowski, "Modeling imidazolium-based ionic liquids with ePC-SAFT", Fluid Phase Equilibria **335**, 64–73 (2012).

[95] C. Held, T. Reschke, R. Müller, W. Kunz, and G. Sadowski, "Measuring and modeling aqueous electrolyte/amino-acid solutions with ePC-SAFT", The Journal of Chemical Thermodynamics **68**, 1–12 (2014).

[96] C. Held, T. Neuhaus, and G. Sadowski, "Compatible solutes: Thermodynamic properties and biological impact of ectoines and prolines", Biophysical Chemistry **152**, 28–39 (2010).

[97] C. Held and G. Sadowski, "Compatible solutes: Thermodynamic properties relevant for effective protection against osmotic stress", Fluid Phase Equilibria **407**, Aqueous Solutions and glycerol 2B, 224–235 (2016).

[98] S. S. Chen and A. Kreglewski, "Applications of the Augmented van der Waals Theory of Fluids.: I. Pure Fluids", Berichte der Bunsengesellschaft für physikalische Chemie **81**, 1048–1052 (1977).

[99] T. Boublík, "Hard-Sphere Equation of State", The Journal of Chemical Physics **53**, 471–472 (1970).

[100] G. A. Mansoori, N. F. Carnahan, K. E. Starling, and T. W. Leland, "Equilibrium Thermodynamic Properties of the Mixture of Hard Spheres", The Journal of Chemical Physics **54**, 1523–1525 (1971).

[101] N. F. Carnahan and K. E. Starling, "Equation of State for Nonattracting Rigid Spheres", The Journal of Chemical Physics **51**, 635–636 (1969).

[102] J. A. Barker and D Henderson, "Perturbation Theory and Equation of State for Fluids: The Square-Well Potential", The Journal of Chemical Physics **47**, 2856–2861 (1967).

[103] J. A. Barker and D Henderson, "Perturbation Theory and Equation of State for Fluids. II. A Successful Theory of Liquids", The Journal of Chemical Physics **47**, 4714–4721 (1967).

[104] Lorentz, "Ueber die Anwendung des Satzes vom Virial in der kinetischen Theorie der Gase", Annalen der Physik **248**, 127–136 (1881).

[105] S. P. Tan, H. Adidharma, and M. Radosz, "Generalized Procedure for Estimating the Fractions of Nonbonded Associating Molecules and Their Derivatives in Thermodynamic Perturbation Theory", Industrial & Engineering Chemistry Research **43**, 203–208 (2004).

[106] J. P. Wolbach and S. I. Sandler, "Using Molecular Orbital Calculations To Describe the Phase Behavior of Cross-associating Mixtures", Industrial & Engineering Chemistry Research **37**, 2917–2928 (1998).

[107] J. M. L. Sengers, "Mean-field theories, their weaknesses and strength", Fluid Phase Equilibria **158**, 3–17 (1999).

[108] M. Yang, T. Zhan, Y. Su, A. Dong, M. He, and Y. Zhang, "Crossover PC-SAFT equations of state based on White's method for the thermodynamic properties of CO2, n-alkanes and n-alkanols", Fluid Phase Equilibria **564**, 113610 (2023).

[109] M. A. Anisimov and J. V. Sengers, "Critical and crossover phenomena in fluids and fluid mixtures", *Supercritical fluids: fundamentals and applications*, edited by E. Kiran, P. G. Debenedetti, and C. J. Peters (Springer Netherlands, Dordrecht, 2000), 89–121.

[110] M. Knierbein, M. Venhuis, C. Held, and G. Sadowski, "Thermodynamic properties of aqueous osmolyte solutions at high-pressure conditions", Biophysical Chemistry **253**, 106211 (2019).

[111]J. M. Prausnitz, R. N. Lichtenthaler, and E. G. d. Azevedo, *Molecular Thermodynamics of Fluid-Phase Equilibria*, 3rd ed. (Prentice Hall, Philadelphia, PA, 1998).

[112]M. L. Michelsen, "The isothermal flash problem. Part I. Stability", Fluid Phase Equilibria **9**, 1–19 (1982).

[113]J. A. Coutinho, S. I. Andersen, and E. H. Stenby, "Evaluation of activity coefficient models in prediction of alkane solid-liquid equilibria", Fluid Phase Equilibria **103**, 23–39 (1995).

[114]J. Marrero and R. Gani, "Group-contribution based estimation of pure component properties", Fluid Phase Equilibria **183**, 183–208 (2001).

[115]J. D. v. d. Waals, "The thermodynamik theory of capillarity under the hypothesis of a continuous variation of density", Zeit. Phys. Chem. **13**, 675–725 (1894).

[116]J. S. Rowlinson, "Translation of J. D. van der Waals' "The thermodynamik theory of capillarity under the hypothesis of a continuous variation of density"", Journal of Statistical Physics **20**, 197–200 (1979).

[117]J. W. Cahn and J. E. Hilliard, "Free Energy of a Nonuniform System. I. Interfacial Free Energy", The Journal of Chemical Physics **28**, 258–267 (1958).

[118]C. Miqueu, B. Mendiboure, C. Graciaa, and J. Lachaise, "Modelling of the surface tension of binary and ternary mixtures with the gradient theory of fluid interfaces", Fluid Phase Equilibria **218**, 189–203 (2004).

[119]B. S. Carey, L. E. Scriven, and H. T. Davis, "Semiempirical theory of surface tensions of pure normal alkanes and alcohols", AIChE Journal **24**, 1076–1080 (1978).

[120]B. S. Carey, L. E. Scriven, and H. T. Davis, "Semiempirical theory of surface tension of binary systems", AIChE Journal **26**, 705–711 (1980).

[121]B. F. McCoy and H. T. Davis, "Free-energy theory of inhomogeneous fluids", Physical Review A **20**, 1201–1207 (1979).

[122]P. M. W. Cornelisse, C. J. Peters, and J. d. S. Arons, "On the fundamentals of the gradient theory of van der Waals", The Journal of Chemical Physics **106**, 9820–9834 (1997).

[123]X. Liang, M. L. Michelsen, and G. M. Kontogeorgis, "Pitfalls of using the geometric-mean combining rule in the density gradient theory", Fluid Phase Equilibria **415**, Path function method to solve DGT rigorously for beta=0, 75–83 (2016).

[124]V Bongiorno, L. Scriven, and H. Davis, "Molecular theory of fluid interfaces", Journal of Colloid and Interface Science **57**, Connection influence parameter (ci) to pair correlation function (g(r))., 462–475 (1976).

[125]A. J. M. Yang, P. D. Fleming, and J. H. Gibbs, "Molecular theory of surface tension", The Journal of Chemical Physics **64**, About cii from microscopic theories, 3732–3747 (1976).

[126]J. M. Garrido, A. Mejía, M. M. Piñeiro, F. J. Blas, and E. A. Müller, "Interfacial tensions of industrial fluids from a molecular-based square gradient theory", AIChE Journal **62**, 1781–1794 (2016).

[127]A. Allal, C. Boned, and A. Baylaucq, "Free-volume viscosity model for fluids in the dense and gaseous states", Physical Review E **64**, 011203 (2001).

[128]E. A. Crespo, L. P. Silva, J. O. Lloret, P. J. Carvalho, L. F. Vega, F. Llovell, and J. A. P. Coutinho, "A methodology to parameterize SAFT-type equations of state for solid precursors of deep eutectic solvents: the example of cholinium chloride", Physical Chemistry Chemical Physics **21**, 15046–15061 (2019).

[129]S. Chapman, "VI. On the law of distribution of molecular velocities, and on the theory of viscosity and thermal conduction, in a non-uniform simple monatomic gas", Philosophical Transactions of the Royal Society of London. Series A, Containing Papers of a Mathematical or Physical Character **216**, 279–348 (1916).

[130]T. H. Chung, M. Ajlan, L. L. Lee, and K. E. Starling, "Generalized multiparameter correlation for nonpolar and polar fluid transport properties", Industrial & Engineering Chemistry Research **27**, 671–679 (1988).

[131]P. D. Neufeld, A. R. Janzen, and R. A. Aziz, "Empirical Equations to Calculate 16 of the Transport Collision Integrals Ω(l, s)* for the Lennard-Jones (12–6) Potential", The Journal of Chemical Physics **57**, 1100–1102 (1972).

[132]C. R. Wilke, "A Viscosity Equation for Gas Mixtures", The Journal of Chemical Physics **18**, 517–519 (1950).

[133]G. Battimelli and G. Ciccotti, "Berni Alder and the pioneering times of molecular simulation", The European Physical Journal H **43**, 303–335 (2018).

[134]S. A. Hollingsworth and R. O. Dror, "Molecular Dynamics Simulation for All", Neuron **99**, 1129–1143 (2018).

[135]W. L. Jorgensen, D. S. Maxwell, and J. Tirado-Rives, "Development and Testing of the OPLS All-Atom Force Field on Conformational Energetics and Properties of Organic Liquids", Journal of the American Chemical Society **118**, 11225–11236 (1996).

[136]B. R. Brooks, R. E. Bruccoleri, B. D. Olafson, D. J. States, S. Swaminathan, and M. Karplus, "CHARMM: A program for macromolecular energy, minimization, and dynamics calculations", Journal of Computational Chemistry **4**, 187–217 (1983).

[137]P. K. Weiner and P. A. Kollman, "AMBER: Assisted model building with energy refinement. A general program for modeling molecules and their interactions", Journal of Computational Chemistry **2**, 287–303 (1981).

[138]M. G. Martin and J. I. Siepmann, "Transferable Potentials for Phase Equilibria. 1. United-Atom Description of n-Alkanes", The Journal of Physical Chemistry B **102**, 2569–2577 (1998).

[139]S. J. Marrink, H. J. Risselada, S. Yefimov, D. P. Tieleman, and A. H. d. Vries, "The MARTINI Force Field: Coarse Grained Model for Biomolecular Simulations", The Journal of Physical Chemistry B **111**, 7812–7824 (2007).

[140]P. C. T. Souza et al., "Martini 3: a general purpose force field for coarse-grained molecular dynamics", Nature Methods **18**, 382–388 (2021).

[141]W. C. Swope, H. C. Andersen, P. H. Berens, and K. R. Wilson, "A computer simulation method for the calculation of equilibrium constants for the formation of physical clusters of molecules: Application to small water clusters", The Journal of Chemical Physics **76**, velocity verlet, 637–649 (1982).

[142]R. Hockney, S. Goel, and J. Eastwood, "Quiet high-resolution computer models of a plasma", Journal of Computational Physics **14**, leap-frog, 148–158 (1974).

[143]J.-P. Ryckaert, G. Ciccotti, and H. J. Berendsen, "Numerical integration of the cartesian equations of motion of a system with constraints: molecular dynamics of n-alkanes", Journal of Computational Physics **23**, 327–341 (1977).

[144] S. Miyamoto and P. A. Kollman, "Settle: An analytical version of the SHAKE and RATTLE algorithm for rigid water models", Journal of Computational Chemistry **13**, SETTLE algorithm, 952–962 (1992).

[145] B. Hess, H. Bekker, H. J. C. Berendsen, and J. G. E. M. Fraaije, "LINCS: A linear constraint solver for molecular simulations", Journal of Computational Chemistry **18**, LINCS, 1463–1472 (1997).

[146] L. Verlet, "Computer "Experiments" on Classical Fluids. I. Thermodynamical Properties of Lennard-Jones Molecules", Physical Review **159**, verlet list, 98–103 (1967).

[147] H. J. C. Berendsen, J. P. M. Postma, W. F. v. Gunsteren, A DiNola, and J. R. Haak, "Molecular dynamics with coupling to an external bath", The Journal of Chemical Physics **81**, 3684–3690 (1984).

[148] G. Bussi, D. Donadio, and M. Parrinello, "Canonical sampling through velocity rescaling", The Journal of Chemical Physics **126**, 014101 (2007).

[149] S. Nosé, "A molecular dynamics method for simulations in the canonical ensemble", Molecular Physics **52**, Nose thermostat, 255–268 (1984).

[150] W. G. Hoover, "Canonical dynamics: Equilibrium phase-space distributions", Physical Review A **31**, Hoover thermostat, 1695–1697 (1985).

[151] M Parrinello and A Rahman, "Polymorphic transitions in single crystals: A new molecular dynamics method", Journal of Applied Physics **52**, 7182–7190 (1981).

[152] S. Nosé and M. Klein, "Constant pressure molecular dynamics for molecular systems", Molecular Physics **50**, parrinello barostat, 1055–1076 (1983).

[153] B. Hess, "Determining the shear viscosity of model liquids from molecular dynamics simulations", The Journal of Chemical Physics **116**, 209–217 (2002).

[154] H. Hulshof, "Ueber die Oberflächenspannung", Annalen der Physik **309**, 165–186 (1901).

[155] A. G. d. Castilla, J. P. Bittner, S. Müller, S. Jakobtorweihen, and I. Smirnova, "Thermodynamic and Transport Properties Modeling of Deep Eutectic Solvents: A Review on gE-Models, Equations of State, and Molecular Dynamics", Journal of Chemical & Engineering Data **65**, 943–967 (2020).

[156] N. F. Gajardo-Parra, M. J. Lubben, J. M. Winnert, Leiva, J. F. Brennecke, and R. I. Canales, "Physicochemical properties of choline chloride-based deep eutectic solvents and excess properties of their pseudo-binary mixtures with 1-butanol", The Journal of Chemical Thermodynamics **133**, 272–284 (2019).

[157] O. G. Sas, R. Fidalgo, I. Domínguez, E. A. Macedo, and B. González, "Physical Properties of the Pure Deep Eutectic Solvent, [ChCl]:[Lev] (1:2) DES, and Its Binary Mixtures with Alcohols", Journal of Chemical & Engineering Data **61**, 4191–4202 (2016).

[158] R. Alcalde, M. Atilhan, and S. Aparicio, "On the properties of (choline chloride + lactic acid) deep eutectic solvent with methanol mixtures", Journal of Molecular Liquids **272**, 815–820 (2018).

[159] R. B. Leron, A. N. Soriano, and M.-H. Li, "Densities and refractive indices of the deep eutectic solvents (choline chloride+ethylene glycol or glycerol) and their aqueous mixtures at the temperature ranging from 298.15 to 333.15K", Journal of the Taiwan Institute of Chemical Engineers **43**, 551–557 (2012).

[160] R. B. Leron and M.-H. Li, "High-pressure volumetric properties of choline chloride–ethylene glycol based deep eutectic solvent and its mixtures with water", Thermochimica Acta **546**, 54–60 (2012).

[161] R. Haghbakhsh and S. Raeissi, “Densities and volumetric properties of (choline chloride + urea) deep eutectic solvent and methanol mixtures in the temperature range of 293.15–323.15 K”, The Journal of Chemical Thermodynamics **124**, 10–20 (2018).

[162] R. Haghbakhsh and S. Raeissi, “Excess volumes of mixtures consisting of deep eutectic solvents by the Prigogine–Flory–Patterson theory”, Journal of Molecular Liquids **272**, 731–737 (2018).

[163] R. Haghbakhsh and S. Raeissi, “Investigation of solutions of ethyl alcohol and the deep eutectic solvent of Reline for their volumetric properties”, Fluid Phase Equilibria **472**, 39–47 (2018).

[164] R. Haghbakhsh and S. Raeissi, “A study of non-ideal mixtures of ethanol and the (1 choline chloride +2 ethylene glycol) deep eutectic solvent for their volumetric behaviour”, The Journal of Chemical Thermodynamics **150**, 106219 (2020).

[165] R. Haghbakhsh and S. Raeissi, “Experimental investigation on the volumetric properties of mixtures of the deep eutectic solvent of Ethaline and methanol in the temperature range of 283.15 to 323.15 K”, The Journal of Chemical Thermodynamics **147**, 106124 (2020).

[166] A. Yadav, S. Trivedi, R. Rai, and S. Pandey, “Densities and dynamic viscosities of (choline chloride+glycerol) deep eutectic solvent and its aqueous mixtures in the temperature range (283.15–363.15)K”, Fluid Phase Equilibria **367**, 135–142 (2014).

[167] A. Yadav and S. Pandey, “Densities and Viscosities of (Choline Chloride + Urea) Deep Eutectic Solvent and Its Aqueous Mixtures in the Temperature Range 293.15 K to 363.15 K”, Journal of Chemical & Engineering Data **59**, 2221–2229 (2014).

[168] A. Abo-Hamad, M. Hayyan, M. A. AlSaadi, and M. A. Hashim, “Potential applications of deep eutectic solvents in nanotechnology”, Chemical Engineering Journal **273**, 551–567 (2015).

[169] K.-S. Kim and B. H. Park, “Volumetric properties of solutions of choline chloride + glycerol deep eutectic solvent with water, methanol, ethanol, or iso-propanol”, Journal of Molecular Liquids **254**, 272–279 (2018).

[170] A. Yadav, J. R. Kar, M. Verma, S. Naqvi, and S. Pandey, “Densities of aqueous mixtures of (choline chloride+ethylene glycol) and (choline chloride+malonic acid) deep eutectic solvents in temperature range 283.15–363.15K”, Thermochimica Acta **600**, 95–101 (2015).

[171] C. Ma, Y. Guo, D. Li, J. Zong, X. Ji, C. Liu, and X. Lu, “Molar Enthalpy of Mixing for Choline Chloride/Urea Deep Eutectic Solvent + Water System”, Journal of Chemical & Engineering Data **61**, 4172–4177 (2016).

[172] C. Ma, Y. Guo, D. Li, J. Zong, X. Ji, and C. Liu, “Molar enthalpy of mixing and refractive indices of choline chloride-based deep eutectic solvents with water”, The Journal of Chemical Thermodynamics **105**, 30–36 (2017).

[173] Y.-H. Hsu, R. B. Leron, and M.-H. Li, “Solubility of carbon dioxide in aqueous mixtures of (reline+monoethanolamine) at T=(313.2 to 353.2)K”, The Journal of Chemical Thermodynamics **72**, 94–99 (2014).

[174] M. Lu, G. Han, Y. Jiang, X. Zhang, D. Deng, and N. Ai, “Solubilities of carbon dioxide in the eutectic mixture of levulinic acid (or furfuryl alcohol) and choline chloride”, The Journal of Chemical Thermodynamics **88**, 72–77 (2015).

[175] R. B. Leron, A. Caparanga, and M.-H. Li, “Carbon dioxide solubility in a deep eutectic solvent based on choline chloride and urea at T=303.15–343.15K and moderate pressures”, Journal of the Taiwan Institute of Chemical Engineers **44**, 879–885 (2013).

[176] R. B. Leron and M.-H. Li, "Solubility of carbon dioxide in a eutectic mixture of choline chloride and glycerol at moderate pressures", The Journal of Chemical Thermodynamics **57**, 131–136 (2013).

[177] C. H. J. T. Dietz, F. Gallucci, M. v. S. Annaland, C. Held, and M. C. Kroon, "110th Anniversary: Distribution Coefficients of Furfural and 5-Hydroxymethylfurfural in Hydrophobic Deep Eutectic Solvent + Water Systems: Experiments and Perturbed-Chain Statistical Associating Fluid Theory Predictions", Industrial & Engineering Chemistry Research **58**, 4240–4247 (2019).

[178] C. H. Dietz, A. Erve, M. C. Kroon, M. v. S. Annaland, F. Gallucci, and C. Held, "Thermodynamic properties of hydrophobic deep eutectic solvents and solubility of water and HMF in them: Measurements and PC-SAFT modeling", Fluid Phase Equilibria **489**, 75–82 (2019).

[179] S. P. Verevkin, A. Y. Sazonova, A. K. Frolkova, D. H. Zaitsau, I. V. Prikhodko, and C. Held, "Separation Performance of BioRenewable Deep Eutectic Solvents", Industrial & Engineering Chemistry Research **54**, 3508–3514 (2015).

[180] A. Samarov, I. Prikhodko, N. Shner, G. Sadowski, C. Held, and A. Toikka, "Liquid–Liquid Equilibria for Separation of Alcohols from Esters Using Deep Eutectic Solvents Based on Choline Chloride: Experimental Study and Thermodynamic Modeling", Journal of Chemical & Engineering Data **64**, 6049–6059 (2019).

[181] I. Polishuk and J. M. Garrido, "Comparison of SAFT-VR-Mie and CP-PC-SAFT in predicting phase behavior of associating systems I. Ammonia–water, methanol, ethanol and hydrazine", Journal of Molecular Liquids **265**, 639–653 (2018).

[182] I. Polishuk and J. M. Garrido, "Comparison of SAFT-VR-Mie and CP-PC-SAFT in predicting phase behavior of associating systems II. Ammonia – Hydrocarbons", Journal of Molecular Liquids **269**, 657–665 (2018).

[183] I. Polishuk and J. M. Garrido, "Comparison of SAFT-VR-Mie and CP-PC-SAFT in predicting phase behavior of associating systems III. Aliphatic hydrocarbons - 1-propanol, 1-butanol and 1-pentanol", Journal of Molecular Liquids **279**, 492–502 (2019).

[184] I. Polishuk and J. M. Garrido, "Comparison of SAFT-VR-Mie and CP-PC-SAFT in predicting phase behavior of associating systems IV. Methanol–aliphatic hydrocarbons", Journal of Molecular Liquids **291**, 111321 (2019).

[185] C. H. J. T. Dietz, J. T. Creemers, M. A. Meuleman, C. Held, G. Sadowski, M. v. S. Annaland, F. Gallucci, and M. C. Kroon, "Determination of the Total Vapor Pressure of Hydrophobic Deep Eutectic Solvents: Experiments and Perturbed-Chain Statistical Associating Fluid Theory Modeling", ACS Sustainable Chemistry & Engineering **7**, 4047–4057 (2019).

[186] E. A. Crespo, J. M. Costa, A. M. Palma, B. Soares, M. C. Martín, J. J. Segovia, P. J. Carvalho, and J. A. Coutinho, "Thermodynamic characterization of deep eutectic solvents at high pressures", Fluid Phase Equilibria **500**, 112249 (2019).

[187] S. L. Perkins, P. Painter, and C. M. Colina, "Experimental and Computational Studies of Choline Chloride-Based Deep Eutectic Solvents", Journal of Chemical & Engineering Data **59**, 3652–3662 (2014).

[188] O. S. Hammond, D. T. Bowron, and K. J. Edler, "Liquid structure of the choline chloride-urea deep eutectic solvent (reline) from neutron diffraction and atomistic modelling", Green Chemistry **18**, 2736–2744 (2016).

[189] E. Altuntepe, V. N. Emel'yanenko, M. Forster-Rotgers, G. Sadowski, S. P. Verevkin, and C. Held, "Thermodynamics of enzyme-catalyzed esterifications: II. Levulinic acid esterification with short-chain alcohols", Applied Microbiology and Biotechnology **101**, 7509–7521 (2017).

[190] M. Atilhan and S. Aparicio, "PρT measurements and derived properties of liquid 1,2-alkanediols", The Journal of Chemical Thermodynamics **57**, C4, 137–144 (2013).

[191] I. V. Prikhod'ko, F. Tumakaka, and G. Sadowski, "Application of the PC-SAFT equation of state to modeling of solid-liquid equilibria in systems with organic components forming chemical compounds", Russian Journal of Applied Chemistry **80**, 542–548 (2007).

[192] R. Haghbakhsh, K. Parvaneh, S. Raeissi, and A. Shariati, "A general viscosity model for deep eutectic solvents: The free volume theory coupled with association equations of state", Fluid Phase Equilibria **470**, 193–202 (2018).

[193] S. Zarei and F. Feyzi, "Boyle temperature from SAFT, PC-SAFT and SAFT-VR equations of state", Journal of Molecular Liquids **187**, 114–128 (2013).

[194] D. NguyenHuynh, C. T. Mai, S. T. Tran, X. T. Nguyen, and O. Baudouin, "Modelling of phase behavior of ammonia and its mixtures using the mg-SAFT", Fluid Phase Equilibria **523**, 112689 (2020).

[195] L. F. Cameretti and G. Sadowski, "Modeling of aqueous amino acid and polypeptide solutions with PC-SAFT", Chemical Engineering and Processing: Process Intensification **47**, 1018–1025 (2008).

[196] C. Florindo, L. Romero, I. Rintoul, L. C. Branco, and I. M. Marrucho, "From Phase Change Materials to Green Solvents: Hydrophobic Low Viscous Fatty Acid–Based Deep Eutectic Solvents", ACS Sustainable Chemistry & Engineering **6**, 3888–3895 (2018).

[197] N. R. Rodriguez, A. v. d. Bruinhorst, L. J. B. M. Kollau, M. C. Kroon, and K. Binnemans, "Degradation of Deep-Eutectic Solvents Based on Choline Chloride and Carboxylic Acids", ACS Sustainable Chemistry & Engineering **7**, 11521–11528 (2019).

[198] S. E. Warrag, C. Pototzki, N. R. Rodriguez, M. v. S. Annaland, M. C. Kroon, C. Held, G. Sadowski, and C. J. Peters, "Oil desulfurization using deep eutectic solvents as sustainable and economical extractants via liquid-liquid extraction: Experimental and PC-SAFT predictions", Fluid Phase Equilibria **467**, 33–44 (2018).

[199] K. Shahbaz, F. Mjalli, M. Hashim, and I. AlNashef, "Prediction of deep eutectic solvents densities at different temperatures", Thermochimica Acta **515**, 67–72 (2011).

[200] K. Shahbaz, S. Baroutian, F. Mjalli, M. Hashim, and I. AlNashef, "Densities of ammonium and phosphonium based deep eutectic solvents: Prediction using artificial intelligence and group contribution techniques", Thermochimica Acta **527**, 59–66 (2012).

[201] W. Guo, Y. Hou, S. Ren, S. Tian, and W. Wu, "Formation of Deep Eutectic Solvents by Phenols and Choline Chloride and Their Physical Properties", Journal of Chemical & Engineering Data **58**, 866–872 (2013).

[202] G. Li, D. Deng, Y. Chen, H. Shan, and N. Ai, "Solubilities and thermodynamic properties of CO2 in choline-chloride based deep eutectic solvents", The Journal of Chemical Thermodynamics **75**, 58–62 (2014).

[203] Y. Ji, Y. Hou, S. Ren, C. Yao, and W. Wu, "Phase equilibria of high pressure CO2 and deep eutectic solvents formed by quaternary ammonium salts and phenol", Fluid Phase Equilibria **429**, 14–20 (2016).

[204] R. Ullah, M. Atilhan, B. Anaya, M. Khraisheh, G. García, A. ElKhattat, M. Tariq, and S. Aparicio, "A detailed study of cholinium chloride and levulinic acid deep eutectic solvent system for CO 2 capture via experimental and molecular simulation approaches", Physical Chemistry Chemical Physics **17**, 20941–20960 (2015).

[205] X. Duan, B. Gao, C. Zhang, and D. Deng, "Solubility and thermodynamic properties of NH3 in choline chloride-based deep eutectic solvents", The Journal of Chemical Thermodynamics **133**, 79–84 (2019).

[206] E. J. Sa, B.-S. Lee, and B. H. Park, "Extraction of ethanol from mixtures with n-hexane by deep eutectic solvents of choline chloride + levulinic acid, + ethylene glycol, or + malonic acid", Journal of Molecular Liquids **316**, 113877 (2020).

[207] H. S. Esfahani, A. Khoshsima, and G. Pazuki, "Choline chloride-based deep eutectic solvents as green extractant for the efficient extraction of 1-butanol or 2-butanol from azeotropic n-heptane + butanol mixtures", Journal of Molecular Liquids **313**, 113524 (2020).

[208] M. Tariq, M. G. Freire, B. Saramago, J. A. P. Coutinho, J. N. C. Lopes, and L. P. N. Rebelo, "Surface tension of ionic liquids and ionic liquid solutions", Chemical Society Reviews **41**, 829–868 (2011).

[209] Q. Gao, N. Wu, Y. Qin, A. Laaksonen, Y. Zhu, X. Ji, and X. Lu, "Molecular insight into wetting behavior of deep eutectic solvent droplets on ionic substrates: A molecular dynamics study", Journal of Molecular Liquids **319**, 114298 (2020).

[210] A. R. C. Duarte, A. S. D. Ferreira, S. Barreiros, E. Cabrita, R. L. Reis, and A. Paiva, "A comparison between pure active pharmaceutical ingredients and therapeutic deep eutectic solvents: Solubility and permeability studies", European Journal of Pharmaceutics and Biopharmaceutics **114**, 296–304 (2017).

[211] M. T. Donato, R. Colaço, L. C. Branco, and B. Saramago, "A review on alternative lubricants: Ionic liquids as additives and deep eutectic solvents", Journal of Molecular Liquids **333**, 116004 (2021).

[212] E Jiménez, M Cabanas, L Segade, S Garcıóa-Garabal, and H Casas, "Excess volume, changes of refractive index and surface tension of binary 1,2-ethanediol + 1-propanol or 1-butanol mixtures at several temperatures", Fluid Phase Equilibria **180**, 151–164 (2001).

[213] K. Shahbaz, F. Mjalli, M. Hashim, and I. AlNashef, "Prediction of the surface tension of deep eutectic solvents", Fluid Phase Equilibria **319**, 48–54 (2012).

[214] H. Ghaedi, M. Ayoub, S. Sufian, A. M. Shariff, and B. Lal, "The study on temperature dependence of viscosity and surface tension of several Phosphonium-based deep eutectic solvents", Journal of Molecular Liquids **241**, 500–510 (2017).

[215] R. Haghbakhsh, M. Taherzadeh, A. R. C. Duarte, and S. Raeissi, "A general model for the surface tensions of deep eutectic solvents", Journal of Molecular Liquids **307**, 112972 (2020).

[216] R. Haghbakhsh, S. Raeissi, and A. R. C. Duarte, "Group contribution and atomic contribution models for the prediction of various physical properties of deep eutectic solvents", Scientific Reports **11**, 6684 (2021).

[217] H. Kahl and S. Enders, "Calculation of surface properties of pure fluids using density gradient theory and SAFT-EOS", Fluid Phase Equilibria **172**, 27–42 (2000).

[218] J. Mairhofer and J. Gross, "Modeling properties of the one-dimensional vapor-liquid interface: Application of classical density functional and density gradient theory", Fluid Phase Equilibria **458**, 243–252 (2018).

[219]O. Niño-Amézquita, S. Enders, P. Jaeger, and R. Eggers, “Interfacial properties of mixtures containing supercritical gases”, The Journal of Supercritical Fluids **55**, 724–734 (2010).

[220]S. Stephan, S. Becker, K. Langenbach, and H. Hasse, “Vapor-liquid interfacial properties of the system cyclohexane + CO2: Experiments, molecular simulation and density gradient theory”, Fluid Phase Equilibria **518**, 112583 (2020).

[221]S. Enders and K. Quitzsch, “Calculation of Interfacial Properties of Demixed Fluids Using Density Gradient Theory”, Langmuir **14**, 4606–4614 (1998).

[222]O. Vilaseca and L. F. Vega, “Direct calculation of interfacial properties of fluids close to the critical region by a molecular-based equation of state”, Fluid Phase Equilibria **306**, 20 years of the SAFT equation of state, 4–14 (2011).

[223]M. B. Oliveira, S. V. Freitas, F. Llovell, L. F. Vega, and J. A. Coutinho, “Development of simple and transferable molecular models for biodiesel production with the soft-SAFT equation of state”, Chemical Engineering Research and Design **92**, Advances in Thermodynamics for Chemical Process and Product Design, 2898–2911 (2014).

[224]N. Haarmann, A. Reinhardt, A. Danzer, G. Sadowski, and S. Enders, “Modeling of Interfacial Tensions of Long-Chain Molecules and Related Mixtures Using Perturbed Chain-Statistical Associating Fluid Theory and the Density Gradient Theory”, Journal of Chemical & Engineering Data **65**, 1005–1018 (2020).

[225]G. Shen, C. Held, X. Lu, and X. Ji, “Modelling interfacial properties of ionic liquids with ePC-SAFT combined with density gradient theory”, Molecular Physics **114**, 2492–2499 (2016).

[226]L. F. Vega, O. Vilaseca, F. Llovell, and J. S. Andreu, “Modeling ionic liquids and the solubility of gases in them: Recent advances and perspectives”, Fluid Phase Equilibria **294**, 15–30 (2010).

[227]M. B. Oliveira, F. Llovell, J. A. P. Coutinho, and L. F. Vega, “Modeling the [NTf2] Pyridinium Ionic Liquids Family and Their Mixtures with the Soft Statistical Associating Fluid Theory Equation of State”, The Journal of Physical Chemistry B **116**, 9089–9100 (2012).

[228]A. Danzer and S. Enders, “Theoretical and experimental investigation of the interfacial properties in the ternary mixtures water + 1-hexanol + acetic acid and water + hexylacetate + acetic acid using density gradient theory and spinning-drop tensiometry”, Journal of Molecular Liquids **283**, 482–490 (2019).

[229]S. P. Tan, H. Adidharma, and M. Radosz, “Statistical Associating Fluid Theory Coupled with Restricted Primitive Model To Represent Aqueous Strong Electrolytes”, Industrial & Engineering Chemistry Research **44**, 4442–4452 (2005).

[230]F. Lima, C. H. J. T. Dietz, A. J. D. Silvestre, L. C. Branco, J. C. Lopes, F. Gallucci, K. Shimizu, C. Held, and I. M. Marrucho, “Vapor Pressure Assessment of Sulfolane-Based Eutectic Solvents: Experimental, PC-SAFT, and Molecular Dynamics”, The Journal of Physical Chemistry B **124**, 10386–10397 (2020).

[231]G. Rodriguez and E. J. Beckman, “Modelling phase behavior of biodiesel related systems with CO2 using a polar version of PC-SAFT”, Fluid Phase Equilibria **485**, 32–43 (2019).

[232]S. F. Baygi and H. Pahlavanzadeh, “Application of the perturbed chain-SAFT equation of state for modeling CO2 solubility in aqueous monoethanolamine solutions”, Chemical Engineering Research and Design **93**, 789–799 (2015).

[233] C. Held, G. Sadowski, A. Carneiro, O. Rodríguez, and E. A. Macedo, "Modeling thermodynamic properties of aqueous single-solute and multi-solute sugar solutions with PC-SAFT", AIChE Journal **59**, 4794–4805 (2013).

[234] A. Grenner, G. M. Kontogeorgis, N. v. Solms, and M. L. Michelsen, "Application of PC-SAFT to glycol containing systems – PC-SAFT towards a predictive approach", Fluid Phase Equilibria **261**, 248–257 (2007).

[235] P. V. Pontes, E. A. Crespo, M. A. Martins, L. P. Silva, C. M. Neves, G. J. Maximo, M. D. Hubinger, E. A. Batista, S. P. Pinho, J. A. Coutinho, G. Sadowski, and C. Held, "Measurement and PC-SAFT modeling of solid-liquid equilibrium of deep eutectic solvents of quaternary ammonium chlorides and carboxylic acids", Fluid Phase Equilibria **448**, 69–80 (2017).

[236] T. Esper, G. Bauer, P. Rehner, and J. Gross, "PCP-SAFT Parameters of Pure Substances Using Large Experimental Databases", Industrial & Engineering Chemistry Research **62**, 15300–15310 (2023).

[237] N. v. Solms, M. L. Michelsen, and G. M. Kontogeorgis, "Applying Association Theories to Polar Fluids", Industrial & Engineering Chemistry Research **43**, 1803–1806 (2004).

[238] F. S. Mjalli, G. Vakili-Nezhaad, K. Shahbaz, and I. M. AlNashef, "Application of the Eötvos and Guggenheim empirical rules for predicting the density and surface tension of ionic liquids analogues", Thermochimica Acta **575**, 40–44 (2014).

[239] A. R. Harifi-Mood and R. Buchner, "Density, viscosity, and conductivity of choline chloride+ethylene glycol as a deep eutectic solvent and its binary mixtures with dimethyl sulfoxide", Journal of Molecular Liquids **225**, 689–695 (2017).

[240] R. K. Ibrahim, M. Hayyan, M. A. AlSaadi, S. Ibrahim, A. Hayyan, and M. A. Hashim, "Physical properties of ethylene glycol-based deep eutectic solvents", Journal of Molecular Liquids **276**, 794–800 (2019).

[241] M. K. AlOmar, M. Hayyan, M. A. Alsaadi, S. Akib, A. Hayyan, and M. A. Hashim, "Glycerol-based deep eutectic solvents: Physical properties", Journal of Molecular Liquids **215**, 98–103 (2016).

[242] M. Francisco, A. v. d. Bruinhorst, L. F. Zubeir, C. J. Peters, and M. C. Kroon, "A new low transition temperature mixture (LTTM) formed by choline chloride+lactic acid: Characterization as solvent for CO2 capture", Fluid Phase Equilibria **340**, 77–84 (2013).

[243] K. A. Omar and R. Sadeghi, "Novel diglycolic acid-based deep eutectic solvents and their applications as a rust remover", Journal of Molecular Liquids **312**, 113380 (2020).

[244] A. Leal-Duaso, P. Pérez, J. A. Mayoral, E. Pires, and J. I. García, "Glycerol as a source of designer solvents: physicochemical properties of low melting mixtures containing glycerol ethers and ammonium salts", Physical Chemistry Chemical Physics **19**, 28302–28312 (2017).

[245] F. S. Mjalli, G. Murshid, S. Al-Zakwani, and A. Hayyan, "Monoethanolamine-based deep eutectic solvents, their synthesis and characterization", Fluid Phase Equilibria **448**, Deep Eutectic Solvents, 30–40 (2017).

[246] A. Hayyan, F. S. Mjalli, I. M. AlNashef, T. Al-Wahaibi, Y. M. Al-Wahaibi, and M. A. Hashim, "Fruit sugar-based deep eutectic solvents and their physical properties", Thermochimica Acta **541**, 70–75 (2012).

[247] A. Hayyan, F. S. Mjalli, I. M. AlNashef, Y. M. Al-Wahaibi, T. Al-Wahaibi, and M. A. Hashim, "Glucose-based deep eutectic solvents: Physical properties", Journal of Molecular Liquids **178**, 137–141 (2013).

[248] F. S. Mjalli, J. Naser, B. Jibril, V. Alizadeh, and Z. Gano, "Tetrabutylammonium Chloride Based Ionic Liquid Analogues and Their Physical Properties", Journal of Chemical & Engineering Data **59**, 2242–2251 (2014).

[249] F. Bergua, M. Castro, J. Muñoz-Embid, C. Lafuente, and M. Artal, "Hydrophobic eutectic solvents: Thermophysical study and application in removal of pharmaceutical products from water", Chemical Engineering Journal **411**, 128472 (2021).

[250] F. S. Mjalli and N. M. A. Jabbar, "Acoustic investigation of choline chloride based ionic liquids analogs", Fluid Phase Equilibria **381**, 71–76 (2014).

[251] Y. Rublova, A. Kityk, F. Danilov, and V. Protsenko, "Mechanistic Study on Surface Tension of Binary and Ternary Mixtures Containing Choline Chloride, Ethylene Glycol and Water (Components of Aqueous Solutions of a Deep Eutectic Solvent, Ethaline)", Zeitschrift für Physikalische Chemie **234**, 399–413 (2020).

[252] Y. Chen, W. Chen, L. Fu, Y. Yang, Y. Wang, X. Hu, F. Wang, and T. Mu, "Surface Tension of 50 Deep Eutectic Solvents: Effect of Hydrogen-Bonding Donors, Hydrogen-Bonding Acceptors, Other Solvents, and Temperature", Industrial & Engineering Chemistry Research **58**, 12741–12750 (2019).

[253] C. M. Romero and M. S. Paéz, "Surface tension of aqueous solutions of alcohol and polyols at 298.15 K", Physics and Chemistry of Liquids **44**, 61–65 (2006).

[254] A. S. Alkindi, Y. M. Al-Wahaibi, and A. H. Muggeridge, "Physical Properties (Density, Excess Molar Volume, Viscosity, Surface Tension, and Refractive Index) of Ethanol + Glycerol", Journal of Chemical & Engineering Data **53**, 2793–2796 (2008).

[255] A. Erfani, S. Khosharay, and C. P. Aichele, "Surface tension and interfacial compositions of binary glycerol/alcohol mixtures", The Journal of Chemical Thermodynamics **135**, 241–251 (2019).

[256] W. A. Fouad and L. F. Vega, "On the anomalous composition dependence of viscosity and surface tension in refrigerant blends", Journal of Molecular Liquids **268**, 190–200 (2018).

[257] A. S. Ferreira, R. Craveiro, A. R. Duarte, S. Barreiros, E. J. Cabrita, and A. Paiva, "Effect of water on the structure and dynamics of choline chloride/glycerol eutectic systems", Journal of Molecular Liquids **342**, 117463 (2021).

[258] V. P. Cotroneo-Figueroa, N. F. Gajardo-Parra, P. López-Porfiri, Leiva, M. Gonzalez-Miquel, J. M. Garrido, and R. I. Canales, "Hydrogen bond donor and alcohol chain length effect on the physicochemical properties of choline chloride based deep eutectic solvents mixed with alcohols", Journal of Molecular Liquids **345**, 116986 (2022).

[259] N. F. Gajardo-Parra, H. T. Do, M. Yang, J. R. Pérez-Correa, J. M. Garrido, G. Sadowski, C. Held, and R. I. Canales, "Impact of deep eutectic solvents and their constituents on the aqueous solubility of phloroglucinol dihydrate", Journal of Molecular Liquids **344**, 117932 (2021).

[260] I. I. Alkhatib, D. Bahamon, F. Llovell, M. R. Abu-Zahra, and L. F. Vega, "Perspectives and guidelines on thermodynamic modelling of deep eutectic solvents", Journal of Molecular Liquids **298**, 112183 (2020).

[261] M. Atilhan and S. Aparicio, "Molecular dynamics simulations of mixed deep eutectic solvents and their interaction with nanomaterials", Journal of Molecular Liquids **283**, 147–154 (2019).

[262] J. Baz, C. Held, J. Pleiss, and N. Hansen, “Thermophysical properties of glyceline–water mixtures investigated by molecular modelling”, Physical Chemistry Chemical Physics **21**, 6467–6476 (2019).

[263] A. Triolo, F. L. Celso, M. Brehm, V. D. Lisio, and O. Russina, “Liquid structure of a choline chloride-water natural deep eutectic solvent: A molecular dynamics characterization”, Journal of Molecular Liquids **331**, 115750 (2021).

[264] E. K. Karakatsani, T. Spyriouni, and I. G. Economou, “Extended statistical associating fluid theory (SAFT) equations of state for dipolar fluids”, AIChE Journal **51**, 2328–2342 (2005).

[265] D. V. D. Spoel, E. Lindahl, B. Hess, G. Groenhof, A. E. Mark, and H. J. C. Berendsen, “GROMACS: Fast, flexible, and free”, Journal of Computational Chemistry **26**, 1701–1718 (2005).

[266] B. Doherty and O. Acevedo, “OPLS Force Field for Choline Chloride-Based Deep Eutectic Solvents”, The Journal of Physical Chemistry B **122**, 9982–9993 (2018).

[267] L. Martínez, R. Andrade, E. G. Birgin, and J. M. Martínez, “PACKMOL: A package for building initial configurations for molecular dynamics simulations”, Journal of Computational Chemistry **30**, 2157–2164 (2009).

[268] T. Darden, D. York, and L. Pedersen, “Particle mesh Ewald: An N -log(N) method for Ewald sums in large systems”, The Journal of Chemical Physics **98**, 10089–10092 (1993).

[269] T. M. Nymand and P. Linse, “Ewald summation and reaction field methods for potentials with atomic charges, dipoles, and polarizabilities”, The Journal of Chemical Physics **112**, 6152–6160 (2000).

[270] H. J. C. Berendsen, J. R. Grigera, and T. P. Straatsma, “The missing term in effective pair potentials”, The Journal of Physical Chemistry **91**, 6269–6271 (1987).

[271] B. Hess, “P-LINCS: A Parallel Linear Constraint Solver for Molecular Simulation”, Journal of Chemical Theory and Computation **4**, 116–122 (2008).

[272] Y. Wang, C. Ma, C. Liu, X. Lu, X. Feng, and X. Ji, “Thermodynamic Study of Choline Chloride-Based Deep Eutectic Solvents with Water and Methanol”, Journal of Chemical & Engineering Data **65**, 2446–2457 (2020).

[273] C. Florindo, F. S. Oliveira, L. P. N. Rebelo, A. M. Fernandes, and I. M. Marrucho, “Insights into the Synthesis and Properties of Deep Eutectic Solvents Based on Cholinium Chloride and Carboxylic Acids”, ACS Sustainable Chemistry & Engineering **2**, 2416–2425 (2014).

[274] A. P. Abbott, R. C. Harris, and K. S. Ryder, “Application of Hole Theory to Define Ionic Liquids by their Transport Properties †”, The Journal of Physical Chemistry B **111**, 4910–4913 (2007).

[275] R. Stefanovic, M. Ludwig, G. B. Webber, R. Atkin, and A. J. Page, “Nanostructure, hydrogen bonding and rheology in choline chloride deep eutectic solvents as a function of the hydrogen bond donor”, Physical Chemistry Chemical Physics **19**, 3297–3306 (2016).

[276] R. Haghbakhsh, S. Raeissi, K. Parvaneh, and A. Shariati, “The friction theory for modeling the viscosities of deep eutectic solvents using the CPA and PC-SAFT equations of state”, Journal of Molecular Liquids **249**, 554–561 (2018).

[277] O. Lötgering-Lin and J. Gross, “Group Contribution Method for Viscosities Based on Entropy Scaling Using the Perturbed-Chain Polar Statistical Associating Fluid Theory”, Industrial & Engineering Chemistry Research **54**, 7942–7952 (2015).

[278] W. A. Fouad and L. F. Vega, “Transport properties of HFC and HFO based refrigerants using an excess entropy scaling approach”, The Journal of Supercritical Fluids **131**, 106–116 (2018).

[279] B. Gurkan, H. Squire, and E. Pentzer, "Metal-Free Deep Eutectic Solvents: Preparation, Physical Properties, and Significance", The Journal of Physical Chemistry Letters **10**, 7956–7964 (2019).

[280] D. v. d. Spoel, P. J. v. Maaren, P. Larsson, and N. Tîmneanu, "Thermodynamics of Hydrogen Bonding in Hydrophilic and Hydrophobic Media", The Journal of Physical Chemistry B **110**, 4393–4398 (2006).

[281] A. Luzar, "Resolving the hydrogen bond dynamics conundrum", The Journal of Chemical Physics **113**, 10663–10675 (2000).

[282] W. A. Fouad, L. Wang, A. Haghmoradi, D. Asthagiri, and W. G. Chapman, "Understanding the Thermodynamics of Hydrogen Bonding in Alcohol-Containing Mixtures: Cross-Association", The Journal of Physical Chemistry B **120**, 3388–3402 (2016).

[283] R. Ahmadi, B. Hemmateenejad, A. Safavi, Z. Shojaeifard, A. Shahsavar, A. Mohajeri, M. H. Dokoohaki, and A. R. Zolghadr, "Deep eutectic–water binary solvent associations investigated by vibrational spectroscopy and chemometrics", Physical Chemistry Chemical Physics **20**, 18463–18473 (2018).

[284] Y. Liu, J. B. Friesen, J. B. McAlpine, D. C. Lankin, S.-N. Chen, and G. F. Pauli, "Natural Deep Eutectic Solvents: Properties, Applications, and Perspectives", Journal of Natural Products **81**, 679–690 (2018).

[285] M. H. Zainal-Abidin, M. Hayyan, A. Hayyan, and N. S. Jayakumar, "New horizons in the extraction of bioactive compounds using deep eutectic solvents: A review", Analytica Chimica Acta **979**, 1–23 (2017).

[286] A. Roosta, R. Haghbakhsh, A. R. C. Duarte, and S. Raeissi, "Machine learning coupled with group contribution for predicting the density of deep eutectic solvents", Fluid Phase Equilibria **565**, 113672 (2023).

[287] H. Monteiro, A. Paiva, A. R. C. Duarte, and N. Galamba, "Structure and Dynamic Properties of a Glycerol–Betaine Deep Eutectic Solvent: When Does a DES Become an Aqueous Solution?", ACS Sustainable Chemistry & Engineering **10**, 3501–3512 (2022).

[288] V. Alizadeh, F. Malberg, A. A. H. Pádua, and B. Kirchner, "Are There Magic Compositions in Deep Eutectic Solvents? Effects of Composition and Water Content in Choline Chloride/Ethylene Glycol from Ab Initio Molecular Dynamics", The Journal of Physical Chemistry B **124**, 7433–7443 (2020).

[289] I. Alfurayj, C. C. Fraenza, Y. Zhang, R. Pandian, S. Spittle, B. Hansen, W. Dean, B. Gurkan, R. Savinell, S. Greenbaum, E. Maginn, J. Sangoro, and C. Burda, "Solvation Dynamics of Wet Ethaline: Water is the Magic Component", The Journal of Physical Chemistry B **125**, 8888–8901 (2021).

[290] S. Rozas, C. Benito, R. Alcalde, M. Atilhan, and S. Aparicio, "Insights on the water effect on deep eutectic solvents properties and structuring: The archetypical case of choline chloride + ethylene glycol", Journal of Molecular Liquids **344**, 117717 (2021).

[291] A. Gutiérrez, M. Atilhan, and S. Aparicio, "Molecular dynamics study on water confinement in deep eutectic solvents", Journal of Molecular Liquids **339**, 116758 (2021).

[292] E. S. C. Ferreira, I. V. Voroshylova, N. M. Figueiredo, and M. N. D. S. Cordeiro, "Molecular dynamic study of alcohol-based deep eutectic solvents", The Journal of Chemical Physics **155**, 064506 (2021).

[293]H Zuidema and G. Waters, “Ring Method for the Determination of Interfacial Tension”, Industrial & Engineering Chemistry Analytical Edition **13**, 312–313 (1941).

[294]Z Cui, Z Li, Z Gao, R Zhang, and J Li, “Vapor-liquid equilbrium for water-1, 2-propanediol binary system at 101.325 kpa”, Chinese Journal of Chemical Engineering **8**, 374–378 (1994).

[295]M. T. Parsons, F. W. Lau, E. G. Yee, and Y. Koga, “Excess Chemical Potentials and Partial Molar Enthalpies in Aqueous 1,2- and 1,3-Propanediols at 25°C”, Journal of Solution Chemistry **32**, 137–153 (2003).

[296]K Jelínek, F Lešek, and M Sivoková, “Vapour-liquid equlibrium in binary water-1,2-propylene glycol, water-diethylene glycol and water-1,4-butandiol systems”, Collection of Czechoslovak Chemical Communications **41**, 2650–2656 (1976).

[297]R. Huang and D. Zhang, “Determination and correlation of isothermal vapor-liquid equilibrium data for the binary system of water-1, 4-butanediol”, Shiyou Huagong, 497–502 (1987).

[298]M. Moosavi and A. A. Rostami, “Densities, Viscosities, Refractive Indices, and Excess Properties of Aqueous 1,2-Etanediol, 1,3-Propanediol, 1,4-Butanediol, and 1,5-Pentanediol Binary Mixtures”, Journal of Chemical & Engineering Data **62**, 156–168 (2017).

[299]T. Sun and A. S. Teja, “Density, Viscosity, and Thermal Conductivity of Aqueous Ethylene, Diethylene, and Triethylene Glycol Mixtures between 290 K and 450 K”, Journal of Chemical & Engineering Data **48**, 198–202 (2003).

[300]M. d. C. Grande, J. A. Juliá, C. R. Barrero, and C. M. Marschoff, “Density, sound velocity and refractive index in the water + 1,2-dimethoxyethane system”, Physics and Chemistry of Liquids **53**, 403–417 (2015).

[301]D. A. Soldatović, J. M. Vuksanović, I. R. Radović, and M. L. Kijevčanin, “Thermodynamic and spectroscopic interpretation of molecular interactions of nicotine+alcohol binary mixtures”, The Journal of Chemical Thermodynamics **102**, 105–129 (2016).

[302]T. Sun and A. S. Teja, “Density, Viscosity and Thermal Conductivity of Aqueous Solutions of Propylene Glycol, Dipropylene Glycol, and Tripropylene Glycol between 290 K and 460 K”, Journal of Chemical & Engineering Data **49**, 1311–1317 (2004).

[303]U. Domańska, P. Papis, J. Szydłowski, M. Królikowska, and M. Królikowski, “Excess Enthalpies of Mixing, Effect of Temperature and Composition on the Density, and Viscosity and Thermodynamic Properties of Binary Systems of {Ammonium-Based Ionic Liquid + Alkanediol}”, The Journal of Physical Chemistry B **118**, 12692–12705 (2014).

[304]J. Bleazard, T. Sun, R. Johnson, R. DiGuillio, and A. Teja, “The transport properties of seven alkanediols”, Fluid Phase Equilibria **117**, 386–393 (1996).

[305]C. Yang, P. Ma, and Q. Zhou, “Excess Molar Volume, Viscosity, and Heat Capacity for the Mixtures of 1,4-Butanediol + Water at Different Temperatures”, Journal of Chemical & Engineering Data **49**, 582–587 (2004).

[306]J. George and N. V. Sastry, “Densities, Dynamic Viscosities, Speeds of Sound, and Relative Permittivities for Water + Alkanediols (Propane-1,2- and -1,3-diol and Butane-1,2-, -1,3-, -1,4-, and -2,3-Diol) at Different Temperatures”, Journal of Chemical & Engineering Data **48**, 1529–1539 (2003).

[307]M. L. Huber, R. A. Perkins, A. Laesecke, D. G. Friend, J. V. Sengers, M. J. Assael, I. N. Metaxa, E. Vogel, R. Mareš, and K. Miyagawa, “New International Formulation for the Viscosity of H2O”, Journal of Physical and Chemical Reference Data **38**, 101–125 (2009).

[308] R. Zangi, "Refinement of the OPLSAA Force-Field for Liquid Alcohols", ACS Omega **3**, 18089–18099 (2018).

[309] J. L. F. Abascal and C. Vega, "A general purpose model for the condensed phases of water: TIP4P/2005", The Journal of Chemical Physics **123**, 234505 (2005).

[310] M. J. Abraham, T. Murtola, R. Schulz, S. Páll, J. C. Smith, B. Hess, and E. Lindahl, "GROMACS: High performance molecular simulations through multi-level parallelism from laptops to supercomputers", SoftwareX **1**, 19–25 (2015).

[311] L. Zhao, X. Wang, L. Wang, and H. Sun, "Prediction of shear viscosities using periodic perturbation method and OPLS force field", Fluid Phase Equilibria **260**, 212–217 (2007).

[312] J. S. Rowlinson and B. Widom, *Molecular Theory of Capillarity*, edited by C. Corporation (2002).

[313] K. Mulia, D. Adam, I. Zahrina, and E. Krisanti, "Green Extraction of Palmitic Acid from Palm Oil using Betaine-Based Natural Deep Eutectic Solvents", International Journal of Technology **9**, 335–344 (2018).

[314] Y. Hou, B. Zhang, M. Gao, S. Ren, and W. Wu, "Densities, viscosities and specific heat capacities of deep eutectic solvents composed of ethanediol + betaine and ethanediol + L-carnitine for absorbing SO2", The Journal of Chemical Thermodynamics **179**, 106999 (2023).

[315] L. A. Rodrigues, M. Cardeira, I. C. Leonardo, F. B. Gaspar, I. R. Redovniković, A. R. C. Duarte, A. Paiva, and A. A. Matias, "Deep eutectic systems from betaine and polyols – Physicochemical and toxicological properties", Journal of Molecular Liquids **335**, 116201 (2021).

[316] F. Z. Nessakh, F. Mutelet, and A. Negadi, "Efficiency of two working fluids constituted of a deep eutectic solvent and water in absorption heat transformer", International Journal of Energy Research **46**, 23578–23594 (2022).

[317] S. Anđelović, M. Božinović, Ćurić, A. Šalić, A. J. Tušek, K. Z. Kučan, M. Rogošić, M. Radović, M. C. Bubalo, and B. Zelić, "Deep Eutectic Solvents for Biodiesel Purification in a Microextractor: Solvent Preparation, Selection and Process Optimization", Bioengineering **9**, 665 (2022).

[318] K. Z. Kučan, M. Perković, K. Cmrk, D. Načinović, and M. Rogošić, "Betaine + (Glycerol or Ethylene Glycol or Propylene Glycol) Deep Eutectic Solvents for Extractive Purification of Gasoline", ChemistrySelect **3**, 12582–12590 (2018).

[319] Q. Chen, N. He, J. Fan, and F. Song, "Physical Properties of Betaine-1,2-Propanediol-Based Deep Eutectic Solvents", Polymers **14**, 1783 (2022).

[320] N. He, Q. Chen, J. Fan, F. Song, Y. Zhang, and H. Mu, "Comprehensive exploration of the adsorption capacity of innovative betaine-based deep eutectic solvents for carbon dioxide capture", The Journal of Chemical Thermodynamics **178**, 106958 (2023).

[321] I. Zahrina, M. Nasikin, E. Krisanti, and K. Mulia, "Deacidification of palm oil using betaine monohydrate-based natural deep eutectic solvents", Food Chemistry **240**, 490–495 (2018).

[322] K Mulia, E Krisanti, Nasruddin, and E Libriandy, "Betaine-based deep eutectic solvents with diol, acid and amine hydrogen bond donors for carbon dioxide absorption", Journal of Physics: Conference Series **1295**, 012039 (2019).

[323] M. Barzegar-Jalali, P. Jafari, and A. Jouyban, "Thermodynamic study of the aqueous pseudo-binary mixtures of betaine-based deep eutectic solvents at T = (293.15 to 313.15) K", Physics and Chemistry of Liquids **60**, 651–666 (2022).

[324]M. Rogošić, A. Krišto, and K. Z. Kučan, "Deep Eutectic Solvents based on Betaine and Propylene Glycol as Potential Denitrification Agents: A Liquid-Liquid Equilibrium Study", Brazilian Journal of Chemical Engineering **36**, 1703–1716 (2020).

[325]F. M. Fuad and M. M. Nadzir, "The formulation and physicochemical properties of betaine-based natural deep eutectic solvent", Journal of Molecular Liquids **360**, 119392 (2022).

[326]G. García, S. Aparicio, R. Ullah, and M. Atilhan, "Deep Eutectic Solvents: Physicochemical Properties and Gas Separation Applications", Energy & Fuels **29**, 2616–2644 (2015).

[327]Q. Zhang, K. D. O. Vigier, S. Royer, and F. Jérôme, "Deep eutectic solvents: syntheses, properties and applications", Chemical Society Reviews **41**, 7108–7146 (2012).

[328]A. P. Abbott, A. Y. Al-Murshedi, O. A. Alshammari, R. C. Harris, J. H. Kareem, I. B. Qader, and K. Ryder, "Thermodynamics of phase transfer for polar molecules from alkanes to deep eutectic solvents", Fluid Phase Equilibria **448**, 99–104 (2017).

[329]C. D'Agostino, R. C. Harris, A. P. Abbott, L. F. Gladden, and M. D. Mantle, "Molecular motion and ion diffusion in choline chloride based deep eutectic solvents studied by 1 H pulsed field gradient NMR spectroscopy", Physical Chemistry Chemical Physics **13**, 21383–21391 (2011).

[330]R. C. Harris, "Physical Properties of Alcohol Based Deep Eutectic Solvents", PhD thesis (University of Leicester, May 2009).

[331]J. M. Klein, H. Squire, W. Dean, and B. E. Gurkan, "From Salt in Solution to Solely Ions: Solvation of Methyl Viologen in Deep Eutectic Solvents and Ionic Liquids", The Journal of Physical Chemistry B **124**, 6348–6357 (2020).

[332]D. Lapeña, L. Lomba, M. Artal, C. Lafuente, and B. Giner, "Thermophysical characterization of the deep eutectic solvent choline chloride:ethylene glycol and one of its mixtures with water", Fluid Phase Equilibria **492**, 1–9 (2019).

[333]E. L. Smith, A. P. Abbott, and K. S. Ryder, "Deep Eutectic Solvents (DESs) and Their Applications", Chemical Reviews **114**, 11060–11082 (2014).

[334]S. M. M. Shuwa, B. Y. Y. Jibril, Y. M. M. Al-Wahaibi, and R. S. S. Al-Hajri, "Heavy-Oil-Recovery Enhancement With Choline Chloride/Ethylene Glycol-Based Deep Eutectic Solvent", SPE Journal **20**, 79–87 (2014).

[335]A. Y. M. Al-Murshedi, H. F. Alesary, and R. Al-Hadrawi, "Thermophysical properties in deep eutectic solvents with/without water", Journal of Physics: Conference Series **1294**, 052041 (2019).

[336]X. Liu, M. Wang, X. Zhang, Y. Sun, W. Song, and Y. Liu, "The correlation between the physicochemical properties of water-based deep eutectic solvents and catalytic activity of lipase Novozym 435", Journal of Molecular Liquids **325**, 115200 (2021).

[337]G. Li, C. Gui, R. Zhu, and Z. Lei, "Deep eutectic solvents for efficient capture of cyclohexane in volatile organic compounds: Thermodynamic and molecular mechanism", AIChE Journal **68**, `10.1002/aic.17535` (2022).

[338]A. Kityk, D. Shaiderov, E. Vasil'eva, V. Protsenko, and F. Danilov, "Choline chloride based ionic liquids containing nickel chloride: Physicochemical properties and kinetics of Ni(II) electroreduction", Electrochimica Acta **245**, 133–145 (2017).

[339]O. S. Hammond, A. Sanchez-Fernandez, R. Tyte, R. Dalgliesh, A. J. Smith, and K. J. Edler, "Mix-and-Match Diols: Adjusting Self-Assembly of Micellar Phases in Choline Chloride Eutectics", Crystals **12**, 1621 (2022).

[340]O. A. O. Alshammari, "Extraction of Natural Products using Deep Eutectic Solvents", PhD thesis (University of Leicester, Dec. 2021).

[341]S. Saleem, "Electropolishing in deep eutectic solvents", PhD thesis (University of Leicester, Jan. 2014).

[342]H. Huang, Y. Zhu, X. Fu, Y. Zou, Q. Li, and Z. Luo, "Integrated natural deep eutectic solvent and pulse-ultrasonication for efficient extraction of crocins from gardenia fruits (Gardenia jasminoides Ellis) and its bioactivities", Food Chemistry **380**, 132216 (2022).

[343]B. Tang and K. H. Row, "Recent developments in deep eutectic solvents in chemical sciences", Monatshefte für Chemie - Chemical Monthly **144**, 1427–1454 (2013).

[344]D. Shah and F. S. Mjalli, "Effect of water on the thermo-physical properties of Reline: An experimental and molecular simulation based approach", Physical Chemistry Chemical Physics **16**, 23900–23907 (2014).

[345]M. Kuddushi, G. S. Nangala, S. Rajput, S. P. Ijardar, and N. I. Malek, "Understanding the peculiar effect of water on the physicochemical properties of choline chloride based deep eutectic solvents theoretically and experimentally", Journal of Molecular Liquids **278**, 607–615 (2019).

[346]M. Li, C. Zhu, T. Fu, X. Gao, and Y. Ma, "Effect of water on amine-based deep eutectic solvents (choline chloride + monoethanolamine): Structure and physicochemical properties", Journal of Environmental Chemical Engineering **10**, 106952 (2022).

[347]B. Nowosielski, M. Jamrógiewicz, J. Łuczak, and D. Warmińska, "Novel Binary Mixtures of Alkanolamine Based Deep Eutectic Solvents with Water—Thermodynamic Calculation and Correlation of Crucial Physicochemical Properties", Molecules **27**, 788 (2022).

[348]F. Gabriele, M. Chiarini, R. Germani, M. Tiecco, and N. Spreti, "Effect of water addition on choline chloride/glycol deep eutectic solvents: Characterization of their structural and physicochemical properties", Journal of Molecular Liquids **291**, 111301 (2019).

[349]L. S. Bobrova, D. A. Shaiderov, K. A.A., V. S. Protsenko, and F. I. Danilov, "The effect of water addition on physicochemical properties of electrochemical systems based on deep eutectic solvents", Promising materials and processes in technical electrochemistry (2016).

[350]M. Sedghamiz and S. Raeissi, "Physical properties of deep eutectic solvents formed by the sodium halide salts and ethylene glycol, and their mixtures with water", Journal of Molecular Liquids **269**, 694–702 (2018).

[351]M. Brehm, M. Thomas, S. Gehrke, and B. Kirchner, "TRAVIS—A free analyzer for trajectories from molecular simulation", The Journal of Chemical Physics **152**, 164105 (2020).

[352]D. Vargas-Hernández, J. Rubio-Caballero, J. Santamaría-González, R. Moreno-Tost, J. Mérida-Robles, M. Pérez-Cruz, A. Jiménez-López, R. Hernández-Huesca, and P. Maireles-Torres, "Furfuryl alcohol from furfural hydrogenation over copper supported on SBA-15 silica catalysts", Journal of Molecular Catalysis A: Chemical **383**, 106–113 (2014).

[353]R. V. Sharma, U. Das, R. Sammynaiken, and A. K. Dalai, "Liquid phase chemo-selective catalytic hydrogenation of furfural to furfuryl alcohol", Applied Catalysis A: General **454**, 127–136 (2013).

[354]Q. Meng, H. Zheng, Y. Zhu, and Y. Li, "Study on the reaction pathway in decarbonylation of biomass-derived 5-hydroxymethylfurfural over Pd-based catalyst", Journal of Molecular Catalysis A: Chemical **421**, 76–82 (2016).

[355]D. Lebedeva, L. W. Schick, D. Cracco, W. Sangsuwan, G. Castiella-Ona, D. O. Silva, A. Marson, E. S. Grape, A. K. Inge, L. M. Rossi, E. Subbotina, A. Manzardo, and J. S. M. Samec, "Sustainable aviation fuel from prehydrolysis liquors", Green Chemistry **26**, 7258–7267 (2024).

[356]A. Rodríguez-Montaña, L. Y. Rache, M. H. Brijaldo, G. P. Romanelli, R. Luque, and J. J. Martinez, "Biocatalytic transformation of furfural into furfuryl alcohol using resting cells of Bacillus cereus", Catalysis Today **372**, 220–225 (2021).

[357]Z. Wang, X. Wang, C. Zhang, M. Arai, L. Zhou, and F. Zhao, "Selective hydrogenation of furfural to furfuryl alcohol over Pd/TiH2 catalyst", Molecular Catalysis **508**, 111599 (2021).

[358]M. Paniagua, J. Melero, J. Iglesias, G. Morales, B. Hernández, and C. López-Aguado, "Catalytic upgrading of furfuryl alcohol to bio-products: Catalysts screening and kinetic analysis", Applied Catalysis A: General **537**, 74–82 (2017).

[359]T. Wongsawa, M. Hronec, T. Soták, N. Leepipatpiboon, U. Pancharoen, and S. Phatanasri, "Ternary (liquid–liquid) equilibrium data of furfuryl alcohol with organic solvents at T =298.2K: Experimental results and thermodynamic models", Fluid Phase Equilibria **365**, 88–96 (2014).

[360]S. Dong, W. Sun, Y. Jiang, and B. Jia, "Liquid-liquid equilibrium study for ternary systems of (water + furfuryl alcohol + solvents) at 298.2 K: Measurement and thermodynamic modelling", The Journal of Chemical Thermodynamics **148**, 106136 (2020).

[361]Y. Han, M. Han, H. Yan, Q. Yin, and Q. Li, "Measurement and Correlation of Liquid–Liquid Equilibrium Data for Ternary Systems of Water + Furfuryl Alcohol + (1-Pentanol and n-Propyl Acetate) at Different Temperatures", Journal of Chemical & Engineering Data **66**, 2921–2928 (2021).

[362]T. Wannachod, M. Hronec, T. Soták, K. Fulajtárová, U. Pancharoen, and A. Arpornwichanop, "Effects of salt on the LLE and tie-line data for furfuryl alcohol — n-butanol–water at T=298.15K", Journal of Molecular Liquids **218**, 50–58 (2016).

[363]V. Brighenti, F. Pellati, M. Steinbach, D. Maran, and S. Benvenuti, "Development of a new extraction technique and HPLC method for the analysis of non-psychoactive cannabinoids in fibre-type Cannabis sativa L. (hemp)", Journal of Pharmaceutical and Biomedical Analysis **143**, 228–236 (2017).

[364]B. Patel, D. Wene, and Z. T. Fan, "Qualitative and quantitative measurement of cannabinoids in cannabis using modified HPLC/DAD method", Journal of Pharmaceutical and Biomedical Analysis **146**, 15–23 (2017).

[365]J.-C. d. Hemptinne, G. M. Kontogeorgis, R. Dohrn, I. G. Economou, A. t. Kate, S. Kuitunen, L. F. Žilnik, M. G. D. Angelis, and V. Vesovic, "A View on the Future of Applied Thermodynamics", Industrial & Engineering Chemistry Research **61**, 14664–14680 (2022).

[366]A. K. Dwamena, "Recent Advances in Hydrophobic Deep Eutectic Solvents for Extraction", Separations **6**, 9 (2019).

[367]J. Cao, M. Yang, F. Cao, J. Wang, and E. Su, "Tailor-made hydrophobic deep eutectic solvents for cleaner extraction of polyprenyl acetates from Ginkgo biloba leaves", Journal of Cleaner Production **152**, 399–405 (2017).

[368]C. Florindo, L. Branco, and I. Marrucho, "Development of hydrophobic deep eutectic solvents for extraction of pesticides from aqueous environments", Fluid Phase Equilibria **448**, 135–142 (2017).

[369]D. J. G. P. v. Osch, C. H. J. T. Dietz, S. E. E. Warrag, and M. C. Kroon, "The Curious Case of Hydrophobic Deep Eutectic Solvents: A Story on the Discovery, Design, and Applications", ACS Sustainable Chemistry & Engineering **8**, 10591–10612 (2020).

[370]J. Cao and E. Su, "Hydrophobic deep eutectic solvents: the new generation of green solvents for diversified and colorful applications in green chemistry", Journal of Cleaner Production **314**, 127965 (2021).

[371]C. Velez and O. Acevedo, "Simulation of deep eutectic solvents: Progress to promises", Wiley Interdisciplinary Reviews: Computational Molecular Science **12**, `10.1002/wcms.1598` (2022).

[372]D. Tolmachev, N. Lukasheva, R. Ramazanov, V. Nazarychev, N. Borzdun, I. Volgin, M. Andreeva, A. Glova, S. Melnikova, A. Dobrovskiy, S. A. Silber, S. Larin, R. M. d. Souza, M. C. C. Ribeiro, S. Lyulin, and M. Karttunen, "Computer Simulations of Deep Eutectic Solvents: Challenges, Solutions, and Perspectives", International Journal of Molecular Sciences **23**, 645 (2022).

[373]S. J. Marrink, L. Monticelli, M. N. Melo, R. Alessandri, D. P. Tieleman, and P. C. T. Souza, "Two decades of Martini: Better beads, broader scope", Wiley Interdisciplinary Reviews: Computational Molecular Science **13**, `10.1002/wcms.1620` (2022).

[374]P. Vainikka, S. Thallmair, P. C. T. Souza, and S. J. Marrink, "Martini 3 Coarse-Grained Model for Type III Deep Eutectic Solvents: Thermodynamic, Structural, and Extraction Properties", ACS Sustainable Chemistry & Engineering **9**, 17338–17350 (2021).

[375]L. I. Vazquez-Salazar, M. Selle, A. H. d. Vries, S. J. Marrink, and P. C. T. Souza, "Martini coarse-grained models of imidazolium-based ionic liquids: from nanostructural organization to liquid–liquid extraction", Green Chemistry **22**, 7376–7386 (2020).

[376]R. Alessandri, J. Barnoud, A. S. Gertsen, I. Patmanidis, A. H. d. Vries, P. C. T. Souza, and S. J. Marrink, "Martini 3 Coarse-Grained Force Field: Small Molecules", Advanced Theory and Simulations **5**, 2100391 (2022).

[377]H. Guerrero, C. Lafuente, F. Royo, L. Lomba, and B. Giner, "PρT Behavior of Several Chemicals from Biomass", Energy & Fuels **25**, 3009–3013 (2011).

[378]L. Negadi, I. Mokbel, N. Chiali-Baba-Ahmed, and L. Kara-Zaitri, "Phase equilibrium properties of binary mixtures containing 2,5-dimethylfuran and furfuryl alcohol or methyl isobutyl ketone at several temperatures", The Journal of Chemical Thermodynamics **70**, 233–238 (2014).

[379]Y. Zhang, S. E. Feller, B. R. Brooks, and R. W. Pastor, "Computer simulation of liquid/liquid interfaces. I. Theory and application to octane/water", The Journal of Chemical Physics **103**, 10252–10266 (1995).

[380]H. Berendsen, D. v. d. Spoel, and R. v. Drunen, "GROMACS: A message-passing parallel molecular dynamics implementation", Computer Physics Communications **91**, 43–56 (1995).

[381]I. G. Tironi, R. Sperb, P. E. Smith, and W. F. v. Gunsteren, "A generalized reaction field method for molecular dynamics simulations", The Journal of Chemical Physics **102**, 5451–5459 (1995).

[382]S. M. Vilas-Boas, M. C. d. Costa, J. A. P. Coutinho, O. Ferreira, and S. P. Pinho, "Octanol–Water Partition Coefficients and Aqueous Solubility Data of Monoterpenoids: Experimental, Modeling, and Environmental Distribution", Industrial & Engineering Chemistry Research **61**, 3154–3167 (2022).

[383]W. J. Dunn, J. H. Block, and R. S. Pearlman, "Partition coefficient: Determination and estimation", (1986).

A. Appendix

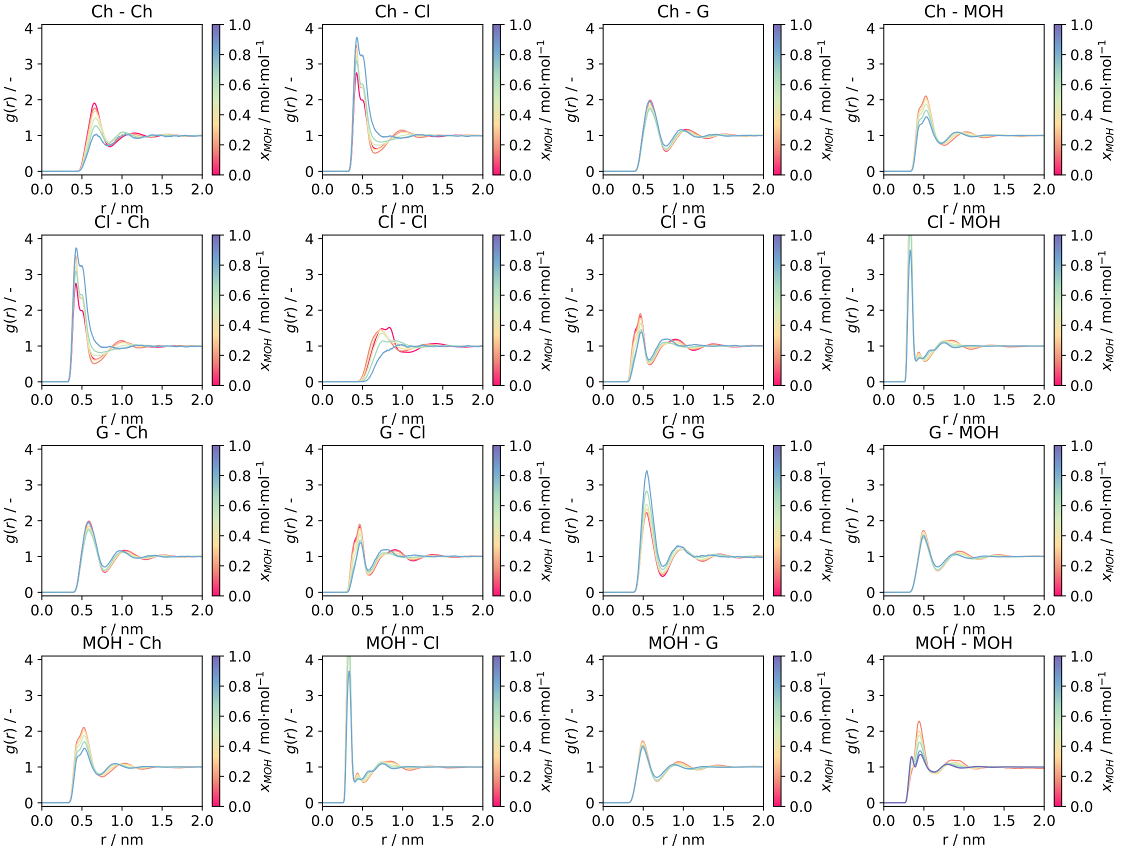

FIGURE A.1: Center-of-mass RDFs for ChCl:G(1:2) plus methanol at different methanol mole fraction.

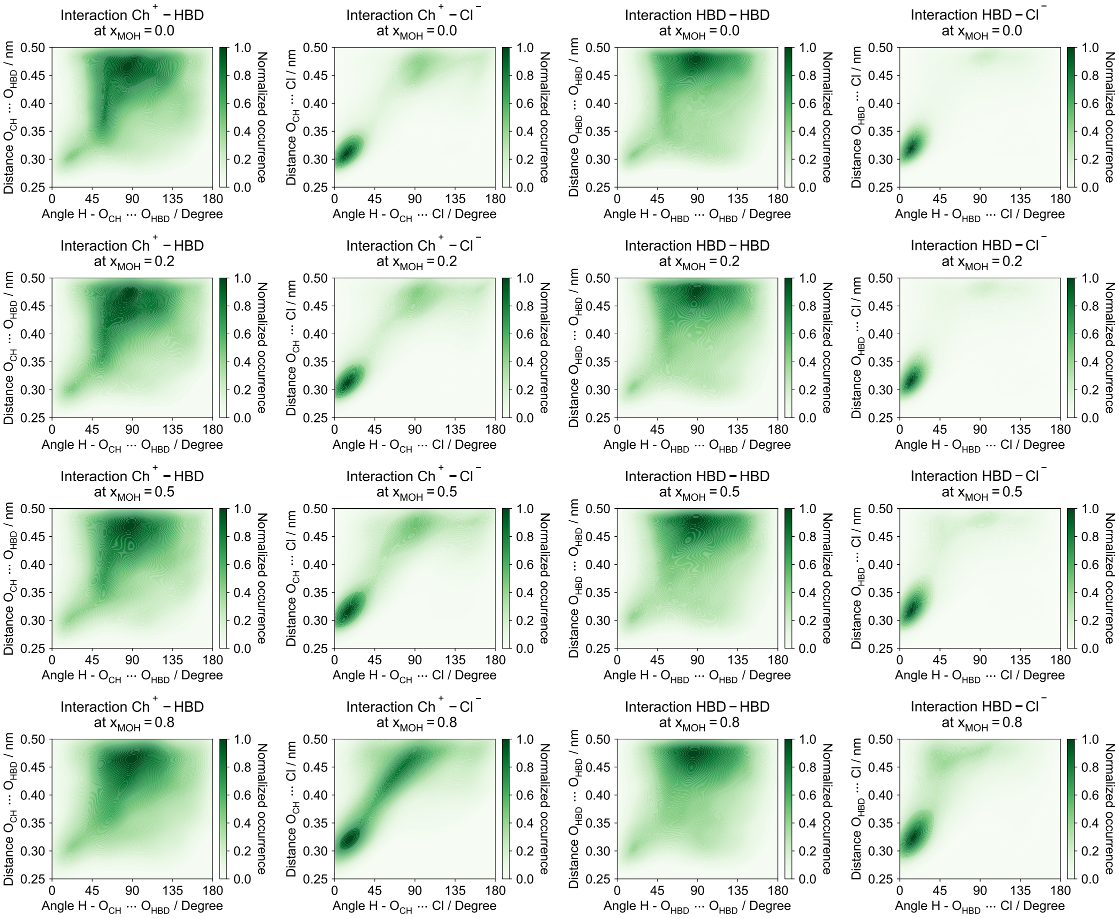

FIGURE A.2: Combined distribution functions for ChCl:G(1:2) plus methanol at different methanol mole fraction. The plot illustrates the relationship between the angle and distance for interactions involving the choline oxygen atom (O_{OH}), the chloride anion (Cl), and the HBD oxygen atoms (O_{HBD}).

B. Appendix

Figures

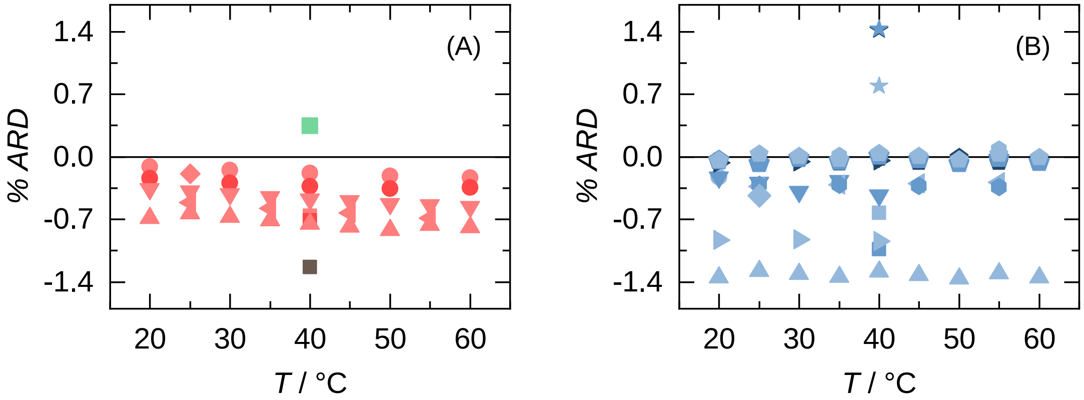

FIGURE B.1: Percentage deviations $\%ARD = 100 * (\rho_{exp} - \rho_{lit})/\rho_{exp}$ of the experimental density data (ρ_{exp}) measured in this work, from the literature values (ρ_{lit}) of Bet-based DESs and (A) EG, 13P or 14B and (B) 12P. Literature data was reported for Bet:EG (red) [313–318], Bet:12P (blue) [313, 318–325] , Bet:13P (green) [313], and Bet:14B (gray) [313].

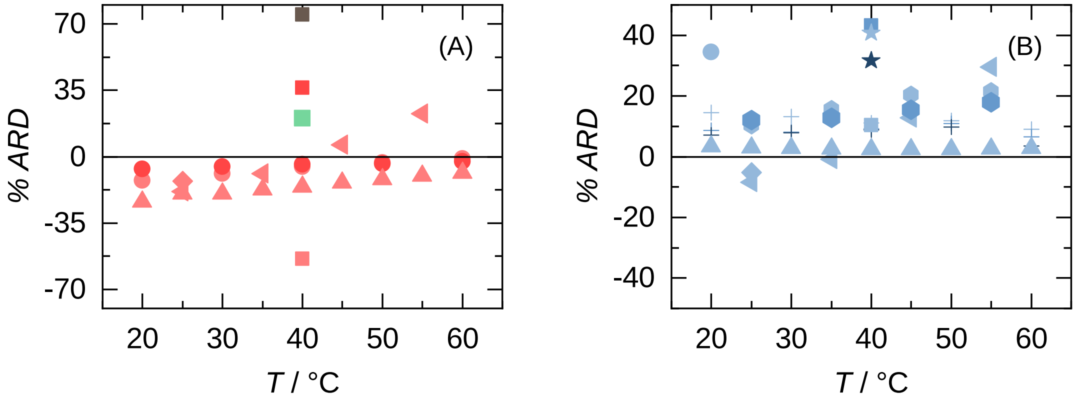

FIGURE B.2: Percentage deviations $\%ARD = 100 * (\eta_{exp} - \eta_{lit})/\eta_{exp}$ of the experimental viscosity data (η_{exp}) measured in this work, from the literature values (η_{lit}) of Bet-based DESs and (A) EG, 13P or 14B, or (B) 12P. Literature data were reported for (i) Bet:EG(1:5) (●) by Mulia et al. [313] (water concentration no reported), and Hou et al. [314] (water concentration of 0.4% w/w); (ii) Bet:EG(1:4) (●) by Mulia et al. [313], water concentration no reported), Hou et al. [314], water concentration of 0.4% w/w reported), Rodrigues et al. [315], (HBA:HBD molar ratio of 1:3 with water concentration of 1.2% w/w reported), Andelovic et al. [317] (HBA:HBD molar ratio of 1:3 with water concentration no reported), and Kucan et al. [318] (HBA:HBD molar ratio of 1:3 with water concentration no reported); (iii) Bet:12P(1:6) (●) by Chen et al. [319] (water concentration no reported), and Zahrina et al. [321] (water concentration of 3.5% w/w reported); (iv) Bet:12P(1:5) (●) by Chen et al. [319] (water concentration no reported), Mulia et al. [313] (water concentration no reported), and Rogosic et al. [324] (water concentration no reported); (v) Bet:12P(1:4) (●) by Chen et al. [319] (water concentration no reported), Fuad et al. [325] (water concentration of 0.4% w/w reported), Mulia et al. [313] (water concentration no reported), Kucan et al. [318] (HBA:HBD molar ratio of 1:3.5 with water concentration no reported), and Rogosic et al. [324] (water concentration no reported), Zahrina et al. [321] (water concentration of 5% w/w reported); (vi) Bet:13P(1:4) (●) by Mulia et al. [313] (water concentration no reported); and (vii) Bet:14B(1:5) (●) by Mulia et al. [313] (with water concentration no reported).

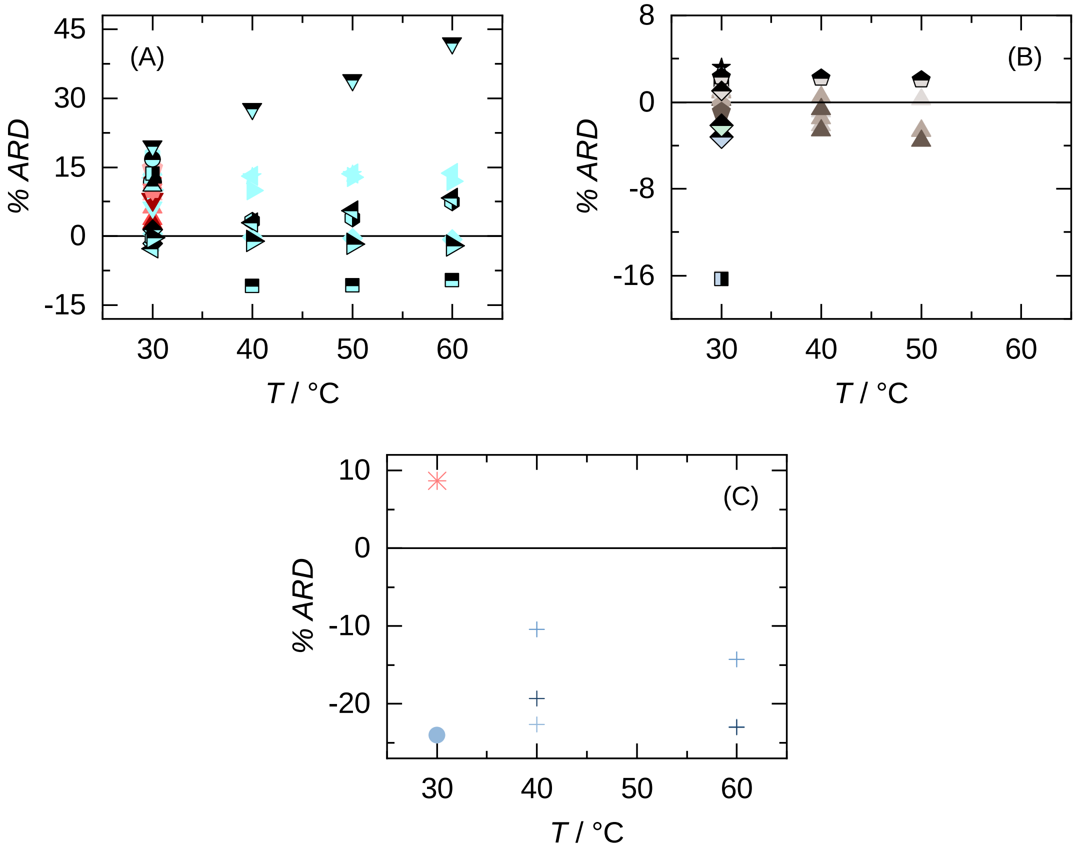

FIGURE B.3: Percentage deviations $\%ARD = 100 \cdot (\gamma_{exp} - \gamma_{lit})/\gamma_{exp}$ of the experimental surface tension data (γ_{exp}) measured in this work as a function of the temperature (°C) at a pressure of 101.3 kPa, from the literature values [156, 207, 213, 238, 240, 252, 274, 319, 328–343] (γ_{lit}) of (A) ChCl-based DESs with EG, (B) ChCl-based DESs with other glycols, and (C) Bet-based DESs.

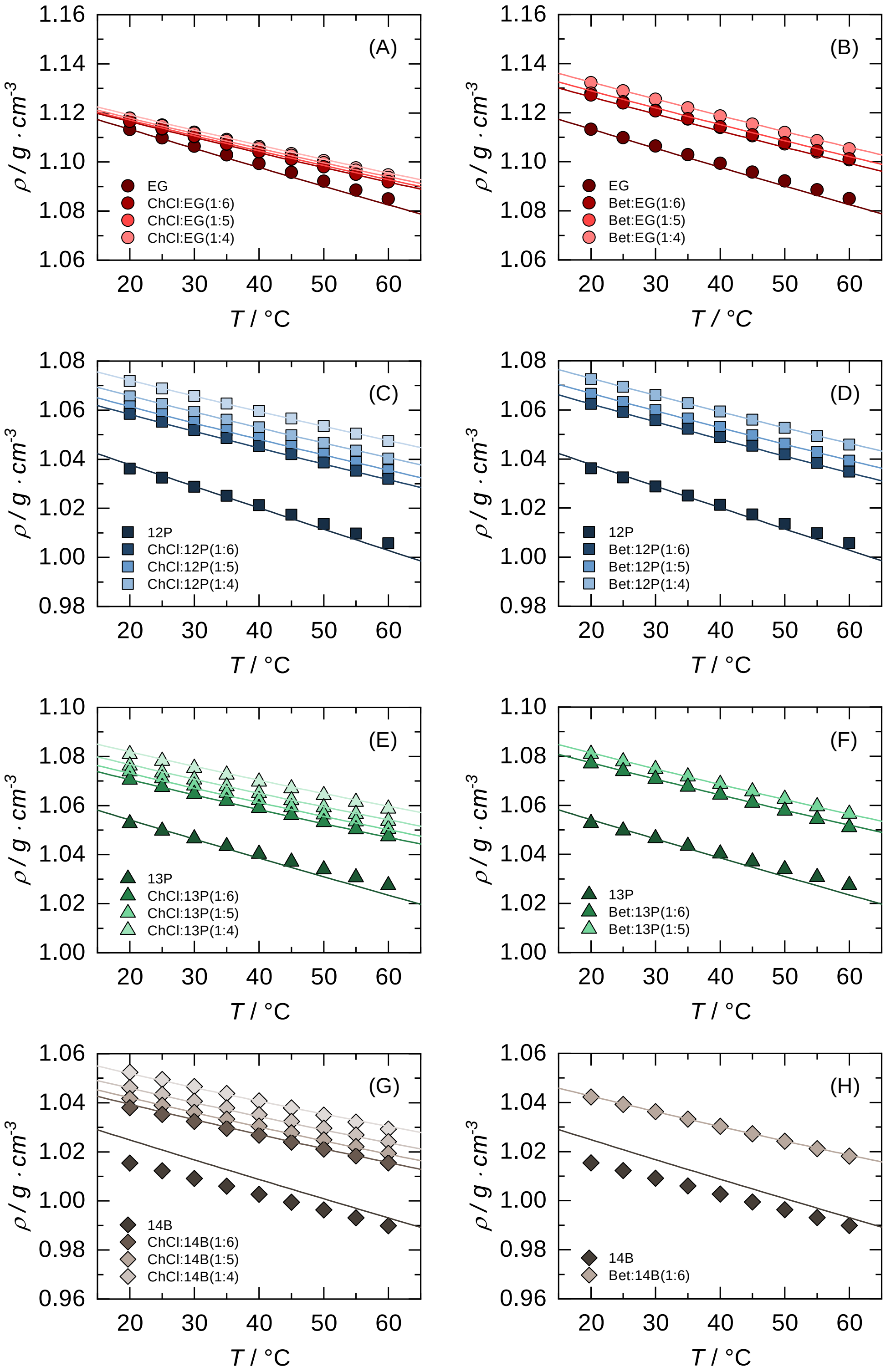

FIGURE B.4: Densities at atmospheric pressure and different temperatures for ChCl-based and Bet-based DESs. Symbols are experimental data. Solid lines represent the PC-SAFT calculation using parameters reported in Tables 7.2 and 7.3.

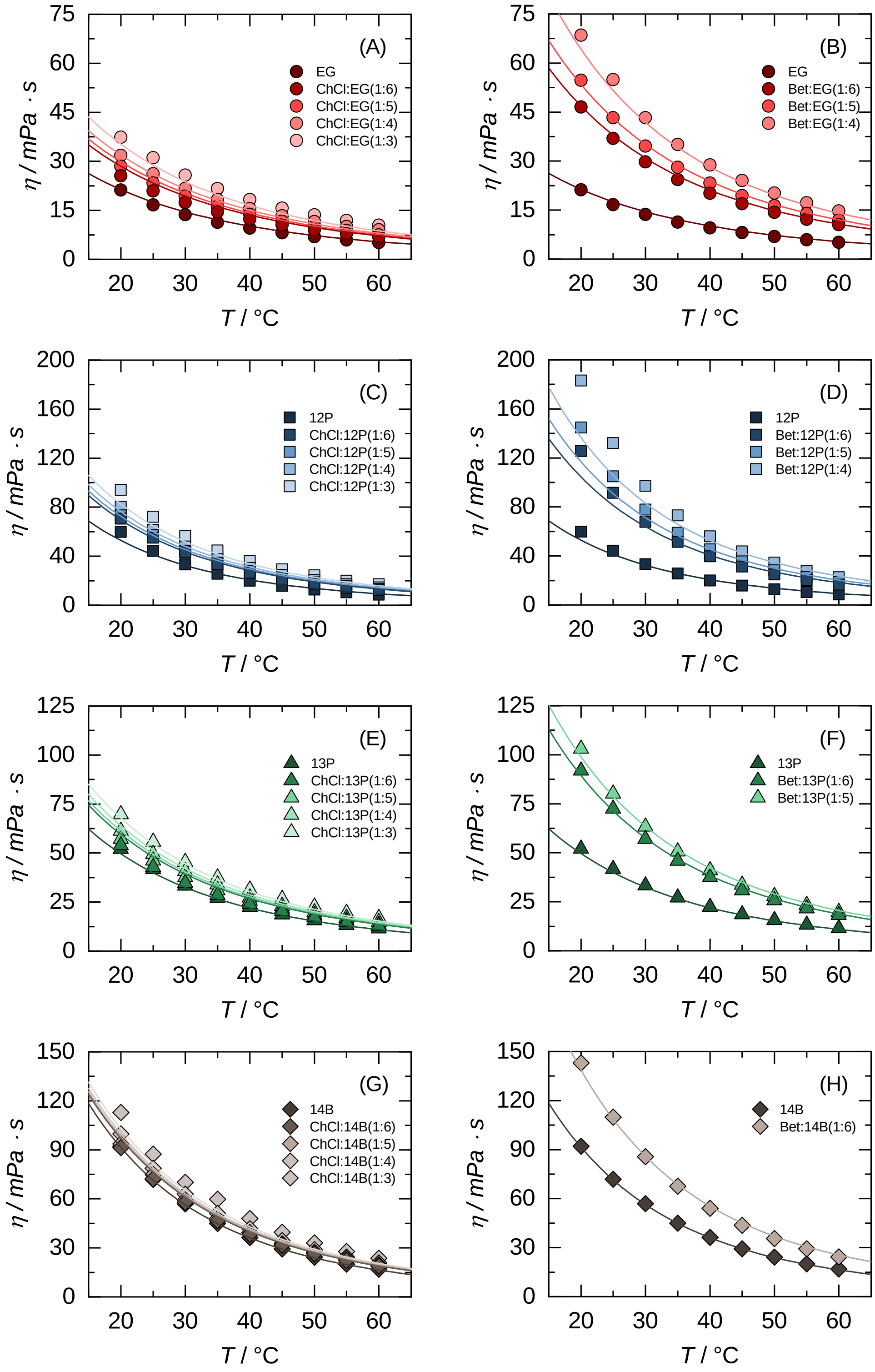

FIGURE B.5: Viscosity at different temperatures for ChCl-based and Bet-based DESs. Symbols are experimental data. Solid lines represent the PC-SAFT+FVT calculation using parameters reported in Tables 7.2, 7.3 and 7.4.

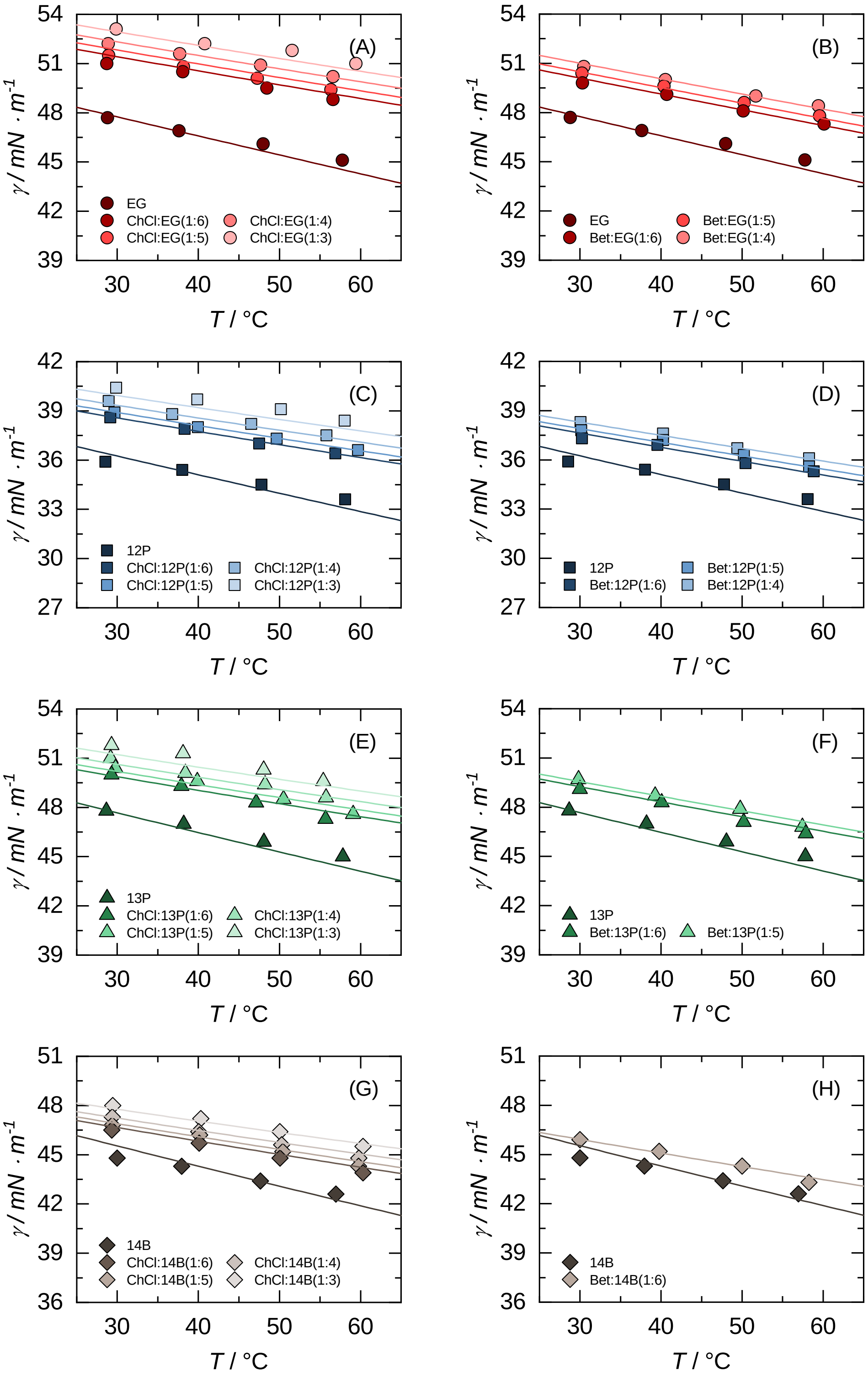

FIGURE B.6: Surface tension at different temperatures for ChCl-based and Bet-based DESs. Symbols are experimental data. Solid lines represent the PC-SAFT + DGT calculation using parameters reported in Tables 7.2, 7.3 and 7.5.

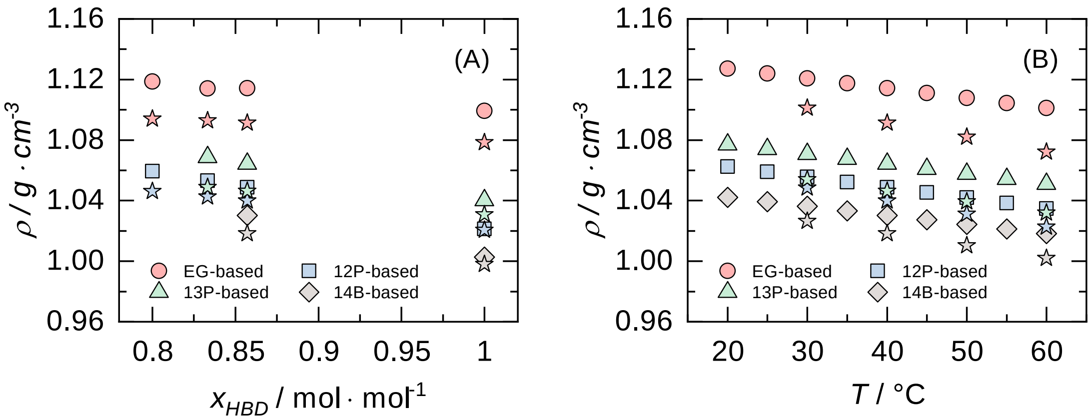

FIGURE B.7: Densities at atmospheric pressure for Bet-based DESs formed with different glycols as a function of the HBD mole fraction at 40°C (A), and as a function of temperature for an HBA:HBD molar ratio of 1:6 (B). Symbols except for stars: experimental data. Stars symbols: MD simulations.

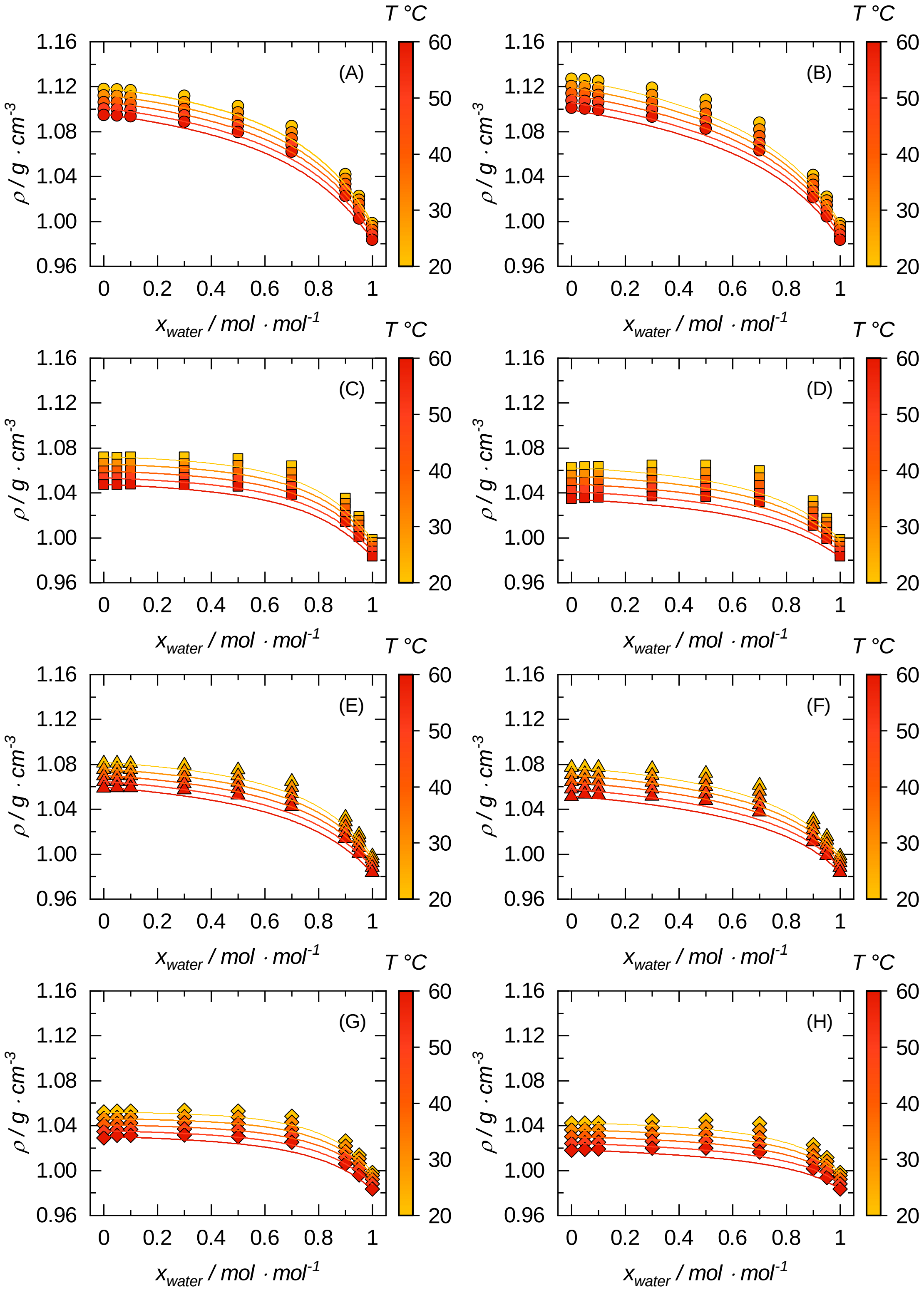

FIGURE B.8: Density for aqueous mixtures of ChCl-based and Bet-based DESs at different temperatures. Symbols are experimental data. Solid lines represent the PC-SAFT calculation using parameters reported in Tables 7.2 and 7.3.

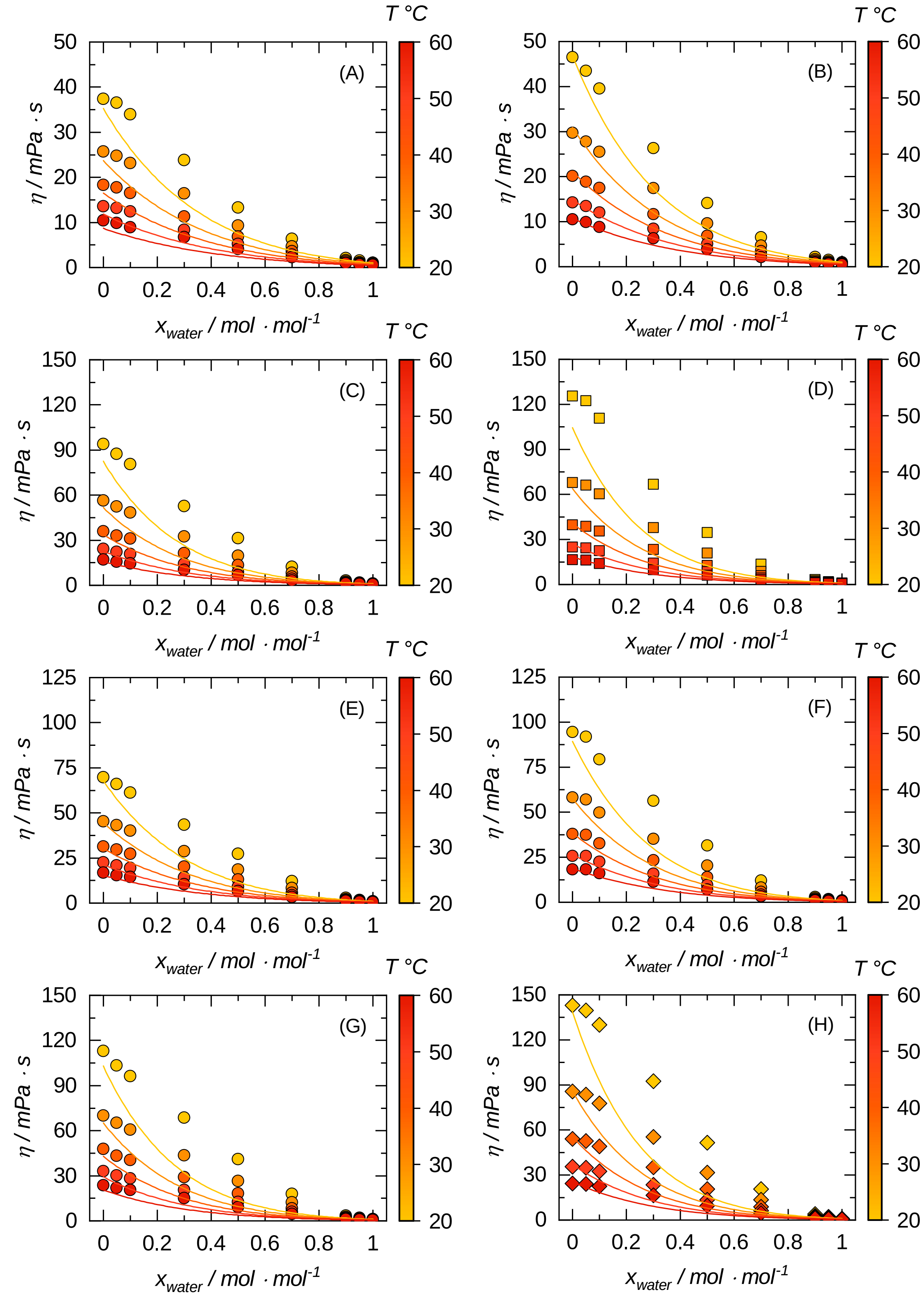

FIGURE B.9: Viscosity for aqueous mixtures of ChCl-based and Bet-based DESs at different temperatures. Symbols are experimental data. Solid lines represent the PC-SAFT + FVT using parameters reported in Tables 7.2, 7.3 and 7.4.

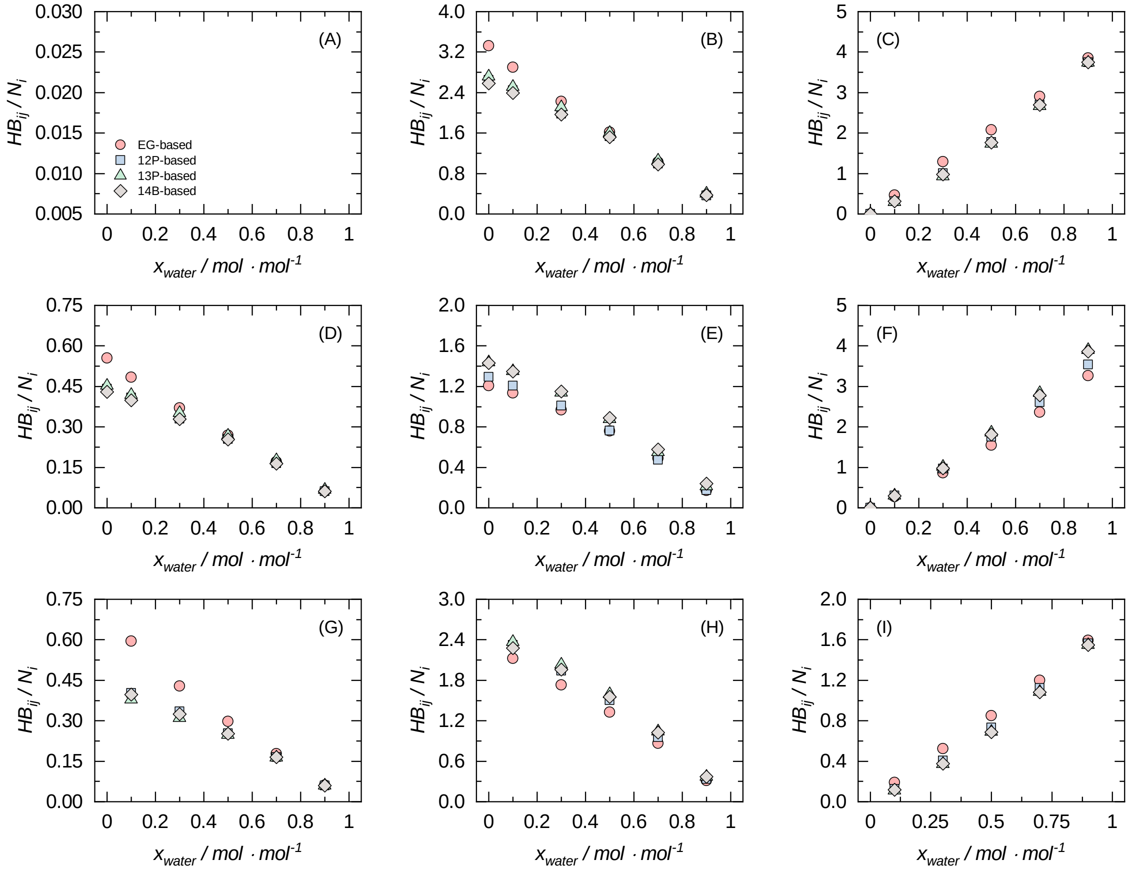

FIGURE B.10: Number of hydrogen bonds between molecule i and j per molecule i (HB_{ij}/N_i) as a function of the water mole fraction at 40°C for ChCl-based DESs obtained through MD. Molecule pairs i-j: (A) HBA-HBA, (B) HBA-HBD, (C) HBA-water, (D) HBD-HBA, (E) HBD-HBD, (F) HBD-water, (G) water-HBA, (H) water-HBD and (I) water-water.

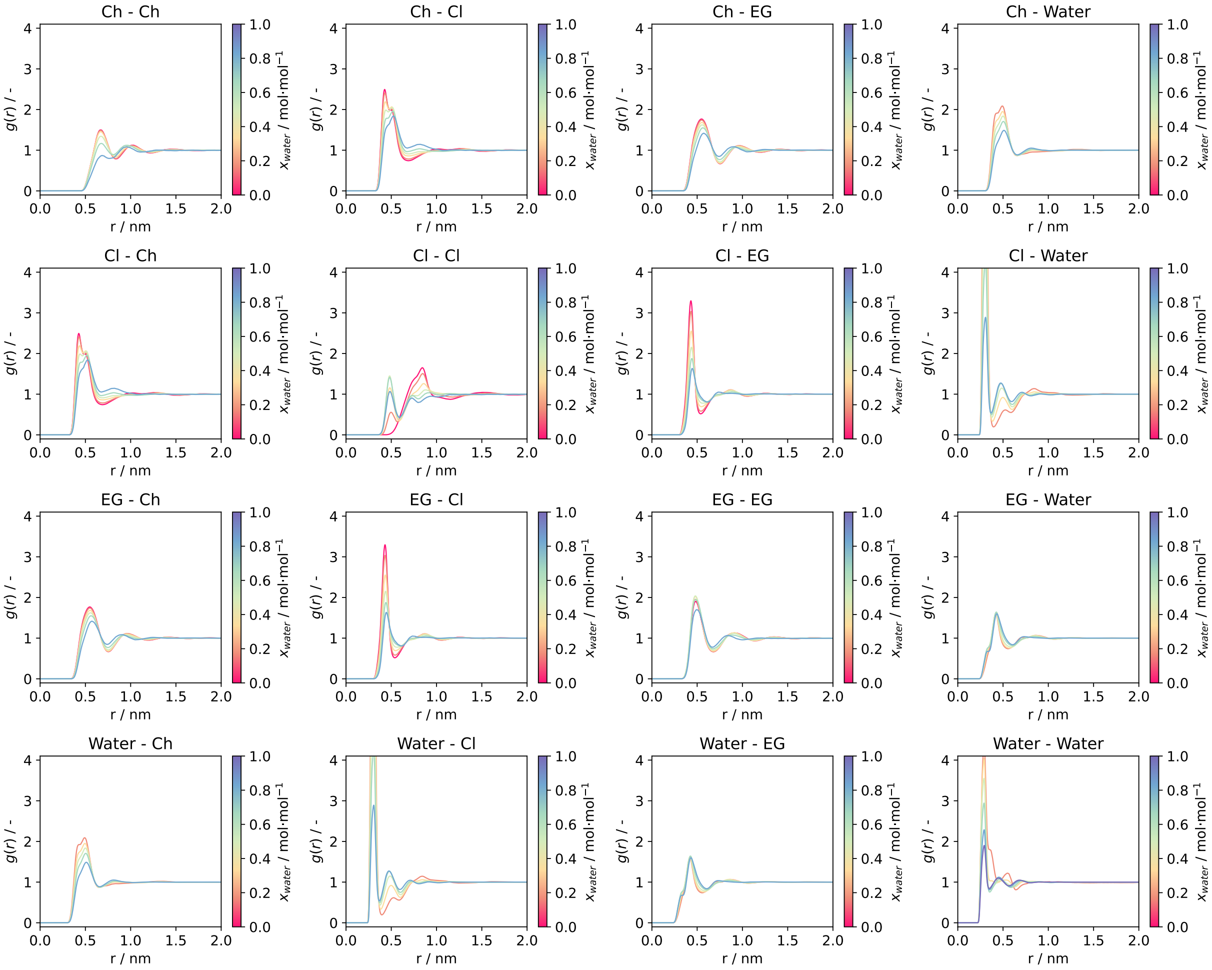

FIGURE B.11: RDFs of ChCl:EG(1:3) + water mixtures as a function of water content.

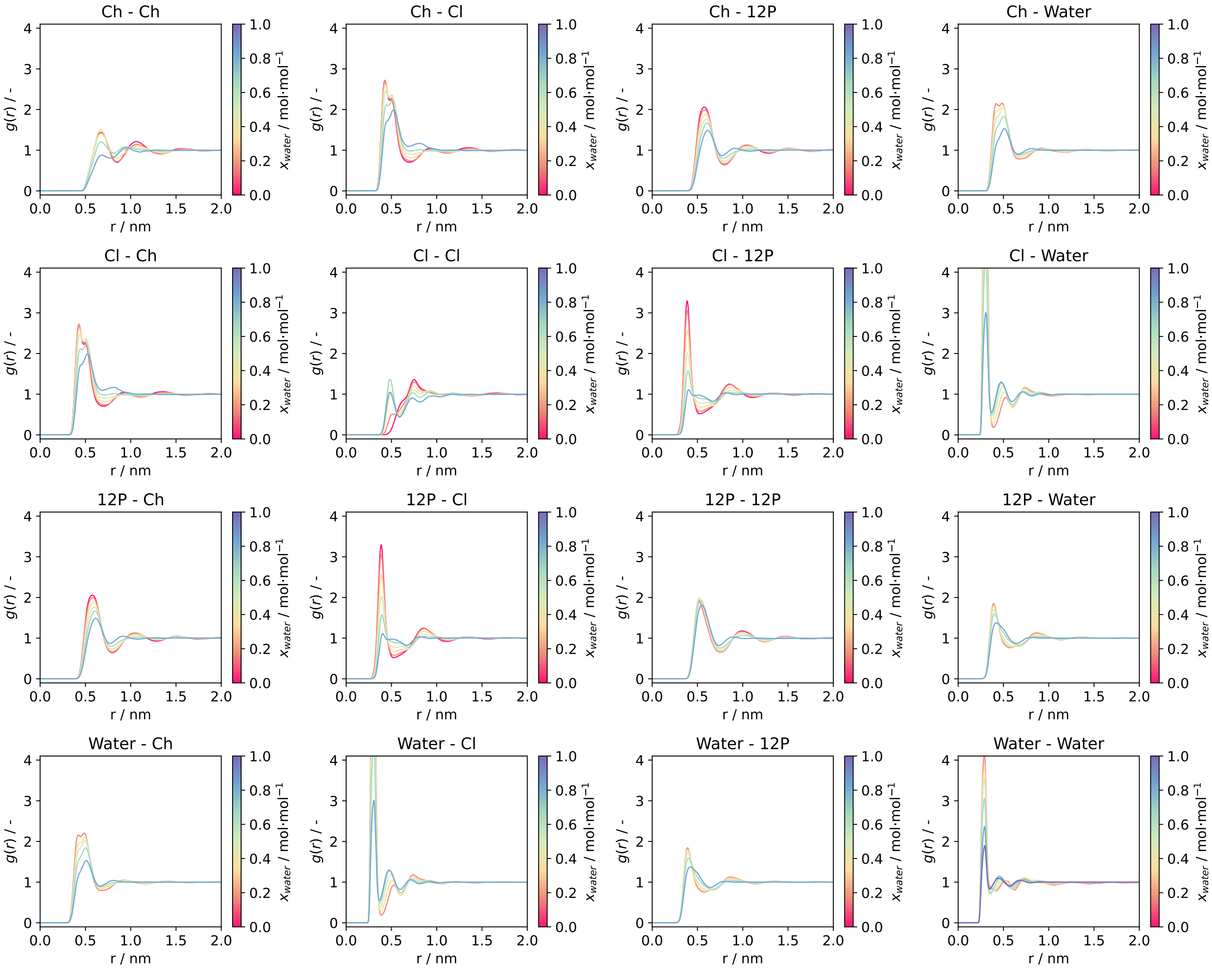

FIGURE B.12: RDFs of ChCl:12P(1:3) + water mixtures as a function of water content (x_{water}).

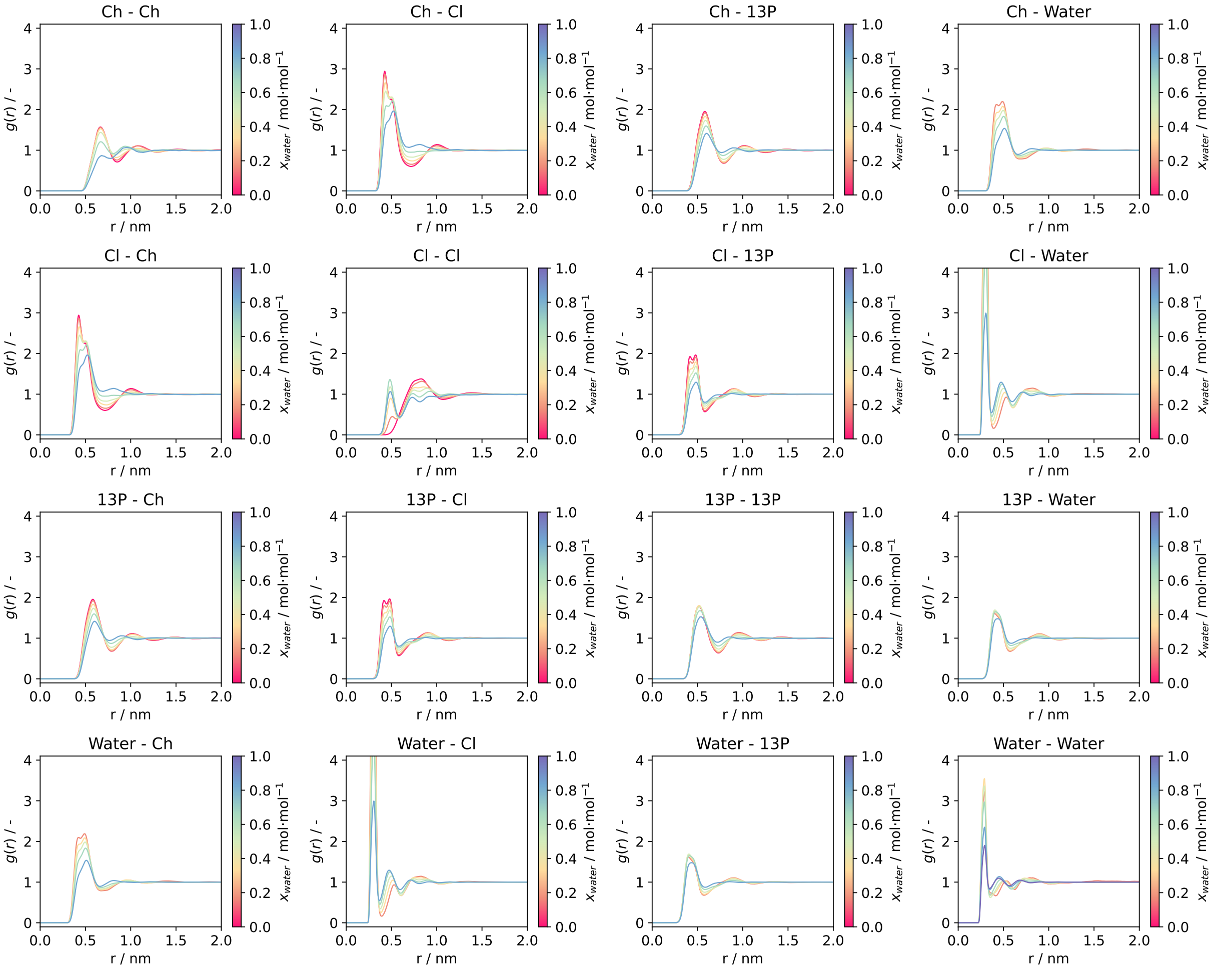

FIGURE B.13: RDFs of ChCl:13P(1:3) + water mixtures as a function of water content (x_{water}).

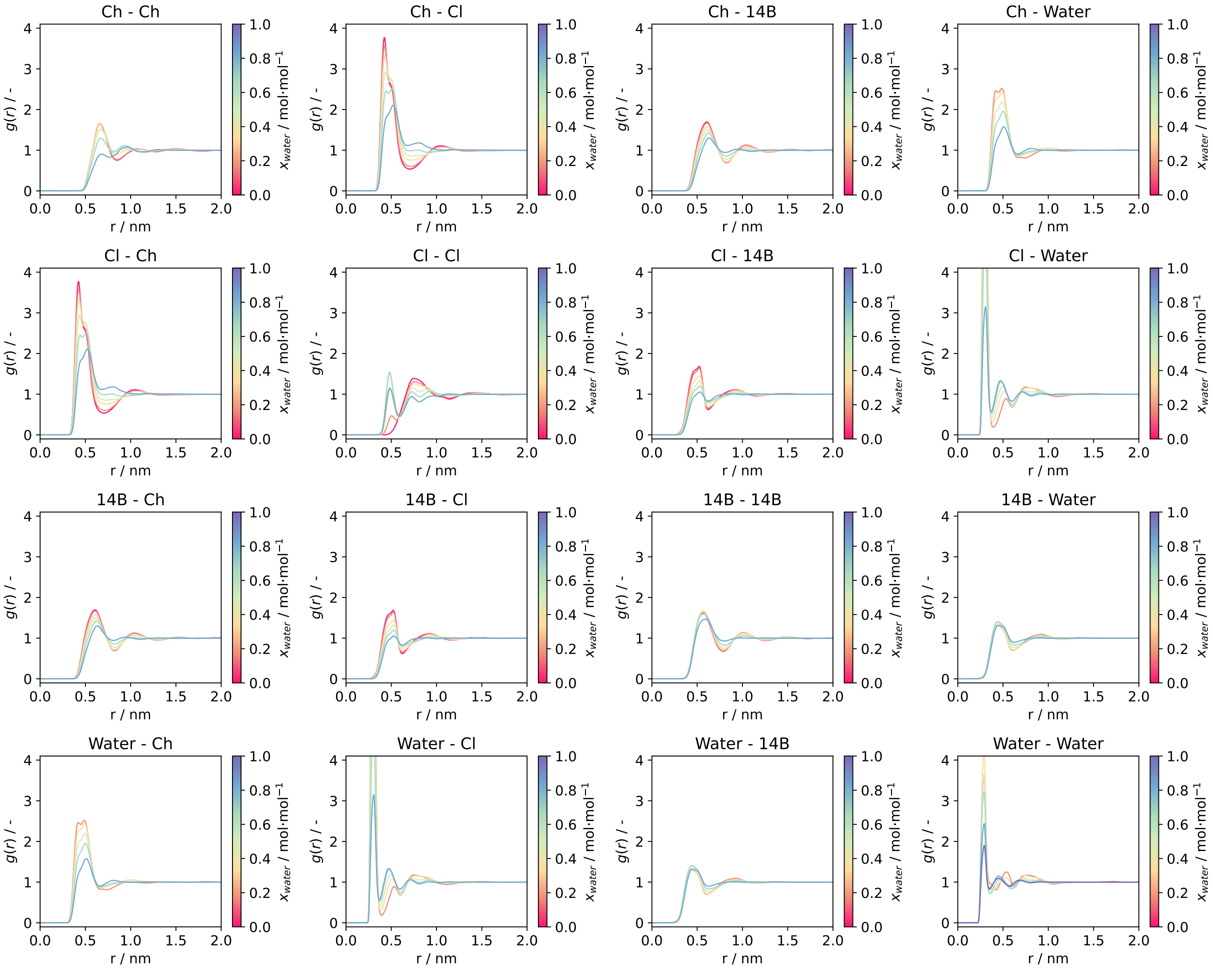

FIGURE B.14: RDFs of ChCl:14B(1:3) + water mixtures as a function of water content (x_{water}).

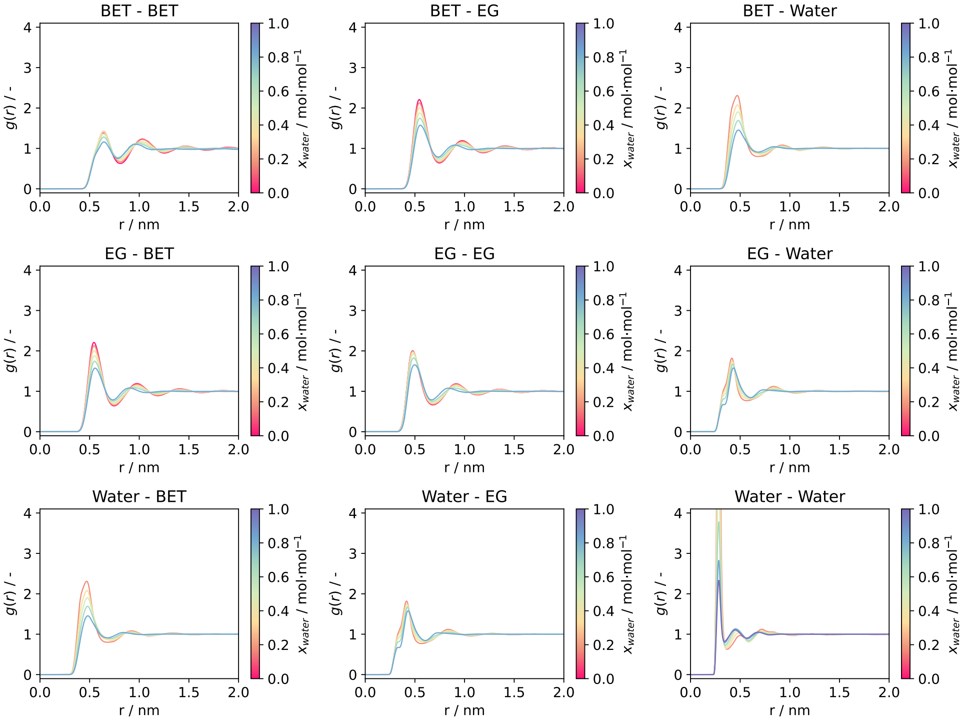

FIGURE B.15: RDFs of Bet:EG(1:6) + water mixtures as a function of water content (x_{water}).

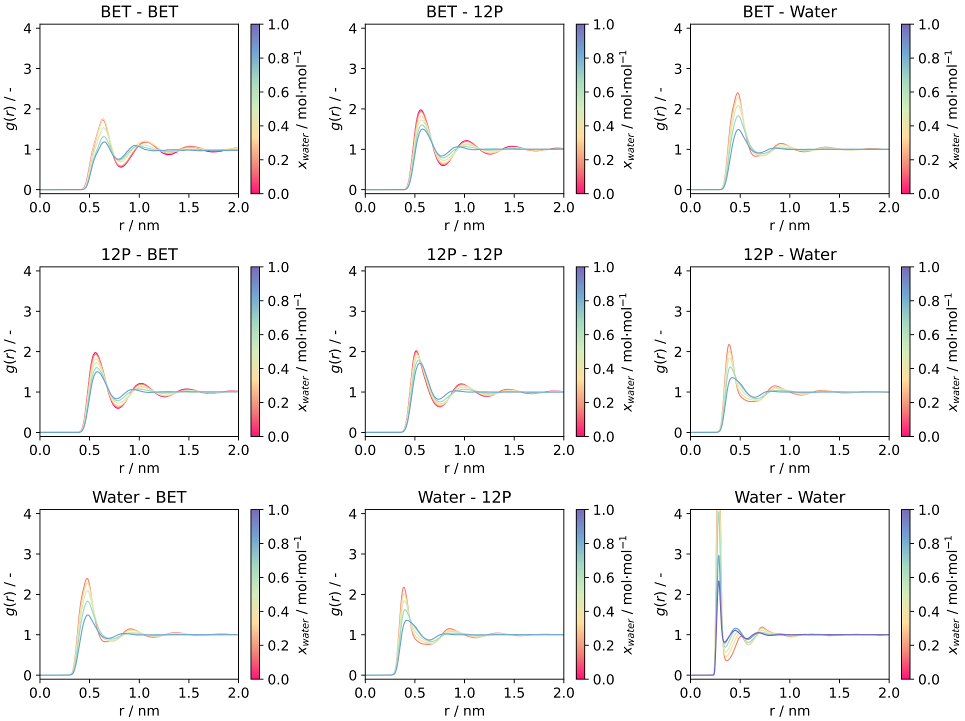

FIGURE B.16: RDFs of Bet:12P(1:6) + water mixtures as a function of water content (x_{water}).

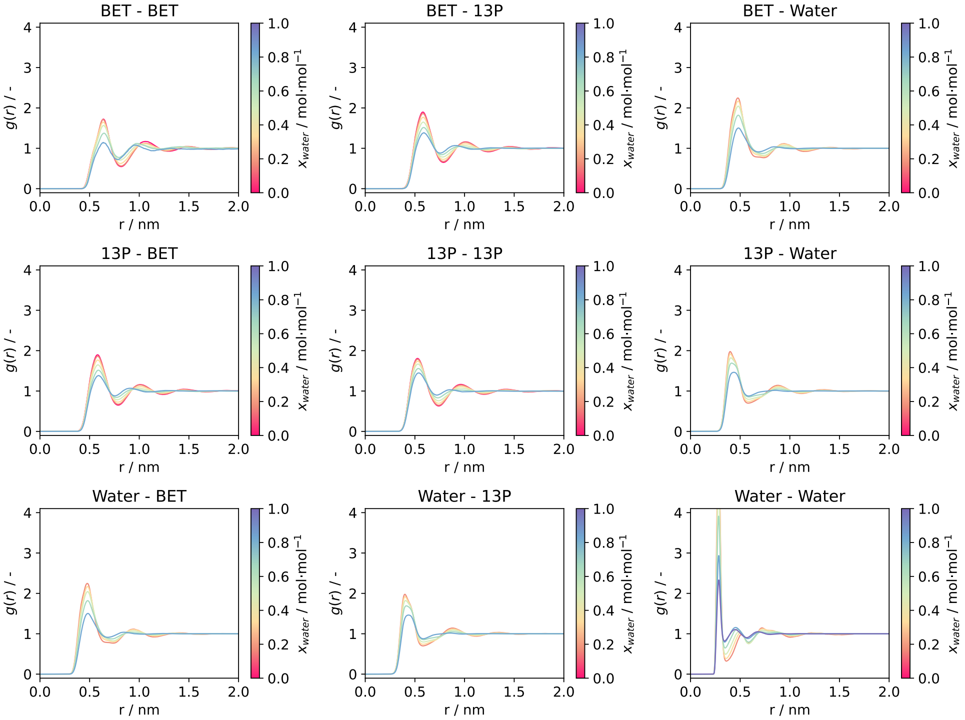

FIGURE B.17: RDFs of Bet:13P(1:6) + water mixtures as a function of water content (x_{water}).

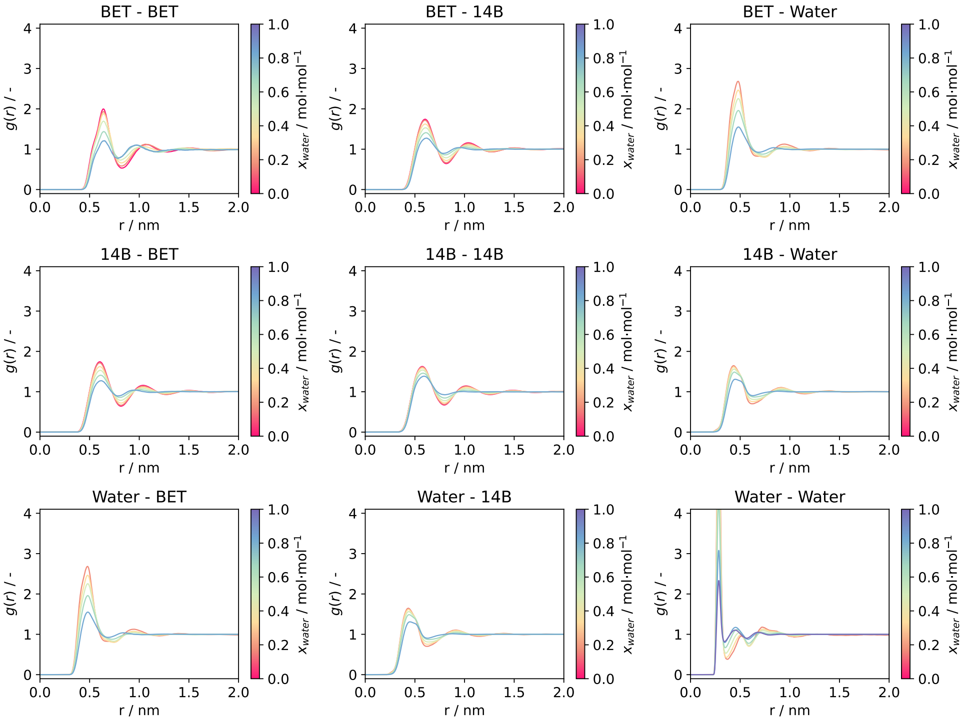

FIGURE B.18: RDFs of Bet:14B(1:6) + water mixtures as a function of water content (x_{water}).

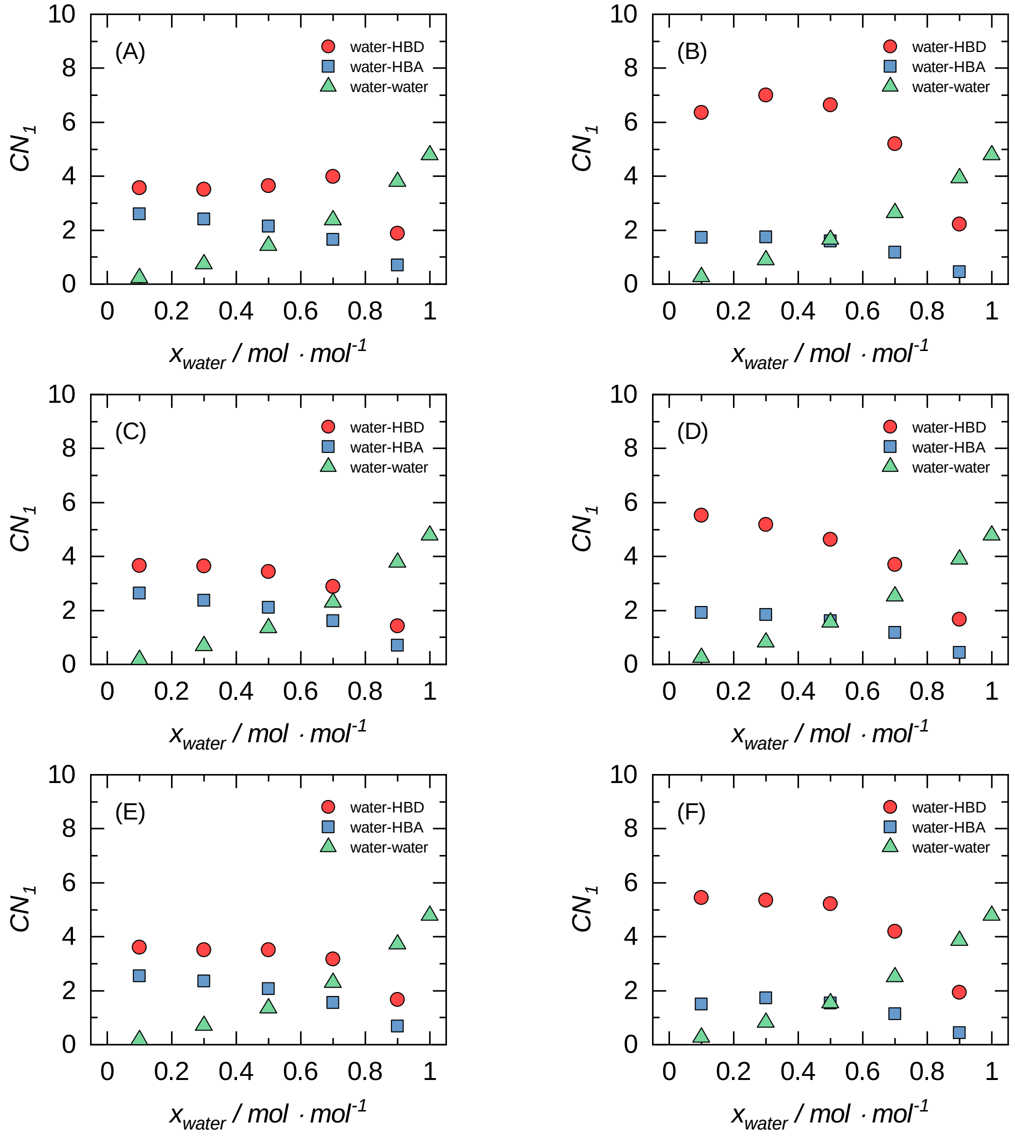

FIGURE B.19: First coordination number (CN_1) obtained for different molecules pairs from MD simulations of ChCl:12P(1:3)(A), Bet:12P(1:6) (B), ChCl:13P(1:3) (C), Bet:13P(1:6) (D), ChCl:14B(1:3) (E) and Bet:14B(1:6) (F) as a function of the water content (x_{water}) at 40°C and 101.3 kPa. Symbols: W-HBD (◆), W-HBA (■) and W-W (▲).

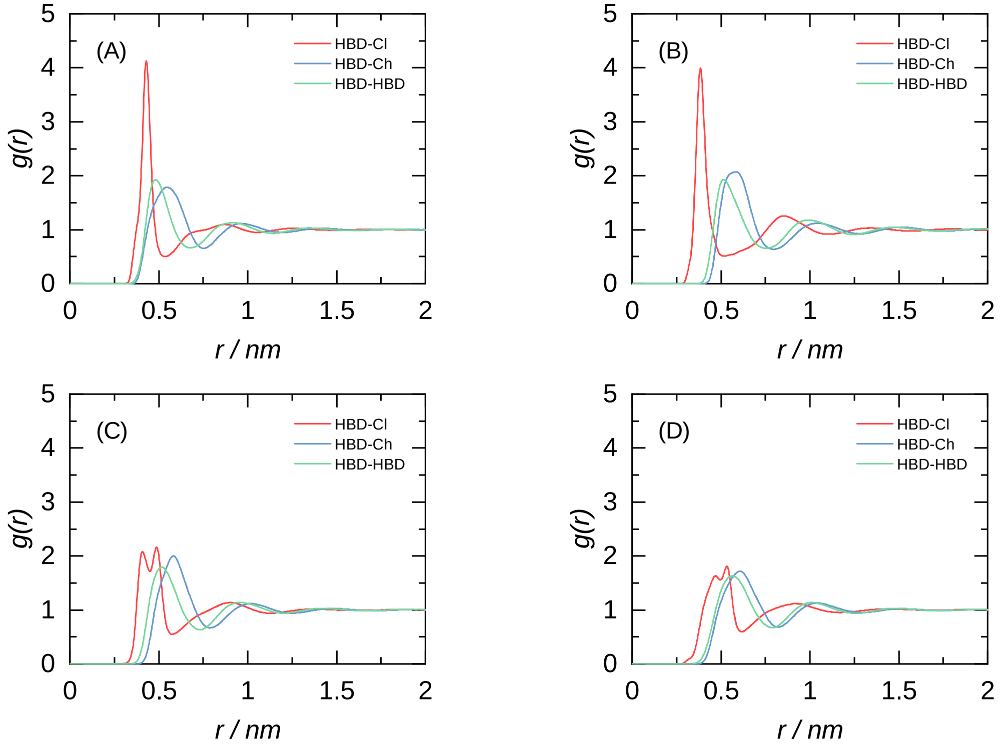

FIGURE B.20: Center-of-mass RDFs involving the HBDs for the DESs: (A) ChCl:EG(1:3), (B) ChCl:12P(1:3), (C) ChCl:13P(1:3) and (D) ChCl:14B(1:3).

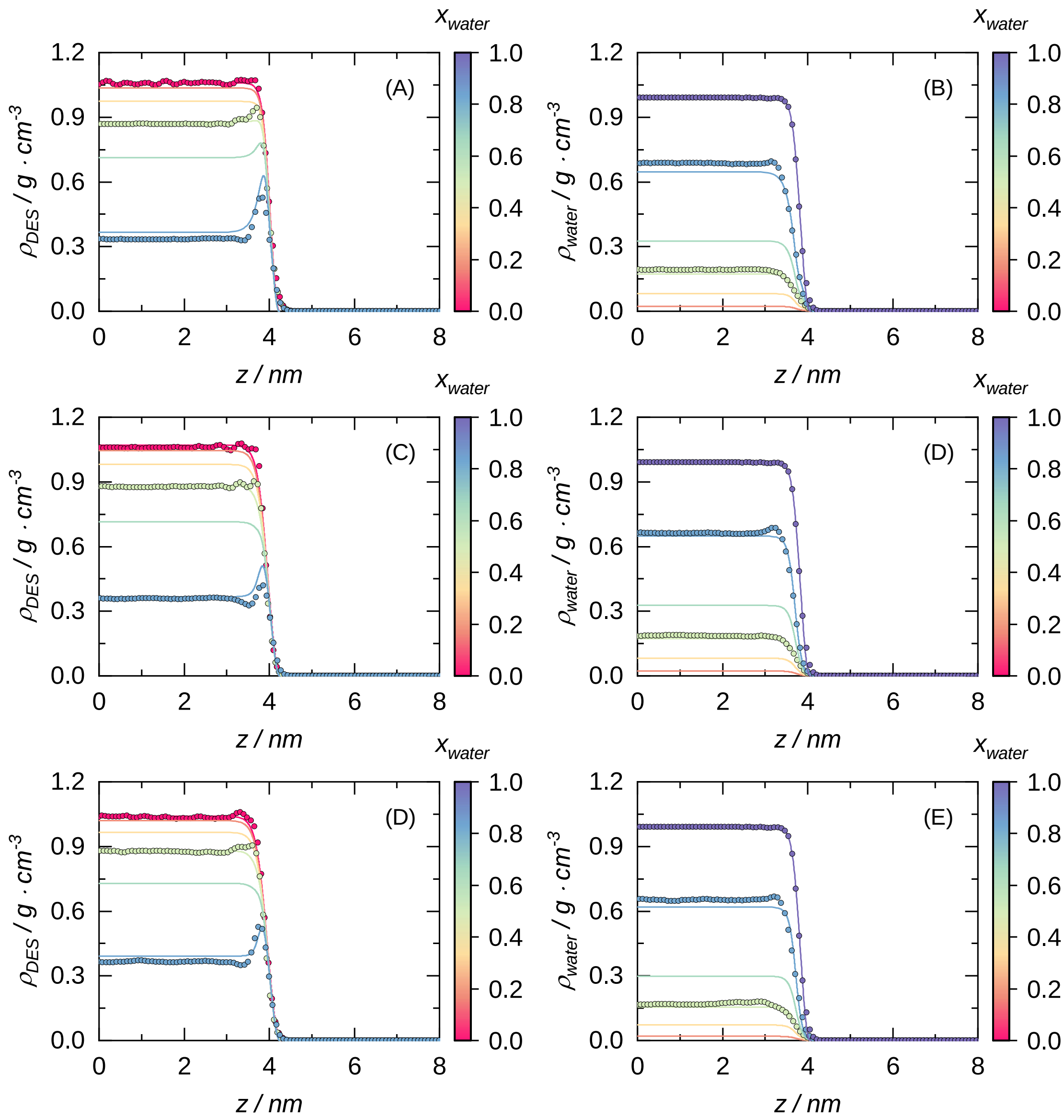

FIGURE B.21: Density profiles (ρ) along the interfacial region (z) of (A) ChCl:12P(1:3) in its mixtures with water, (B) water in its mixtures with ChCl:12P(1:3), (B) ChCl:13P(1:3) in its mixtures with water, (D) water in its mixtures with ChCl:13P(1:3), (E) ChCl:14B(1:3) in its mixtures with water, and (F) water in its mixtures with ChCl:14B(1:3) at a temperature of 40°C and a pressure of 101.3 kPa. Symbols: MD simulation results. Lines: PC-SAFT + DGT model results using parameters reported in Tables 2, 3 and 4.

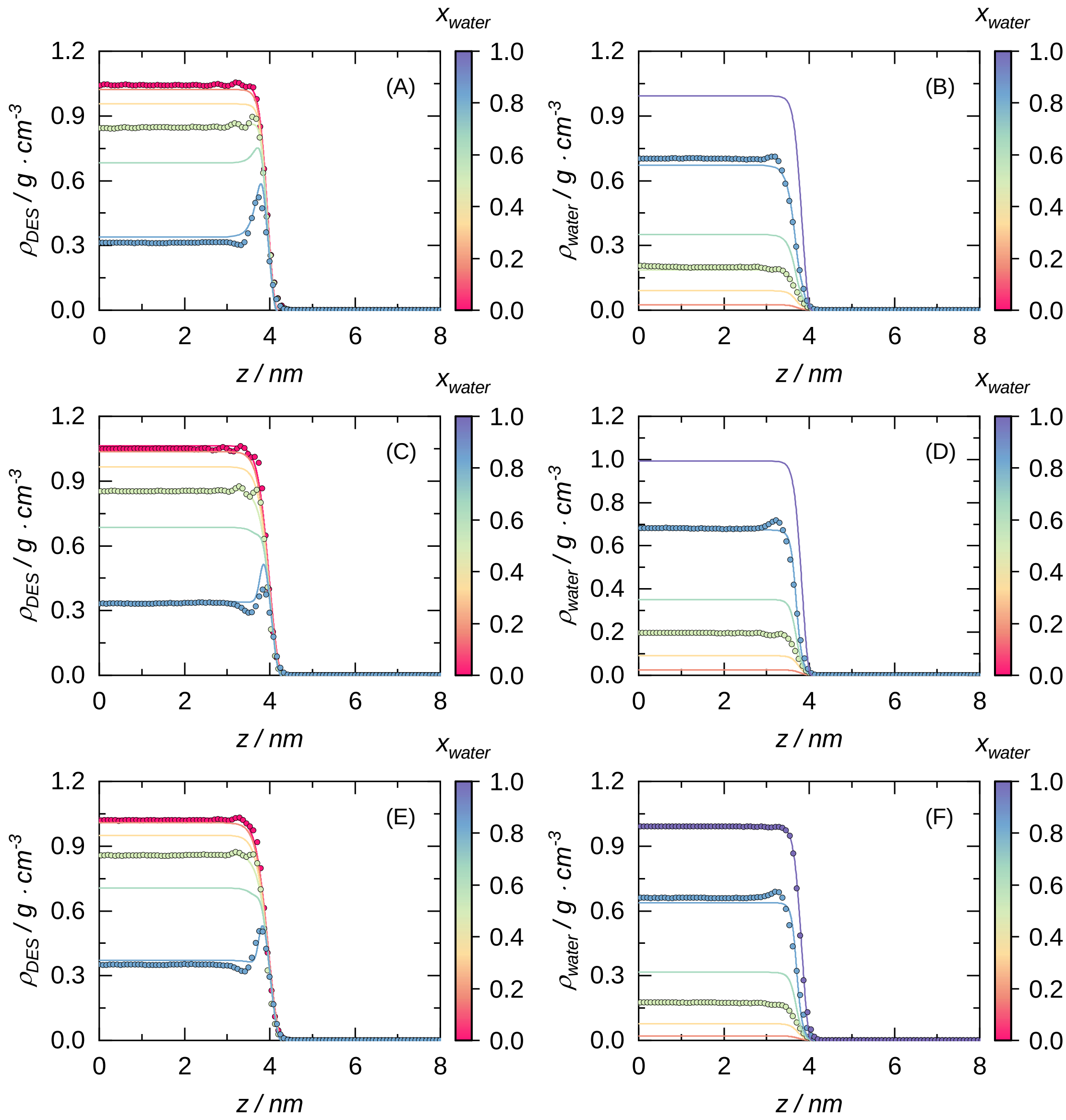

FIGURE B.22: Density profiles (ρ) along the interfacial region (z) of (A) Bet:12P(1:6) in its mixtures with water, (B) water in its mixtures with Bet:12P(1:6), (B) Bet:13P(1:6) in its mixtures with water, (D) water in its mixtures with Bet:13P(1:6), (E) Bet:14B(1:6) in its mixtures with water, and (F) water in its mixtures with Bet:14B(1:6) at a temperature of 40°C and a pressure of 101.3 kPa. Symbols: MD simulation results. Lines: PC-SAFT + DGT model results using parameters reported in Tables 2, 3 and 4.

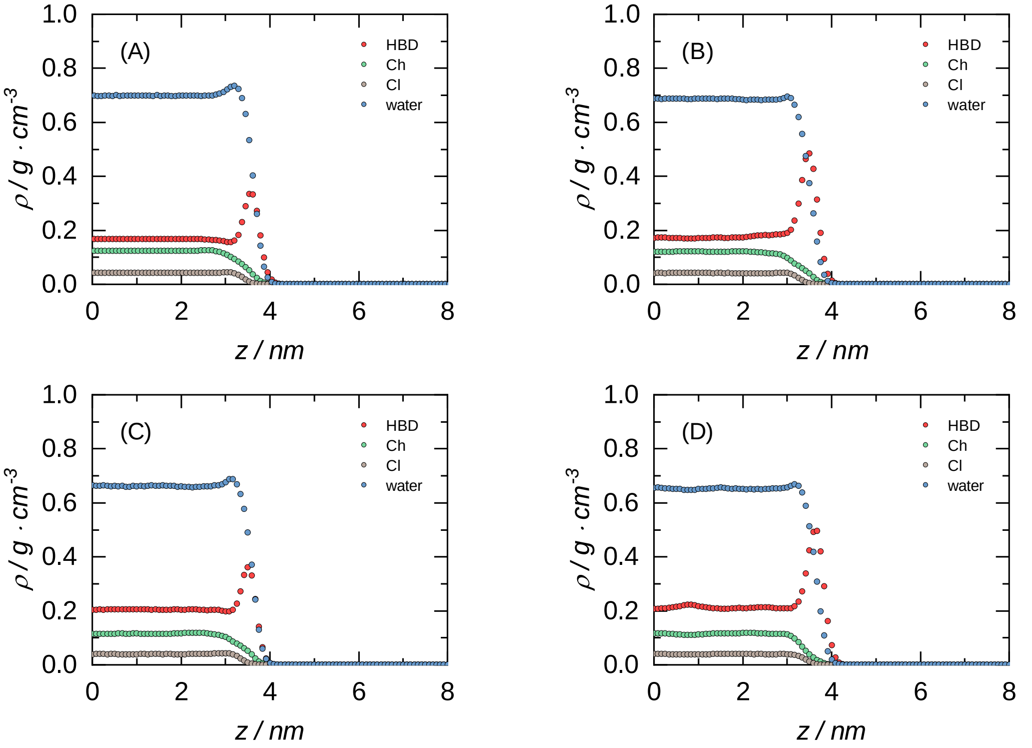

FIGURE B.23: MD density profiles (ρ) along the interfacial region (z) of (A) ChCl:EG(1:3), (B) ChCl:12P(1:3), (C) ChCl:13P(1:3) and (D) ChCl:14B(1:3) with $x_{water} = 0.9$ at 40°C and 101.3 kPa.

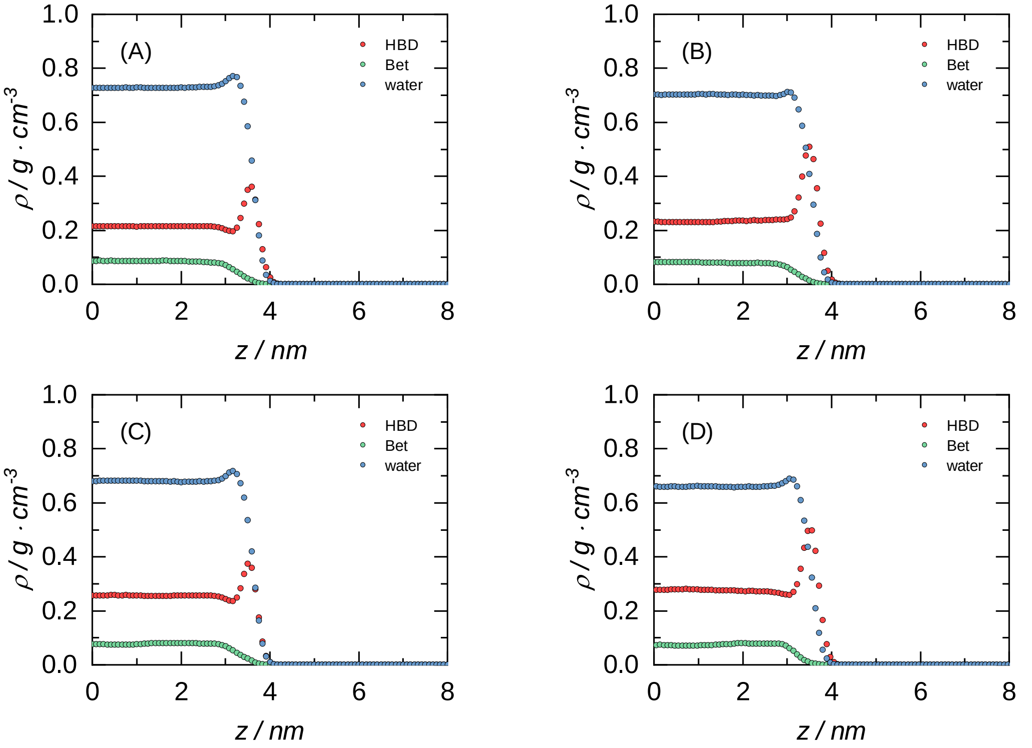

FIGURE B.24: MD density profiles (ρ) along the interfacial region (z) of (A) Bet:EG(1:6), (B) Bet:12P(1:6), (C) Bet:13P(1:6) and (D) Bet:14B(1:6) with $x_{water} = 0.9$ at 40°C and 101.3 kPa.

Tables

TABLE B.1: Abbreviation, components, molar ratio, molar mass and water content for each DES used in this work.

Abbreviation	**HBA**	**HBD**	**Mole ratio [HBA:HDB]**	**M_{DES} [g/mol]**	**Water content [ppm]**
ChCl:EG(1:6)	ChCl	EG	1:6.02	73.11	740
ChCl:EG(1:5)	ChCl	EG	1:5.00	75.00	729
ChCl:EG(1:4)	ChCl	EG	1:4.00	77.58	737
ChCl:EG(1:3)	ChCl	EG	1:3.02	81.36	782
ChCl:12P(1:6)	ChCl	12P	1:6.01	85.15	765
ChCl:12P(1:5)	ChCl	12P	1:5.00	86.68	567
ChCl:12P(1:4)	ChCl	12P	1:4.00	88.79	695
ChCl:12P(1:3)	ChCl	12P	1:3.00	91.96	1039
ChCl:13P(1:6)	ChCl	13P	1:6.01	85.15	2258
ChCl:13P(1:5)	ChCl	13P	1:5.00	86.67	2224
ChCl:13P(1:4)	ChCl	13P	1:4.02	88.74	2345
ChCl:13P(1:3)	ChCl	13P	1:3.01	91.93	1998
ChCl:14B(1:6)	ChCl	14B	1:6.01	97.18	210
ChCl:14B(1:5)	ChCl	14B	1:5.03	98.33	236
ChCl:14B(1:4)	ChCl	14B	1:4.00	100.02	166
ChCl:14B(1:3)	ChCl	14B	1:3.00	102.49	149
Bet:EG(1:6)	Bet	EG	1:6.07	69.86	320
Bet:EG(1:5)	Bet	EG	1:5.00	71.25	891
Bet:EG(1:4)	Bet	EG	1:4.00	73.08	363
Bet:12P(1:6)	Bet	12P	1:6.00	81.96	654
Bet:12P(1:5)	Bet	12P	1:5.00	82.93	744
Bet:12P(1:4)	Bet	12P	1:4.00	84.29	670
Bet:13P(1:6)	Bet	13P	1:6.00	81.96	2475
Bet:13P(1:5)	Bet	13P	1:5.01	82.93	2566
Bet:14B(1:6)	Bet	14B	1:6.00	93.98	720

Combined expanded uncertainty $U_c(mole\ ratio)$ = 0.005 with a 0.95 level of confidence. Relative standard uncertainty $u_r(ppm)$ = 0.04.

TABLE B.2: Nominal water content, molar ratio, molar mass and water content for each DES + water mixture prepared in this work.

Nominal water [% mol/mol]	**Mole ratio [HBA:HBD]**	**$M_{mixture}$ [g/mol]**	**Real water [% mol/mol]**	**Mole ratio [HBA:HBD]**	**$M_{mixture}$ [g/mol]**	**Real water [% mol/mol]**
	ChCl:EG(1:3) + water			**Bet:EG(1:3) + water**		
0	1:3.02	81.13	0.4	1:6.07	69.80	0.1
5	1:3.00	78.42	4.8	1:6.01	67.36	4.9
10	1:3.00	74.95	10.3	1:6.01	64.72	10.0
30	1:3.00	61.40	31.6	1:6.01	54.35	30.0
50	1:3.00	48.29	52.3	1:6.01	43.95	50.0
70	1:3.00	37.13	69.9	1:6.01	33.61	70.0
90	1:3.00	24.39	90.0	1:6.01	23.21	90.0
95	1:3.00	21.18	95.0	1:6.01	20.61	95.0
	ChCl:12P(1:3) + water			**Bet:12P(1:3) + water**		
0	1:3.00	91.74	0.3	1:6.00	81.77	0.3
5	1:3.01	88.40	4.8	1:6.01	78.54	5.3
10	1:3.01	84.75	9.7	1:6.01	75.21	10.5
30	1:3.00	69.13	30.9	1:6.01	62.69	30.1
50	1:3.00	55.03	50.0	1:6.01	49.78	50.3
70	1:3.00	40.26	69.9	1:6.01	37.21	70.0
90	1:3.00	25.43	90.0	1:6.01	24.40	90.0
95	1:3.00	21.72	95.0	1:6.01	21.22	95.0
	ChCl:13P(1:3) + water			**Bet:13P(1:3) + water**		
0	1:3.01	91.18	1.0	1:6.00	81.24	1.1
5	1:3.00	88.18	5.1	1:6.00	78.26	5.8
10	1:3.00	84.36	10.3	1:6.00	75.09	10.7
30	1:3.00	69.60	30.2	1:6.00	62.52	30.4
50	1:3.00	54.94	50.1	1:6.00	49.81	50.3
70	1:3.00	40.21	70.0	1:6.00	37.14	70.1
90	1:3.00	25.37	90.1	1:6.00	24.45	89.9
95	1:3.00	21.72	95.0	1:6.00	21.26	94.9
	ChCl:14P(1:3) + water			**Bet:14P(1:3) + water**		
0	1:3.00	102.42	0.1	1:6.00	93.70	0.4
5	1:3.00	96.44	7.2	1:6.00	90.23	4.9
10	1:3.00	92.47	11.9	1:6.00	86.18	10.3
30	1:3.00	76.19	31.1	1:6.00	71.08	30.1
50	1:3.00	60.09	50.2	1:6.00	56.00	50.0
70	1:3.00	43.23	70.2	1:6.00	40.89	69.9
90	1:3.00	26.11	90.4	1:6.00	25.65	90.0
95	1:3.01	21.81	95.5	1:6.00	21.85	95.0
	ChCl:EG(1:6) + water					
0	1:6.00	70.01	5.7			
10	1:6.00	67.27	10.7			
30	1:6.00	56.43	30.3			
50	1:6.00	45.54	50.1			
70	1:6.00	34.09	70.8			
90	1:6.00	23.67	89.8			
95	1:6.00	20.77	95.0			

Standard uncertainty u are $u(\%\ \textit{real water content}) = 0.5$. Combined expanded uncertainty $U_c(\textit{mole ratio}) = 0.005$ with a 0.95 level of confidence.

TABLE B.3: Experimental densities, viscosity and surface tension of Bet-based DESs at different temperatures.

T [°C]	ρ [g/cm3]	η [mPa s]	γ [mN/m]	ρ [g/cm3]	η [mPa s]	γ [mN/m]	ρ [g/cm3]	η [mPa s]	γ [mN/m]
	Bet:EG(1:6)			**Bet:EG(1:5)**			**Bet:EG(1:4)**		
20	1.12716	46.55		1.12794	54.71		1.13222	68.50	
25	1.12396	36.92		1.12445	43.30		1.12885	54.93	
30	1.12072	29.75	49.8	1.12091	34.61	50.4	1.12543	43.27	50.8
35	1.11748	24.31		1.11744	28.13		1.12198	35.11	
40	1.11424	20.14	49.1	1.11403	23.26	49.6	1.11861	28.83	50.0
45	1.11099	16.96		1.11058	19.44		1.11529	24.03	
50	1.10774	14.29	48.1	1.10723	16.39	48.6	1.11187	20.24	49.0
55	1.10447	12.19		1.10394	13.97		1.10855	17.21	
60	1.10119	10.54	47.3	1.10081	11.97	47.8	1.10523	14.76	48.4
	Bet:12P(1:6)			**Bet:12P(1:5)**			**Bet:12P(1:4)**		
20	1.06249	125.59		1.06653	144.79		1.07253	183.09	
25	1.05913	91.37		1.06322	104.99		1.06933	132.04	
30	1.05572	67.82	37.3	1.05986	77.84	37.8	1.06602	97.16	38.3
35	1.05229	51.44		1.05648	58.90		1.06269	73.09	
40	1.04884	39.72	36.9	1.05308	45.34	37.2	1.05936	55.94	37.6
45	1.04537	31.26		1.04967	35.53		1.05601	43.59	
50	1.04189	24.91	35.8	1.04625	28.21	36.3	1.05265	34.52	36.7
55	1.03837	20.20		1.04280	22.76		1.04928	27.78	
60	1.03484	16.55	35.3	1.03934	18.54	35.6	1.04589	22.66	36.1
	Bet:13P(1:6)			**Bet:13P(1:5)**			**Bet:14B(1:6)**		
20	1.07708	91.89		1.08090	103.01		1.04224	142.96	
25	1.07395	72.42		1.07785	80.18		1.03926	109.88	
30	1.07075	57.10	49.1	1.07481	63.32	49.7	1.03627	85.70	45.9
35	1.06754	45.91		1.07177	50.65		1.03328	67.62	
40	1.06429	37.43	48.3	1.06872	41.04	48.7	1.03027	54.07	45.2
45	1.06103	30.78		1.06568	33.66		1.02728	43.66	
50	1.05779	25.72	47.1	1.06263	27.92	47.9	1.02427	35.58	44.3
55	1.05433	21.62		1.05958	23.38		1.02124	29.31	
60	1.05108	18.32	46.4	1.05652	19.76	46.8	1.01819	24.31	43.3

Standard uncertainties u are $u(T)$ = 0.01 K, $u(P)$ = 1 kPa , $u(\rho) = 0.0005\ g \cdot cm^{-3}$, $u_r(\eta) = 0.02$ and $u(\gamma) = 0.1\ mN \cdot m^{-1}$.

TABLE B.4: Experimental surface tension of ChCl-based DESs and glycols at different temperatures.

HBD	**T**	**Mole ratio ChCl:HBD**					
	[°C]	**(1:∞)**	**(1:6)**	**(1:5)**	**(1:4)**	**(1:3)**	**(1:2)**
EG	30	47.7	51.0	51.5	52.2	53.1	55.5
	40	46.9	50.5	50.8	51.6	52.2	54.6
	50	46.1	49.5	50.1	50.9	51.8	54.0
	60	45.1	48.8	49.4	50.2	51.0	53.4
12P	30	35.9	38.6	38.9	39.6	40.4	
	40	35.4	37.9	38.0	38.8	39.7	
	50	34.5	37.0	37.3	38.2	39.1	
	60	33.6	36.4	36.6	37.5	38.4	
13P	30	47.8	50.0	50.4	51.0	51.8	
	40	47.0	49.3	49.6	50.1	51.3	
	50	45.9	48.3	48.5	49.4	50.3	
	60	45.0	47.3	47.6	48.6	49.6	
14B	30	44.8	46.5	46.8	47.3	48.0	
	40	44.3	45.7	46.2	46.4	47.2	
	50	43.4	44.8	45.2	45.6	46.4	
	60	42.6	43.9	44.3	44.8	45.5	

Standard uncertainties u are $u(P)$ = 1 kPa and $u(\gamma) = 0.1\ mN \cdot m^{-1}$.

TABLE B.5: Experimental densities (g/cm^3) of DES + water mixtures at various temperatures and water mole fractions.

T [°C]	$\mathbf{x}_{water}$	**ChCl:EG (1:6)**	**ChCl:EG (1:3)**	**ChCl:12P (1:3)**	**ChCl:13P (1:3)**	**ChCl:14B (1:3)**	**Bet:EG (1:6)**	**Bet:12P (1:6)**	**Bet:13P (1:6)**	**Bet:14B (1:6)**
20	0.05	1.11601	1.11767	1.07169	1.08103	1.05289	1.12655	1.06305	1.07749	1.04244
	0.10	1.11492	1.11669	1.07182	1.08080	1.05305	1.12525	1.06347	1.07725	1.04277
	0.30	1.10959	1.11178	1.07202	1.07910	1.05361	1.11909	1.06480	1.07599	1.04411
	0.50	1.10023	1.10268	1.07060	1.07497	1.05314	1.10846	1.06481	1.07210	1.04490
	0.70	1.08161	1.08470	1.06382	1.06456	1.04859	1.08773	1.05989	1.06150	1.04181
	0.90	1.03895	1.04187	1.03521	1.03275	1.02644	1.04125	1.03288	1.03044	1.02286
	0.95	1.01862	1.02280	1.01896	1.01755	1.01401	1.02186	1.01744	1.01576	1.01175
30	0.05	1.10987	1.11178	1.06561	1.07556	1.04745	1.12004	1.05635	1.07150	1.03658
	0.10	1.10887	1.11089	1.06576	1.07532	1.04764	1.11888	1.05676	1.07128	1.03692
	0.30	1.10350	1.10596	1.06595	1.07365	1.04814	1.11274	1.05803	1.06993	1.03819
	0.50	1.09428	1.09702	1.06451	1.06955	1.04754	1.10220	1.05801	1.06619	1.03883
	0.70	1.07600	1.07933	1.05783	1.05930	1.04295	1.08192	1.05325	1.05585	1.03575
	0.90	1.03480	1.03774	1.03059	1.02870	1.02195	1.03706	1.02811	1.02631	1.01827
	0.95	1.01521	1.01938	1.01538	1.01426	1.01049	1.01849	1.01383	1.01253	1.00822
40	0.05	1.10370	1.10596	1.05954	1.07008	1.04203	1.11361	1.04953	1.06550	1.03072
	0.10	1.10279	1.10509	1.05969	1.06985	1.04220	1.11243	1.04992	1.06528	1.03104
	0.30	1.09734	1.10017	1.05980	1.06816	1.04263	1.10629	1.05113	1.06388	1.03221
	0.50	1.08821	1.09128	1.05830	1.06403	1.04188	1.09583	1.05104	1.06011	1.03265
	0.70	1.07019	1.07379	1.05161	1.05378	1.03718	1.07586	1.04637	1.04997	1.02950
	0.90	1.03015	1.03314	1.02551	1.02418	1.01705	1.03236	1.02282	1.02168	1.01319
	0.95	1.01120	1.01533	1.01116	1.01031	1.00634	1.01444	1.00956	1.00858	1.00402
50	0.05	1.09751	1.10017	1.05344	1.06464	1.03663	1.10712	1.04264	1.05947	1.02486
	0.10	1.09650	1.09930	1.05359	1.06439	1.03680	1.10595	1.04301	1.05924	1.02515
	0.30	1.09113	1.09436	1.05360	1.06265	1.03709	1.09977	1.04411	1.05776	1.02618
	0.50	1.08203	1.08547	1.05199	1.05842	1.03616	1.08933	1.04391	1.05393	1.02637
	0.70	1.06418	1.06809	1.04525	1.04819	1.03128	1.06963	1.03930	1.04388	1.02310
	0.90	1.02505	1.02815	1.02007	1.01924	1.01175	1.02719	1.01709	1.01658	1.00768
	0.95	1.00651	1.01059	1.00638	1.00579	1.00163	1.00978	1.00465	1.00399	0.99920
60	0.05	1.09129	1.09439	1.04733	1.05917	1.03126	1.10059	1.03566	1.05340	1.01898
	0.10	1.09028	1.09350	1.04765	1.05891	1.03140	1.09940	1.03599	1.05316	1.01922
	0.30	1.08486	1.08852	1.04736	1.05711	1.03154	1.09317	1.03697	1.05158	1.02002
	0.50	1.07572	1.07957	1.04558	1.05274	1.03038	1.08273	1.03667	1.04761	1.01999
	0.70	1.05798	1.06222	1.03874	1.04242	1.02525	1.06317	1.03205	1.03757	1.01651
	0.90	1.01951	1.02277	1.01424	1.01379	1.00595	1.02158	1.01095	1.01085	1.00176
	0.95	1.00132	1.00257	1.00106	1.00062	0.99615	1.00458	0.99918	0.99885	0.99382

Standard uncertainties u are $u(T)$ = 0.01 K, $u(P)$ = 1 kPa and $u(\rho)$ = 0.0005 $g \cdot cm^{-3}$.

TABLE B.6: Experimental viscosities (mPa·s) of DES + water mixtures at various temperatures and water mole fractions.

T [°C]	$\mathbf{x}_{water}$	ChCl:EG (1:6)	ChCl:EG (1:3)	ChCl:12P (1:3)	ChCl:13P (1:3)	ChCl:14B (1:3)	Bet:EG (1:6)	Bet:12P (1:6)	Bet:13P (1:6)	Bet:14B (1:6)
20	0.05	25.93	36.51	87.34	66.00	103.39	43.51	122.42	91.89	139.58
	0.10	24.39	33.98	80.67	61.22	96.16	39.58	110.67	79.40	130.01
	0.30	18.01	23.85	52.76	43.40	68.57	26.35	66.70	56.31	92.46
	0.50	10.79	13.24	31.29	27.30	41.05	14.16	34.52	31.58	51.55
	0.70	5.58	6.39	12.18	12.15	17.95	6.53	13.49	12.08	20.57
	0.90	2.10	2.13	3.04	2.80	3.53	2.17	3.28	2.97	3.96
	0.95	1.55	1.50	1.83	1.75	2.04	1.52	1.92	1.83	2.17
30	0.05	17.74	24.78	52.34	43.17	65.18	27.81	66.13	57.10	83.49
	0.10	16.71	23.12	48.25	40.20	60.69	25.50	60.33	49.78	77.76
	0.30	12.56	16.45	32.37	28.73	43.45	17.48	37.84	35.25	55.43
	0.50	7.61	9.34	19.75	18.39	26.59	9.63	20.88	20.45	31.57
	0.70	4.08	4.69	8.16	8.21	12.37	4.68	8.67	8.19	13.48
	0.90	1.61	1.65	2.24	2.11	2.58	1.66	2.36	2.20	2.83
	0.95	1.20	1.18	1.40	1.36	1.55	1.18	1.45	1.40	1.62
40	0.05	12.78	17.70	33.12	29.71	43.35	18.88	38.68	37.43	52.64
	0.10	12.17	16.53	31.00	27.31	40.38	17.49	35.58	32.68	49.06
	0.30	9.15	11.25	21.25	20.04	29.07	11.68	23.28	23.32	35.18
	0.50	5.59	6.87	13.36	13.00	18.21	6.87	12.67	14.03	20.61
	0.70	3.10	3.57	5.75	5.59	8.34	3.49	5.90	5.82	8.75
	0.90	1.28	1.32	1.72	1.65	1.97	1.31	1.77	1.69	2.11
	0.95	0.97	0.95	1.11	1.08	1.24	0.95	1.13	1.10	1.26
50	0.05	9.38	13.18	22.33	20.95	30.12	13.48	24.30	25.72	34.83
	0.10	8.38	12.43	20.68	19.56	28.15	12.04	22.47	22.50	32.48
	0.30	6.40	8.39	14.15	14.14	20.41	8.43	14.29	15.88	23.51
	0.50	4.25	5.22	8.91	8.96	12.52	5.09	8.57	9.65	13.59
	0.70	2.43	2.80	4.23	4.22	5.87	2.69	4.22	4.29	6.22
	0.90	1.04	1.08	1.36	1.32	1.55	1.06	1.44	1.35	1.63
	0.95	0.79	0.79	0.90	0.89	1.01	0.79	0.91	0.90	1.01
60	0.05	6.86	9.85	15.79	15.52	21.82	9.92	16.24	18.32	24.05
	0.10	6.39	8.93	14.65	14.49	20.38	8.81	13.93	16.15	22.47
	0.30	4.93	6.77	10.17	10.53	14.98	6.30	9.78	11.38	16.45
	0.50	3.33	4.09	6.79	6.75	9.16	3.89	6.08	7.06	9.60
	0.70	1.95	2.25	3.26	3.28	4.43	2.13	3.15	3.27	4.59
	0.90	0.87	0.91	1.11	1.12	1.28	0.89	1.12	1.10	1.30
	0.95	0.67	0.67	0.75	0.75	0.84	0.66	0.76	0.75	0.83

Standard uncertainties u are $u(T)$ = 0.01 K and $u(P)$ = 1 kPa. Relative standard uncertainty $u_r(\eta)$ = 0.02.

TABLE B.7: Experimental surface tension (mN/m) of DES + water mixtures at 40°C and various water mole fractions.

$\mathbf{x}_{water}$	**ChCl:EG (1:3)**	**ChCl:12P (1:3)**	**ChCl:13P (1:3)**	**ChCl:14B (1:3)**	**Bet:EG (1:6)**	**Bet:12P (1:6)**	**Bet:13P (1:6)**	**Bet:14B (1:6)**
0.05	52.9	39.7	50.9	47.3	48.0	36.8	48.4	45.1
0.10	53.0	39.7	51.0	47.3	49.1	37.0	48.4	45.2
0.30	53.1	40.1	51.4	47.4	50.0	37.5	49.0	45.4
0.50	54.0	40.4	51.7	47.6	51.5	38.6	49.7	45.7
0.70	55.7	42.1	53.4	48.5	54.3	40.6	51.9	46.6
0.90	61.0	50.5	57.4	52.5	60.8	48.7	57.1	51.6
0.95	63.9	56.0	61.3	56.3	64.1	54.7	60.8	55.6

Standard uncertainties u are $u(P)$ = 1 kPa and $u(\gamma)$ = 0.1 $mN \cdot m^{-1}$.

TABLE B.8: AARD of density, viscosity and surface tension obtained through MD for DES + water mixtures for each family

	AARD ρ	**AARD** η	**AARD** γ	**AARD** ρ	**AARD** η	**AARD** γ
HBD	**ChCl-based DESs**			**Bet-based DESs**		
EG	0.29%	21.42%	7.24%	1.15%	40.08%	5.40%
12P	0.27%	228.27%	24.85%	0.82%	71.11%	24.61%
13P	0.53%	274.05%	16.71%	1.28%	75.19%	16.24%
14B	0.25%	143.41%	7.44%	0.54%	40.69%	8.73%

TABLE B.9: Density, viscosity and surface tension of DESs + water mixtures at 40°C and a pressure of 101.3 kPa from MD calculations.

x_{water}	ρ [g/cm3]	η [mPa s]	γ [mN/m]	ρ [g/cm^3]	η [mPa s]	γ [mN/m]
	ChCl:EG(1:3) + water			**Bet:EG(1:6) + water**		
0.0	1.0956 ± 1e-4	22.30 ± 4.09	58.3 ± 0.9	1.0913 ± 1e-4	6.20 ± 0.48	52.7 ± 0.7
0.1	1.0969 ± 1e-4	19.46 ± 2.76	58.7 ± 0.6	1.0908 ± 1e-4	5.79 ± 0.47	53.0 ± 0.5
0.3	1.0957 ± 1e-4	13.32 ± 1.52	58.4 ± 0.6	1.0889 ± 1e-4	5.29 ± 0.34	53.4 ± 0.5
0.5	1.0896 ± 1e-4	8.65 ± 0.66	57.3 ± 0.5	1.0833 ± 1e-4	4.46 ± 0.22	54.2 ± 0.4
0.7	1.0746 ± 1e-4	4.65 ± 0.16	58.2 ± 0.4	1.0687 ± 1e-4	3.03 ± 0.07	56.0 ± 0.3
0.9	1.0323 ± 1e-4	1.51 ± 0.04	61.1 ± 0.2	1.0283 ± 1e-4	1.33 ± 0.01	59.7 ± 0.2
1.0	0.9903 ± 1e-4	0.69 ± 0.01	64.6 ± 0.1	0.9903 ± 1e-4	0.69 ± 0.01	64.6 ± 0.1
	ChCl:12PD(1:3) + water			**Bet:12PD(1:6) + water**		
0.0	1.0563 ± 1e-4	161.90 ± 28.09	49.7 ± 1.7	1.0398 ± 2e-4	65.31 ± 13.03	47.4 ± 1.8
0.1	1.0567 ± 1e-4	149.90 ± 22.58	-	1.0407 ± 3e-4	58.82 ± 10.51	-
0.3	1.0580 ± 1e-4	82.78 ± 11.33	-	1.0426 ± 2e-4	48.12 ± 5.57	-
0.5	1.0563 ± 1e-4	42.07 ± 5.42	50.7 ± 1.5	1.0429 ± 1e-4	28.03 ± 2.25	49.3 ± 1.2
0.7	1.0489 ± 1e-4	12.00 ± 1.01	-	1.0375 ± 1e-4	9.46 ± 0.31	-
0.9	1.0207 ± 1e-4	2.09 ± 0.04	-	1.0148 ± 1e-4	1.93 ± 0.04	-
1.0	0.9903 ± 1e-4	0.69 ± 0.01	64.6 ± 0.1	0.9903 ± 1e-4	0.69 ± 0.01	64.6 ± 0.1
	ChCl:13PD(1:3) + water			**Bet:13PD(1:6) + water**		
0.0	1.0591 ± 2e-4	159.17 ± 25.23	62.4 ± 1.8	1.0464 ± 2e-4	64.16 ± 3.96	58.5 ± 1.1
0.1	1.0603 ± 2e-4	141.78 ± 13.41	-	1.0475 ± 1e-4	63.75 ± 5.17	-
0.3	1.0619 ± 2e-4	99.81 ± 8.46	-	1.0480 ± 1e-4	50.82 ± 3.18	-
0.5	1.0602 ± 2e-4	46.90 ± 3.15	61.3 ± 1.0	1.0467 ± 1e-4	28.28 ± 1.39	58.8 ± 0.7
0.7	1.0504 ± 1e-4	13.15 ± 0.81	-	1.0382 ± 1e-4	9.26 ± 0.21	-
0.9	1.0191 ± 1e-4	2.03 ± 0.04	-	1.0127 ± 1e-4	1.83 ± 0.03	-
1.0	0.9903 ± 1e-4	0.69 ± 0.01	64.6 ± 0.1	0.9903 ± 1e-4	0.69 ± 0.01	64.6 ± 0.1
	ChCl:14BD(1:3) + water			**Bet:14BD(1:6) + water**		
0.0	1.0337 ± 2e-4	123.33 ± 14.35	49.5 ± 1.3	1.0183 ± 2e-4	59.87 ± 5.27	48.6 ± 1.4
0.1	1.0358 ± 1e-4	122.21 ± 16.89	-	1.0202 ± 1e-4	58.34 ± 5.49	-
0.3	1.0392 ± 2e-4	86.20 ± 8.98	-	1.0250 ± 1e-4	57.35 ± 5.87	-
0.5	1.0420 ± 1e-4	49.90 ± 4.72	51.1 ± 1.0	1.0285 ± 1e-4	36.95 ± 2.31	49.8 ± 1.0
0.7	1.0391 ± 1e-4	16.89 ± 1.60	-	1.0274 ± 1e-4	13.92 ± 0.41	-
0.9	1.0163 ± 1e-4	2.51 ± 0.06	-	1.0096 ± 1e-4	2.38 ± 0.03	-
1.0	0.0010 ± 1e-4	0.69 ± 0.01	64.6 ± 0.1	0.9903 ± 1e-4	0.69 ± 0.01	64.6 ± 0.1

C. Appendix

Coarse-grained force field

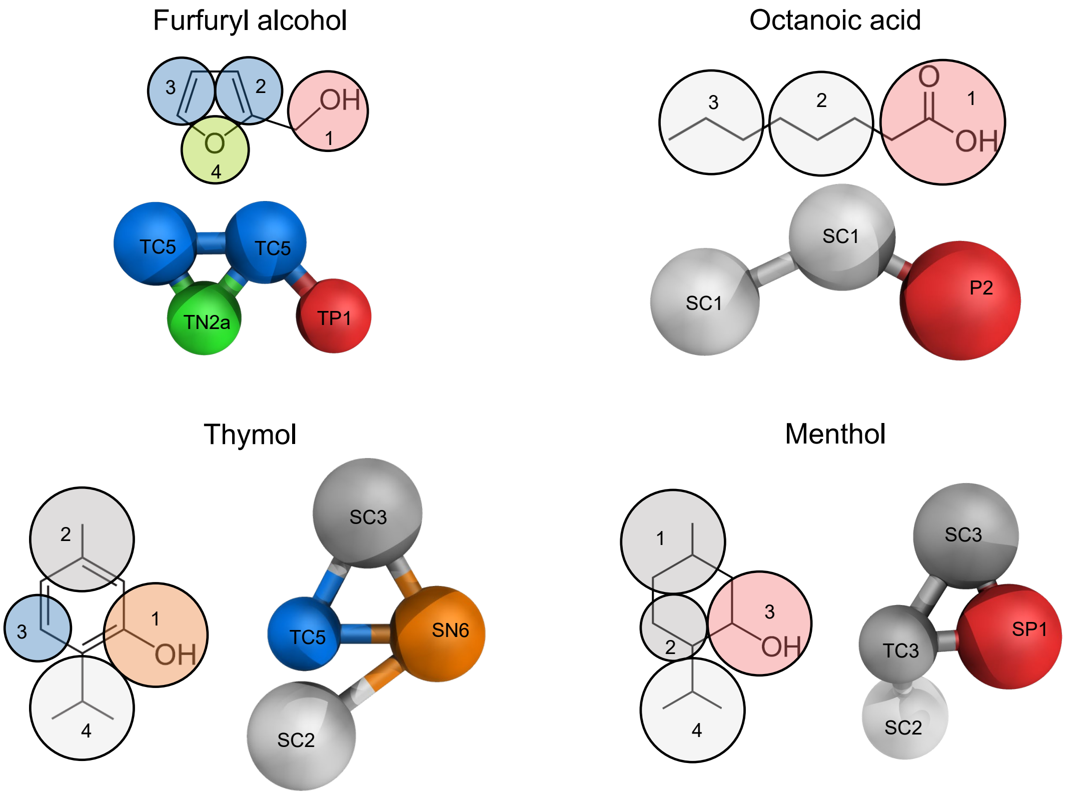
Furfuryl alcohol

Octanoic acid

Thymol

Menthol

FIGURE C.1: Coarse-grained (CG) mappings for furfuryl alcohol, octanoic acid, thymol and menthol.

Furfuryl alcohol

TABLE C.1: Bead types and masses of furfuryl alcohol.

Number	**Bead** type	**Mass**
1	TP1	31.03
2	TC5	25.03
3	TC5	26.04
4	TN2a	16.00

TABLE C.2: Bonded interactions parameters of furfuryl alcohol.

Bonded interactions		**func. type**	**Reference**	**Force constant**
Bond stretching	1 - 2	1	0.250 nm	5000 kJ mol^{-1} nm^{-2}
Constraint distance	2 - 3	1	0.260 nm	
Constraint distance	3 - 4	1	0.240 nm	
Constraint distance	2 - 4	1	0.240 nm	
Angle vibration	1 - 2 - 3	2	130°	1000 kJ mol^{-1}

Octanoic acid

TABLE C.3: Bead types and masses of octanoic acid.

Number	**Bead type**	**Mass**
1	P2	59.02
2	SC1	42.08
3	SC1	43.09

TABLE C.4: Bonded interactions parameters of octanoic acid.

Bonded interactions		**func. type**	**Reference**	**Force constant**
Bond stretching	1 - 2	1	0.340 nm	5000 kJ mol^{-1} nm^{-2}
Bond stretching	2 - 3	1	0.380 nm	5000 kJ mol^{-1} nm^{-2}
Angle vibration	1 - 2 - 3	2	140°	100 kJ mol^{-1}

Thymol

TABLE C.5: Bead types and masses of thymol.

Number	Bead type	Mass
1	SN6	42.0
2	SC3	40.0
3	TC5	25.0
4	SC2	43.0

TABLE C.6: Bonded interactions parameters of thymol.

Bonded interactions		func. type	Reference	Force constant
Bond stretching	1 - 4	1	0.350 nm	5000 kJ mol^{-1} nm^{-2}
Constraint distance	1 - 2	1	0.320 nm	
Constraint distance	1 - 3	1	0.275 nm	
Constraint distance	2 - 3	1	0.290 nm	
Angle vibration	2 - 1 - 4	2	100°	250 kJ mol^{-1}
Angle vibration	2 - 3 - 4	2	145°	250 kJ mol^{-1}

Menthol

Parameters retrieved from Vainikka et al. [374]

TABLE C.7: Bead types and masses of menthol.

Number	Bead type	Mass
1	SC3	39.0
2	TC3	27.0
3	SP1	44.0
4	SC2	43.0

TABLE C.8: Bonded interactions parameters of menthol.

Bonded interactions		**func. type**	**Reference**	**Force constant**
Bond stretching	2 - 4	1	0.365 nm	5000 kJ mol^{-1} nm^{-2}
Constraint distance	1 - 2	1	0.250 nm	
Constraint distance	1 - 3	1	0.300 nm	
Constraint distance	2 - 3	1	0.320 nm	
Angle vibration	1 - 2 - 3	1	60°	100 kJ mol^{-1} rad^{-2}
Angle vibration	1 - 3 - 2	1	50°	200 kJ mol^{-1} rad^{-2}
Angle vibration	4 - 2 - 1	1	125°	250 kJ mol^{-1} rad^{-2}
Angle vibration	4 - 3 - 1	1	110°	250 kJ mol^{-1} rad^{-2}

1H-NMR spectrum analysis

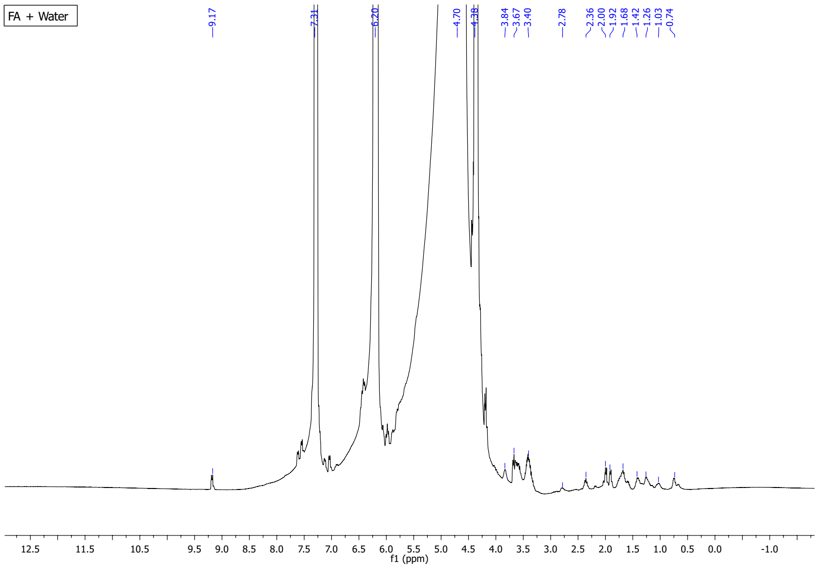

FIGURE C.2: ^{1}H-NMR spectra for the binary system composed of furfuryl alcohol (FA) + water.

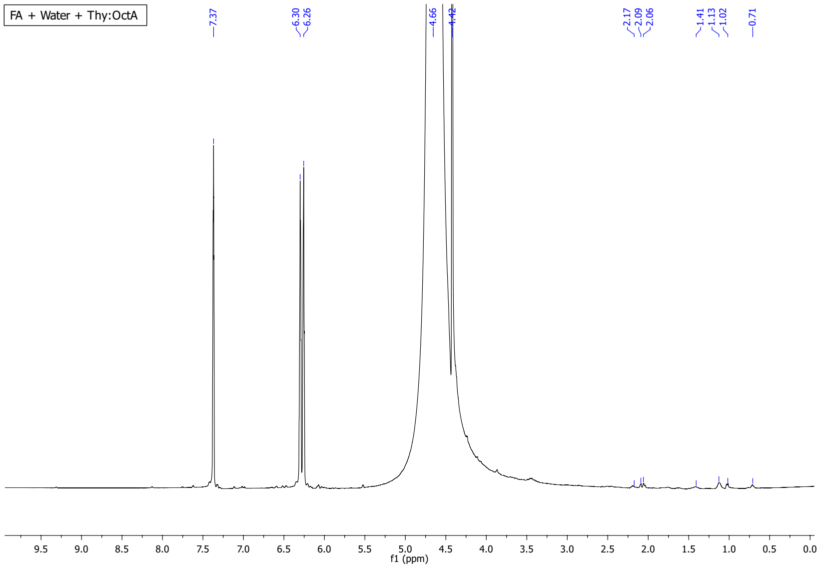

FIGURE C.3: ^{1}H-NMR spectra for detecting DES in the aqueous phase of the ternary system composed of furfuryl alcohol (FA) + water + Thy:OctA(1:2) at equilibrium conditions.

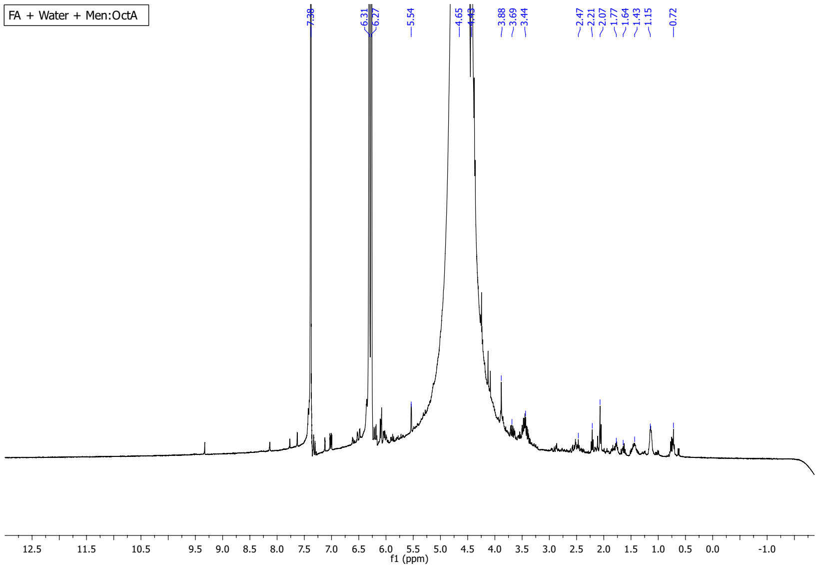

FIGURE C.4: ^{1}H-NMR spectra for detecting DES in the aqueous phase of the ternary system composed of furfuryl alcohol (FA) + water + Men:OctA(1:2) at equilibrium conditions.

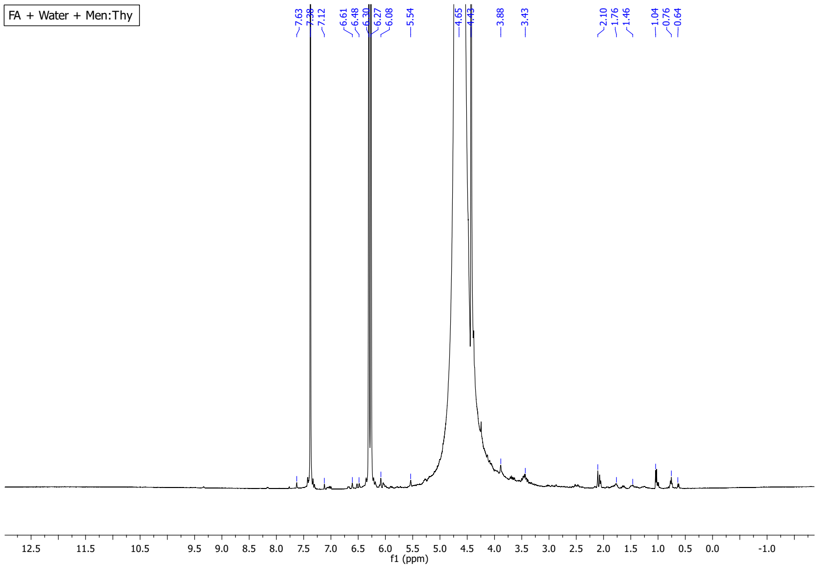

FIGURE C.5: ^{1}H-NMR spectra for detecting DES in the aqueous phase of the ternary system composed of furfuryl alcohol (FA) + water + Men:Thy(1:1) at equilibrium conditions.

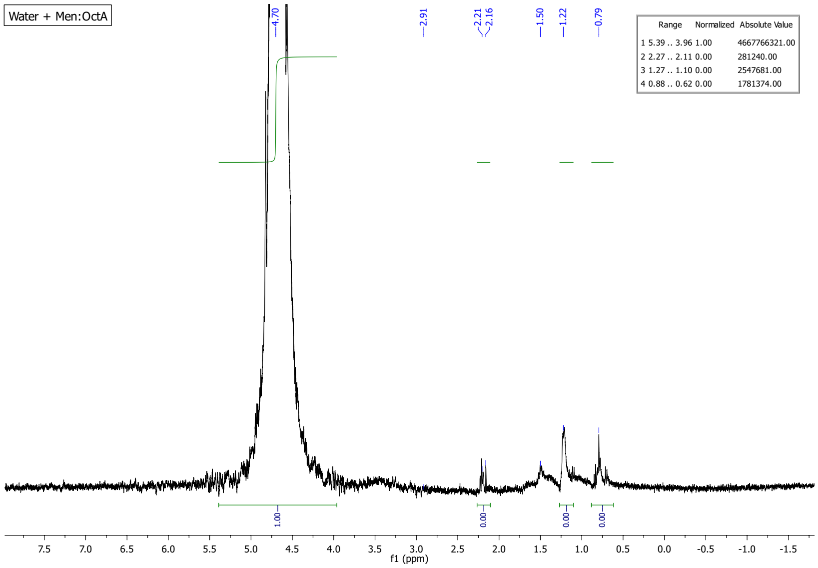

	Range	Normalized	Absolute Value
1	5.39 .. 3.96	1.00	4667766321.00
2	2.27 .. 2.11	0.00	281240.00
3	1.27 .. 1.10	0.00	2547681.00
4	0.88 .. 0.62	0.00	1781374.00

FIGURE C.6: ^{1}H-NMR spectra for detecting DES in the aqueous phase of the binary system composed of water + Men:OctA(1:2) at equilibrium conditions.

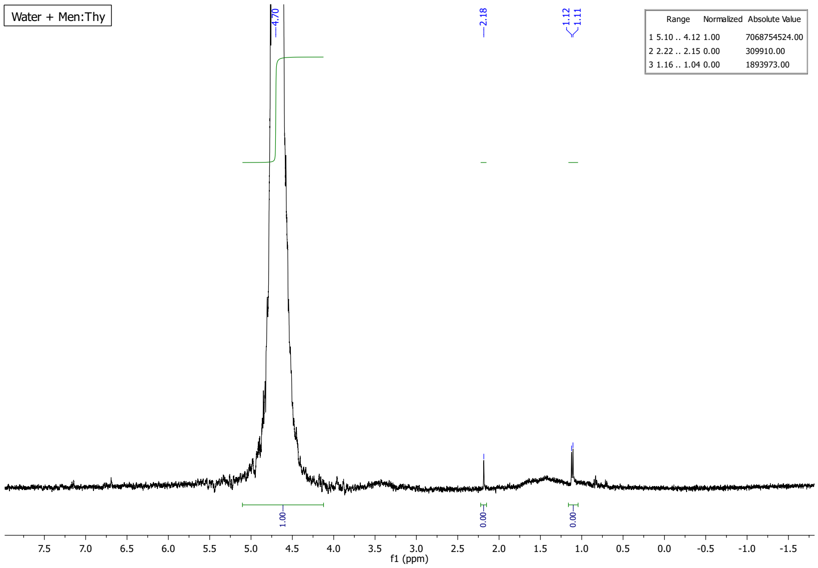

	Range	Normalized	Absolute Value
1	5.10 .. 4.12	1.00	7068754524.00
2	2.22 .. 2.15	0.00	309910.00
3	1.16 .. 1.04	0.00	1893973.00

FIGURE C.7: ^{1}H-NMR spectra for detecting DES in the aqueous phase of the binary system composed of water + Men:Thy(1:1) at equilibrium conditions.